DISSERTATION

Simulation based Neutron Background Studies for the CRESST and COSINUS Dark Matter Search Experiments

ausgeführt am

Atominstitut (ATI)
der Technischen Universität Wien

Institut für Hochenergiephysik
der Österreichischen Akademie der Wissenschaften

zum Zwecke der Erlangung des akademischen Grades eines
Doktors der Technischen Wissenschaften

unter der Anleitung von
Univ.Prof. Dipl.-Phys. Dr.rer.nat. Jochen Schieck
Dipl.-Phys. Dr.rer.nat. Holger Kluck
Ass. Prof. Dipl.-Phys. Dr.rer.nat. Florian Reindl

durch
Dipl.-Ing. Alexander Fuß, BSc
Matrikelnummer: 01026908

eingereicht an der Technischen Universität Wien
Fakultät für Physik

Wien, Oktober 2022

Only the disciplined ones in life are free. If you are undisciplined, you are a slave to your moods and your passions.

- Eliud Kipchoge

Kurzfassung

Dunkle Materie ist eines der größten Mysterien der modernen Physik und das Streben nach Erforschung ihrer Natur daher ein hochaktuelles Forschungsgebiet. Während zahlreiche Beobachtungen zu einem breiten wissenschaftlichen Konsens über die Existenz dieser postulierten Form von Materie geführt haben, fehlt weiterhin ein endgültiger Beweis. Experimente nutzen komplementäre Techniken, um einen möglichst breiten Bereich an denkbaren Teilchenmassen und Interaktionsmechanismen zu untersuchen. Durch direkte Detektion wird versucht, Interaktionen von in unserem galktischen Halo befindlichen Dunkle Materie-Teilchen mit Atomen in Detektoren auf der Erde nachzuweisen.

CRESST ist eines der führenden Experimente im Bereich der direkten Suche nach leichten Dunkle Materie-Teilchen unter Verwendung kryogener Detektoren. Wärme und Szintillationslicht werden simultan gemessen, um die Unterscheidung der Untergrund-Signale, induziert durch Elektronen und Gammas, von Kernrückstößen, die von Dunkler Materie erwartet werden, zu ermöglichen und dadurch die Sensitivität des Experiments zu steigern.

Auf Basis der in CRESST entwickelten Detektor-Technologie startet nun auch das COSINUS Experiment, welches die Resultate der DAMA/LIBRA-Kollaboration überprüfen will. Diese misst seit Jahren ein moduliertes Signal, das von seinen Verfechtern bereits als experimenteller Beweis für die Existenz Dunkler Materie angesehen wird, aber nicht allgemein anerkannt ist.

Sowohl in CRESST als auch in COSINUS bilden Kernrückstöße, die von Neutronen verursacht werden, Hintergrundsignale, welche ununterscheidbar von erwarteten Signalen induziert durch Dunkle Materie sind. Deshalb ist die Minimierung des Neutronen-Untergrundes von höchster Priorität. Die Experimente befinden sich daher zur Abschirmung von Myonen in Untergrundlaboren und nutzen speziell ausgewählte Materialien in der Umgebung ihrer Detektoren zur zusätzlichen Reduktion Myonen-induzierter Neutronen und Umgebungsneutronen.

In der vorliegenden Arbeit werden Studien des Neutron-Untergrundes in CRESST und COSINUS präsentiert. Zu diesem Zweck wurde die genaue Geometrie der experimentellen Aufbauten in einem Geant4-basierten Teilchensimulationsprogramm implementiert. Zusätzlich zu den vorhandenen Methoden im Simulations-Toolkit wurden weitere notwendige Funktionen zur Simulation von Myon-induzierten und durch (α,n)-

Prozesse oder spontane Kernspaltung entstandenen Neutronen programmiert. Um simulierte Daten mit Messungen vergleichen zu können, wurde außerdem ein Postprozessierungs-Algorithmus weiterentwickelt, welcher die Zeit- und Energieauflösung der Detektoren berücksichtigt.

Im Vergleich zu älteren Studien werden erstmals ein zusätzliches inneres Polyethylen-Schild und das neue CRESST-III Detektor-Design berücksichtigt. Außerdem beschreibt diese Arbeit erstmals den Neutronen-Untergrund in CRESST bis hinab zur Nachweisgrenze der aktuellen Detektoren im Bereich von $\mathcal{O}(10..100\,\mathrm{eV})$. Da die Energiekalibrierung bei diesen niedrigen Energien äußerst wichtig ist, werden neue Kalibrierungsmethoden mittels Neutronen vorgeschlagen.

Für COSINUS präsentiert diese Arbeit die Simulationsstudien, welche die Grundlage für das Design der passiven Abschirmung und für den Aufbau des Myon-Vetos darstellen. Die Konstruktion des experimentellen Aufbaus ist während Verschriftlichung dieser Arbeit bereits im Gange.

Die in der vorliegenden Arbeit enthaltenen Ergebnisse liefern sowohl für CRESST als auch COSINUS essentielle Beiträge zur Interpretation der gemessenen Signale und zur Evaluierung und weiteren Planung der Abschirmungskonzepte.

Abstract

The true nature of dark matter is one of the key puzzles in modern physics. While large scientific consensus has been achieved about its existence, in contrast to theories about modified gravity, an experimental proof still has to be found. Various experiments are employing complementary techniques to probe different masses and interaction mechanisms of potential dark matter particles. With so-called direct searches, dark matter in our local galactic halo shall be probed.

CRESST has lead the path for direct detection searches over many years, pioneering the development of cryogenic detectors, especially suited for detection of low-mass dark matter. A simultaneous phonon and scintillation light read-out is used for particle detection and discrimination. Looking for dark matter-induced nuclear recoils, this method leads to great reduction of the background due to electrons and gammas.

Employing the same detection technique but different target material (NaI instead of $CaWO_4$), the COSINUS experiment is aiming to cross-check the results of the DAMA/LIBRA experiment. DAMA/LIBRA is reporting an annually modulated signal interpreted by its proponents as an actual model-independent evidence of galactic dark matter. However, this interpretation is not generally accepted by the community. COSINUS will thus use the same target material as DAMA/LIBRA, i.e. NaI, and is currently in prototyping and early construction phase.

In both CRESST and COSINUS, neutrons entering the detectors can lead to nuclear recoils indistinguishable from a dark matter-induced signal and are thus considered a dangerous background. To shield against neutrons and other types of background, the experimental setups are hence located in deep underground laboratories and use dedicated shielding layers surrounding their detectors.

This work presents neutron background simulation studies performed for CRESST and COSINUS to estimate the spectra, rates and sources of detectable neutrons. For this purpose, the detailed geometry of the corresponding setup was implemented in a Geant4-based particle simulation software, together with many new features necessary to perform the desired simulations of neutrons originating from muon interactions, (α,n) reactions and spontaneous fission processes. To compare to measured data, a postprocessing tool was greatly extended, considering the time and energy resolution of the detectors.

For CRESST, this work is the first neutron background study taking into account an additional inner polyethylene shielding as well as the latest CRESST-III detector design. Furthermore, this work constitutes a principal study of the spectral shape and rate of the neutron background in CRESST at energies as low as $\mathcal{O}(10..100\,\mathrm{eV})$, at the currently achieved detector thresholds. In addition, the potential for new neutron-based calibration techniques are discussed which are crucial in this low-energy regime.

With COSINUS currently being on the verge of building the experimental setup, the studies in this thesis have formed the basis of the passive shielding design as well as of the layout of the active muon veto.

For both experiments, the results presented in this work provide crucial contributions to the understanding and interpretation of measured signals as well as to the development and evaluation of the shielding geometries and background models.

Contents

1 Introduction

The nature of dark matter (DM) is one of the big remaining mysteries in modern cosmology and astro-particle physics. Our standard cosmological model predicts a form of non-luminous, non-baryonic matter accounting for more than 80 percent of the total matter density in the observable universe [1]. While this prediction is quite robust against concurring theories and supported by various cosmological observations lead by precision measurements of the cosmic microwave background (CMB), we still lack an experimental proof [2]. Various experiments are thus currently searching for dark matter via collider-based, indirect or direct detection techniques, with the latter having the advantage of directly probing features of our proposed galactic dark matter halo. A prominent dark matter candidate are so-called weakly interacting massive particles (WIMPs), thus searched for by many experiments, while still a large variety of other particle candidates exists [3].

Among the direct search experiments, CRESST [4] (Cryogenic Rare Event Search with Superconducting Thermometers) has pioneered developing cryogenic detectors with a two-channel read-out based on phonon and scintillation light signals used for particle discrimination [5]. As WIMP-like dark matter is expected to interact with the nuclei in the target, this technique allows to vastly reduce the background due to electrons and gammas depositing energy in the detectors mainly via interactions with electrons. On the other hand, neutrons entering the detectors can lead to nuclear recoils indistinguishable from a dark matter induced signal and may hence be considered the most critical background.

Employing the same detection technique but different target material (NaI instead of $CaWO_4$), the COSINUS [6] (Cryogenic Observatory for SIgnatures seen in Next-generation Underground Searches) experiment is aiming to probe the results of the DAMA/LIBRA experiment [7], reporting an annually modulated signal interpreted by its proponents as a model-independent evidence of galactic dark matter. COSINUS uses the same target material as DAMA/LIBRA, i.e. NaI, and is currently in prototyping and construction phase.

This thesis comprises studies of the neutron background based on Monte Carlo simulations, crucial for the understanding and interpretation of measured signals and for the evaluation of the employed experimental geometries in both CRESST and COSINUS. There are two principal sources for neutrons: muon-induced neutrons produced in interactions of cosmic muons, and radiogenic neutrons originating from (α,n) and spontaneous fission processes due to radioactive contamination in materials surrounding the detectors. An integrate investigation of both sources, and hence of the total neutron background is the main topic of this work.

In both experiments, the setup is located at a deep underground laboratory in order to shield the detectors against cosmic radiation. In addition, detectors are surrounded by layers of passive shields, i.e. distinct materials serving the purpose of minimizing the event rate due to known external background sources. In CRESST, most parts of the respective shielding are in place since many years. However, this study is the first neutron background estimation taking into account an internal part of the passive neutron shielding that was added in 2012. Furthermore, for the first time the latest detector design, i.e. the so-called CRESST-III design, is considered. As the current detectors enable CRESST to measure nuclear recoils of energies as low as $\mathcal{O}(10..100\,\mathrm{eV})$, this study in addition allows to test the validity of the simulation models at unprecedentedly low nuclear recoil energies. In this energy regime, a further pressing topic are suitable energy calibration sources. Inelastic neutron interactions are investigated as a candidate for providing sub-keV signals potentially being able to serve this purpose. The COSINUS simulation studies presented in this thesis, on the other hand, form the basis of the planned shielding geometry. A careful evaluation of the results has lead to choosing the design which minimizes the external background and is being constructed at the time of writing this thesis.

Necessary for the simulation study in both cases is a reconstruction of the core experimental geometry in a general purpose Monte Carlo simulation framework. Additionally, a set of new features has to be implemented in the code to enable the possibility to simulate homogeneous bulk contaminations in shielding materials yielding radiogenic neutrons, and muons reaching the underground laboratory leading to muon-induced neutrons.

As CRESST has already collected data over the past years, the simulations can be validated against neutron calibration data and, if statistics allows to, against background recorded during the physics data taking campaigns. To provide a realistic neutron background model, the characteristics of the detectors – e.g. energy resolution, threshold and signal survival probability – have to be taken into account. Hence, a postprocessing scheme for signal reconstruction based on the simulated data collected in multiple detectors is developed. Finally, the attained background rates and spectra are used to determine the contributions of neutrons to CRESST's background budget and to discuss potential improvements of the shielding design. Furthermore, the results of this work are valuable inputs to improve CRESST's data analysis by further constraining the likelihood fit used for exclusion limit calculations and increasing its sensitivity to possible unknown signals.

The shielding design of COSINUS uses a water based Cherenkov detector to passively shield and actively veto neutrons. With the principal simulation campaign presented in this work, initially the passive shielding design has been evaluated and optimized. At the start of this work, the cryostat and detector geometries had not yet been finalized. Hence, this study started with a preliminary design and was successively updated in accordance with the design progress. After fixing the passive shielding design, dedicated simulations were performed to assess the efficiency of an active Cherenkov veto. Various arrangements of photo multiplier tubes (PMTs) and the impact of a reflective foil at the tank walls were evaluated considering different trigger conditions.

Guiding through this work, Chapter 2 gives a historical overview about dark matter research, deals with particle candidates and detection methods and describes the current status of the research. In Chapter 3, particle-induced backgrounds limiting the sensitivity of obtained results, with a focus on direct detection experiments, are discussed. Chapter 4 deals with the Monte Carlo simulation of neutron interactions and the implementation in a Geant4 based simulation code, before entering the main parts of this work, the simulation studies conducted for CRESST and COSINUS. These are presented in Chapter 5 and 6, respectively. Chapter 5 first describes the CRESST experiment in all relevant aspects and then discusses the neutron calibration and background simulations and their results. Afterwards, Chapter 6 provides a detailed description of COSINUS, mentioning its motivation and physics goals, followed by a presentation of the simulations establishing the passive and active shielding design of the experiment. Finally, after the separate conclusions on the CRESST and COSINUS studies, a summary is provided in Chapter 7.

2 | Dark Matter

This chapter serves as an introduction to dark matter, starting from a historical overview on the development of the idea that additional matter exists in the universe. The observational evidence collected over the years as well as the standard cosmological model incorporating dark matter are then discussed. Finally, candidates for dark matter are mentioned, followed by the various complementary approaches in the experimental searches for them.

2.1 A Historical Overview

For a historical view on how the concept of dark matter evolved, one has to look much further back than to the famous work by Fritz Zwicky in the 1930s and Vera Rubin in the 1970s, often quoted as the birth of dark matter research. The history of the evolution of cosmological models and finally the idea of dark matter is long and rich of details. In the following, only a condensed overview shall thus be given. For more details, the reader is referred to Ref. [8] and references therein.

Humankind has always had the urge to explore and to understand the world we live in. The ancient Greeks may have been the first to construct a simple cosmological model based on observations and ideas [8]. While the geocentric model described in detail by Aristotle has been the most accepted description of the universe as known at that time, it shall be left to historians to explain the emergence of controversies between advocates of geocentric and heliocentric models. The important point at this stage is that the models were based on observations made with the bare eyes.

New technology was necessary to look deeper into the universe and gain more understanding of its constituents, which became possible in the early 17th century via the invention of the telescope by Galileo. Newton's laws of gravity, published in 1687 [9], additionally allowed for a theoretical description of the dynamics of astronomical objects. With these new tools in hand, new discoveries were possible.

In 1844, possibly the first prediction of undiscovered astronomical bodies, companion stars of Sirius and Procyon, was made solely based on the gravitational effects observed in their surrounding [8, 10]. The same happened in 1846 when the planet Neptune was predicted due to the study of the motion of Uranus [11]. It was around the late

19th century that scientists then furthermore started discussing the possibility of dark objects in the universe, that may only be seen indirectly due to bright objects in their background [12, 13].

Beginning of the 20th century, it was Lord Kelvin who provided a first estimation of dark bodies in the milky way by applying the theory of gases as an approximation, assuming that the stars act like particles in a gas interacting via gravity. He famously wrote: "Many of our stars, perhaps a great majority of them, may be dark bodies" [14]. Henri Poincaré, referring to Kelvin's work in 1906, introduced the phrase "matière obscure" [15] which to date still is the French term for dark matter. Following up on these principal ideas, the astronomers James Jeans [16], Bertil Lindblad [17], Jacobus Kapteyn and his student Jan Oort [18] made the next steps in describing the size and shape of the Milky Way and the motion of stars within it. With their work, they pioneered calculations of upper limits and estimates of the local dark matter density.

The next milestone was achieved via the study of galaxy clusters by the probably most cited trailblazer in dark matter research, Fritz Zwicky. He studied the redshifts of galaxies in the Coma Cluster to estimate the velocity dispersion and compared it to the expected dispersion calculated from the average kinetic energy attained via applying the virial theorem. Finding that the observed velocity dispersion was much larger than the one expected, he concluded that, if confirmed, the amount of dark matter in the Coma Cluster would be much larger than the amount of luminous matter [19]. Further galaxy clusters were studied over the coming years, with findings for example compiled by Martin Schwarzschild in 1954 [20]. While the scientific community was still divided about the dark matter hypothesis in the 1960s, studies and ideas evolved around the potential constituents of the missing mass [8], all still based on configurations of known baryonic matter. The studies of velocity dispersions in galaxies continued based on optical spectrographs as well as new radio telescopes observing the 21 cm line caused by atomic hydrogen. Many scientists contributed to the research. Here, the works by Morton Roberts [21] and Kenneth Freeman [22] on rotation curves based on the 21 cm line as well as the optical studies by Vera Rubin and collaborators [23, 24] shall be mentioned as some of the most famous. The rather flat rotation curves found in their work yielded and confirmed theories regarding dark matter halos extending to large radii.

In the 1980s and 1990s, a prominent candidate for the missing mass were compact objects made of baryonic matter, similar to stars, but almost non-luminous. With the new technique of gravitational lensing, scientists tried to search for such objects via microlensing effects when observing galaxies. While first results by the MACHO [25] and the EROS [26] collaborations in 1993 seemed promising, the results after a few years of data taking showed that such objects cannot account for the majority of the missing mass [27]. Around the same time, the measurements of the baryon density in the universe became more and more precise. At the end of the 1990s, measurements of the primordial deuterium abundance (e.g. [28]) and early studies of the cosmic microwave background (e.g. [29, 30]) began to show that there is very little room for additional baryonic matter in galaxies.

From this time until today, precision measurements and detailed observations continued (e.g. [1, 31]) and various mainly non-baryonic candidates for dark matter were discussed, some of which will be introduced in Section 2.4. In parallel, theories of modified gravitational laws evolved [32], omitting the need for additional matter. At the current status of research, the latter have been driven into a narrow corner by various observations (e.g. [33]). In the following section, a summary of current observational evidence for dark matter and its implications is presented, before describing the standard cosmological model as of today.

2.2 Current Observational Evidence

Throughout the brief historical recap of dark matter research in the previous section, a few observations which lead to the introduction of dark matter to the cosmological model as well as studies which further constrained its amount and characteristics have already been discussed. However, a list of the main observational evidence together with some implications shall be presented in the following.

Velocity Distribution in Large Gravitationally Bound Systems

Observations of velocity distributions in large gravitationally bound systems started in the 1930s with Zwicky. Later studies were able to more precise probe the motion of galaxies in clusters as well as individual rotation curves of stars around their galactic center. In all cases, it was found that the velocities do not follow the expectation considering solely the gravitational force of all luminous matter [20]. Outer stars in spiral galaxies, for example, in this model should follow a similar velocity distribution as planets in our Solar system. Balancing the gravitational force with the centrifugal force, one finds that the velocity should decrease with the square root of the radius of their orbit around the center of the galaxy,

$$v = \sqrt{\frac{G \cdot M}{r}} \quad .$$

However, many studied galaxies feature almost constant velocities over a large radial distance, see Figure 2.1 as an example. A potential solution to this observation would be a spherical halo of dark matter, extending beyond the outskirts of the visible galaxy. This would lead to an additional contribution

$$v_{\mathrm{a}} = \sqrt{\frac{G \cdot M_{DM}(r)}{r}}$$

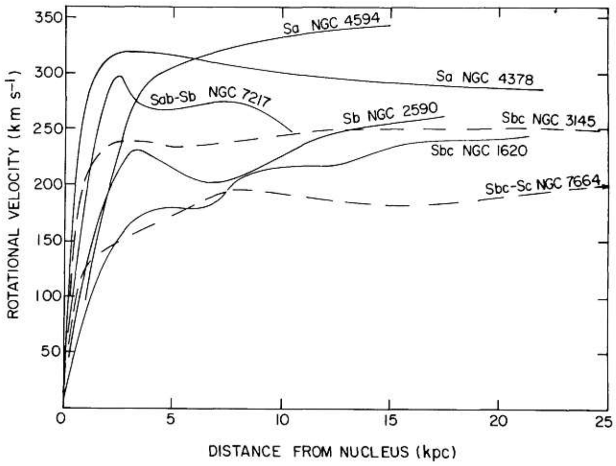

Figure 2.1.: Galaxy rotation curves as published in Ref. [24].

to the velocity distribution, where the dark matter mass $M_{DM}(r)$ inside the orbital radius r would increase with distance. Hence, depending on the density distribution, also the velocity may increase with r, together with the decrease due to luminous matter leading to a rather flat observation.

Gravitational Lensing

Gravitational lensing is an effect that was postulated within the model of general relativity. In this geometrical description, massive objects warp spacetime such that light from distant sources, following the geodesics, is bent on the path to the observer. In other words, they act as optical lenses. In the case of highly dense lenses, the effect can lead to the observation of multiple images of the background source or to light arcs and so-called Einstein rings. These phenomena are summarized as strong gravitational lensing effects. In weak gravitational lensing, on the other hand, distorted images of the background are observed and the positions and shapes of multiple background sources have to be statistically analyzed in order to make a statement about the mass distribution in the foreground. For a review about gravitational lensing see [34].

With respect to dark matter, the most attractive studies using weak gravitational lensing are those of colliding galaxy clusters. Here, the explanation will focus on a prominent example, the so-called Bullet Cluster [35], shown in Figure 2.2. However, the same findings have been confirmed in the study of additional cluster collisions. In Figure 2.2, the distribution of matter in the colliding clusters is colored with respect to two different observables. In blue, the matter distribution according to the gravitational lensing study is shown, while the pink distribution is the result of an X-ray survey. This picture can be understood as follows. If two galaxies collide, the compact objects like stars and planets pass each other almost entirely without being affected, except for the

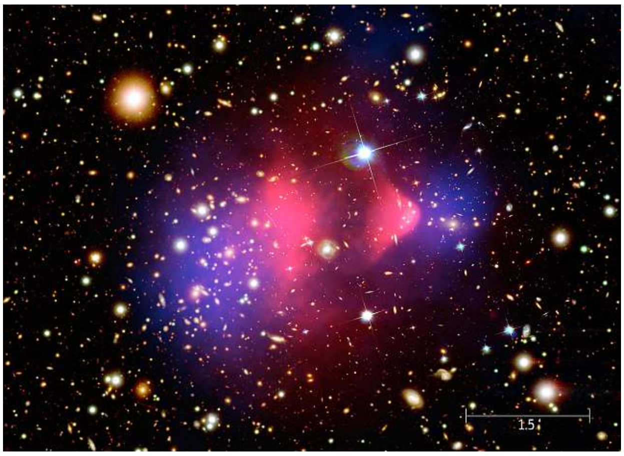

Figure 2.2.: Picture of the Bullet Cluster, showing the matter distribution according to weak gravitational lensing (blue) as well as X-ray observations (pink) [36].

small gravitational interaction. The mean distances are too large to lead to collisions for the majority of these objects. On the other hand, the intergalactic gas interacts electromagnetically and gets slowed down significantly as visible in X-ray observations. As the gas amounts for the majority of luminous matter in the galaxy clusters, the weak lensing mass distribution would be expected to coincide with its distribution, if all matter in the cluster was luminous. However, this is clearly not the case. While posing a challenge to modified gravity theories, dark matter could again explain the findings. Furthermore, the results strongly indicate that dark matter is non-baryonic. For the dark matter halos to pass through each other almost unaffectedly, it would additionally require them to either consist of compact objects or of particles with a rather weak or vanishing self-interaction.

Cosmic Microwave Background

The cosmic microwave background (CMB) is an imprint of radiation emitted at the time of recombination in the early universe. At a temperature above ~3000 K, the universe consisted of a photon-baryon plasma. Only after cooling down and expanding sufficiently, ~380,000 years after the Big Bang, stable neutral hydrogen atoms were formed and photons could travel freely without consistent interaction [2]. These photons emitted at the time of matter-radiation decoupling are still measurable today with their redshifted wavelength due to the expansion of the universe. The CMB features an almost perfect black body spectrum with a temperature of ~2.725 K. Only small deviations from isotropy in the measured spectrum can be found, which are in the order of 10^{-5}. These fluctuations can be decomposed in spherical harmonics and represented in an angular power spectrum. The most precise measurements of the CMB and its anisotropies have been performed by the WMAP [31] and Planck [1] satellites. A measurement of the

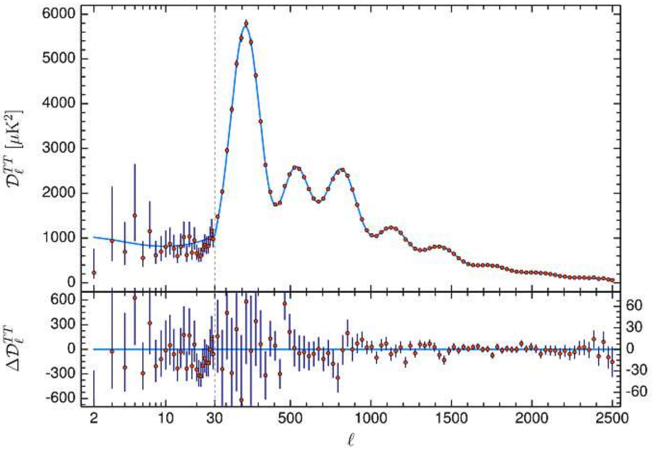

Figure 2.3.: CMB temperature power spectrum taken from Ref. [1].

temperature power spectrum together with a fit of the theoretical model (cf. Section 2.3) is shown in Figure 2.3. The distinct acoustic peaks yield important information about the parameters of the model and provide the most strict bounds on the constituents of the universe. While the location of the first peak represents the size of structures in the CMB and thus correlates with the curvature of the universe, the amplitudes of the subsequent peaks as well as the ratio between even and odd peaks determines the matter density and the relative contribution from baryonic and dark matter.

Structure Formation

Structure formation refers to the process of forming overdensities from small fluctuations in the almost homogenous universe after Big Bang, leading to stars, galaxies and large scale structure observed today. Before matter-radiation decoupling, overdensities are washed out via radiation pressure. Thus, ordinary matter is only able to condense into large structures after this period in time. However, calculations and simulations show that based on the initial conditions extracted from the CMB, the time would not have been sufficient to lead to the structure observed today. Based on estimates using the linear growth of fluctuations in a matter-dominated universe [2], the fluctuations in the CMB would have had to be about two orders of magnitude larger than observed. However, dark matter may solve the problem, as it does not interact with radiation and can thus decouple and form structures earlier. The decisive point in time for DM to form structures is the matter-radiation equality and the transition to a matter-dominated universe, where particles become non-relativistic [2]. The structure formed by dark matter then represents the seed for clustering of baryonic matter. This, however, is only possible if dark matter travels at non-relativistic speed at this period in time. If the condition is fulfilled, we speak of so-called cold dark matter (CDM). In the

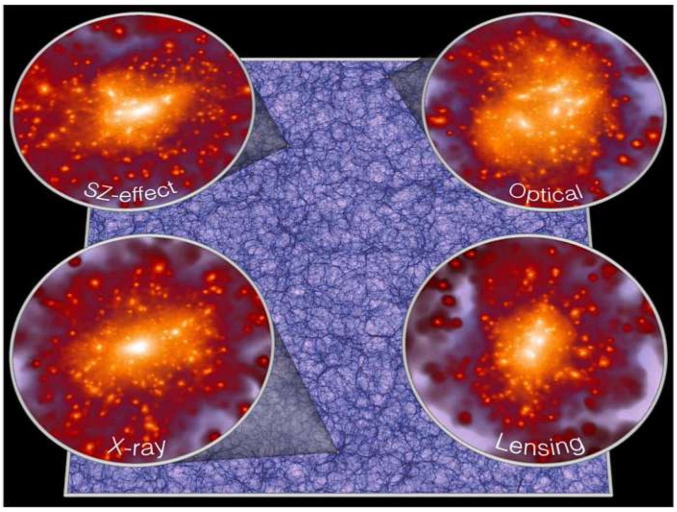

Figure 2.4.: Dark matter density in the Millennium-XXL simulation at redshift $z = 0.25$. A slice of 27 MPc thickness and 2050 MPc width is shown together with a zoom to the largest clusters identified when using four main observation techniques: Sunyaev-Zel'dovich signal, optical galaxy count, X-ray emission and gravitational lensing. The figure is taken from Ref. [39].

case of warm or hot dark matter, with velocities potentially extending close to the speed of light, clustering and structure formation would not be possible. With large N-body simulations based on initial conditions due to CMB measurements and assuming the ΛCDM model (cf. Section 2.3), large scale structures as observed today could be reconstructed. An example are the so-called Millennium simulations [37, 38]. Figure 2.4 shows an exemplary visualization of some of their results. Only using the prevalent CDM model in these simulations leads to the correct observations. Structure formation poses strict constraints on the velocity and thus on warm and hot dark matter models, providing an additional reason for the current standard cosmological model, which is described in the following section.

2.3 The ΛCDM Model

In the standard cosmological model of today, ordinary matter is accompanied by cold dark matter (CDM) and a cosmological constant Λ as the three main constituents of the energy density in the universe. Thus, the model is called ΛCDM. The dynamics of this model can be deduced from general relativity and the cosmological principle. In general relativity, a relation is made between the metric of spacetime and the energy content in the universe. Adding the cosmological constant, the Einstein equations [40] read

$$R_{\mu\nu} - \frac{1}{2}g_{\mu\nu}R + \Lambda g_{\mu\nu} = \frac{8\pi G}{c^4}T_{\mu\nu} \quad , \tag{2.1}$$

where $R_{\mu\nu}$ and R are the Ricci tensor and scalar, $g_{\mu\nu}$ the metric, G Newton's gravitational constant, and $T_{\mu\nu}$ the stress-energy tensor. The cosmological principle states that on large enough scale the universe is homogeneous and isotropic, yielding a diagonal metric tensor. For an expanding universe with scale factor $a(t)$, the corresponding line element in spherical coordinates is given by the Friedmann-Lemaître-Robertson-Walker metric as

$$ds^2 = dt^2 - a^2(t)\left[\frac{dr^2}{1-kr^2}r^2(d\theta^2 + sin^2\theta\, d\phi^2)\right] \quad , \tag{2.2}$$

with k denoting the curvature, taking the value -1, 0 or 1.

Solving for the expansion rate of the universe H, the first Friedmann equation is obtained,

$$H^2 = \left(\frac{\dot{a}}{a}\right)^2 = \frac{8\pi G}{3}\rho - \frac{kc^2}{a^2} + \frac{\Lambda c^2}{3} \quad , \tag{2.3}$$

which describes the evolution of the scale factor as a function of the matter density ρ, curvature and cosmological constant. With the second Friedmann equation,

$$\frac{\ddot{a}}{a} = \frac{\Lambda c^2}{3} - \frac{4\pi G}{3c^2}(\rho c^2 + 3p) \quad , \tag{2.4}$$

the interpretation of the cosmological constant as a negative pressure leading to an accelerated expansion furthermore becomes clear.

A present-day critical density,

$$\rho_c = \frac{3H_0^2}{8\pi G} \quad , \tag{2.5}$$

is obtained by setting both the curvature and the cosmological constant to zero. Hence, the critical density is that of a flat universe with zero vacuum energy density. Fractional contributions to the actual energy density in the universe are then defined via

$$\Omega_x = \frac{\rho_x(t_0)}{\rho_c} \quad . \tag{2.6}$$

Thus, the first Friedmann equation can be rewritten as

$$1 = \Omega_m - \Omega_k + \Omega_\Lambda \quad . \tag{2.7}$$

The first term on the right side, Ω_m, is further split up into the contributions due to baryonic matter Ω_b, dark matter Ω_c and radiation Ω_r. The respective values of all the contributions in this model can be obtained from a fit to measured data. In this context, an interpretation of the CMB observations gives the most precise bounds on all the model parameters. According to the latest results of the Planck collaboration

[1], the curvature of the universe is consistent with zero. The values obtained for matter and cosmological constant are $\Omega_m \approx 0.315$ and $\Omega_\Lambda \approx 0.685$, respectively, with contributions to the former by baryonic matter and dark matter of $\Omega_b \approx 0.049$ and $\Omega_c \approx 0.265$. According to the ΛCDM model, dark energy in the form of the cosmological constant, leading to the accelerated expansion of the universe, thus dominates the current universe. Ordinary matter makes up only about 5 % of the entire energy density and is five times less abundant than dark matter. An explanation for the nature of the latter, however, cannot be given through this model.

2.4 Dark Matter Candidate Theories

While the previous sections showed that there is overwhelming evidence for dark matter and that it is thus an important ingredient in the standard cosmological model, its manifestation in the universe is still unknown. Only some basic properties are assumed within the ΛCDM model. These follow from the observations discussed in Section 2.2. Dark matter, in this model, is assumed to be cold, non-baryonic, dissipationless (i.e. no dissipation via emission of photons) and almost collisionless (i.e. interaction with each other and with SM paticles only via gravity and potentially a weak force). Massive compact halo objects (MACHOs) made of baryonic matter have thus been excluded as a DM candidate end of the 1990s (cf. Section 2.1). However, compact objects formed before big bang nucleosynthesis, so-called primordial black holes (PBHs), could still contribute to the observed DM density. A detailed overview on current constraints regarding PBHs can be found in Ref. [41]. In the following, some of the more popular DM candidates as of today are presented.

2.4.1 Particle Dark Matter

The most widely accepted DM models postulate some form of new undiscovered particle(s). This particle, or at least the majority of these particles in case of a whole dark particle sector, would have to be non-baryonic and cold (CDM). Furthermore, their lifetime would have to be long compared to the age of the universe [42]. Upper bounds on their self-interaction cross section can be deduced [43] and the interaction with Standard Model (SM) particles, in addition to gravity, should be weak. As dark matter is observed to be non-luminous, the constraints on "milli-electric" charge are tight [44]. In the following, a few of the most popular particle candidates, as displayed in Figure 2.5, are discussed in alphabetical order.

Axions & ALPs

In the Standard Model of particle physics, CP violation in the strong interaction is predicted and would yield a neutron electric dipole moment (nEDM). However, a nEDM

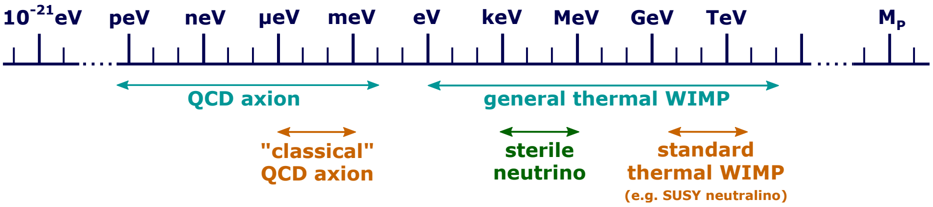

Figure 2.5.: Mass range of selected dark matter particle candidates on the entire spectrum of potential dark matter particle masses, adopted from Ref. [3].

is not found yet and constrained to much lower level than predicted. Thus, a cancellation via another term in the QCD Lagrangian would be necessary, an issue known as the strong CP problem. To resolve the problem, the Peccei-Quinn symmetry [45] can be introduced, which breaks spontaneously at a certain energy scale. From symmetry breaking, a pseudo Nambu Goldstone boson, the axion, arises which is found to be a viable dark matter candidate [46]. As any spontaneously broken U(1) symmetry would lead to similar particles, a variety of models could be constructed, which likewise lead to additional candidates. These particles are collectively called axion like particles (ALPs). For a detailed overview on this type of particles, the reader is referred to Ref. [47].

(Sterile) Neutrinos

In the analysis of the CMB data provided by the Planck collaboration [1], the neutrino contribution is assumed as a constituent of the matter density Ω_m, but provides only a very low share of it. Travelling at relativistic speed, they would furthermore only fit into a hot dark matter scenario, disfavoured by observed structure formation. Additionally, their masses might not be large enough to explain a large part of dark matter. However, the fact that neutrinos are not massless demands an extension to the SM. In such an extension, the existence of right-handed neutrinos may be suggested. These would only interact with the SM sector gravitationally and via their coupling to the left-handed neutrinos. Hence, they are called "sterile" neutrinos in contrast to the "active" left-handed neutrinos of the SM. In the so-called see-saw mechanism [48], the mass eigenvalues of active and sterile neutrinos would be inversely proportional, such that very low masses of active neutrinos would imply rather large masses of sterile neutrinos. Under certain conditions, these hypothesized particles could explain dark matter [49].

WIMPs

A very prominent class of dark matter candidates are so-called Weakly Interacting Massive Particles (WIMPs). These particles are hypothesized to be produced in the very early universe and stayed in thermal equilibrium with SM particles until the universe sufficiently cooled down, leading to their freeze-out from equilibrium. The observed relic density of dark matter can, in this model, be used to estimate the WIMP pair-annihilation cross section. To obtain the relic DM density, a cross section in the order of $10^{-36}\,\mathrm{cm}^2$ [3] is found, similar to the one in the weak interaction. The dependence on the mass of the DM particle is only minor, such that any GeV- to TeV-scale particle would lead to a cross section in this order of magnitude. Together with applying Fermi Theory, where the cross section is proportional to $\mathrm{G}_\mathrm{F}^2\mathrm{M}_\chi^2$ and hence a WIMP mass of a few GeV would be calculated, this statement is often referred to as the "WIMP miracle". The apparent coincidence triggered large scientific curiosity. While early searches focused on the typical electroweak (EW) scale, WIMP masses in principle are not well confined and to form a candidate for CDM could reach from the keV to the TeV scale [3]. WIMPs have been a prime research theme also because of the theory of supersymmetry (SUSY), which would naturally provide a particle candidate. In the minimal supersymmetric model (MSSM), this would be the neutralino, the lightest stable supersymmetric particle. As supersymmetric models are, however, strongly constrained today by LHC [50], further models and various mass scales are currently tested. Still, the WIMP paradigm is potentially the most eminent model of dark matter.

2.4.2 Modified Gravity

As an alternative to additional matter in the universe, theories about modified laws of gravity exist. They are motivated by the fact that to this day DM has only been indirectly observed via its gravitational interaction. Instead of introducing new massive particles accounting for this effect, some scientists advanced theories about the observable mass interacting differently on large scales [32, 51].

MOND

A model introduced in the early 1980s to explain galaxy rotation curves is called Modified Newtonian Dynamics (MOND) [32]. It proposes a simple modification of Newton's second law, $F = m\,a$, by introducing an interpolating function $\mu(\frac{a}{a_0})$, such that $F = m\,a\,\mu(\frac{a}{a_0})$. In the Newtonian and the so-called deep-MOND limits, the interpolating function has to approach 1 and $\frac{a}{a_0}$, respectively. However, in its original form, MOND does not obey conservation laws and has difficulties describing observations like gravitational lensing of colliding galaxy clusters and the CMB power spectrum. Thus, elaborate extensions are necessary, as discussed in the following.

TeVeS

Tensor-Vector-Scalar (TeVeS) [51] gravity is a relativistic extension to the MOND formalism. It complies with conservation laws and is able to provide explanations for gravitational lensing observations. However, the issue that not all cosmological observations can be interpreted persists. An exhaustive review on successes and limitations

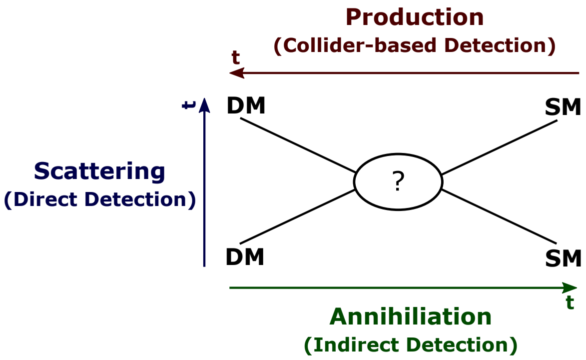

Figure 2.6.: DM interaction with SM particles and respective detection methods based on the time direction in the simplified Feynman diagram.

of theories on modified gravitational laws is presented in Ref. [52].

2.5 Detection Methods

The focus in this work from here on is set on particle DM and its sought-for detection. In this endeavor, different methods and techniques can be applied. Assuming DM and SM particles do not solely interact gravitationally, potential detection methods can be categorized by the time arrow in the associated Feynman diagram. Figure 2.6 summarizes the three categories which are individually discussed in the subsequent sections with a distinct focus on WIMPs.

2.5.1 Collider-based Searches

In high-energy particle collisions at colliders, a huge amount of secondary particles is created. Assuming some type of weak interaction between SM and DM particles and a collision energy large enough for DM pair production, pairs of DM particles may be produced. If the conditions are met, for example in the LHC, such processes may occur. However, as DM is assumed to be very weakly interacting, it would not create a signal in the surrounding detectors. It could thus only be observed via the missing transverse momentum it carries away. Other particles could mimic this behavior, such that a precise knowledge of the background is important for a detailed analysis. Neutrinos, for example, which can be created in large amounts in the particle collisions, also leave the detectors without depositing any energy. While such background can be reduced by carefully studying all observed event data to infer the number and energy of neutrinos, the residual uncertainty on the neutrino background can be large. Furthermore, if a new particle would be discovered via this method, it might still be unclear if it fulfils all the requirements for DM, e.g. being stable with respect to the age of the universe.

Complementary approaches to test DM are thus of utmost importance. For a review on collider-based searches and their role within the broader picture of DM searches, the reader is referred to Ref. [53].

2.5.2 Indirect Searches

Opposite to high-energy particle collisions, in which DM pairs may be produced, experiments can also search for DM via the inverse process, namely pair-annihilation. Respective approaches are called indirect searches, as inferences on DM particles are made solely via the observation of SM particles. Besides annihilation, decays of DM particles, for example of sterile neutrinos into active neutrinos, could lead to similar signatures. Annihilation and decay signals would be most prominently originating from regions of large DM density. Such regions are expected in the center of DM halos, i.e. in the center of galaxies and galaxy clusters. Depending on the type of DM particle, different final states are expected, such that complementary searches for the distinct signatures are necessary. Among the particles created in potential DM annihilation processes are photons. In this context, large gamma-ray telescopes are pointed at respective regions in the sky to analyze a potential excess over the astrophysical background. Another product of DM annihilation would be neutrinos. Large neutrino experiments are hence used to study the neutrino flux from the galactic center (GC) as well as from the Sun, where a substantial amount of dark matter may be gravitationally trapped. Apart from the electrically neutral photons and neutrinos, also charged SM particles can be created in DM annihilation. Their interactions, however, often prevent long path lengths, lead to diffusion and make it more difficile to detect and identify a respective signal on Earth. A comprehensive review of indirect searches for DM can be found in Ref. [54].

2.5.3 Direct Searches

Direct searches aim for the observation of DM-SM interactions in Earth-bound detectors based on the assumption that a non-vanishing local DM density exists. In this sense, direct searches are the unique class of DM searches that are sensitive to the local DM halo. This is at least true in searches for WIMP-like DM. On the other hand, in searches for axions and ALPs, in which strong magnetic fields are used to enhance the conversion probability to photons in the experimental setups, different approaches exist. While haloscopes probe the local DM halo, helioscopes test axions originating from the Sun and laboratory experiments try to produce axions and subsequently detect their reconversion into photons. Probably the majority of direct searches, however, is looking for WIMPs. The expected signal observed in the detectors then mainly depends on the assumed interaction mechanism and the particle mass. Usually, elastic and inelastic scattering off atomic nuclei is assumed. Due to the lack of electric charge and the comparatively large mass of WIMPs, scattering off electrons is expected to be less

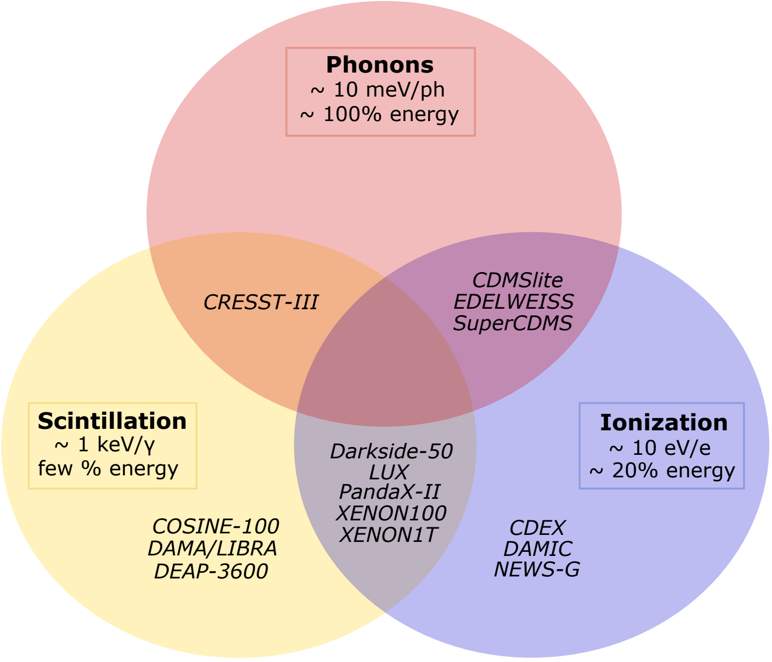

Figure 2.7.: Main detection channels in direct detection dark matter searches. Energies necessary for the creation of a single excitation or particle and percentage of total deposited energy available in the respective channel are given according to Ref. [55]. The values are a rough order of magnitude approximation and valid for electron recoils rather than nuclear recoils. In nuclear recoils, due to quenching, less energy may be available in the scintillation or ionization channels. A choice of experiments using different combinations of signal channels is listed based on the ones represented in the limit plot displayed in Figure 2.11.

likely. Based on these assumptions and on a model of the local DM halo, which will be discussed in the following section, data are analyzed in the search for the expected signal. To reduce the background, most of the direct search experiments are located in underground laboratories. An extended review of direct DM detection has lately been published in Ref. [3].

2.6 Event Signatures in Direct Searches

The work at hand focuses on direct detection experiments searching for WIMP-like DM. Thus, additional details on the detection principle and expected signatures are discussed in the following. The description starts with the signal channels that can be analyzed by direct detection searches, followed by the kinematics of the recoils and expected rate.

Direct Detection Channels

Figure 2.7 shows the three major signal channels used in direct detection experiments, i.e. phonon excitation, scintillation and ionization. It furthermore lists the typical percentage of total recoil energy available in the respective channel as well as the typical total energy deposition necessary for the creation of a single excitation in the respective channel. The stated values are an order of magnitude approximation considering electron recoils and primarily serve the purpose of illustrating the different sensitivity limits of the respective channels to low energy recoil signals. Experiments may employ a single- or multi-channel readout. The choice of experiments listed in the graphic is motivated by the ones represented in the exclusion limit plot displayed in Section 2.7.

While the phonon signal gives a robust measurement of the total deposited energy, only a few percent are converted to scintillation light in scintillators or to ionization in semiconductors. This percentage is particle-dependent and can, with a multi-channel readout, be used to discriminate between electron and nuclear recoils on an event-by-event basis. So-called quenching mechanisms lead to a reduced signal for nuclear recoils in both cases. The quantification of quenching factors (QFs) in different materials is extensively tested experimentally. In the case of scintillation, they may follow the Birks model [56], in the case of ionization the Lindhard model [57]. These models yield different QFs, such that a combination of scintillation and ionization readout still allows for particle discrimination. Single-channel detectors typically do not have this capability. Only in particular cases, pulse shape discrimination may be applicable for this purpose. Otherwise, an analysis of the attained data in these experiments relies on assumptions regarding the type of recoil obtained.

Scattering Theory

When calculating the expected recoil rate for a certain recoil energy, factors like the local velocity distribution of DM, the local DM density, the DM mass and the scattering cross section are playing a role. In the standard halo model (SHM) based on the assumption of isothermal spheres, some of these parameters are fixed. The DM velocity distribution $f(v)$ follows a Maxwell-Boltzmann distribution with a mean velocity equal to the rotation speed of the solar system around the GC, i.e. $\langle v \rangle \approx 220\,\mathrm{km/s}$, considering DM sitting in the galactic rest frame. It furthermore has a cut-off at the galactic escape velocity $v_{esc} \approx 544\,\mathrm{km/s}$. The local DM density in the SHM is assumed to be $0.3\,(\mathrm{GeV/c^2})/\mathrm{cm^3}$. These commonly used parameters in experimental data analysis are reviewed in Ref. [58], where additionally some shortcomings of this simplified model are discussed and updated model parameters are suggested, as the underlying model can slightly alter the calculated exclusion limits. The differential recoil rate for scattering off a target nucleus of mass m_N is given by

$$\frac{dR}{dE_R} = \frac{\rho_0}{m_N m_\chi} \int_{v_{min}}^{v_{esc}} v f(v) \frac{d\sigma}{dE_R} dv \quad . \tag{2.8}$$

If the halo model parameters are fixed, the remaining free parameters are the dark matter mass m_χ and the cross section $\frac{d\sigma}{dE_R}$. The minimum velocity v_{min} can easily be calculated from non-relativistic kinematics, where the recoil energy is given by

$$E_R = E_\chi \frac{2m_N m_\chi}{(m_N + m_\chi)^2}(1 - \cos\theta) = \frac{\mu^2 v^2}{m_N}(1 - \cos\theta) \quad , \tag{2.9}$$

with θ being the scattering angle and μ the reduced mass

$$\mu = \frac{m_N m_\chi}{m_N + m_\chi} \quad . \tag{2.10}$$

Assuming a head-on collision, leading to the maximum energy transfer, the minimum velocity to induce a recoil energy E_R can be written as

$$v_{min} = \sqrt{\frac{m_N E_R}{2\mu^2}} \quad . \tag{2.11}$$

Based on measured recoil spectra and rates in an experiment, Eq. 2.8 can then be used to calculate exclusion limits for pairs of DM masses and cross sections, where for the latter still an assumption on the interaction mechanism has to be made.

Typically, the cross section is split into a spin-independent and spin-dependent part, where the former is proportional to mass number squared and the latter to the net nuclear spin. Spin-dependent interaction can thus only be probed with target nuclei featuring an odd number of protons or neutrons. Spin-independent interactions, on the other hand, can be probed with any target, but are enhanced for heavy nuclei. However, heavy nuclei may lead to lower recoil energies, which are more difficult to detect, as the rate observed in the experiment is only obtained above the detector threshold E_{thresh}. The expected counts N can be calculated by integrating over Eq. 2.8,

$$N = M\,T \int_{E_{thresh}}^{E_R^{max}} \frac{dR}{dE_R}\epsilon(E_R)dE_R \quad , \tag{2.12}$$

where $\epsilon(E_R)$ is the energy-dependent efficiency to detect a recoil signal. M represents the detector mass and T the run time of the experiment, together forming the so-called exposure often quoted in units of kg·d. The upper bound of the integral is given by the maximum recoil energy, which in the SHM is defined by inserting the escape velocity in Eq. 2.9 and assuming a head-on collision,

$$E_R^{max} = E_\chi^{max} \frac{4m_N m_\chi}{(m_N + m_\chi)^2} = \frac{2\mu^2 v_{esc}^2}{m_N} \quad . \tag{2.13}$$

More important, however, is the lower bound given by the detector threshold, especially for low-mass DM searches, as the differential recoil rate can be described by a featureless

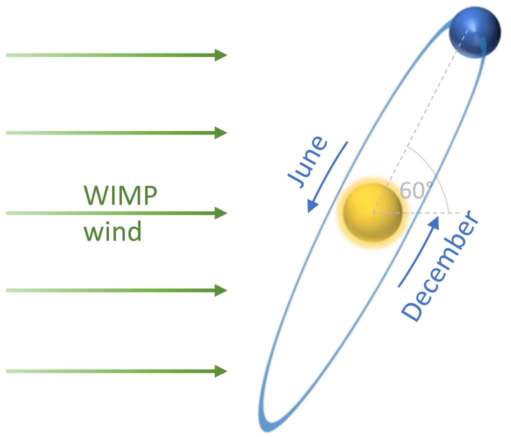

Figure 2.8.: Schematic picture of the movement of the Earth around the Sun with respect to the WIMP wind, leading to an annual modulation in the average relative velocity and thus the expected recoil rate.

exponentially falling spectrum [59],

$$\frac{dR}{dE_R} \sim \exp\left(-\frac{E_R}{E_0}\frac{4m_N m_\chi}{(m_N+m_\chi)^2}\right) \quad , \tag{2.14}$$

such that the largest part of the expected recoil spectrum is concentrated at low energies.

Annual Modulation

As stated above, the expected recoil energy spectrum due to DM particle scattering is featureless and exponentially falling. This can lead to difficulties discerning a DM signal from other particle-induced backgrounds which will be discussed in Section 3. However, experiments may search for ancillary signatures in the time domain of their attained data.

The solar system as a whole is exposed to the so-called WIMP wind. In the SHM, the average speed of this wind is calculated by adding the peculiar motion of the Sun to the local circular velocity with respect to the galactic rest frame. The Earth in addition rotates around the Sun with a speed of $v_\oplus \approx 30\,\text{km/s}$ at an inclined angle of $\theta \approx 60°$. This leads to a seasonal variation of the Earth's velocity through the DM halo. This velocity with respect to the WIMP wind can be written as

$$v_E = v_\odot + v_\oplus \cos\theta \cos\left(2\pi\frac{t-t_0}{T}\right) \quad , \tag{2.15}$$

where $v_\odot \approx 232\,\text{km/s}$, the period is $T = 1\,\text{yr}$ and the phase is $t_0 =$ June 2, which corresponds to the time when $v_\odot$ and $v_\oplus$ are perfectly aligned and add up to the maximal velocity v_E^{max}. The situation is schematically depicted in Figure 2.8.

Due to the modulated average velocity with respect to the WIMP wind, the obtained rate in direct detection experiments is also expected to feature an annual modulation. In first approximation, the differential recoil rate can be written as

$$\frac{dR}{dE_R}(E_R,t) \approx \left(\frac{dR}{dE_R}(E_R)\right)_0 + \left(\frac{dR}{dE_R}(E_R)\right)_m \cos\left(2\pi\frac{t-t_0}{T}\right) \quad , \qquad (2.16)$$

where the first summand is the unmodulated and the second summand the modulated rate.

The specific manifestation of the modulation, however, can be highly dependent on the form factor describing the scattering process on the respective target nucleus. Furthermore, it can vary with the measured recoil energy [60]. In some cases, the modulation amplitude could become negative and/or the phase could be shifted, such that the maximum relative velocity not necessarily coincides with the maximum recoil rate.

Additionally, the fraction of the modulated to the total obtained signal rate may depend on the energy threshold of the detectors. While the velocities of the Earth and the Sun with respect to the WIMP wind compare as $(v_\oplus cos\theta)/v_\odot \approx 0.06$, one can think of an exemplary detection threshold which almost exclusively allows for obtaining a signal during a season when the possible energy transfer is maximal. Then, the measured modulated rate could even be larger than the measured constant rate.

In each scenario, background mitigation and a good understanding of any process that could lead to similar annually modulated rates are of utmost importance to retain sensitivity to this signature.

2.7 Current Status of WIMP Dark Matter Search

The complementarity between collider-based, indirect and direct searches is essential for the understanding of the nature of DM. All these types of searches cover different and partly overlapping parameter spaces and test various particle physics and cosmological models. Following up on a potential future detection in one single experiment, only an overarching analysis will finally be able to constrain all features of DM particles.

Here, a brief overview of the current research status using the different approaches of collider-based, indirect and direct detection is presented. The focus in this regard is again set on WIMP-like DM. A general picture of current exclusion limits and observed anomalies is outlined, without making a claim to completeness. A current list and summary of the respective research status can additionally be found in the latest review of the Particle Data Group [2].

Starting with collider-based searches, the most stringent limits naturally come from the currently most powerful hadron collider, the LHC. The calculated limits in the analysis of the obtained data with the ATLAS [62] and CMS [63] detectors are, however,

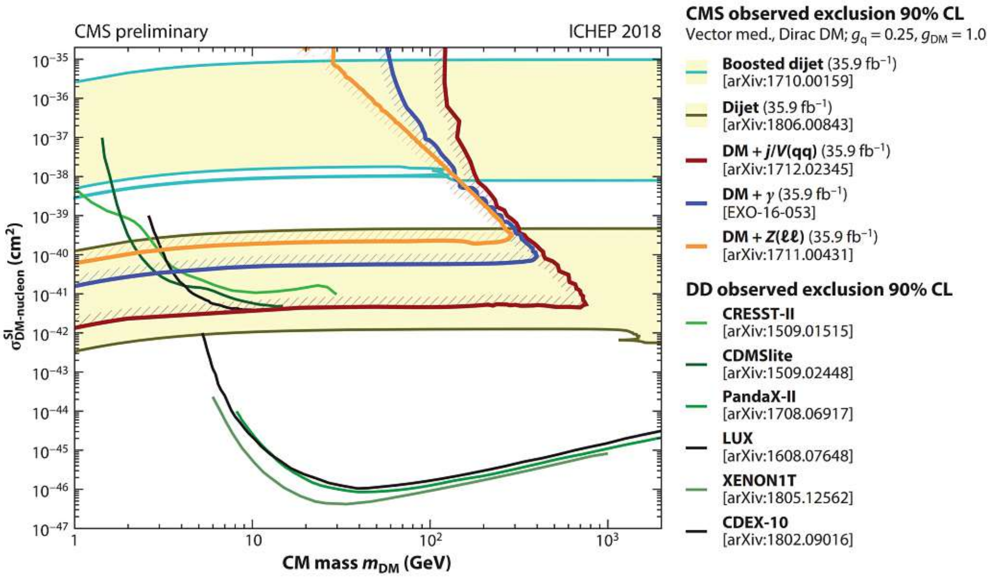

Figure 2.9.: Spin-independent DM-nucleon scattering cross section limits extrapolated from CMS results for the specific model indicated in the top right (vector mediator, Dirac DM, specific coupling strengths). Figure taken from Ref. [53], which adapted data from Ref. [61].

very much model-dependent when compared to direct detection searches. Principally, the collision data yield results on missing transverse momenta. These can be interpreted in the sense of *production* cross sections based on particular underlying processes. Only in the next step, based on the attained constraints on mediator masses and couplings, an interpretation in terms of a *scattering* cross section is possible. Together with the necessary conversion from the collision of quarks to the scattering off the entire nucleon, model-dependent results are attained. Keeping this in mind, extrapolated exclusion limits from CMS using different model assumptions are exemplary shown in Figure 2.9. For comparison, some direct detection limits are additionally depicted in this plot. Depending on the model assumptions, exclusion regions may be very competitive in the medium and especially the low WIMP mass regime. While direct detection experiments suffer from very low energy depositions, which partly lie below their respective thresholds in the case of low DM masses, collider searches do not lose sensitivity. However, at low masses ($\lesssim 1$ GeV) the conversion to nucleon level and model-dependent interpretation becomes more tedious, such that a comparison to direct detection searches is difficult. At high masses, at the same time, collider searches lose sensitivity once the collision energy is insufficient to produce potential heavy DM particles. The latest shown limits by the ATLAS and CMS collaborations are attained from data of the second operational run of LHC, which ended in December 2018. Currently, the third operational run has started, which shall be followed by the upgrade to the “High Luminosity” LHC (HL-

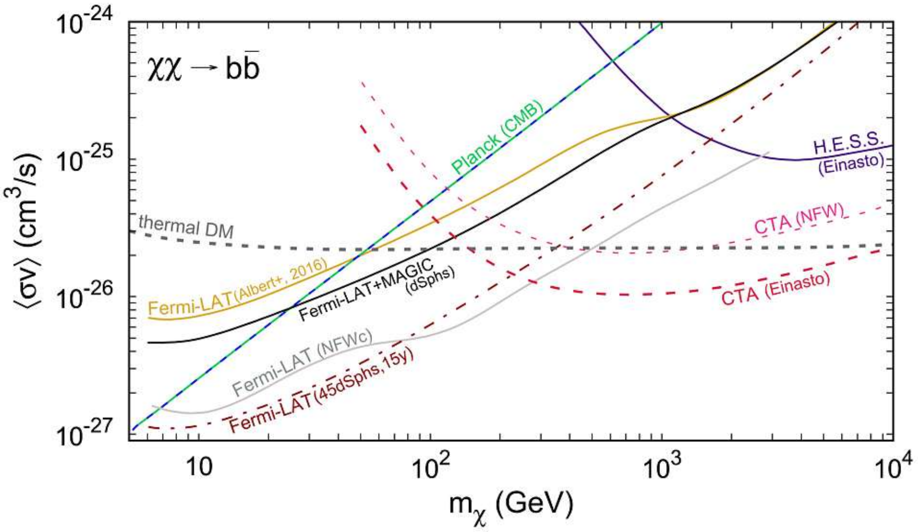

Figure 2.10.: Annihilation cross section limits for $\chi\chi \to b\bar{b}$. The most stringent limits below ~1 TeV are obtained from a combined analysis of Fermi-LAT and MAGIC observing dwarf galaxies (solid black) as well as Fermi-LAT observing the Inner Galaxy (solid grey). Above this mass range, the H.E.S.S. observation of the galactic center is most sensitive. The annihilation cross section for thermal WIMP production (dashed grey) is shown for reference. Projections are presented for Fermi-LAT observing 45 dwarf galaxies for 15 years (dash-dotted dark red) as well as for the future Cherenkov Telescope Array (CTA, dashed pink and dashed red). Figure taken from Ref. [65].

LHC), increasing the luminosity by a factor of ~10. Projected limits on particular dark matter scenarios in this future LHC phase are summarized in Ref. [64].

Continuing with indirect searches, current limits are obtained by experiments measuring photons, neutrinos and charged anti-particles from astronomical sources, where a large DM density is expected. These particles are produced as secondaries or final state radiation in annihilation processes of DM. Inherently, the interpretation of measurements is dependent on the astrophysical model of DM halos as well as on the model of the galactic foregrounds and potential interactions on the path from the source to the detector. Results are attained in terms of the annihilation cross section, based on assuming certain final states and DM density profiles. As the annihilation process is equivalent to the process responsible for the thermal freeze-out of DM in the early universe, the measurements can give stringent limits on the possibility of certain DM masses to act as a thermal WIMP. In principle, DM particles may at tree level annihilate into any pair of SM leptons, quarks, weak gauge bosons or the Higgs boson. All these annihilation channels can be analysed, but the annihilation to $b\bar{b}$ is often assumed as the standard scenario used for comparisons [66]. In Figure 2.10, current limits and projections for DM annihilating into a $b\bar{b}$ pair are thus presented. The best limits for this final state are attained with gamma-ray telescopes, which are hence shown in the plot. Fermi-LAT [67] is a space telescope directly measuring the gamma-ray energy and direction with a tracker system and an electromagnetic calorimeter. A current limit as well as a projection for the analysis of 45 dwarf galaxies in 15 years of data are shown. MAGIC [68] and H.E.S.S. [69], on the other hand, are ground-based Air Cherenkov Telescopes (ACTs), which measure the Cherenkov light produced by the secondary particles created by high-energy gammas entering the atmosphere. They feature better sensitivity at large DM masses but also a higher threshold. The CTA experiment [70] is a future ACT array, strongly improving the overall sensitivity according to the depicted projections. Besides the dependence of the limits on the assumed final state, the two projections show the impact of different DM halo parametrizations, i.e. NFW [71] or Einasto [72]. For comparison to the obtained limits, the thermal annihilation cross section is shown, yielding that a large WIMP parameter space for annihilation into $b\bar{b}$ can be excluded. In general, indirect searches have comparatively good sensitivity for very large DM masses and thus provide complementarity to the other detection channels.

Finally, direct detection experiments and their current exclusion limits are discussed. In Section 2.6, the signatures that can be used in these experiments have already been presented. Also the advantage of using multiple signals to distinguish the origin of the signal and discriminate backgrounds has briefly been mentioned. In general, the tested parameter space and attained sensitivity often directly and indirectly depends on the type of signal chosen as an observable. In the case of measuring the phonon signal, detectors have to be cooled down to milli-Kelvin temperatures, which is only possible in special cryostats providing limited space. This usually leads to lower target masses. On the other hand, the attained phonon signal provides a direct measurement of nuclear recoil energies typically with a low energy threshold, thus allowing to probe low-mass DM. Using the scintillation or ionisation signature instead of the phonon signal, one may be able to attain larger exposures. However, at the same time only electron-equivalent energies can usually be attained which may have to be converted to the nuclear recoil scale depending on the assumed interaction mechanism of the detected events. In this conversion, the results suffer from the quenching of nuclear recoils, leading to reduced signals and thus higher nuclear recoil detection thresholds. In Figure 2.11, the exclusion limits of various direct detection experiments, as collected in Ref. [3], are shown. The liquid noble gas experiments, such as XENON1T which has the leading limit above $\sim 3\,\mathrm{GeV/c^2}$ DM mass [75, 76], use tonne-scale target masses and feature very low intrinsic contamination levels and hence background rates. Their sensitivity is thus mostly exposure-limited. On the other hand, experiments using cryogenic calorimeters, such as CRESST-III which has the best limit below $\sim 1.8\,\mathrm{GeV/c^2}$ [4] in the quoted limit plot when disregarding Migdal analyses, have sensitivity to lower masses while dealing with higher intrinsic background levels. In the low-mass range, the exclusion curve is thus often background-limited. Recently, analyses making use of the Migdal effect [77] (limits labeled with “(M)” in the plot) got more prominent, while the effect is still to

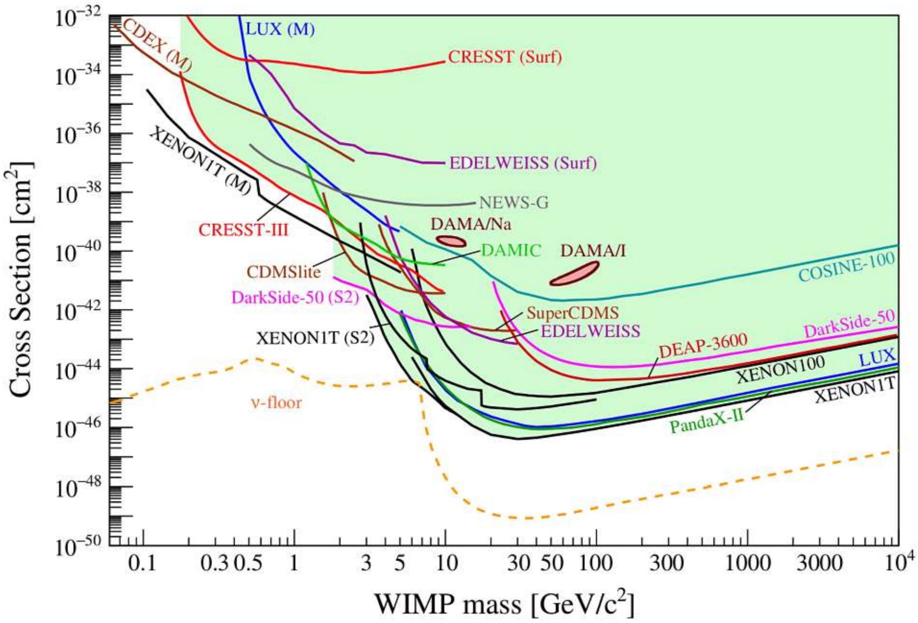

Figure 2.11.: Spin-independent DM-nucleon scattering cross section limits from various direct detection experiments. Limits labeled with "(Surf)" are from data taken above ground, those labeled with "(M)" are making use of the Migdal effect. The ν-floor is shown for a Ge target. Besides exclusion limits, the islands for the DM interpretation of the DAMA/LIBRA modulation signal [73] are presented. The leading limits, disregarding Migdal analyses, in this plot are from CRESST-III in the range 0.16 - 1.8 GeV/c^2 [4], Darkside-50 between 1.8 - 3 GeV/c^2 [74] and XENON1T above 3 GeV/c^2 [75, 76]. The figure is taken from Ref. [3].

be proven experimentally. Essentially, the Migdal effect would lead to a transfer of the nuclear recoil energy to electrons, such that especially experiments whose threshold for electron recoils is lower than that for nuclear recoils would effectively gain sensitivity to lower DM masses. Indeed, the effect not only describes a transfer of the nuclear recoil energy to electrons, but an inelastic process involving the incident particle as well as both the nucleus and the electron cloud. Hence, even experiments that measure the total recoil energy can gain sensitivity due to a more efficient transfer of energy to the electron cloud [78]. In general, the direct detection exclusion limits for WIMP masses above a few GeV are close to reaching the neutrino floor and the next phases of the respective experiments probing this parameter space, i.e. XENONnT [79], LZ [80] and PandaX-4t [81], which are currently under commissioning or already taking data, will push further towards this atmospheric neutrino background limit. Discussions and projections can be found in Ref. [3]. For the low-threshold experiments, especially the reduction of background has to be a prime goal. At the moment, many experiments are limited by a yet unknown source of background leading to a sharply rising event rate, usually starting well below 1 keV recoil energy. To tackle this limitation, the EXCESS workshop [82], of which the author of this thesis was one of the organizers, has been initiated to discuss about possible origins and interpretations within the DM (and CEνNS[1]) community. The final goal of the common initiative is to overcome this sensitivity-limiting background. Apart from the limit curves, Figure 2.11 also shows two so-called islands, which represent the interpretation of the DAMA/LIBRA signal [83] in the standard scenario of WIMP-nucleus scattering [73]. DAMA/LIBRA solely measures scintillation light signals and observes an annual modulation in the obtained rate at low energies which is compatible with expectations for DM. Its origin, however, is still unclear and cross-checks by other experiments using the same target material are currently planned and ongoing, e.g. COSINUS (see Chapter 6). See also Section 6.1.1 for a more detailed discussion of the DAMA/LIBRA claim.

---

[1] Coherent elastic neutrino nucleus scattering

3 Particle-induced Background in Direct Searches

Any particle, apart from the searched-for DM, depositing energy in a detector poses a background to direct detection experiments. As the interaction of DM particles with SM particles is supposedly very weak, only few signal events are expected to be obtained such that a minimization of background in the region of interest (ROI) of the experiment is crucial. Otherwise, in the light of the featureless exponentially falling spectrum, a statistically significant observation would be extremely challenging. Even with background minimization techniques, a perfect understanding of all residual events is crucial to interpret the data. Besides by particles interacting with the target material, background signals may also be induced by detector effects, for example stress relaxations. In this work, however, the focus is set on particle-induced background. Typical sources are listed in the next section, followed by a discussion on possibilities to experimentally discern different types of background as well as how to overall mitigate them.

3.1 Background Categories

In this section, prominent background sources are categorized mostly based on their interaction with the detector material.

3.1.1 Electron Recoil Background

Encompassed within the term electron recoil (ER) backgrounds are any types of signals induced by particles interacting with the atomic electrons of the target material. The most typical ER background components are β- and γ-particles. Overall, these usually give the highest contribution to the entire background rate obtained by experiments. They originate from a large variety of radionuclides. These are, for example, the nuclides of the natural ^{232}Th, ^{238}U and ^{235}U decay chains as well as other natural radionuclides such as ^{40}K. In addition, a lot of radioactive nuclides are produced by cosmogenic activation, with ^{3}H being one of the most prominent, especially when considering background components leading to signals at low energies. Finally, also anthropogenic nuclides, such as ^{60}Co or ^{137}Cs can be found in many materials and act as a source of ER background. Depending on the type of decay, produced particles and released energy, the spectral signatures seen by a detector can be vastly different. In the following, after discussing electron and gamma signals, muons and neutrinos are mentioned as a further potential source of ER background.

Electrons and Gammas

In a typical β^- (β^+) decay, i.e. $n \rightarrow p + e^- + \bar{\nu}_e$ ($p \rightarrow n + e^+ + \nu_e$), the released energy is split between the electron (positron) and the antineutrino (neutrino). While the latter is typically undetected, the electron (positron) is quickly stopped in a bulk material and its entire energy is recorded. This leads to a broad β-spectrum with an endpoint at the total energy released in the decay. As electrons and positrons have a very short path length, they can only be detected from sources intrinsic to the sensitive detector material or from sources sitting on their surfaces or on the surfaces of materials directly surrounding the target.

Electron capture (EC) reactions ($p + e^- \rightarrow n + \nu_e$) are a different mode of converting a proton into a neutron in an atomic nucleus. However, in this case an atomic electron from an inner shell (usually K- or L-shell) is captured by a proton in the nucleus, reacting to form a neutron under the emission of a single neutrino. In this reaction, the released energy remains undetected as it is carried away by the neutrino. However, in a secondary process, the empty place in the inner shell is being occupied by an outer electron, releasing a characteristic energy equal to the difference between the shell binding energies. This may happen via the emission of an X-ray or via the emission of an electron through the Auger effect. Similar to the normal β decay processes, the energies can only be observed from radionuclides intrinsic or very close to the sensitive detector material due to the short path length of electrons and low-energy X-rays. The spectrum, in this case, are characteristic peaks corresponding to the shell binding energies.

As a by-product of a typical radioactive decay, the resulting nucleus is often in an excited state which immediately deexcites by emitting a γ-particle. The interaction of the γ-particle with matter subsequently is very much dependent on its energy and on the traversed material. The three main interaction mechanisms [85] are the photoelectric effect, Compton scattering and pair production. Mass attenuation coefficients for two different materials, $CaWO_4$ and Al_2O_3, are exemplary shown in Figure 3.1 attained from the XCOM online database [84]. In an interaction via the photoelectric effect, the entire gamma energy is transferred to an atomic electron, which is emitted from its shell and then gets quickly stopped in the material, leading to a characteristic peak in the experimental data at the gamma energy. The attenuation coefficient for this process is proportional to Z^4/E^3. It is hence larger for heavy nuclei and low energies.

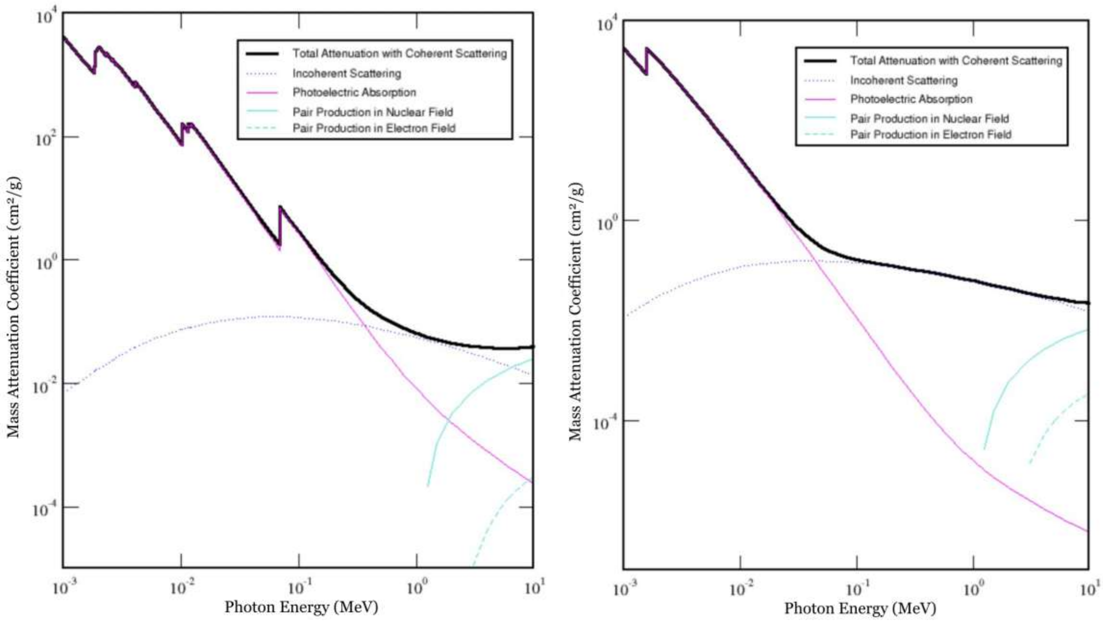

(a) (b)

Figure 3.1.: Mass attenuation coefficients for gammas traversing (a) $CaWO_4$ and (b) Al_2O_3, according to the XCOM online database [84].

Compton scattering, on the other hand, is an incoherent scattering process off a weakly bound atomic electron, in which only a part of the gamma energy is transferred. A broad energy spectrum up to a characteristic maximum energy can thus be observed. The interaction probability for this process is mainly dependent on the electron density, which is rather similar between different materials, and varies slowly with energy. As can be seen in Figure 3.1, the photoelectric absorption hence dominates up to larger energies in heavier materials compared to Compton scattering.

The third main interaction mechanism, pair production, can only occur for gamma energies above 1022 keV, i.e. the rest energy of an electron-positron pair. In a strong electromagnetic field, especially close to a nucleus, such a particle pair can then be generated. The probability for pair production is roughly proportional to Z^2 and increases with energy above the threshold value. Electron and positron subsequently lose their kinetic energy in the material, and the positron annihilates with an electron, releasing two 511 keV gammas. The resulting signatures in detectors are up to three characteristic peaks, one at the full gamma energy in case both annihilation gammas are detected, and the further two at 511 keV and 1022 keV below the full-energy peak due to single- or double-escape of the gammas.

For DM searches, however, only the processes leading to energy depositions at low energies (in the ROI) play a role as a background. Thus, concerning gammas, mostly Compton scattering as well as photoelectric absorption of very low-energetic particles are of importance.

Muons

Additional to electrons and gammas, there are further particles that can lead to an ER background. Cosmic ray muons are, for example, able to reach typical underground locations of DM experiments and lead to electromagnetic interactions in the detectors. They do, however, typically feature large energies and are highly ionizing such that they create signals above the ROI for DM searches, if they traverse the detector. Still, lower-energetic signals can be induced either by partial deposition of the primary muon's energy or via secondary particles. An ER background may hence be produced by particles in an electromagnetic shower reaching the detector. Furthermore, high-energy muons traversing a dielectric material may induce Cherenkov photons, which, if the material is in line of sight of the sensitive target volume and if the target material can absorb these photons, could lead to very low-energetic signals.

Neutrinos

A further ER background originates from neutrino-electron scattering. The main contribution comes from solar neutrinos, where the largest components are pp neutrinos featuring a continuous energy spectrum up to 420 keV and ^{7}Be neutrinos with characteristic energies of 383 keV and 862 keV [86], which can thus lead to electron recoils up to a few hundred keV. Due to the small elastic neutrino-electron scattering cross section, the rate may be rather low. However, the neutrino background is in principle unavoidable. Thus, if the target material used for a DM detector is extremely clean and other background components from surrounding parts and the environment could be perfectly shielded, these neutrino interactions will still pose a limit on the attainable sensitivity in DM searches. It is worth mentioning in the context of this thesis, however, that the CRESST (see Section 5.1) and COSINUS (see Section 6.1) experiment are far from being limited by this process.

3.1.2 Nuclear Recoil Background

The category of nuclear recoil (NR) backgrounds involves any detector signal induced by an interaction with the nuclei in the target material. These interactions may occur with neutral particles entering the detectors, such as neutrons, neutrinos or gammas. As the recoiling positively charged nucleus is quickly stopped in the material, the obtained signals typically correspond to the total energy of the recoil. NR signals are often considered the most critical type of background in DM searches, as their signature is resembling that of WIMP-like particles, which are similarly expected to interact with the nuclei of the target material.

Neutrons

The most prominent component of NR background originates from neutrons entering the detectors. A typical source of neutrons are radioactive decays of heavy nuclides in the natural decay chains. In this case, there are two possible origins: either neutrons are directly released in a spontaneous fission (s.f.) process, or they may be produced following an α decay. In the latter case, creation of free neutrons might occur via (α,n) reactions, whose cross sections strongly depend on the material. The reaction is suppressed by the Coulomb barrier of the nucleus and the cross section is thus lower in high-Z materials. In both cases, s.f. and (α,n), the neutron background for DM search is originating from materials external to the sensitive detector. Otherwise, intrinsic to the sensitive volume, any neutron-induced signal is accompanied by the large energy release from the s.f. or (α,n) reaction and thus lies well above the ROI.

Additional higher-energetic external neutrons can be created via cosmic ray muons. In underground searches, these cosmogenic neutrons are mostly induced by hadronic and electromagnetic showers, while muon capture processes are rather negligible [87]. In hadronic showers, the main production channels are deep-inelastic π A interactions as well as π^- A captures. The dominant process in electromagnetic showers, on the other hand, is photoproduction in giant dipole resonance (GDR), mainly by real and subdominantly by virtual photons. Overall, however, the hadronic component is the largest. An approximate universal formula for the muon-induced neutron yield in underground experiments can be written as $Y_n = b \cdot E_\mu^\alpha \cdot A^\beta$ with parameters $b = 4.4 \cdot 10^{-7}\,\mathrm{cm}^2/\mathrm{g}$, $\alpha = 0.78$ and $\beta = 0.95$ [88]. Cosmogenic neutron production is thus enhanced for increasing muon energies and in high-A materials. The exact values for α and β, however, vary between different analyses (see discussion in Ref. [89]).

Radiogenic neutrons have energies in the MeV range, while those of cosmogenic neutrons can extend up to the GeV range. The main interaction with nuclei in the target material at these energies is elastic or inelastic scattering. Figure 3.2 shows the cross sections for different interaction mechanisms of neutrons for the example of a ^{6}Li target according to the ENDF online database [90, 91]. Besides Li being used in some of the latest CRESST detector crystals, the target choice for this theoretical description is mainly motivated by the well separated curves representing the cross sections for elastic, inelastic and neutron capture processes. Elastic scattering, shown in green and dominating at larger neutron energies, leads to a similar featureless exponentially falling recoil energy spectrum as expected for WIMPs (cf. Section 2.6), with a maximum recoil energy according to Eq. 2.13, where the WIMP energy and mass have to be replaced with the energy and mass of the neutrons.

Additionally, neutrons may lead to inelastic processes. These can be inelastic scattering reactions, in which the nucleus gets excited and deexcites via the emission of γ-particles. Furthermore, part of the neutron flux will get slowed down and thermalized due to interactions in surrounding materials before reaching the detectors. In this case, the neutrons cannot induce signals above typical detector thresholds via ordinary

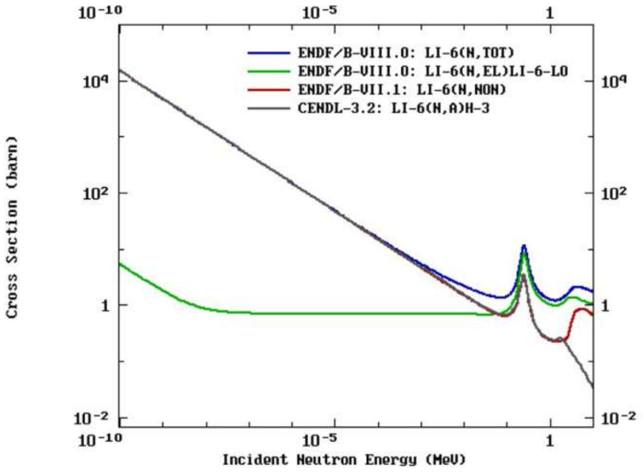

Figure 3.2.: Cross section data for neutrons impinging on ^{6}Li, according to the ENDF online database [90, 91]. The depicted curves represent the total cross section (blue) as well as the individual cross sections for elastic (green), inelastic (red) and specifically (n,α) processes (gray).

scattering (see again Eq. 2.13). However, additional inelastic interaction mechanisms may gain in importance. Thermal neutrons can be captured by a variety of nuclei and may lead to subsequent reactions. The example of ^{6}Li in Figure 3.2 shows a very high thermal capture cross section for (n,α) processes. In this case, the energy release would be in the MeV range [92] and the corresponding signal would hence not contribute as a background in the ROI for DM search.

Specific capture reactions in certain materials can however lead to low-energy nuclear recoil signatures. These are radiative (n,γ) capture processes, in which one or many gammas are emitted. In the case of a single gamma being emitted, the nucleus undergoes a recoil of defined energy due to momentum conservation. The respective gammas typically have energies in the MeV range and can thus, in the case of small detectors, leave without a signature. Only the characteristic low-energetic nuclear recoil may then remain to be seen, if its energy is above the detector threshold. In the case of gamma cascades, a broad low-energy background may be obtained instead of a characteristic recoil peak. Radiative neutron capture processes are, for example, prominent with tungsten nuclei, which are present in the $CaWO_4$ crystals used in CRESST. Additional cross section graphics, similar to the one shown in Figure 3.2, for materials most prominently dealt with throughout this thesis are presented in Appendix A.

Neutrinos

A further NR background component originates from coherent elastic neutrino nucleus scattering (CEνNS). A neutrino scattering off a nucleus leaves a similar signature as a WIMP or a neutron. Compared to neutrino-electron scattering, the coherent scattering cross section is enhanced. However, the possible energy transfer to the nucleus is much lower than to the lighter electrons. CEνNS signals are hence typically very low-energetic. Depending on the energy threshold of the experiment and the ER/NR discrimination capability, neutrino-electron scattering events may hence still dominate over the obtained CEνNS rate [86]. Both types of neutrino events anyhow pose a principally unavoidable background. When assuming DM scattering off nuclei, background due to CEνNS is irreducible, while background due to neutrino-electron scattering may be distinguishable. The coherent neutrino scattering signal thus leads to the so-called neutrino floor, which essentially represents a discovery limit. In the exclusion plots of direct detection experiments (cf. Figure 2.11) this neutrino floor is typically shown together with the current experimental limits. The lower-mass range is limited by the solar neutrino flux, while the higher-mass range is limited by atmospheric neutrinos extending to larger energies. Specific technologies could be used to overcome this limitation. Detectors with directional sensitivity, for example, have the potential to discriminate between neutrino- and WIMP-induced signals [93].

Photons

Similar to neutrinos, photons can also scatter coherently off atoms. Three main mechanisms are contributing to this effect and may lead to a NR background in low-mass DM searches [94]: Rayleigh, nuclear Thomson and Delbrück scattering. The dominant Rayleigh scattering process mostly generates very low-energetic recoils, while nuclear Thomson and Delbrück scattering lead to a higher-energetic tail due to enhanced backscattering probability of the photon. Photons leading to this type of background should at least feature MeV scale energies and could originate from radioactive decays, for example from the decay of ^{40}K leading to a 1.461 MeV gamma. Still, for a photon of approximately 1 MeV, the recoil energies $E_R = q^2/2M$ due to the small momentum transfer q to a nucleus of mass M typically only extend up to the eV scale [95].

3.1.3 Alpha Background

In some sense, alpha background has similarities to nuclear recoil background, as an α-particle represents a ^{4}He nucleus which is subject to similar energy loss mechanisms as a recoiling target nucleus. However, the creation of alphas is very different from the scattering processes leading to nuclear recoils. Alphas are typically released in radioactive decays of heavy natural radionuclides, in which they receive large kinetic energies $\mathcal{O}$(MeV). If the decay happens within the target material, the energy deposition therefore is well above the ROI for DM search. Thus, alpha background is only relevant if the radionuclides sit on the surface of the target itself or the materials directly surrounding the target. In this case, there is a possibility that the majority of the released energy is not entering the sensitive detector volume. A critical component for this type of background, which experiments are trying to avoid, is ^{222}Rn emanation on the surfaces of materials and subsequent decays of its daughter nuclides (e.g. [96, 97]).

3.2 Particle Discrimination

Following the discussion of the various particle background components in direct detection DM searches, this section deals with the distinction and hence reduction of particular background contributions. Usually, the assumption is made that WIMP-like DM particles interact with the nuclei of the target material. Thus, experiments can apply techniques to distinguish NR backgrounds from ER backgrounds to improve their sensitivity. As the total event rate is typically dominated by ER backgrounds, this approach has a strong motivation. In Section 2.6, a short summary of the three main direct detection channels has already been presented together with a brief description of the quenching mechanisms for scintillation and ionization. However, the potential for particle discrimination based on these processes is discussed in more detail in the following.

When using a single-channel detector sensitive to only one of the possible signatures, i.e. either phonons, scintillation light or ionization, a distinction between ER and NR signals on an event-by-event basis is difficile. In this case, pulse shape discrimination, if attainable, would be one of the few options for ER rejection. Otherwise, only statistical methods can be applied to discriminate backgrounds based on a precise knowledge about contributions to the measured events. These contributions are usually subject to a dedicated background model for each experiment, considering at least the major components of ER and NR signal sources. Furthermore, an interpretation and assumption on the interaction mode of all signals has to be made and a precise knowledge on the relation between NR and ER energy scales, i.e. quenching factors (QFs) relating these two, is necessary. Usually, gammas of known energies are used to calibrate the detector response. Hence, all events are reconstructed on the ER energy scale, commonly denoted as electron-equivalent energy deposition. These factors play a role especially in scintillation-only or ionization-only experiments, as those channels are subject to quenching mechanisms for NR events. While with the Birks [56] and the Lindhard [57] model for scintillation and ionization quenching, respectively, some phenomenological treatment and parametrization is possible, more exact descriptions of the detector behavior via experimental data is usually required. Thus, dedicated QF measurements, especially at low recoil energies, are common and essential supplements to direct detection experiments [98–103].

Information on QFs is also important for two-channel detectors, which simultaneously measure two of the recoil signatures. In this case, however, they are not only used for an interpretation of residual events, but first and foremost for discrimination between background and potential DM signal, i.e. between ER and NR events. This possibility is enabled by the difference in quenching of NR signals between all three possible detection channels. While the phonon signal in general provides a good measure of the total recoil energy both for ER and NR events, nuclear recoils in the scintillation and ionization channels are subject to different quenching mechanisms. This allows to use any of the combinations for building a detector with particle discrimination capability on an event-by-event basis. In this work, the focus is set on scintillating calorimeters, which combine the readout of phonon and light channel. Different amount of scintillation light for the same energy in the phonon channel is then used for ER/NR discrimination. The efficiency of this distinction depends on the QF for the material, the recoil energy and the detector resolution. Low-energy recoils pose a tough challenge to this approach. Only a few percent of the total deposited energy are typically converted to scintillation light. Hence, below ∼1 keV only a few photons are emitted, leading to an overlap of the ER and NR acceptance bands due to Poisson statistics governing the amount of emitted and detected light, and due to the energy resolution of the light detector. At these and even lower energies, particle discrimination breaks down and the two-channel experiments are in a similar situation as the single-channel ones regarding the interpretation of residual signals. The advantage of using the phonon channel, however, is that ER and NR signals are in principle measured on the same energy scale.

With particle discrimination, at least down to recoil energies of ∼1 keV the majority of background signals can be efficiently vetoed. NR events induced by neutrons as well as by neutrinos or gammas, however, are in principle indistinguishable from those induced by WIMP-like DM particles. As long as the leakage from ER events into the NR acceptance region is subdominant, NR signals can hence be seen as the most crucial and dangerous background component.

3.3 Background Mitigation

In the previous sections, background sources and particle discrimination have been discussed. Some sources may be partly unavoidable, irreducible or indistinguishable from WIMPs, while others can be vetoed and shielded. As any type of background either limits the sensitivity of the experiment due to events in the ROI or otherwise leads to dead time, as a period around any background event may be excluded from the collected data, background mitigation is of utmost importance. A discovery potential for the very rare scattering of DM particles in the detectors can only be achieved by minimizing the background rate and understanding the expected residual events. Thus, low background techniques employed in direct detection DM experiments, as comprehensively summarized in Ref. [104], are reviewed in the following.

3.3.1 Underground Laboratories

A common strategy among all DM experiments is to locate the setup in a deep underground laboratory. This is an important step to reduce cosmic ray and cosmic

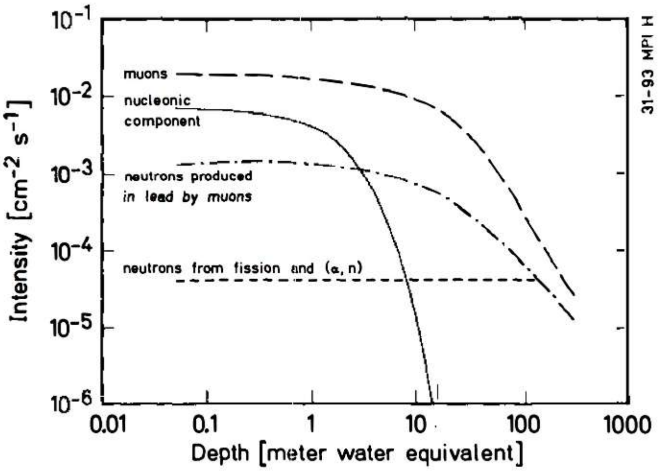

Figure 3.3.: Muon and neutron flux as a function of vertical depth, taken from Ref. [104].

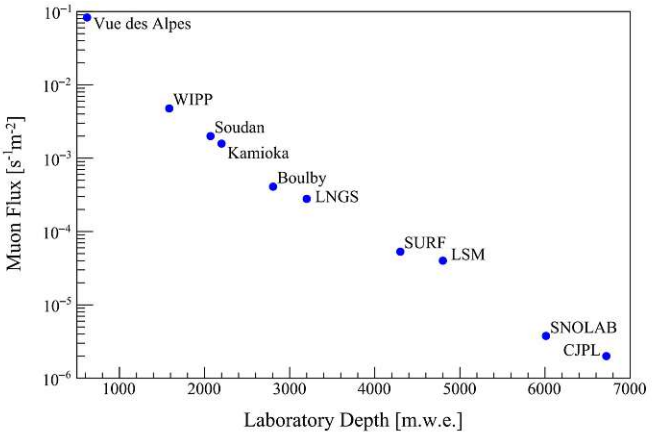

Figure 3.4.: Muon flux at various deep underground laboratories, taken from Ref. [105].

ray-induced background. Worldwide, currently 17 such laboratories exist, housing DM experiments as well as other rare event searches. The overburden of these sites is typically converted into units of meter water equivalent (m.w.e.), depending on depth and rock or soil composition, to compare the attained reduction of particle fluxes. While the nucleonic cosmic-ray component, mostly consisting of neutrons, is already negligible after $\mathcal{O}(10\,\text{m.w.e.})$, muons have a much larger mean free path. In deep underground laboratories, their flux is reduced by some orders of magnitude and their spectrum is shifted to higher energies. Figure 3.3 shows the behavior of various particle fluxes at shallow depths and up to $\mathcal{O}(100\,\text{m.w.e.})$. The muons themselves can lead to secondary neutrons as discussed in Section 3.1.2. In the figure, the flux of neutrons produced by muons traversing lead, which is a typical shielding material, is considered. Additionally, for reference, radiogenic neutrons from s.f. and (α,n) reactions due to naturally


(a) (b)

Figure 3.5.: Photograph of (a) the CRESST experimental facility seen from the outside within Hall A and (b) the COSINUS construction site as of June 2022 in Hall B of the LNGS underground laboratory.

decaying nuclides in the continental upper crust are indicated, whose flux may start dominating at more than a few hundred m.w.e. underground. In Figure 3.4, the muon flux at various deep underground laboratories is shown versus their average vertical depth. Obviously, the deeper the location, the less muons and hence muon-induced neutrons will be observed.

The Laboratori Nazionali del Gran Sasso (LNGS), located in Italy, is one of the European underground laboratories and renowned as the largest one in the world. It is mentioned specifically, as the experimental setups of both CRESST and COSINUS are hosted in its underground halls. A picture of the CRESST facility in Hall A at LNGS is shown in Figure 3.5a. A photograph of the COSINUS construction site in Hall B is presented in Figure 3.5b.

The LNGS is located beneath the Gran Sasso massif approximately 120 km east of Rome. Its underground halls are situated at approximately 963 m above sea level [106], with the mountains directly on top of it extending to roughly 2300 m. The average vertical overburden is typically quoted as 1400 m of rock, equivalent to approximately 3600 m.w.e. [107] shielding against cosmic rays. This leads to a reduction of the muon flux with respect to the surface by approximately six orders of magnitude [108]. The remaining flux reaching LNGS is $\sim 1\,\mathrm{m^{-2}\,h^{-1}}$. CRESST is located in Hall A of the laboratory, next to the CUORE [109] and GERDA [110] experiment. COSINUS is currently under construction in Hall B between the XENONnT [79] and LUNA-MV [111] experiment.

3.3.2 Passive and Active Shielding

As the neutron flux from environmental sources in the surrounding rock and soil generally dominates at the depths of deep underground laboratories, additional dedicated shielding layers are used to surround the detectors of the experiments. These shields are typically designed to mitigate both the ambient neutron as well as the ambient gamma flux. To shield neutrons, low-Z materials and especially materials with a large H content are best suited, because the energy transfer in elastic scattering is most efficient for a target of the same or similar mass. Gammas, on the other hand, are most effectively shielded by high-Z materials (cf. Section 3.1.1). However, as discussed in Section 3.1.2, muon-induced neutron production is enhanced in such materials. Thus, an elaborate compromise has to be made between the usage of high-Z and low-Z materials. Experimental setups may hence make use of subsequent shielding layers made of different materials. A typical high-Z material, employed for shielding gammas, is lead. Commonly used materials for mitigating neutrons are water and polyethylene. Selecting materials for the experimental setup usually involves a comprehensive material screening campaign. When shielding the environmental particle fluxes, one has to make sure not to introduce additional background via contaminated materials. Copper is hence often used as an additional shielding layer and for structures close to the detectors, as it is known to be very radiopure. Furthermore, to avoid airborne radon contamination on surfaces of shielding layers a constant flushing with nitrogen gas may be applied.

After installing the passive shielding layers, depending on the depth of the location, the dominating neutron background component may again be the muon-induced one. Experiments thus have to be careful with the use of high-Z materials (like lead), as they lead to an enhanced cosmogenic neutron production cross section. These muon-induced neutrons have energies extending to the GeV range and are hence more difficult to shield. Passive shielding layers are often not sufficiently reducing the cosmogenic neutron rate. Further active layers to veto these events then have to be employed. Most muon veto systems consist either of plastic scintillator panels or of large water tanks. In both cases PMTs are used to detect the signal of a muon traversing the medium, either via the produced scintillation or Cherenkov light. Any detector signal coincident with the muon veto triggering would then be vetoed.

3.3.3 Control of Intrinsic Radioactive Contamination

Besides the mitigation of external background components, the intrinsic radioactivity of the target material has to be controlled and minimized. For this, different purification techniques of the raw materials may be applied. Additionally, care has to be taken that cosmogenic activation is avoided. Transport of materials via plane should thus be omitted and prompt storage in underground locations, shielded against the nucleonic cosmic-ray component, is advantageous.

3.3.4 Combined View

A combination of the mentioned strategies, controlling the intrinsic radioactivity and shielding against external particles and radiation, leads to the reduction of most types of background with the exception of neutrinos. As discussed in Section 3.1, neutrinos are essentially irreducible and may via CEνNS mimic the signal of standard elastic DM-nucleus scattering, posing an ultimate discovery limit. As presented in Figure 2.11, however, the sensitivity of direct detection experiments has not yet reached this floor, especially for low-mass DM searches. In this low-mass parameter space, the sensitivity of experiments is background limited. Thus, besides the mitigation of background, the best possible understanding of residual events is essential. Achieving the latter via computer simulations based on material screening results and measured as well as calculated particle fluxes is a main topic of this thesis. Therefore, in the next chapter, the simulation software and strategy used and developed throughout the studies conducted in the course of this thesis is presented, before discussing the distinct applications in background studies for the CRESST [4] and COSINUS [6] experiment in Chapters 5 and 6, respectively.

4 Monte Carlo Simulation of Particle Interactions

An approach to model various types of particle-induced backgrounds is using a general purpose Monte Carlo simulation software. Several existing software packages and toolkits may be applicable to this task, e.g. MCNPX [112], Fluka [113, 114] or Geant4 [115–117]. The latter is forming the basis of the so-called ImpCRESST simulation software [118], mainly developed within the CRESST collaboration, but lately also adopted for the simulation studies performed for COSINUS. In this chapter, the capabilities of the software as well as its new features, implemented in the course of this thesis, are described. Furthermore, auxiliary programs used in the preparation and the post-processing of the simulations are explained.

4.1 Particle Simulation using ImpCRESST

ImpCRESST is the particle simulation software developed and employed within CRESST as well as lately also within COSINUS. It is based on the Geant4 toolkit and tailored towards the application to low-threshold experiments. In the following, the basic ingredients provided by Geant4 as well as the data structure and additional features available within ImpCRESST are discussed.

4.1.1 The Geant4 Toolkit

Geant4 (short for "Geometry and tracking") is a toolkit for the tracking of particles traversing and interacting with matter. Its original focus was mostly set on high-energy physics. However, over the years it became a multi-purpose toolkit for several particle physics, nuclear physics and medical physics applications. Some of the basic features available through the toolkit are the definition of geometries, materials and particles, and the enabling of certain types and models of interactions via the choice of physics lists. For a thorough description of the toolkit, the reader is referred to the official Geant4 references [115–117] as well as the user documentation [119]. However, some basics necessary for the understanding of the ImpCRESST software and of the simulations presented in Chapters 5 and 6 are provided in the following.

Primary Particle Generation

Simulations in Geant4 are event-based. The data of different events are always independent. Each single event starts with the definition of one or more primary particles and vertices. A base class is provided within Geant4 from which any type of particle generator can be derived. A typical example is the so-called "general particle source" already available in the toolkit. With this source, the user may define the particle type, the spectrum from which its energy should be sampled as well as the spacial and angular distribution. However, different primary particle generators may be necessary for distinct use cases, which will be described along with the new implementations in ImpCRESST in Section 4.1.4.

Geometries

In addition to the description of the primary particles, a geometry through which these particles have to be tracked needs to be defined. In Geant4, geometries are hierarchically structured and placed within each other. The outermost volume is called the *world* volume. Further volumes are essentially placed inside this *world* using three steps. First, a so-called *solid* is used to define the shape. Second, a *logical volume* based on the *solid* is issued, assigning attributes like the material definition to it. And third, a copy of the *logical volume* is placed into the simulated geometry via the definition of a *physical volume*. These steps can be repeatedly used to define any simple or more complicated experimental geometry.

Sensitive Volumes

Sensitive volumes are a special category of volumes constituting the geometry. The sensitive attribute can be attached to a *logical volume* and is used for those of which detailed data need to be acquired. Typically, these are the target volumes of an experiment or any other volumes, in which the details about interactions and energy loss processes are relevant. The methods that a user can prescribe for sensitive volumes may then allow to attain and store all the physics processes, energy depositions and further crucial information for the subsequent analysis of the simulated data.

Particle Tracking

After defining the primary particles as well as the geometry, the event-by-event simulation can be started, during which the key ingredient is the tracking of all primary and secondary particles. Essentially, tracking describes the transport of a particle based on all potential physics processes, user-defined step limits and geometrical boundaries. In the Monte Carlo procedure, the discrete physics processes propose a step length sampled according to their interaction lengths. The shortest sampled step length defines the step and determines which interaction is invoked, unless the proposed step length is larger than a maximum step size, the so-called step limit, or the distance to the next geometrical boundary. In addition to processes happening at the end of the step (*post step processes*) which define the step length, continuous energy loss processes (*along step processes*) during the step are considered. Furthermore, if an unstable or excited particle is at rest, then the time is used as a metric for proposing a step instead of the length, e.g. based on the possible decay or de-excitation processes (*at rest processes*). These possible tracking actions continue until all particles are stopped or leave the *world* volume.

Physics Lists

As a foundation for particle tracking, the physics processes associated with each particle type have to be defined. Individual processes are defined within Geant4 and summarized in various physics lists, tailored towards different applications and energy ranges. The choice of the physics list is hence one of the most crucial settings of the simulation. Only effects due to processes correctly implemented in Geant4 (or added by the user) and associated with a particle via the physics list used in the simulation, can be accurately modeled.

4.1.2 Physics List used in ImpCRESST

As the physics list essentially determines the behavior and outcome of the simulation via the defined and activated processes and models, it is worth a separate discussion. The physics list used in ImpCRESST is an adapted version of the pre-defined Geant4 *Shielding* physics list. The physics list guide of Geant4 [119] recommends the usage of this list for simulation of deep shielding and neutron transport. Necessary ingredient to this physics list is the G4NDL (Geant4 Neutron Data Library) database. For neutrons below 20 MeV, this database provides parametrized cross sections taken from ENDF (Evaluated Nuclear Data Files [90, 91]) libraries, as well as final state information. Different pre-defined classes in Geant4 are furthermore included to govern the various interactions of neutral and charged particles. A brief overview of the classes registered by default in the ImpCRESST physics list is presented in the following:

- **G4EmStandardPhysics_option4** is one of the default lists for electromagnetic physics in Geant4. Four of these standard options are available, of which the last one is recommended for precise simulations at low energies. According to Geant4's "Book for Application Developers" [119], it includes the most accurate models of the standard and low energy processes. The minimum energy for applicability within this class is set to 100 eV, but in general it is not recommended to lower it below 250 eV [120]. At the energy range of interest in direct detection DM searches, the Implementation of electromagnetic physics processes happens via the following Geant4 classes:

  - For gamma interactions via photoelectric effect, Compton scattering, gamma conversion and Rayleigh scattering, the classes *G4LivermorePhotoElectricModel*, *G4LowEPComptonModel*, *G4BetheHeitler5DModel* and *G4RayleighScattering* are used respectively.
  - Electron ionization is modeled via *G4eIonisation* above and *G4LivermoreIonisationModel* below 100 keV. Additionally, bremsstrahlung is based on *G4SeltzerBergerModel* below 1 GeV and potential multiple scattering is processed by *G4GoudsmitSaundersonMscModel* below 100 MeV.
  - Muon interactions are modeled via the classes *G4MuIonisation*, *G4MuMultipleScattering* using *G4WentzelVIModel*, *G4CoulombScattering*, *G4MuBremsstrahlung* and *G4MuPairProduction*.
  - Interactions of α-particles and heavier ions are governed by *G4hMultipleScattering*, *G4ionIonisation* and *G4NuclearStopping*. In the case of ions with atomic number greater than 2, the ionization process is based on *G4IonParametrisedLossModel*, which provides tabulated data of stopping powers. *G4IonParametrisedLossModel* is loading data from the G4EMLOW library of Geant4, which contains stopping power data from the ICRU (International Commission on Radiation Units) reports.

  In the above list, solely the models for the main types of interactions leading to electromagnetic background are mentioned. For a more detailed description of *G4EmStandardPhysics_option4*, the reader is referred to the Geant4 physics list guide [119].

- **G4EmExtraPhysics** is included to furthermore enable gamma-nuclear processes by default, which can play a role for example in the simulation of electromagnetic showers induced by high-energy muons.
- **G4DecayPhysics** handles the decay of nuclei in excited states.
- **G4RadioactiveDecayPhysics** handles the radioactive decay processes. In addition to Geant4's standard implementation, ImpCRESST also treats the radioactive decay of ^{3}H.
- **G4UAtomicDeexcitation** handles the atomic deexcitation processes.
- **G4HadronElasticPhysicsHP** denotes the high precision (HP) model for elastic neutron scattering below energies of 20 MeV, which evolved from the former NeutronHP model. For this low-energy range, the G4ParticleHPElastic model is used to handle the neutron processes based on the cross section and final state data loaded from the G4NDL libraries. Above this energy range, further models are added via *G4HadronElastic*.
- **G4HadronPhysicsShielding** is the class that handles inelastic hadron processes. For neutrons below 20 MeV, HP models are again implemented, called by the *G4NeutronPHPBuilder*, which adds the *G4ParticleHPInelastic*, *G4Particle-*

HPCapture and *G4ParticleHPFission* models, based as well on the G4NDL data libraries. Above this energy and up to the GeV range, the *G4BertiniNeutronBuilder* governs inelastic scattering, and *G4NeutronRadCapture* together with *G4LFission* determine capture and fission reactions.

- **G4NeutronHPThermalScattering** refines the elastic neutron scattering models below neutron energies of 4 eV by replacing the *G4ParticleHPElastic* model.
- **G4StoppingPhysics** treats the capture of charged particles after stopping (at rest). A specific process added by this class is the capture of negative muons via the model in *G4MuonMinusCapture*.
- **G4IonElasticPhysics** registers and handles elastic scattering processes of ions.
- **G4IonQMDPhysics** registers and handles inelastic processes of ions above certain energy thresholds.
- **G4StepLimiter** adds the possibility to set a user-defined maximum step length for certain particle types. In ImpCRESST this option is enabled for ions to allow for more accurate modeling of stopping of recoiling nuclei in matter in case necessary.
- **G4ProductionCutsTable** is used to set the energy threshold for the production of secondary particles in any reaction. The default value in Geant4 is 990 eV. Particles that would have kinetic energies below this value are not created. Instead, the energy is directly added to the energy deposition in the corresponding process. In ImpCRESST, this prodcution cut is reduced to 250 eV following an example in the Geant4 Book for Application Developers [119]. In addition to this hard energy cut, a range cut is defined. This range cut allows only for the production of secondary particles whose mean free path multiplied by five is larger than the defined value. For each secondary particle that would be created, the range cut is converted to an energy cut. If that energy was lower than the energy production cut, the defined 250 eV would still be applied as the lower limit. In Geant4, the default range cut is 0.7 mm. As with ImpCRESST, precision at lowest energies is of highest priority, this default value is reduced to only 1 nm. An exception regarding the production cut is made for ions, which are defined to be created with arbitrarily low energies in order to obtain low energy nuclear recoils. Using these default cut values, ions with kinetic energies above 0 eV as well as charged leptons and gammas with kinetic energies above 250 eV are typically created for further tracking in any material. If less precision is required, distinct regional production cuts can be defined, which will be discussed in Section 4.1.4.
- **G4OpticalPhysics** is deactivated by default, but would allow for the simulation of optical processes and the creation of optical photons.

For the exact description of the mathematical model implementation of the physics processes within the mentioned code classes, the reader is again referred to the Geant4 Physics Reference Manual [119].

4.1.3 Data Attained with ImpCRESST

Running a simulation in ImpCRESST is based on the concepts presented in Section 4.1.1 and the physics lists discussed in Section 4.1.2. After selecting an implemented experimental geometry and choosing a primary particle generator, the events are simulated according to the tracking algorithm considering the possible physics processes. During this simulation, data are written to a ROOT [121] tree for subsequent analysis. In ImpCRESST, these data include information about entire particle tracks as well as details about all interactions happening in sensitive volumes. Among the most important information are the energy deposition in each simulated step, the corresponding particle, interaction mechanism and time. While a lot of additional auxiliary data are stored for specific analysis, e.g. the amount of energy converted into scintillation light in case the sensitive volume is a scintillator, the mentioned data branches are most crucial for the purpose of the studies presented in Chapters 5 and 6.

4.1.4 Newly Implemented ImpCRESST Features

For the simulation studies conducted in the course of this thesis, specific features are necessary which have not been available within Geant4 or ImpCRESST beforehand. Hence, the code had to be extended and the following additional functionalities were added.

Bulk Contamination Particle Generator

Geant4 itself allows to simulate bulk contamination in volumes only for very limited cases. With its basic functionality, a single enclosing volume can be defined and primary particles would be sampled from all geometric objects fully enclosed by this volume. In case of a complex geometry made of different materials, this is not feasible. A feature thus had to be added which allows a more versatile selection of volumes for the simulation of a homogeneous contamination. For this purpose, a new primary particle generator was implemented in ImpCRESST. This generator allows the user to select volumes to be included for the primary particle generation via different optional commands. The user can choose all volumes made of a certain material, all volumes geometrically enclosed by a specified volume, one specific volume according to its name, or a combination of all of these possibilities. A more technical description of the usage of the commands is given in Appendix B.1.

SOURCES Interface

The simulation of bulk contaminations as discussed above is for example needed for modeling the radiogenic neutron background due to (α,n) and s.f. reactions (see Section 3.1.2). For this, the decaying nuclide could be placed homogeneously distributed in the respective material. However, up until recently, Geant4 was considered not to model (α,n) processes as accurately as dedicated codes developed for the purpose of these calculations, such as SOURCES [122, 123], NeuCBOT [124] or NEDIS [125]. The authors of Ref. [126] lately followed up on this topic with a study showing that current Geant4 versions, which have the possibility to read ENDF file format and thus use a parametrized interaction model, are now actually capable of providing similar accuracy. Still, in the course of this thesis, SOURCES has been employed for this task.

SOURCES takes as an input a list of decaying nuclides and then uses its internal data tables to calculate the neutron yield based on number and energy of emitted alphas, neutron production cross sections and stopping powers. The numbers obtained in the comparison in Ref. [126] show a very good agreement with measurements, only in some cases diverging up to ~20 %.

The neutron spectra attained from SOURCES have to be fed to Geant4 for further simulation. For this purpose, an interface has been coded which can read the output files from SOURCES and sample neutrons according to these data while using the bulk contamination particle generator. Instead of starting from the decaying nuclides in ImpCRESST, hence neutrons are the primary particles in the radiogenic background simulations. The respective UI commands to use this feature are further explained in Appendix B.2.

MUSUN Interface

Further auxiliary programs, called MUSIC and MUSUN [127], are employed for the sampling of muons in underground laboratories. Although Geant4 could be used for the propagation of sea level muons through hundreds of meters of rock, it is not the most feasible option. Geant4 would treat the creation and tracking of secondary particles on the entire path in too much detail, leading to large CPU times. A fine-tuning of production cuts and physics lists would be needed to avoid this behavior. However, dedicated muon transport codes exist, which solely deal with the transport of muons without considering secondary particles. MUSIC performs this task based on a map of the overburden in each direction. Data for several underground laboratories are readily available, e.g. for the LNGS (Laboratori Nazionali del Gran Sasso) where the CRESST experiment is and COSINUS will be located. MUSUN can then be used to sample muons on a user-defined surface at the respective underground location. Indead, MUSUN's output are exact properties of each sampled muon, denoting its energy, position and momentum direction.

To continue the simulation of the muons underground, traversing the experimental setup, with Geant4, an interface was now programmed in the course of this thesis. Essentially, the interface constitutes a primary particle generator that reads the output of MUSUN line-by-line for the event-by-event simulation. A more detailed description is given in Appendix B.3.

Regions with Distinct Cuts

The concept of regions and region-based production cuts is native to Geant4. However, it has not been used before in ImpCRESST, as most simulations up until recently were solely using the detector geometries, which require the highest level of detail. For this reason, the default production cut in ImpCRESST is set to 1 nm, as stated in Section 4.1.2. When simulating the entire experimental setup, however, this cut value has to be adapted to save CPU time, while making sure that the physics results obtained in the detectors remain unaffected. A shell-like structure of regions can thus be defined, in which the production cuts gradually increase from inside to outside, keeping the value of 1 nm in the detectors themselves unchanged.

Parallel World Tracking

The concept of a *parallel world* in Geant4 denotes a virtual copy of the entire geometry (*world volume*). Specific volumes can be added in this *parallel world*, similar to the usual geometry definition in Geant4. The entire *parallel world* does not affect the tracking of particles at all, but can be used to attain additional tracking information. Specifically, so-called *scorers* can be added to volumes in the *parallel world*. The *parallel world scoring* methods developed in the course of this thesis allow to store the number of certain particles entering or exiting a specific volume and their energies event-by-event. User-defined *scorers* for any geometry can easily be added via UI commands at run time. A detailed explanation of the usage of respective UI commands is given in Appendix B.4. The scorers may be utilized to map particle fluxes as well as incident particle energies at different levels of the experimental setup. Hence, they are an additional tool for evaluating the efficiency of mitigating or enhancing background particle fluxes by the use of the distinct shielding layers.

New Geometries

Many geometries were refined and new geometries added for the purpose of the simulation studies in this thesis. Especially for COSINUS, no geometry has been available before, as part of this work comprises the principal simulation study of the experiment. Details on newly implemented geometries will be presented in the respective sections in Chapters 5 and 6.

Separate Data Structure for Cherenkov Veto Simulation

For the optical simulation of the Cherenkov muon veto in COSINUS, the data structure of ImpCRESST had to be reworked. ImpCRESST itself, as mentioned in Section 4.1.3, is focused on storing energy depositions in sensitive detector volumes. However, for the muon veto simulation, all optical photons had to be tracked with a focus on storing the positions at geometrical boundaries, where they may get reflected or absorbed. For this purpose, a branched-off ImpCRESST version featuring a vastly different data accumulation strategy and storage was created. Details on the respective simulation and data analysis will be presented in Section 6.4.

4.2 Detector Response Modeling with CresstDS

CresstDS (DS = Detector Simulation) is an ancillary software to ImpCRESST, used to process and reduce the amount of collected data. Essentially, this software takes into account the finite time and energy resolution of detectors. While ImpCRESST stores the energy loss information in every step of a particle traversing a sensitive detector volume, CresstDS summarizes all within the typical time window resolved by the detectors and applies an energy smearing to the energy deposition according to the detector resolution. Previously the program could only handle one detector with hard coded energy resolution within the program itself. In the course of this work, the program was greatly enhanced and can now dynamically read in energy resolutions for different detectors from a user-provided configuration file. Besides the energy deposition, specific data need to be stored to evaluate the type of interaction and, for example, calculate the scintillation light quenching. Hence, the processed ROOT tree created via CresstDS has further been extended by the name of the incident particle leading to a detector hit, the contributions of various particle types to the total energy deposition and the energy available for scintillation light creation.

5 | Neutron Studies for CRESST

After the general discussion of particle background in DM search experiments and the simulation software that can be used to study this type of background, the following sections finally deal with the concrete application in the background studies of a direct detection DM experiment. The chapter at hand discusses the neutron simulation studies conducted for the CRESST [4] (Cryogenic Rare Event Search with Superconducting Thermometers) experiment. In Section 5.1, the CRESST experiment itself is introduced. Its detector concept, physics reach and latest results as well as the experimental setup, which is essential for any background consideration, are described. This description is followed up by discussing the details of the geometry implementation and particle generation in ImpCRESST in Section 5.2. In the subsequent sections, the various neutron simulation studies performed in the course of this thesis are then presented. The studies start with reconstructing the typical neutron calibration of the detectors in Section 5.3. Due to the findings in this simulation, Section 5.4 presents a novel energy calibration method based on the usage of the neutron source. Section 5.5 eventually discusses the detailed evaluation of the major neutron background sources and their estimated contributions to the obtained spectrum and event rate in the CRESST-III detectors. Finally, Section 5.6 provides a summary and conclusion of the attained results.

5.1 The CRESST Experiment

The CRESST experiment, located at the LNGS, is searching for DM via direct detection since more than 20 years, when the initial stage of the experiment, CRESST-I, delivered first results [128]. CRESST pioneered the approach of using low-temperature detectors in calorimetric mode for DM detection [5, 129]. In CRESST-I, only a phonon channel was used without an additional channel for particle identification. Later, in the second stage of the experiment, CRESST-II, a second readout channel for measuring scintillation light was introduced to allow for particle discrimination on an event-by-event basis. The shielding of the experiment was updated according to the then remaining most dangerous background, i.e. neutrons. Additionally, in the course of CRESST-II, lower thresholds as well as improved intrinsic background levels due to the use of dedicated self-grown target crystals have been achieved [96, 130]. Currently, CRESST is in its third operating stage, CRESST-III, employing target crystals of reduced size optimized for low-mass DM search [4]. In the following sections, the detector concept, experimental setup and latest results are summarized.

5.1.1 Detector Concept

CRESST developed and deployed cryogenic calorimeters for both its phonon and light detectors. This technology together with necessary tools and devices for its use is described below.

Cryogenic Scintillating Calorimeters

The CRESST detector technology has been developed with the goal of measuring the heat created in particle interactions in a target crystal by using phonon collectors in connection with an extremely sensitive thermometer. This approach provides an advantage over scintillation or ionization detectors concerning sensitivity at low energies, as almost the entire deposited energy can be available in the form of phonons (cf. Section 2.6). A prerequisite for detecting the phonons produced in the interaction is an extremely low operating temperature. Only in this case, the temperature change due to a particle interaction may be measurable on top of the thermal (baseline) noise fluctuations. Sensitivity to low energy depositions ΔE can additionally be enhanced by reducing the heat capacity C of the detector, as the resulting temperature change ΔT is equal to $\Delta E / C$ [131]. This is one of the main reasons for reducing the size of the target crystals in CRESST-III and will further be discussed in Section 5.1.2.

Given the correct and stable operating conditions, a highly specialized temperature sensor for reading out the signal is furthermore needed [129]. Besides the phonon detectors, cryogenic light detectors have been developed in CRESST-II to provide a second channel for particle discrimination when operating scintillating target crystals [5]. The detector technology developed by CRESST is very versatile and allows to probe various target materials. Any single crystal may potentially be operated as a phonon detector target and, in case it scintillates, combined with the light detector readout. The most prominent target material used in CRESST is $CaWO_4$. However, in CRESST-I as well as in the latest stages, Al_2O_3 has also been used. Furthermore, additional materials like for example Si (not scintillating), $LiAlO_2$ [132] or Li_2MoO_4 [133] have lately been tested.

Light nuclei enhance the sensitivity to low-mass DM. At the same time, the spin-independent scattering cross section scales with the mass number squared (cf. Section 2.6) and thus favours interactions with heavy nuclei. If a majority of the events would still lead to signals above the detector threshold, heavy targets may hence be preferred. With compound materials, combining light and heavy nuclei, both respective advantages

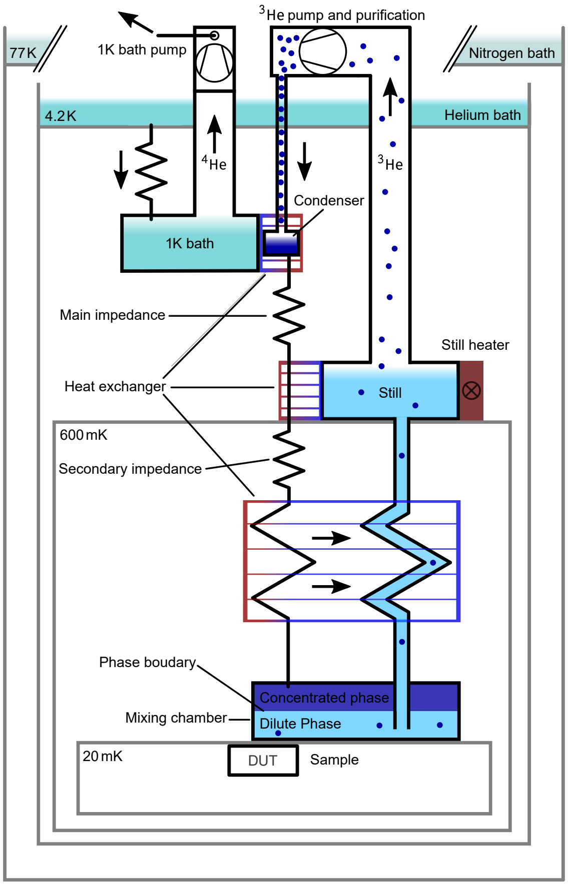

Figure 5.1.: Schematic illustration of the working principle of a wet dilution refrigerator, taken from Ref. [134].

can be exploited. Furthermore, the combination of different nuclei can improve the understanding of background and signal events. The necessary technologies as well as concepts and detector signatures are presented in the following.

Dilution Refrigerator

To cool down the detectors to their typical operating temperature of $\mathcal{O}(15\,\mathrm{mK})$, a cryostat with a so-called dilution refrigerator unit is used. The pre-cooling system of the CRESST cryostat provides a temperature of around 1 K. In its first temperature stages, liquid nitrogen (lN_2) and liquid helium (lHe) baths are used. The latter is further connected to the so-called 1 K-pot via a capillary, where vacuum pumping leads to a temperature slightly above 1 K. Cryostats employing this pre-cooling design with the use of liquid gases are commonly referred to as “wet” cryostats. In contrast, “dry” cryostats provide the pre-cooling via pulse tubes without the use of liquids.

The principle of the dilution refrigerator used for the further cooling down to mK

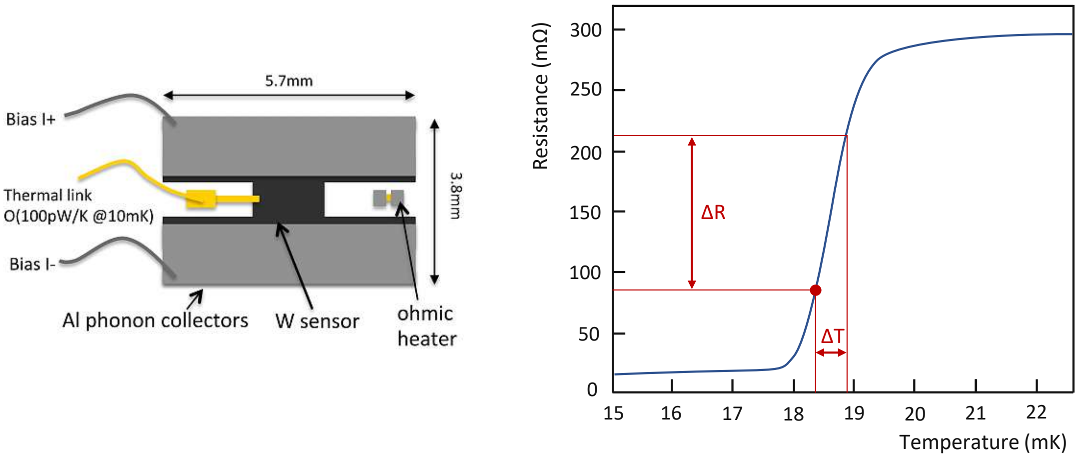

Figure 5.2.: TES layout for a phonon detector and transition curve. On the left, the layout of a W-TES as used by CRESST is depicted. This illustration is taken from Ref. [135]. The sketch on the right shows a typical transition curve and indicates the operating point as well as an exemplary temperature and resistance change potentially induced by a particle interaction.

temperatures is then based on using a mixture of ^{3}He and ^{4}He. At temperatures below ~870 mK, this mixture forms two separate phases. One consists of ~93.4 % ^{4}He and ~6.6 % ^{3}He (dilute phase), the other almost entirely of ^{3}He (concentrated phase). These phases are in principle in equilibrium in the so-called mixing chamber. However, for the purpose of cooling, the endothermic process of moving ^{3}He through the phase boundary to the dilute phase is used. Hence, the dilute phase is connected to the so-called still, where essentially pure ^{3}He gas is pumped from the mixture. In a closed circuit, after condensing and cooling the ^{3}He again, it is reintroduced to the concentrated phase. This constantly drives part of the isotopes through the phase boundary and leads to the cooling power. While there is no fundamental lower temperature limit for this process, the achievable operating temperatures, for the example of CRESST, are typically in the order of a few mK. The working principle, as worded above, is illustrated in Figure 5.1 on the example of a wet cryostat for better comprehensibility.

Signal Readout

The detectors are thermally coupled to the mixing chamber temperature stage and operated with so-called transition edge sensors (TESs). As the name may suggest, these sensors are kept in the transition between superconducting and normal conducting phase and in this steep transition, they act as very sensitive thermometers. In CRESST, thin-film W-TESs have been developed and are used together with Al phonon collectors to attain the heat signal. Figure 5.2 shows the schematic layout of a TES as well as an exemplary sketched transition curve. Indicated is a typical temperature change in the

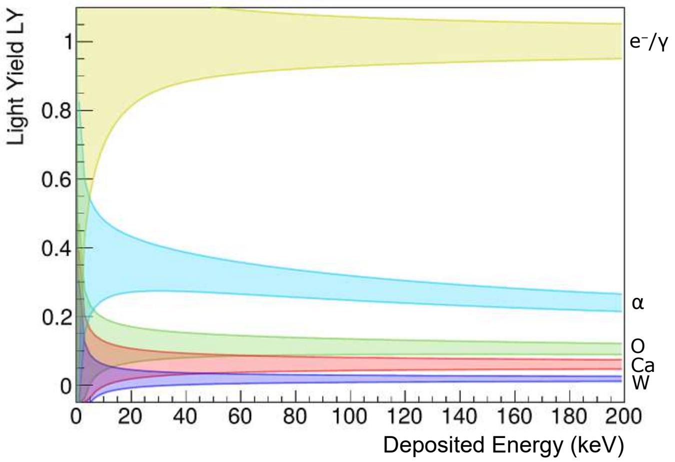

Figure 5.3.: Schematic depiction of the light yield LY of different particles and nuclei in $CaWO_4$, showing the separation between β/γ and nuclear recoil bands due to the light quenching mechanism.

order of μK following a particle interaction, leading to a resistance change in the order of mΩ. The readout of the resistance change is achieved via a SQUID (Superconducting Quantum Interference Device). Typical detected pulses feature a fast rise and rather slow decay time. The detectors hence return to the baseline operating point usually on a time scale of $\mathcal{O}(100\,\mathrm{ms})$. The operating point in CRESST detectors is often chosen around the middle of the transition, as the linearity of the measured curves is typically better in the upper half of the transition. A compromise between maximizing the dynamic range while optimizing the position in the linear region thus has to be made. The stabilization of the operating point is achieved by using an ohmic heater evaporated onto the crystal next to the TES.

The same readout technique is used for the cryogenic light detectors. In CRESST-III, these consist of silicon-on-sapphire (SOS) or pure silicon wafers for absorbing the scintillation light. The absorbed light is again converted into phonons and read out via similar TESs.

Light Yield and Particle Discrimination

In CRESST-I, only the phonon signal was measured and an identification of the type of interaction was thus impossible. However, since simultaneously reading out the light signal, event-by-event particle discrimination can be achieved, as already extensively discussed in Section 3.2. Here, the specifics of particle discrimination in CRESST are briefly described.

Due to the quenching mechanism in the scintillation light production, different event classes lead to a different amount of light for the same recoil energy measured in the phonon channel. We define the ratio between light and phonon signal as the so-called light yield (LY), typically normalized to one for electron and gamma interactions. In principle, the LY for gamma interactions is slightly lower than for electrons [136], but for the sake of simplicity both are often summarized in a single interaction band. A schematic LY plot is presented in Figure 5.3, where this e^-/γ band is shown together with the quenched alpha and nuclear recoil bands for the example of a $CaWO_4$ target. The width of the bands is dominated by the light detector resolution as well as by the statistics involved in the production and collection of scintillation light. At low energies, this leads to an overlap of the bands, reducing the particle discrimination capability. To define the position and energy dependence of the bands, especially for nuclear recoils, prior knowledge about the quenching factors is necessary. In the so-called *background data*, which are the data recorded during a physics run, the nuclear recoil bands are usually hardly and ideally not at all populated and hence need to be defined based on dedicated neutron calibration measurements (*neutron calibration data*).

5.1.2 Experimental Setup

The CRESST detectors follow the concept described in the previous section and are mounted in a dedicated experimental setup. The detector modules are situated at the heart of the cryostat, centered within passive and active shielding layers. Furthermore, the CRESST experiment is located at the LNGS underground laboratory for additional reduction of background sources. The typical choice of location and shielding layers for background mitigation have already been extensively discussed in Section 3.3. Now, the focus is set on the specific details regarding the setup of the CRESST experiment.

Passive and Active Shielding Design

A schematic drawing of the current experimental setup of the CRESST experiment is presented in Figure 5.4. The cryostat is placed at the center of the setup. It was specifically designed to feature a narrow neck below the dilution refrigerator unit. Through this neck, a so-called coldfinger of 1.5 m length transfers the mixing chamber temperature to the detector volume. In this detector volume at the heart of the bottom part of the cryostat, the so-called detector carousel is located, in which the detectors are mounted. The central detector volume is surrounded by various shielding layers. In the figure, all current shielding components are shown. However, some of them have only been added over the course of time and stages of the experiment. In the initial stage of CRESST (CRESST-I), as mentioned previously, no particle discrimination was possible due to only detecting the phonon signal. Thus, the main background component were electrons and gammas, which naturally occur in much larger rates than neutrons. Hence, the shielding was tailored to mitigate the external contribution to this background component through the use of large amounts of high-Z material. The original passive shielding around the central detector volume consisted of a low-radioactivity copper shield of at least 14 cm in each direction, further surrounded by

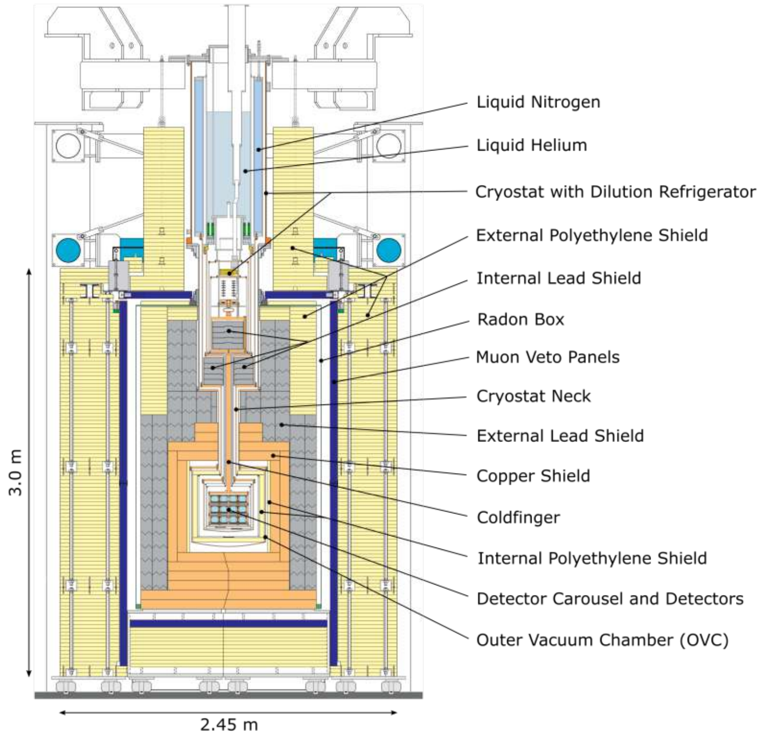

Figure 5.4.: Schematic drawing of the experimental setup of CRESST-III. Important parts are specifically denoted. The lower part of the cryostat, housing the detector carousel in which the detectors are mounted, is centered in passive shielding layers made of copper, lead and polyethylene. Plastic scintillator panels provide an active muon veto.

at least 20 cm of lead. Furthermore, an internal lead shielding above the neck of the cryostat and around the cold finger was installed, as well as an air-tight steel container, the so-called radon box, enclosing the entire shielding. This latter box is constantly flushed with nitrogen gas to avoid radon deposition on material surfaces. Overall, the cryostat design allows to minimize the line of sight between the upper part of the dilution unit and the detector volume, and the lead and copper shielding minimize the external background radiation. However, none of the polyethylene shielding layers were present.

Only between the years 2005 and 2007, in preparation of the CRESST-II commissioning, the additional outer polyethylene shielding as indicated in Figure 5.4, was implemented due to the necessity of mitigating neutrons. Indeed, in CRESST-II the light channel has been introduced to the detectors, such that β/γ background could be discriminated. Neutrons mimicking the nuclear recoil signature of potential DM particles thus became the most crucial background component. The polyethylene shield surrounding the radon box features a thickness of at least 45 cm on each side except for the bottom, where the steel wagon only allowed for a thickness of 30 cm. Together

Figure 5.5.: Photos of the inner polyethylene shielding of the CRESST experiment. In (a), the part outside the cryostat is seen on the left side of the picture in the excision of the copper shielding, while (b) presents the segmented part inside the OVC of the cryostat. Not shown is a polyethylene disk which is placed on top around the coldfinger once the OVC is closed.

with the outer polyethylene shielding, an active muon veto system was installed. This system consists of 20 plastic scintillator panels, each instrumented with a PMT to read out the light signal. The panels, indicated in blue in Figure 5.4, directly surround the radon box and cover the entire solid angle except for a circular opening at the top where the cryostat passes through.

In preparation for CRESST-II phase 2, a further additional shielding was introduced, the so-called inner polyethylene shielding. Although it was unclear where the residually observed neutron background events in the previous phase 1 originated from [137], the idea was to further mitigate any external neutron background. The inner polyethylene shield is indicated in Figure 5.4 and consists of various parts. One part is surrounding the cylindrical OVC (outer vacuum chamber) of the cryostat inside the copper shielding, which itself provides a cuboid inner excision, the so-called cold box. This polyethylene part is thus placed into the cuboid cold box and reduces the inner excision to a cylindrical volume to fit the cryostat. Part of this volume is shown in the picture in Figure 5.5a, taken with the opened shielding. The closed cryostat, hanging from the top, is visible in this picture as well. A look into the opened OVC pot provides a glimpse on the additional parts of the inner polyethylene shielding and is presented in Figure 5.5b. The shielding inside the OVC consist of circular plates on top and bottom as well as four segments on the sides that are visible on the picture. The gaps between the segments are oriented towards the corners of the cold box, where the thickness of the polyethylene outside the OVC is largest, and shall facilitate the neutron calibration when placing the source directly outside the OVC at the corresponding positions.

The experimental setup as described above is in place until today and has thus been continuously used during data taking for the latest stage of the experiment, CRESST-III, which is the focus of this thesis. Additional details and visualizations of the experimental setup are shown in Section 5.2.3, where the geometries implemented in the simulation are discussed.

Detector Modules and Detector Carousel

Throughout the various phases of the experiment, CRESST has been using diverse detector designs. These featured different holding schemes, target crystal sizes and materials. In this work, the focus is set on the latest stage of the experiment, as the neutron background studies detailed in Section 5.5 are considering the experimental setup used in the first run of CRESST-III. Hence, the detector modules operated in this run are described in the following.

A new detector design has been introduced in the third stage of the experiment. As the main goal of CRESST-III was to enhance the sensitivity to low energy recoils, detector parameters have been adapted for this purpose. The sensitivity of TESs has been optimized and crystal sizes have been reduced. Compared to e.g. the $(32 \times 32 \times 40)\,\mathrm{mm}^3$ crystal used in the TUM40 detector module of CRESST-II [97], the "CRESST-III design" features a target size of $(20 \times 20 \times 10)\,\mathrm{mm}^3$, corresponding to a reduction by roughly one order of magnitude in volume and mass. This improves the sensitivity due to the energy threshold following the proportionality relation $\mathrm{E}_{th} \propto \mathrm{m}^{2/3}$ [131]. In the base CRESST-III design, as sketched and photographed in Figure 5.6, the target crystal is made of CaWO_4 and held by three sticks of the same material. As seen on the picture, the TES is directly evaporated onto the crystal. Next to the target crystal, a $(20 \times 20 \times 0.5)\,\mathrm{mm}^3$ SOS light detector is placed, which is likewise held by three CaWO_4 sticks. Both phonon and light detector together are fully encapsulated in a copper housing, whose inner surface is coated with a reflective and scintillating foil (Vikuiti) to enhance the light collection efficiency and veto surface alpha background. In the case of surface alpha events, part of the energy may leave the target crystal and be deposited in the foil, leading to a large scintillation signature, which can be discriminated from other types of signals. To further improve the detection of near surface backgrounds, also the holding sticks are instrumented with TESs in the baseline CRESST-III design and hence called "iSticks" (short for instrumented sticks).

Additional to the module design described above, the so-called "Beaker design" has further been developed and used in the experimental runs of CRESST-III. Figure 5.7 shows a schematic drawing and photo of this design. The main differences compared to the CRESST-III modules are that the target crystal is interfaced to a separate ring and carrier crystal, which themselves are instrumented with TESs, and that the light

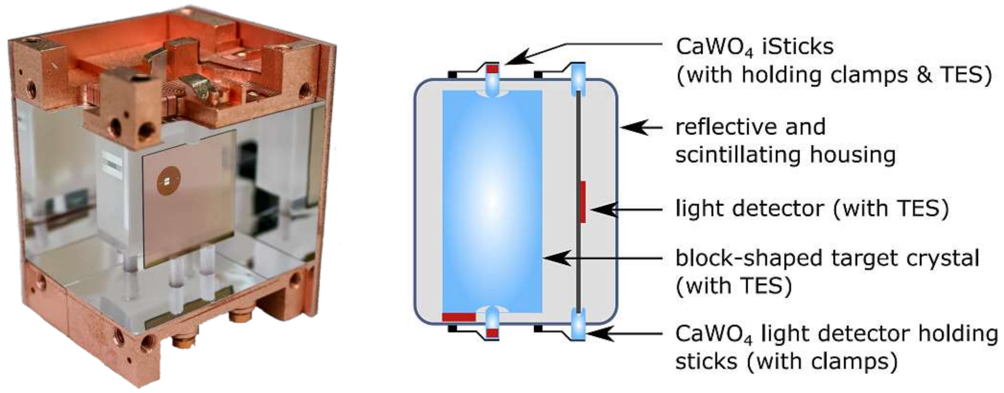

Figure 5.6.: CRESST-III detector module, showing a photo of an opened on the left and a schematic drawing of its individual parts, taken from Ref. [4], on the right.

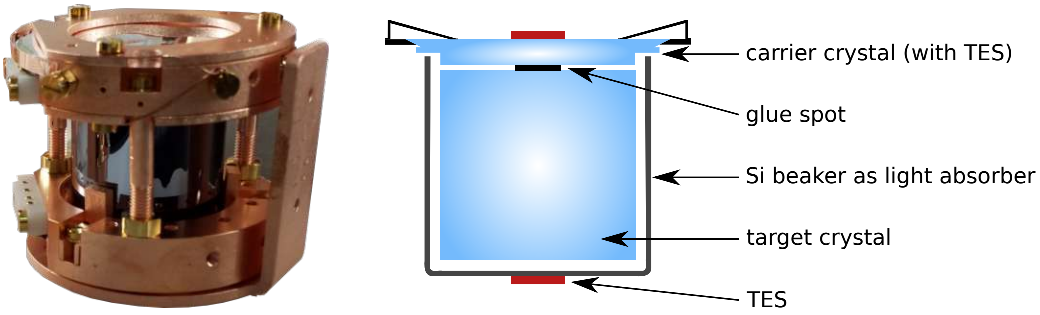

Figure 5.7.: Beaker module, showing a photo of a closed detector on the left and a schematic drawing of its individual parts on the right.

detector is realized by a silicon beaker. This provides an alternative design with a surface background veto efficiency comparable to the CRESST-III module design, but enhanced light collection efficiency.

The detectors in the experimental setup are mounted in the so-called detector carousel, located in the bottom part of the cryostat indicated in Figure 5.4. A picture of the detector carousel of CRESST-III Run34 is presented in Figure 5.8. Originally, the carousel was designed for housing 33 cylindrical detector modules. Nine outer and three inner copper rails were used to mount the detectors. The outer rails could each hold three modules, while the space on the inner ones only allowed for two on each rail.

With the use of the cuboid CRESST-III detector modules, however, a new detector arrangement was planned and a dedicated holder was installed on the bottom of the carousel. On the picture, this holder is only vaguely perceptible. Thus, Figure 5.9 shows the technical drawing of the holder with the detectors mounted on it. Ten detector modules in two rows of five each are placed closely next to each other. Additional to the ten CRESST-III modules, three beaker modules were operated in Run34. This

Figure 5.8.: Photo of the detector carousel of CRESST-III Run34. In this finalized state, the outer copper rails with the white plastic connectors only allow a narrow glimpse on the detectors mounted inside.

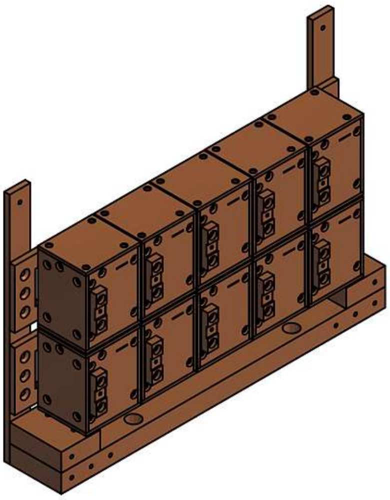

Figure 5.9.: Drawing of the new detector mount for the cuboid CRESST-III modules used in Run34. The mount is placed centered on the bottom of the detector carousel.

exact layout is specific for CRESST-III Run34, while the arrangement of cuboid as well as beaker modules in subsequent experimental runs was further modified. Additional details about the geometry are discussed in Section 5.2.3 in the context of the simulation studies.

5.1.3 Latest Results (CRESST-III Run34)

The latest results published by the CRESST collaboration are on spin-dependent DM scattering on lithium targets [132, 133]. However, in the most standard scenario DM is assumed to interact via spin-independent scattering with ordinary matter. Focusing on this type of interaction, the latest published limit by CRESST originates from a $CaWO_4$ detector operated in Run34 [4].

Detector A

The detector used to acquire the published limit is referred to as *detector A* in the following. Detector A is the CRESST-III detector module which featured the lowest detection threshold for nuclear recoils in Run34 with a value of 30.1 eV which corresponds to a sensitivity down to DM particle masses of 160 MeV/c^2. This recoil energy threshold is set according to the condition that only a single noise trigger above threshold per kg·d of exposure is allowed. With this 23.6 g $CaWO_4$ detector, an exposure of 5.6 kg·d before cuts was collected between October 2016 and January 2018.

Detector Calibration

To define the energy scale from the measured signal heights, a calibration source of known energy is used, in this case ^{57}Co mainly providing 122 keV gammas. As the CRESST-III detectors are typically only sensitive at lower recoil energies, in $CaWO_4$ target crystals the tungsten K_α escape peaks at around 63.2 keV can be used for initial calibration. Later, during the run, this calibration can further be adjusted using the characteristic Hf X-ray lines at 2.6 keV (M_1 shell), 10.74 keV (L_2 shell) and 11.27 keV (L_1 shell) [118] originating from the cosmogenic activation of tungsten and delayed EC decay of ^{179}Ta. In addition to this energy calibration, a neutron calibration with an AmBe source is performed to precisely define the location of the nuclear recoil and β/γ bands in the LY plot.

Applied Cuts & Signal Survival Probability

The obtained events in the detector are subject to distinct cuts. Events with abnormal LYs or with pulse shapes deviating too much from the nominal standard shape are removed from the data set. The same is true for events featuring coincidences with the muon veto as well as with other detectors. A signal survival probability, i.e. the probability that a valid event survives the applied cuts, is attained by superimposing simulated events of nominal shape and desired energy (= injected energy) on empty noise baselines and passing them through the same analysis chain as the actual events. The survival probability for detector A is shown in Figure 5.10 together with the trigger efficiency. The combination of both is commonly referred to as the *efficiency* of the

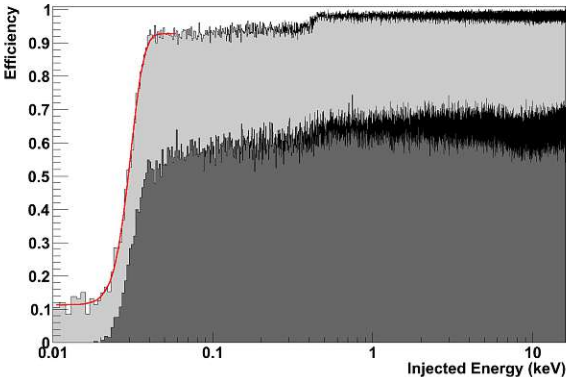

Figure 5.10.: Efficiency for events of certain recoil energies to survive all cuts (dark gray) in detector A of CRESST-III Run34. In light grey, solely the trigger efficiency is drawn. The injected energy on the x-axis corresponds to the true simulated energy of the pulse that is passed through the analysis chain. The plot is taken from [4].

detector, as labeled on the y-axis of Figure 5.10.

DM result

The surviving events in the background data set can then be plotted in the LY vs energy plane, as depicted in Figure 5.11a. In this representation, the ROI of detector A between threshold and 16 keV recoil energy is shown. An acceptance region for the LY of the events is defined in the nuclear recoil bands below the mean value for O recoils, before looking at the data. This is done to maximize the potential signal while minimizing the leakage of events from the β/γ-band into the nuclear recoil acceptance region. The nuclear recoil events are assumed to be symmetrically distributed around the mean of the band. Leakage events would rather populate the region of higher LY. Location and width of the bands are obtained from neutron calibration data. The energy spectrum of the accepted events is shown in Figure 5.11b. The majority of the background can efficiently be discriminated by the LY cut. No single event is surviving above the low-energy region, where the bands start overlapping. However, especially below ~200 eV a steeply rising excess event rate towards lower energies is observed. These events limit the sensitivity of the experiment as they have to be conservatively assumed to be potential DM events, although a dark matter explanation seems highly unlikely due to different shapes and rates of such an excess signal observed in different detectors. The exclusion curve calculated from the surviving events is the CRESST-III limit displayed in Figure 2.11. It is to date the best direct detection limit on spin-independent DM-nucleus scattering between 0.16 - 1.8 GeV/c^2, without taking into account limits calculated using the Migdal effect.

Unfortunately, the origin of the excess events observed in CRESST, which limit the sensitivity, is yet unknown. Different experiments see similar effects in their detectors,

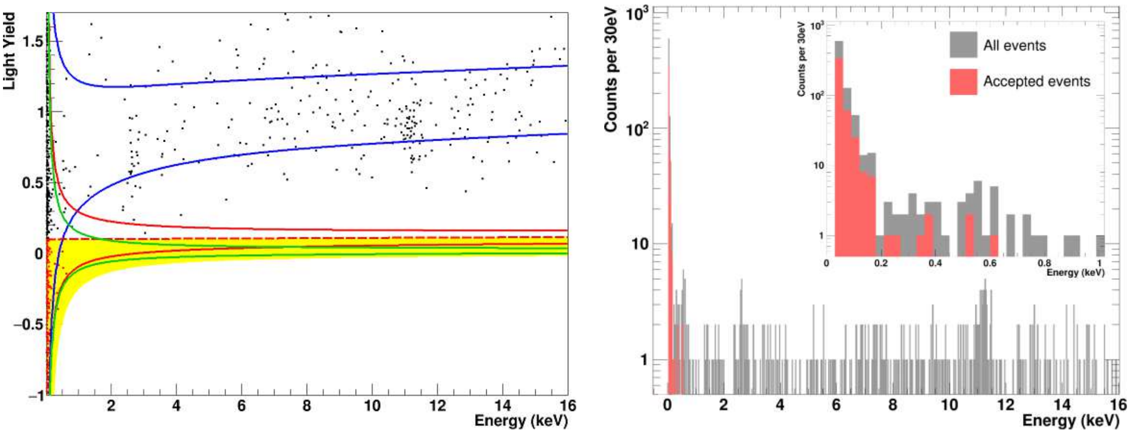

(a) (b)

Figure 5.11.: Background data obtained in detector A in CRESST-III Run34. (a) All events plotted in the LY vs recoil energy plane, where the acceptance region in the nuclear recoil bands is colored in yellow. (b) Energy spectrum of all events (gray) and accepted events (red). Both plots are taken from [4].

such that a common initiative was started to discuss data and interpretations within the EXCESS workshop [82]. In all the experiments, even a statement on whether the events have an electron recoil or a nuclear recoil origin seems difficult. Thus, one question posed to the neutron simulation studies performed for this thesis, in addition to the overall estimation of the neutron background rate, is, if one of the neutron background contributions could realistically lead to a similarly rising event rate.

5.2 Simulation of Neutron Generation and Interaction

The simulation-focused sections start with the description of the neutron and muon generation with SOURCES [122, 123] and MUSUN [127] and the description of the geometry implemented in ImpCRESST [118] as well as the event building in the simulations.

5.2.1 Neutron Generation with SOURCES 4C

Radiogenic neutrons are created by nuclides in the natural decay chains which undergo α-decays or s.f. processes. In Table 5.1, these nuclides in the ^{238}U, ^{235}U and ^{232}Th chain are listed together with their half lives and branching ratios as well as the released energy in the α-decay. Only the heaviest nuclides have a non-vanishing s.f. probability, with

Table 5.1.: List of α-decaying nuclides in the natural decay chains. Half lives, decay branching ratios (BRs) and Q-values are obtained from the NuDat 3.0 online database [138]. Only nuclides with α-decay BR and abundance in the decay chain larger than 1 % are given.

Nuclide	Half life	α-decay BR	Q_α (keV)	s.f. BR
^{238}U	$4.468 \cdot 10^9$ yr	100 %	4269.9	$5.4 \cdot 10^{-5}$ %
^{234}U	$2.455 \cdot 10^5$ yr	100 %	4857.5	$1.6 \cdot 10^{-9}$ %
^{230}Th	$7.54 \cdot 10^4$ yr	100 %	4770.0	–
^{226}Ra	1600 yr	100 %	4870.7	–
^{222}Rn	3.8235 d	100 %	5590.4	–
^{218}Po	3.098 min	100 %	6114.8	–
^{214}Po	163.6 μs	100 %	7833.5	–
^{210}Po	138.376 d	100 %	5407.5	–
^{235}U	$7.04 \cdot 10^8$ yr	100 %	4678.1	$7.0 \cdot 10^{-9}$ %
^{231}Pa	$3.276 \cdot 10^4$ yr	100 %	5149.9	$< 3 \cdot 10^{-10}$ %
^{227}Ac	21.772 yr	1.38 %	5042.3	–
^{227}Th	18.697 d	100 %	6146.6	–
^{223}Ra	11.43 d	100 %	5979.0	–
^{219}Rn	3.96 s	100 %	6946.2	–
^{215}Po	1.781 ms	100 %	7526.3	–
^{211}Bi	2.14 min	99.72 %	6750.4	–
^{232}Th	$1.40 \cdot 10^{10}$ yr	100 %	4081.6	$1.1 \cdot 10^{-9}$ %
^{228}Th	1.9125 yr	100 %	5520.2	–
^{224}Ra	3.63 d	100 %	5788.9	–
^{220}Rn	55.6 s	100 %	6404.7	–
^{216}Ra	0.145 s	100 %	6906.3	–
^{212}Bi	60.55 min	35.94 %	6207.3	–
^{212}Po	0.299 μs	100 %	8954.2	–

^{238}U contributing by far the most to this neutron production channel. All other listed nuclides may contribute to the neutron yield via (α,n) reactions on suitable targets.

In this work, SOURCES [122, 123] is used to calculate the neutron yield and spectrum originating from contamination in materials of the experimental setup for further propagation with the Geant4 based ImpCRESST simulation software. This newly developed interface from SOURCES output to ImpCRESST has been discussed in Section 4.1.4. As the original SOURCES 4A [122] code only treats (α,n) reactions up to α-energies of 6.5 MeV, a modified version with extended cross section data up to 10 MeV [139–141] was employed. For the usage in this work, the obtained extended libraries were integrated in the SOURCES 4C [123] code. This adapted software was then used to attain the neutron flux and spectrum due to the (α,n) and s.f. processes in the respective materials of the experimental setup.

For this purpose, the targets for (α,n) reactions have to be specified in the input file. Additionally, the contamination with radioactive nuclides has to be listed by the user in units of atoms / cm^3. The internal data tables of SOURCES 4C are then used in the calculation of the resulting neutrons. These tables contain the energies of α particles created by typical α-decaying radionuclides as well as decay constants and s.f. branching ratios. Furthermore, the libraries include the stopping power dE/dx for α particles in various materials together with the respective (α,n) reaction cross sections $\sigma_i(E)$ on nuclides i. Considering the energy loss, the probability of an α particle of energy E_α to undergo an (α,n) reaction on a specific nuclide before being stopped in the material is hence given by [123]

$$P_i(E_\alpha) = \int_0^{E_\alpha} \frac{N_i \sigma_i(E)}{-dE/dx} dE \quad , \tag{5.1}$$

where N_i is the atom density of nuclide i in the material.

Typically, lighter elements are more susceptible to (α,n) processes, because the α particle first has to overcome or tunnel through the Coulomb barrier of the nucleus. From this fact alone, the cross section is already a function of the α energy. A rough approximation can be given by calculating the energy needed to approach the vicinity of the nucleus,

$$E_{\infty,r_{nuc}} \approx \int_\infty^{r_{nuc}} -\frac{Z_\alpha Z_{nuc}}{4\pi\epsilon_0 r^2} dr \approx \frac{Z_\alpha Z_{nuc}}{4\pi\epsilon_0 r_{nuc}} \xrightarrow{r_{nuc}\sim 10\,\mathrm{fm}} 288\,\mathrm{keV} \cdot Z_{nuc} \quad . \tag{5.2}$$

Here, the radius of the nucleus is estimated at 10 fm to yield an approximated numerical result. This is a generous and non-universal assumption for the sake of simplicity. Non-vanishing cross sections may already be obtained for lower energies due to tunneling probabilities. Still, the equation shows that the barrier for (α,n) reactions on heavy nuclei is large.

Additional to this fact, the possibility for an (α,n) reaction on any given target nucleus has to be considered. For this, the Q-value of the reaction and its respective threshold can be assessed. In Table 5.2, these data are summarized for the nuclides present in polyethylene, copper and lead, based on the QCalc Q-value calculator [92]. The natural abundances, that are used to attain the isotope fractions present in the materials, are

Table 5.2.: Q-values and thresholds of (α,n) reactions for isotopes present in polyethylene, copper and lead. Respective values are acquired from QCalc [92] and rounded to two digits after the comma. The second column gives the percentage of isotopes present in the respective material, i.e. the natural abundance scaled by the fraction of the element present in the material (e.g. 1/3 C and 2/3 H in CH_2).

	Isotope	Abundance in Material (%)	Q-value (MeV)	Threshold (MeV)
Polyethylene	H	66.656	-23.68	117.80
	D	0.011	-4.19	12.52
	^{12}C	32.96	-8.50	11.34
	^{13}C	0.369	2.22	0
Copper	^{63}Cu	69.174	-7.50	7.98
	^{65}Cu	30.826	-5.82	6.18
Lead	^{204}Pb	1.424	-13.61	13.88
	^{206}Pb	24.145	-13.07	13.32
	^{207}Pb	22.083	-12.15	12.38
	^{208}Pb	52.348	-14.96	15.25

taken from the best measurements of isotopic abundances in single terrestrial sources cited in Ref. [142]. According to the thresholds, (α,n) reactions are possible on ^{13}C in polyethylene and on the natural isotopes in copper. In the latter case, however, the reactions can only be induced by high-energetic α particles. As only ^{212}Po releases α-particles with energies larger than the threshold of the reaction on ^{63}Cu (see Table 5.1), mostly ^{65}Cu will play a role in this neutron production channel. In lead, no (α,n) reactions are possible at all and the entire neutron yield originates from nuclides in the natural decay chains that undergo spontaneous fission.

The neutron spectra and yields attained in the shielding materials due to measured radioactive contamination levels are presented in the context of the internal radiogenic background simulations in Section 5.5.2.

5.2.2 Muon Generation with MUSUN

To attain the flux and energy spectrum of muons at LNGS, a simulation using MUSUN [127] is performed. This software calculates the muon spectrum, flux and angular distribution after traversing large overburdens and returns the respective results. A

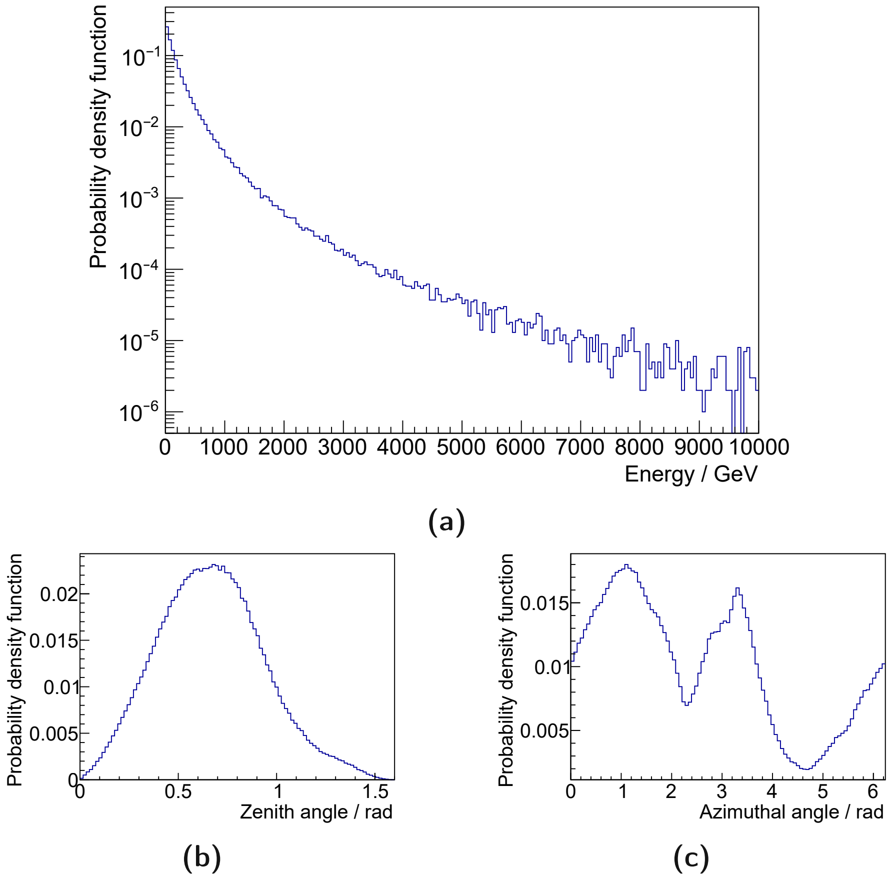

(a)

(b)

(c)

Figure 5.12.: Energy spectrum (a), zenith angle (b) and azimuthal angle (c) of muons at the LNGS underground laboratory, obtained with MUSUN [127].

specific version of the code which already includes the detailed overburden of the LNGS underground laboratory is used. Hence, the correct slant depth distribution is taken into account. As the code has been verified against data collected in the LVD and MACRO experiments located at LNGS, the attained values are similar to those found in literature [143] and deemed to be reliable for the purpose of our study. The results of the MUSUN calculation are depicted in Figure 5.12, showing the probability density function of the energy as well as the angular distribution of muons. The mean energy of the muons is obtained to be 270 GeV and the angular distributions follow the profile of the Gran Sasso mountain overburden, yielding an average zenith angle of 0.67 rad. The acquired MUSUN files are plain text files listing the exact position, direction and energy of each single muon line by line. To attain suitable positions, the user defines the size of the surface on which the muons shall be sampled.

The interface to a newly developed primary particle generator in ImpCRESST, which makes use of these muon data files provided by MUSUN, is already described in Section

4.1.4. Further details and results of its application are presented in the context of the cosmogenic neutron background in Section 5.5.3.

5.2.3 Geometry and Tracking in ImpCRESST

In the neutron simulation studies for the CRESST experiment presented in the subsequent sections, ImpCRESST (versions 7.3.0 and 7.5.0), based on Geant4 (version 10.6.3) has been used for all the simulations of particles traversing the setup. The physics lists used for the respective tracking of the various particles have already been presented in detail in Section 4.1.2. Besides the physics, the actual geometry implemented in the code is of highest importance for an accurate modeling of particle interactions expected to be obtained in the detectors.

To attain reliable results, the entire shielding geometry of the experiment has to be recreated. Thus, in the course of the studies presented in this thesis and based on an already existing elaborate geometry implementation, the required parts were modeled in ImpCRESST. Sizes and thicknesses of various shielding layers were extracted from technical drawings and partly cross-checked by manually measuring them at LNGS. The implementation in ImpCRESST is realized up to a reasonable level of detail. This means for example that small screws or cables are not included. However, shapes and sizes of massive parts and especially of volumes close to the detectors and of the detectors themselves are carefully implemented. A visualization of the complete shielding geometry is shown in Figure 5.13. The parts of the geometry are equivalent to those presented in Figure 5.4 and discussed in Section 5.1.2. This core experimental geometry is used for the simulation studies presented in the next sections. The facility building around the shielding setup is not considered, as its thin walls are not expected to significantly enhance or mitigate any neutron background contribution. The geometry as presented in the figure is placed into a cuboid space surrounded by rock mimicking the location in hall A of the LNGS laboratory. The production cuts per region (cf. Section 4.1.4) used in the simulations performed in this setup are listed in Table 5.3. As discussed previously, these cuts provide a gradual increase in precision going from outside to inside in the simulated geometry, preserving the highest level of detail inside the detector modules.

Prior to the work presented in this thesis, the main parts of the shielding geometry had already been implemented in ImpCRESST. However, some volumes surrounding the detector modules were lacking details. After taking measurements at LNGS, especially the shapes and thicknesses of the cryoshields of the cryostat were refined. Furthermore, the inner polyethylene shielding was added to the geometry, as the following simulation studies are the first to consider this additional neutron shield.

The most crucial part required for the simulation, apart from the shielding layers, is the detector carousel. Its layout and the detector modules placed inside have a crucial

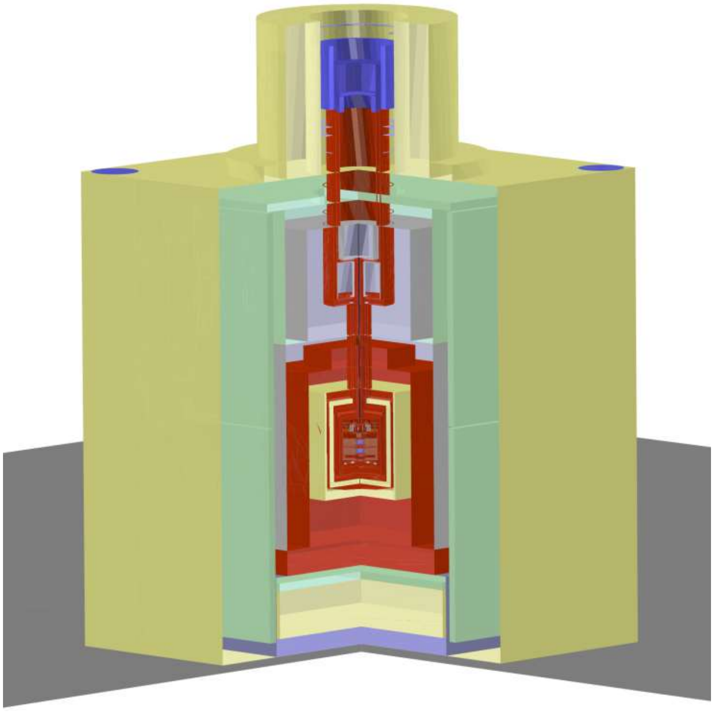

Figure 5.13.: Visualization of the CRESST shielding geometry as implemented in ImpCRESST.[1] The contours of the shielding layers can well be seen and are in accordance with the schematic drawing of Figure 5.4. From outside to inside, there is the outer polyethylene shielding (yellow), the muon veto panels (light green), the lead shielding (grey), the copper shielding (ochre), the inner polyethylene shielding (yellow), and the central cryostat housing the detector carousel.

Table 5.3.: Production cuts per region in the simulations using the CRESST shielding geometry. Values decrease towards the detector modules, precision hence increases.

Region	Production cut (mm)
Rock (surrounding the setup)	50
Outer polyethylene and lead shielding	3
Copper shielding	1
Inner polyethylene shielding	0.1
Detector carousel	0.01
Detector modules	10^{-6}

influence on the rates and spectra obtained in the detectors. Especially concerning the

---

[1] The representation is attained via an exported GDML (Geometry Description Markup Language) file. The TEveViewer of ROOT only shows the contours of the volumes without filling.

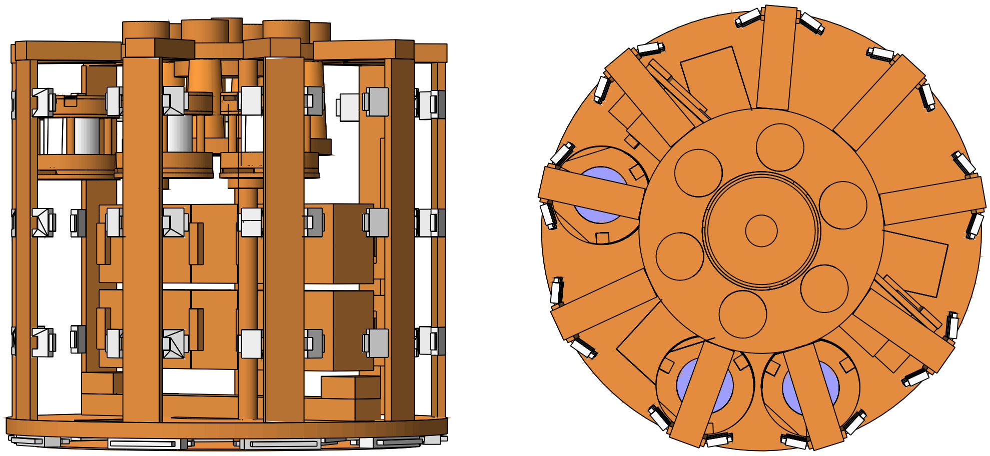
(a) side view (b) top view

Figure 5.14.: Detector carousel of CRESST-III Run34 visualized with ImpCRESST using the DAWN software available for Geant4. Ten cuboid CRESST-III detector modules are placed on the central detector holder, three additional Beaker modules are mounted on the outer copper rails.

low energy background in the ROI for the DM search, the parts closest to the target crystals play an essential role. For the implementation of the carousel, the CRESST-III detector module geometry was refined and the Beaker modules were additionally implemented in the code. While the latter are not the main objective when comparing results to detector A data, they are needed to rebuild the carousel as precisely as possible. All modules were hence placed at the positions according to the layout of the detector carousel in CRESST-III Run34. A visualization of this carousel, as implemented in ImpCRESST, is shown in Figure 5.14. The representation is similar to the photo shown in Figure 5.8, but solely displaying the carousel without the parts of the cryostat above it that can be seen on the photo. This detector carousel is located in the center of the geometry, surrounded by the shielding layers, visible in Figure 5.13.

Pictures and drawings of the detector modules used in CRESST-III Run34 have been shown in Figure 5.6, 5.7 and 5.9 in Section 5.1.2. Their layouts were implemented in ImpCRESST up to necessary level of detail. This means that the main geometry of the copper housing and of all the active parts is rebuilt, paying attention to recovering the correct sizes and masses of all these volumes. However, small parts like screws, cables or the TESs have been omitted thus far.

A visualization of a CRESST-III detector module from ImpCRESST is presented in Figure 5.15. On the left, the module is viewed from the outside, only providing a look at the cuboid copper housing. The additional copper part attached to it resembles the connector for the press contact of the cable connection, as partly visible in Figure 5.9 as well. On the right, a wireframe representation of the module is shown, presenting

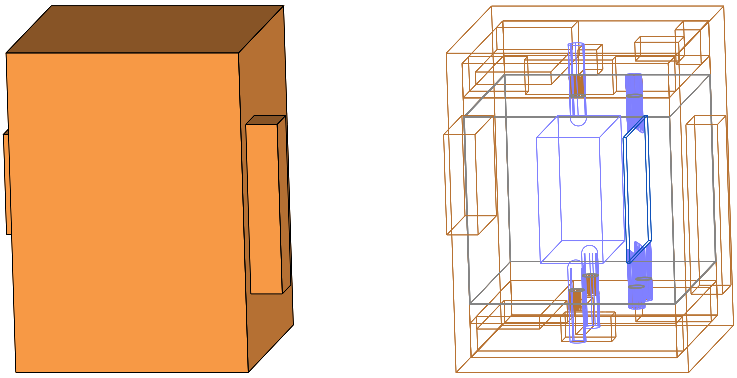

Figure 5.15.: CRESST-III detector module visualized with ImpCRESST. On the left: view on the outer surfaces of the detector, showing the cuboid copper housing as well as the copper part corresponding to the press contact for the cable connection. On the right: Wireframe representation providing a view to the inside, where the phonon and light detector crystals are held by sticks and surrounded by a reflective and scintillating foil.

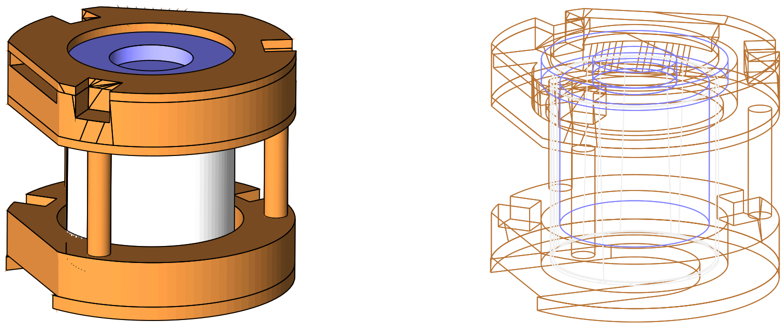

Figure 5.16.: Beaker module visualized with ImpCRESST. On the left: view on the outer surfaces of the detector, showing the copper housing, which does not entirely encapsulate the active parts, as well as the silicon beaker light detector. On the right: Wireframe representation providing a view to the inside, where the cylindrical phonon detector is attached to a carrier crystal and surrounded by the silicon beaker.

the interior of the module with the phonon and light detector both held by $CaWO_4$ sticks and the inner surface of the copper housing being covered with reflective and scintillating foil.

A visualization of the Beaker module is displayed in Figure 5.16. On the left, again a view from the outside onto the module is presented, showing the copper holder which does not fully encapsulate the detector, and the silicon beaker light detector. On the right, the wireframe representation provides a look inside, showing the cylindrical phonon detector crystal attached to a carrier crystal and surrounded by the beaker.

In the following simulation studies, the presented geometries in ImpCRESST are used for tracking the traversing particles and assessing the spectra and rates obtained in the detectors due to various neutron sources. The ten CRESST-III detector modules on the central detector mount are denoted by letters A to J, with the top row representing detectors A to E and the bottom one F to J. Detector A, the one of most interest due to providing the best DM limit as discussed in Section 5.1.3, has thus been the top left module looking at Figure 5.9 and 5.14a.

5.2.4 Event Building from Simulated Data

This section briefly discusses the main data extracted from the particle simulations, that are of interest to assess the neutron background in the CRESST experiment, and the processing of the data to model the detector response. While a detailed data set about interactions in the sensitive detector volumes is initially stored, only part of the data is required for the analysis in this work. The data acquired with ImpCRESST are hence postprocessed using the ancillary CresstDS software (cf. Section 4.2) in its version 2.1.0.

First and foremost, the information of highest importance is the energy deposition in each sensitive detector per simulated event. ImpCRESST stores the energy deposition in each Monte Carlo simulation step as well as the respective particle and process. With CresstDS, the individual energy depositions are summed up according to the time resolution of the detector to form a total registered energy E in the event. A time window of 2 ms is used for the detector event building. To not lose all the additional information on the contributions to this detected energy, the fractions of energy deposited by various particle types as well as the type of particle initiating and the one contributing most to the energy deposition are stored. This information is subsequently used to assess the type of interaction and to distinguish between O, Ca and W recoils.

Furthermore, the energy resolution of detector A is applied to the summed event energy deposition. This energy dependent resolution is provided by the CRESST analysis team and calculated via a Gaussian fit to the obtained gamma peaks in the collected data. The function

$$\sigma(E) = \sqrt{p_0^2 + p_1^2 \cdot (E^2 - E_{th}^2)} \tag{5.3}$$

is used to describe the width of the peaks, resulting in parameters $p_0 = 0.0045$ keV and $p_1 = 0.0104$ for detector A. The resolution may not be valid when extrapolating to the energy region above the official data set, i.e. above 16 keV, as it has to be done for some analyses in this work.

Threshold and efficiency are considered in the dedicated ROOT scripts used to analyze the processed data. They are modeled via the energy-dependent signal survival probability presented in Figure 5.10, approximated by a function

$$eff = \begin{cases} 0.3 + 0.3 \cdot \tanh[150 \cdot (E - E_{th})] & , E < 0.5\,\text{keV} \\ 0.66 & , E > 0.5\,\text{keV} \end{cases} \tag{5.4}$$

where E is the energy deposition and $E_{th} = 0.03\,\text{keV}$ the energy threshold of detector A.

Based on the obtained energy spectra and rates in the detectors, most of the analysis can already be performed. As an additional aspect, however, a look at the light yield (LY) is of interest as well. The LY is the ratio between the scintillation light and the phonon energy measured in the cryogenic detectors, as described and depicted in Section 5.1.1. The measured light energy L is defined to be a scaled quantity leading to a LY equaling unity for electromagnetic interactions in the phonon energy region of the calibration peaks. Studying the scintillation light production in simulations, though, is not a straightforward task. A theoretical model to describe the scintillation light output exists in the form of Birks' law [56],

$$\frac{dL}{dx} = \frac{A \cdot \frac{dE}{dx}}{1 + kB \cdot \frac{dE}{dx}} \quad , \tag{5.5}$$

relating the scintillation light created per path length $\frac{dL}{dx}$ to the energy deposition per path length $\frac{dE}{dx}$, using a proportionality factor A and Birks' constant kB. It has been shown in a previous study [95], however, that this phenomenological model is not perfectly suited to describe the measured LY bands of nuclear recoils and that it is generally difficult to correctly apply the model in assessing events at low energies. The main reason for the inapplicability is the calculation of step lengths in Geant4, where the charged ions below certain energies are stopped in a single step. This leads to a wrong treatment of the combination of electronic and nuclear stopping power and overall to an imprecise treatment of the energy loss per step length. A partial solution discussed in Ref. [95] could be provided by introducing a maximum step length. However, this leads to much extended computing times and the results, especially at low energies, still seem to diverge from measurements. Hence, this ab initio approach is not feasibly applicable and a standard solution is to use a parametrization of the light yields for nuclear recoils according to Ref. [100]. This parametrization is described via

$$LY_x(E_R) = LY_x^{\infty}(1 + f_x \exp(-E_R/\lambda_x)) \quad , \tag{5.6}$$

where LY_x^{∞} corresponds to the limit of the LY at nuclear recoil energy $E_R \to \infty$, and f_x together with λ_x describe the energy-dependence of the LY. The values of these parameters, determined in Ref. [100], are listed in Table 5.4. In the following sections, whenever presenting a LY plot, this parametrization for the nuclear recoils is employed, while electron and gamma events are treated via Birks' law. Using this approach for nuclear recoils may lead to slightly narrower bands than expected, as the difference in LY between the various isotopes of an element is not considered, which would be expected due to their difference in mass and hence stopping power and ionization density. Still, it is assumed to give the most realistic representation.

As also the light detector has a finite energy resolution, the reconstructed and scaled light energy L, attained from the simulated data via Birks' law for electrons and gammas

Table 5.4.: Parametrization of nuclear recoil LY according to Eq. 5.6, as presented in Ref. [100]. 1σ confidence limits of the statistical errors are included.

	LY_x^∞	f_x	λ_x
O	0.07908 ± 0.00002	0.7088 ± 0.0008	567.1 ± 0.9
Ca	0.0595 ± 0.0008	0.189 ± 0.002	801 ± 19
W	0.021 ± 0.002	—	—

and via the parametrization of the LY and calculating $E_R\, LY_x(E_R)$ for recoiling nuclei, is smeared with a Gaussian distribution. The energy-dependent width of the distribution is parametrized via

$$\sigma(L) = \sqrt{\sigma_{L,0}^2 + S_1 L + S_2 L^2} \quad , \tag{5.7}$$

with parameters $\sigma_{L,0} = 0.094$ keV, $S_1 = 0.186$ keV and $S_2 = 0.026$ for detector A.

5.3 Detector Calibration with an AmBe Neutron Source

A calibration with a neutron source is conducted in the experiment mainly to determine the difference in the light output due to nuclear recoils compared to electron recoils. Essentially, the attained data are thus utilized for fitting the energy-dependent quenching factors of the target crystal. In this section, the simulation of such a calibration run is performed and subsequently compared to the actual data taken with detector A in Run34.

5.3.1 The AmBe Neutron Source in ImpCRESST

In CRESST, an AmBe source is typically used as a neutron source for detector calibration. For Run34, a source emitting 50 neutrons per second is placed outside the OVC of the cryostat. The total calibration data taking period amounted to 840 hours.

To compare to the actual measurement, the simulation was set up by placing the source at the assumed position in the experiment and simulating the amount of neutrons corresponding to the life time of data taking. The source position used in the simulation is indicated in Figure 5.17. It has to be mentioned that the exact location of the source in the real experimental setup has not been recorded. It has been attached to a string hanging from one of the screws of the OVC flange at the marked position of one of the dedicated excisions in the inner polyethylene shielding. However, in practise, the excision in the inner polyethylene shield may not precisely be oriented at 45° and the

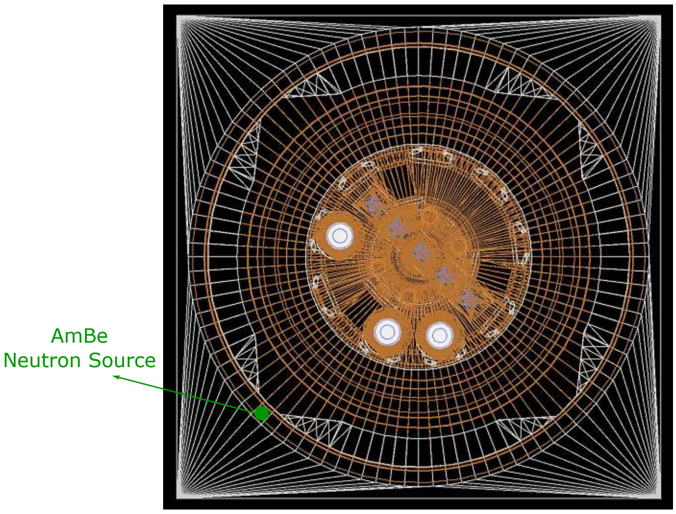

Figure 5.17.: A wireframe view of the cold box from the top, indicating the position of the AmBe neutron source outside the OVC. It is placed at one of the excisions of the inner polyethylene shielding and at the height of the upper detector row. The inner polyethylene shielding (white) and the cylindrical thermal shields of the cryostat as well as all other parts made of copper (ochre) are visible, with the Carousel housing the detectors of Run34 placed in the center.

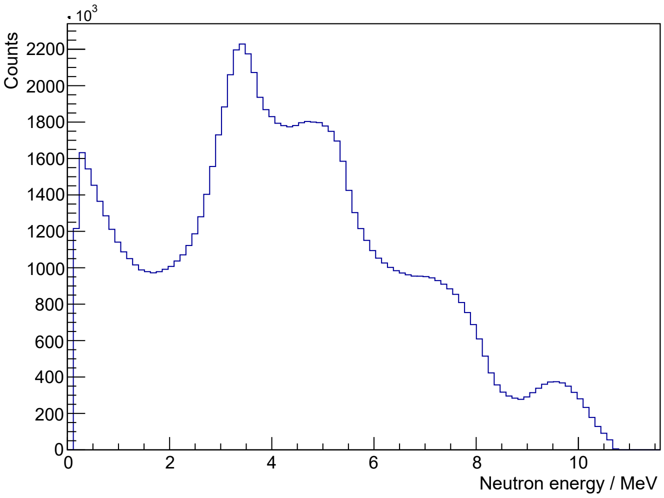

Figure 5.18.: Spectrum of the primary neutrons emitted from the AmBe source used for the neutron calibration in CRESST.

angular position of the OVC screw may not entirely line up with this angle either. As the length of the string is furthermore not strictly defined, the exact horizontal and vertical positions of the source are unknown. Figure 5.17 shows that the simulation assumed the source being placed in the middle of the excision horizontally. The vertical position of the source is set to the height of the upper detector row due to information received via internal communication.

For the simulation of the source, a simplification was made by not simulating the exact composition of the Am and Be mixture, and the series of processes in which the α-decay of ^{241}Am leads to an (α,n) process on ^{9}Be to create a neutron. The precise geometry of the source and its encapsulation was not provided and would hence have been difficult to model. Together with the treatment of the (α,n) process by Geant4, the geometry may have lead to additional uncertainties, such that it was decided that taking a generic neutron spectrum of the source and starting the simulation from neutrons as primary particles is most accurate. The spectrum is the same as used in a previous simulation study of the neutron calibration discussed in Ref. [137]. It is presented in Figure 5.18, featuring energies extending up to roughly 11 MeV. According to this spectrum, 151 million neutrons are sampled and tracked through the experimental geometry, corresponding to the real life time of 840 hours of the neutron calibration data with a source emitting 50 neutrons per second. The only downside of this method is that MeV-scale gammas, which are created in coincidence with the neutron if the resulting ^{12}C is produced in an excited state, are not considered in this simulation. The respective γ-ray to neutron emission ratio is approximately 0.575 [144, 145].

5.3.2 Light Yield of Neutron Induced Events

The LY spectrum obtained in the cryogenic $CaWO_4$ detectors according to the ImpCRESST simulation is presented in Figure 5.19 up to a recoil energy of 1000 keV. No finite resolutions of phonon or light detector are considered for this representation to provide a clear look at the characteristic features. The entries in the graph are colored according to the type of interaction. In case of various processes contributing to the same detected event, the first interaction leading to an energy deposition is taken. The red band, centered around a LY of 1, is the β/γ-band. This band is typically used to set the absolute scale of the LY in the real measurement. Here, the light energy and subsequently the LY are calculated using Birks' law (Eq. 5.5).

As discussed before, the LY of nuclear recoil processes in the simulation is approximated using the parametrization of Eq. 5.6 with the values quoted in Table 5.4. The bands due to elastic scattering on O, Ca, W or a combination of them can hence be identified at low LYs. Besides these elastic scattering bands, some bands with vertical orientation are found. These correspond to inelastic scattering processes, mostly on W isotopes, in which part of the energy is deposited via nuclear recoils and part via secondary electrons or gammas. For the further analysis of the simulated data, the focus will mostly be set on the energy spectrum seen in the phonon detector. This will essentially be a projection of the LY plot to the x-axis. Furthermore, the energy range will be reduced according to the dynamic range of the current CRESST-III detector modules.

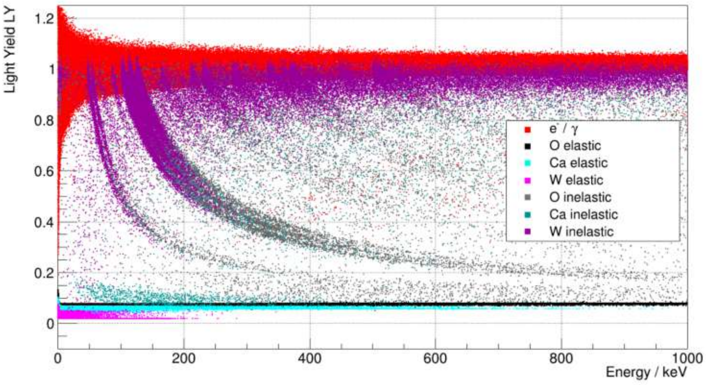

Figure 5.19.: Simulated light yield (LY) versus energy deposition in the $CaWO_4$ detectors during neutron calibration. No smearing according to the phonon or light detector resolutions is applied. Different colors denote distinct interactions. In case of mixed processes, the first type of interaction leading to an energy deposition is displayed.

5.3.3 Nuclear Recoil Spectra

The raw spectrum of energy depositions in the $CaWO_4$ detectors is presented on the left side of Figure 5.20. As the spectral shapes obtained in the various $CaWO_4$ detectors are statistically consistent among each other, a combined spectrum is shown to increase statistics, instead of limiting the results solely to the events observed in detector A. A time cut of one year for delayed energy depositions is applied during the analysis leading to the displayed spectrum to remove events which occur well after the neutron calibration and potentially even after background data taking. An example is the decay of ^{41}Ca, which can be activated from ^{40}Ca via thermal neutron capture. ^{41}Ca decays via electron capture to ^{41}K with a half life of approximately 10^5 yr. Without the time cut, a prominent corresponding peak around 3.6 keV is seen in the spectrum, while this peak vanishes once the time cut is considered. The spectrum in Figure 5.20 is shown up to 100 keV recoil energy, while the official analysis of detector A only extends up to 16 keV due to saturation at higher energies. However, the extended energy region shown in the plot allows to spot additional features like the various characteristic X-ray lines of W [146] between roughly 58–70 keV. Furthermore, a number of lines originating from the electron capture decay of ^{181}W (half life: 121.2 d) can be identified [146]. These lines always appear in pairs separated by 6.23 keV, due to the branching ratio being split between direct transition to the ground state of ^{181}Ta and transition to an excited state leading to an additionally emitted γ-particle of said energy. The origin of visible peaks below 16 keV is discussed further below.

On the right side of Figure 5.20, the simulated data are additionally processed by applying the energy resolution, threshold and efficiency of detector A to each detected event. As mentioned in Section 5.2.4, the parametrized resolution may not be entirely

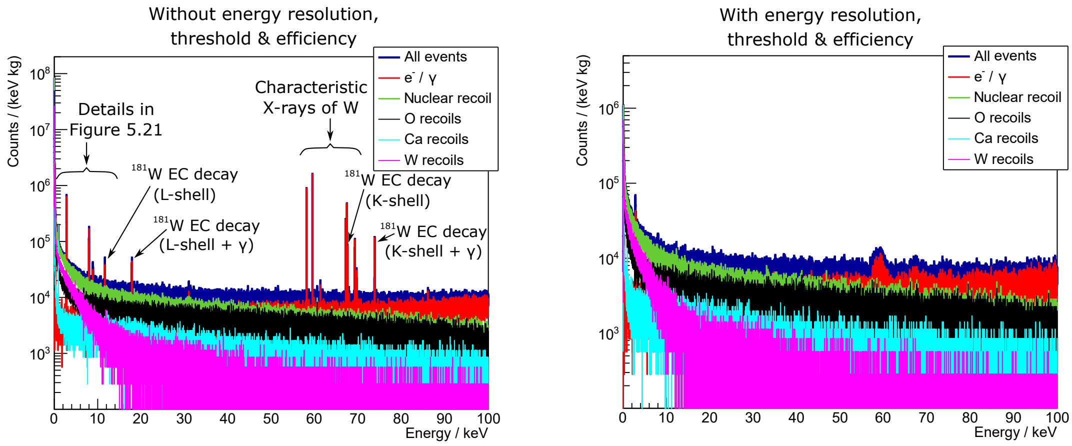

Figure 5.20.: Simulated energy deposition in $CaWO_4$ crystals during the CRESST neutron calibration in the range 0–100 keV, considering a maximum delayed event time of one year. Left: Exact spectrum attained from the simulation. Right: Applying the energy resolution as well as the threshold and the efficiency of detector A (cf. Section 5.1.3) to the attained data event-by-event.

applicable above the analyzed ROI, which extends from threshold to 16 keV. Hence, in the following, the discussions are further restricted to this range, in which the simulation can be compared to the measurement.

In Figure 5.21, the simulated spectrum in the ROI of detector A between 0 and 16 keV is presented, again with an event time cut-off of one year. On the left, the exact spectrum as attained from the simulation is shown to allow for better identification and understanding of the various spectral features. On the right side, energy resolution as well as threshold and efficiency are considered for a realistic picture of the detector response. In this energy range, the nuclear recoil events on the different target elements occur with the following percentages: 39.0 % O, 9.8 % Ca and 51.2 % W. While there are four times as many O as W nuclei in $CaWO_4$, the possible recoil energies are concentrated at lower values for heavier nuclei. Hence, the W nuclei show a more squeezed and steeper rising recoil spectrum than O. The cross-over between the O and W recoil spectra can be obtained from Figure 5.21 and is relevant for the expected shape of the measured nuclear recoil spectrum.

Focusing on the spectral features in the simulated data, around 11.6 keV a small peak corresponding to the direct transition to the ground state of ^{181}Ta in the L-shell electron capture decay of ^{181}W is obtained. The lines at approximately 8.0 keV and 8.9 keV can be identified as originating from Cu K_α and Cu K_β X-rays [146], respectively. At 2.8 keV, the K-shell electron capture decay of ^{37}Ar (half life: 35.04 d) is furthermore visible [146]. This process is preceded by the production of ^{37}Ar due to (n,α) reactions on ^{40}Ca. Finally, around 0.9 keV the simulation produces a peak due to the radiative

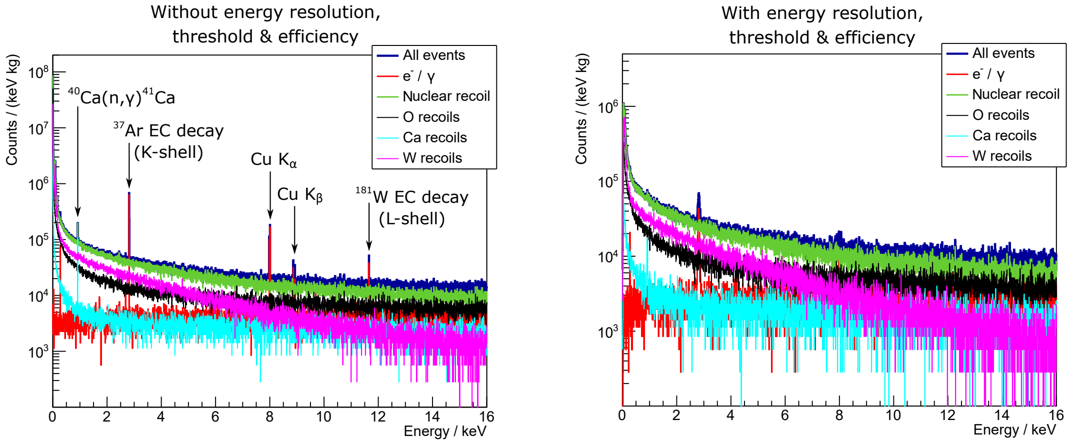

Figure 5.21.: Simulated energy deposition in CaWO$_4$ crystals during the CRESST neutron calibration in the range 0–16 keV, considering a maximum delayed event time of one year. Left: Exact spectrum attained from the simulation. Right: Applying the energy resolution as well as the threshold and the efficiency of detector A (cf. Section 5.1.3) to the attained data event-by-event.

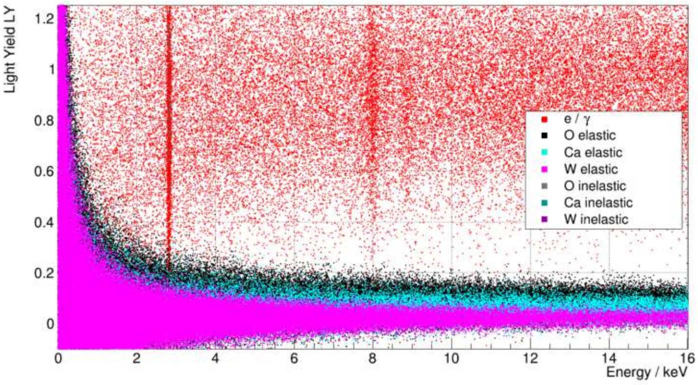

Figure 5.22.: Simulated light yield (LY) spectrum in the ROI of detector A during neutron calibration. Phonon and light detector resolutions are applied, leading to the smearing of the bands. Color coding is equivalent to Figure 5.19. Below a few keV, the β/γ-band starts overlapping with and leaking into the nuclear recoil bands. The distinct vertical event populations are identified and labeled in Figure 5.21.

neutron capture on ^{40}Ca. This peak, however, is an artifact due to wrong calculation of the recoil energy in the respective process in Geant4, as discussed later.

The total integral count rate in the ROI attained from the analysis specifically for detector A in the simulated geometry is approximately 15.5 h^{-1}. The official neutron calibration data set of detector A contains approximately 7600 events, which converts to a rate of 9.0 h^{-1} in the 840 h of exposure to the source. Two possible explanations

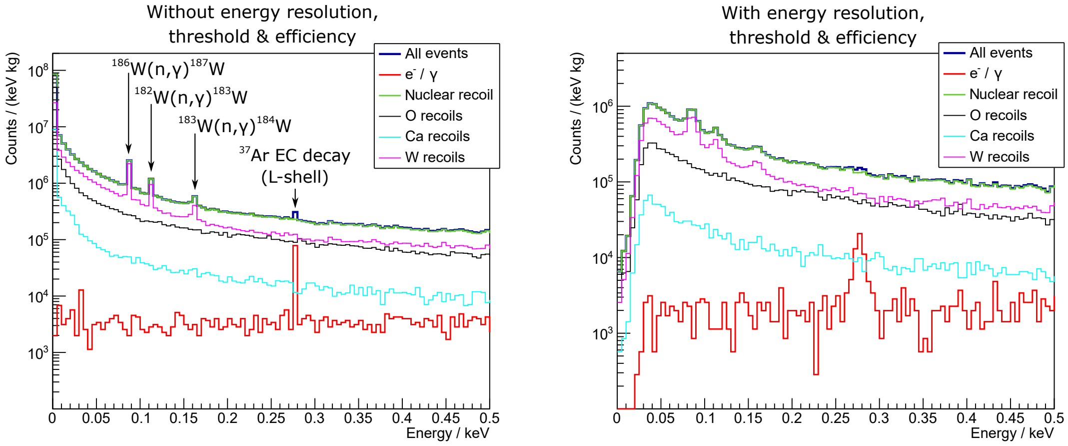

Figure 5.23.: Simulated energy deposition in $CaWO_4$ crystals during the CRESST neutron calibration in the range 0–0.5 keV, considering a maximum delayed event time of one year. Left: Exact spectrum attained from the simulation. Right: Applying the energy resolution as well as the threshold and the efficiency of detector A (cf. Section 5.1.3) to the attained data event-by-event.

for this discrepancy may be found.

First, the official efficiency from the background data set has been applied to the simulation. While there is no precise analysis of the efficiency during neutron calibration, it can be assumed to be lower due to a larger event rate and more pile-up.

Second, as mentioned in the beginning of this section the source position is not precisely known. While in the simulation the source is perfectly centered in the excision of the inner polyethylene shielding, this may not have been the case during the actual calibration campaign. A shift by a few centimeters can lead to the source being partly shielded by the polyethylene inside the OVC and hence to a reduced rate in the detectors. A combination of these two unknowns can be thought to account for the difference in the obtained rates.

Figure 5.22 shows a corresponding LY plot in the range 0–16 keV, where the phonon detector resolution described by Eq. 5.3 as well as the light detector resolution according to Eq. 5.7 are applied. In this visualization of the LY bands of the simulated neutron calibration data, the overlap of the nuclear recoil bands themselves as well as the one between nuclear recoils and β/γ events at low energies can well be seen.

To discuss the data at lowest energies, a zoom to the region between 0 and 0.5 keV is presented in Figure 5.23. At 0.27 keV, a small peak due to the L-shell electron capture decay of ^{37}Ar [146] is visible in this plot. Additionally, besides the typical elastic nuclear recoil spectra due to neutrons scattering off O, Ca and W nuclei, a few distinct peaks in the W nuclear recoil band are observed. These prominent features are still visible when considering the energy resolution of detector A and are found to originate from thermal

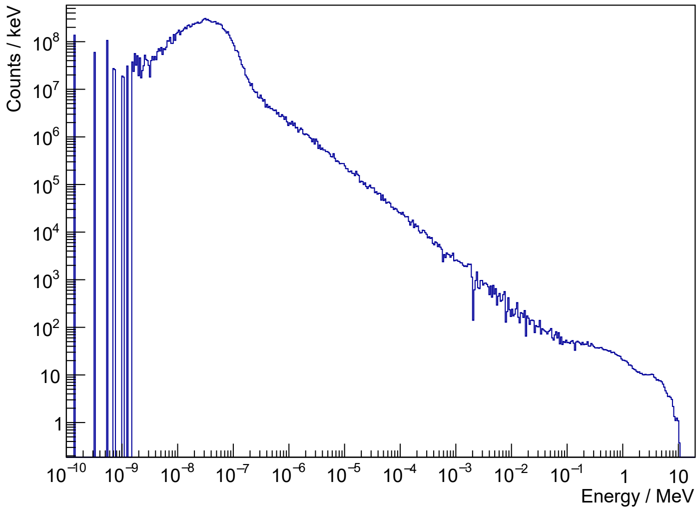

Figure 5.24.: Simulated incident energy of neutrons entering the $CaWO_4$ target crystals during the neutron calibration of CRESST Run34.

neutron capture and subsequent γ-emission. Indeed, extracting the energy spectrum of the neutrons entering the $CaWO_4$ target crystal during the neutron calibration, it is understood that a significant amount of the primary neutrons is thermalized. The corresponding incident neutron spectrum is displayed in Figure 5.24. 21.5 % (13.5 %) of the neutrons are featuring energies below 10 eV (100 meV). This distribution enhances the rate of neutron capture reactions in the crystals, which then in turn lead to distinctive peaks in the measured energy spectra. Such low-energy peaks had not been described and discovered in CRESST prior to the analysis presented in this thesis. Their origin and possible observation in the real measurement is discussed in the following.

5.4 Radiative Neutron Capture as a Novel Calibration Technique

With the observation of (n,γ) peaks in the simulation, the idea was born to potentially use such peaks for low energy calibration of $CaWO_4$ detectors mounted in the CRESST detector carousel without having to place an alternative calibration source closer to the detectors. To discuss this possibility, the physics of the reactions and the feasibility of an actual observation in real data are given a closer look.

5.4.1 Spectral Features Caused by Radiative Neutron Capture

The low-energy nuclear recoil peaks as seen in Figure 5.23 are originating from (n,γ) reactions on different W isotopes, in case a single γ-particle is emitted in the process. The recoil energy of the nucleus can then easily be calculated via $E_R = E_\gamma^2/(2Mc^2)$, where M is the mass of the nucleus. Q-values of 5467.0 keV, 5794.1 keV, 6190.7 keV and 7411.2 keV for (n,γ) reactions on ^{186}W, ^{184}W, ^{182}W and ^{183}W [147, 148] respectively, lead to nuclear recoil energies of 85.8 eV, 96.1 eV, 112.4 eV and 160.2 eV. This information is summarized in Table 5.5. The three visible peaks in the simulated spectrum due to these reactions are labeled in Figure 5.23. A very similar idea and study of these peaks was proposed independently at the same time by the CRAB (Calibrated Recoils for Accurate Bolometry) initiative [149]. It has been found by their collaborators, however, that Geant4 does not treat these processes correctly regarding the branching ratios to different gamma cascades and calculation of the recoil energy. The simulation framework in each case calculates the nuclear recoil energy from the total Q-value of the reaction. This calculation is similar to the assumption of single gamma emission. Hence, the simulated peak heights using Geant4 can be interpreted as only considering the natural abundance as well as the thermal neutron capture cross section.

However, in reality they need to be further scaled according to the branching ratios to single gammas. These values can be collected from literature. Refs. [147, 148] provide the branching ratios for the various possible gamma cascade emissions. Additionally, the thermal neutron capture cross sections can be compared with Ref. [91]. The respective values are listed in Table 5.6 together with the natural abundance of the W isotopes. As introduced in Ref. [149], the values in the last row are the multiplication of natural abundance, neutron capture cross section and branching ratio for single gamma emission. This represents the relative importance of the individual peaks. It is thus obvious that in reality, the 112.4 eV peak due to capture on ^{182}W is supposed to be the most prominent by far.

Similar to the nuclear recoil peaks of W, a peak due to the reaction ^{40}Ca(n,γ)^{41}Ca seems to arise around 916 eV in the simulation. However, in this case the branching ratio to the emission of a single gamma of the reaction Q-value of 8362.7 keV is even found to be zero [148]. Hence, as already mentioned in the context of Figure 5.21, this peak is another artefact due to the wrong treatment in Geant4.

In a re-analysis of the simulated data, presented in Figure 5.25, a rough scaling according to the single gamma branching ratios [147, 148] is applied to attain the relative heights of the peaks. A thorough re-analysis, however, would require the implementation of the correct gamma cascades in the code. While this has been done by the authors of Ref. [149], the scaling presented in this thesis is an approximation solely based on the branching ratio to single gamma emission, providing a rough picture of the expected outcome. The resulting re-scaled energy spectrum shown in the figure considers the

Table 5.5.: Q-values and respective nuclear recoil energies of the four most abundant W isotopes in the case of single gamma emission in radiative neutron capture reactions.

	^{182}W	^{183}W	^{184}W	^{186}W
(n,γ) Q-value (keV) [147, 148]	6190.7	7411.2	5794.1	5467.0
1γ recoil energy (eV)	112.4	160.2	96.1	85.8

Table 5.6.: Natural abundance (NA), thermal neutron capture cross sections ($\sigma_{n-capture}$) and single gamma emission branching ratios (BR-1γ) of the four most abundant, stable W isotopes. Table adapted from Ref. [149].

	^{182}W	^{183}W	^{184}W	^{186}W
NA (%) [147, 148]	26.50	14.31	30.64	28.42
$\sigma_{n-capture}$ (barn) [91]	20.31	9.87	1.63	37.88
BR-1γ (%) [147, 148]	13.936	5.829	1.477	0.263
NA · $\sigma_{n-capture}$ · BR-1γ	7500.6	823.3	73.8	283.1

energy resolution of detector A to facilitate the comparison to the real measurement. The previously clearly detectable peaks are now hardly visible on top of the large elastic scattering background. However, looking carefully, a small bump around 112.4 eV may still be seen. Additionally, the branching ratios found in Ref. [147, 148] tell that besides the 13.936 % chance of emitting a single gamma of 6190.7 keV in the capture reaction on ^{182}W, there is a 5.079 % chance of emitting a gamma of 6144.2 keV, which could contribute to the same peak in reality, with a calculated recoil energy around 110 eV. This shows the importance of thoroughly treating the correct gamma cascade emissions in the simulations in the future. This task was out of the scope of this thesis and had in parallel been developed by the CRAB collaboration. Their code as of writing this thesis, however, has not yet been made publicly available.

The overall results of this study could be of great interest for the CRESST experiment, because the obtained nuclear recoil peak, if observable in real data, might provide an important ingredient to a precise energy calibration at low recoil energies, which will be discussed in the following.

5.4.2 Energy Calibration Based on Radiative Neutron Capture

As briefly stated already in Section 5.1.3, an energy calibration is necessary at the beginning of each experimental run to correctly convert the measured signal amplitudes

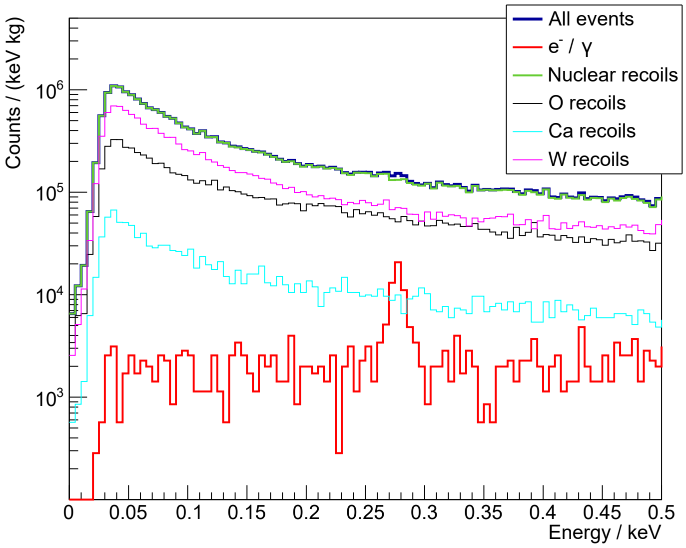

Figure 5.25.: Simulated energy deposition in $CaWO_4$ crystals during the CRESST neutron calibration, considering the scaling of the nuclear recoil peaks according to the branching ratio to single gamma emission (cf. Table 5.6). Energy resolution, threshold and efficiency of detector A have been applied, such that this plot can be compared to the right side of Figure 5.23.

to deposited energies in the crystal. In CRESST, a ^{57}Co source is traditionally used, which – through its decay – provides γ radiation of mainly 122 keV and 136.5 keV. These energies are high enough, such that a sufficient amount of gamma particles can penetrate the Cu walls of the cryostat, when placing the source at the same position as indicated for the neutron source in Figure 5.17. This again provides the advantage that the source can be removed after the calibration is finished. However, with the latest, highly sensitive CRESST detectors, the signals corresponding to these energies are strongly saturated and cannot easily be used for calibration. In $CaWO_4$, one way of accessing lower-energetic peaks, using the same calibration source, is by looking at the K_α escape peaks of W around 63.2 keV. Still, this energy might already lead to saturated signals. As less energetic gammas will not penetrate the cryostat and reach the detectors in sufficient amounts, other tools for energy calibration become necessary.

Already used for this purpose are peaks due to intrinsic radioactive contamination in the detector crystals or sources placed inside the detector modules. An example in $CaWO_4$ detectors are calibration lines due to cosmogenic activation of ^{182}W, prior to the storage of the crystals underground, creating ^{179}Ta nuclei via (p,α)-processes. These nuclei themselves decay via electron capture with a half life of 1.82 years, leading to peaks at energies of 65.35 keV (K-shell), 11.27 keV (L_1-shell), 10.74 keV (L_2-shell) and 2.60 keV (M_1-shell). However, there are some obvious issues with this method.

First, these lines usually only become visible after long measuring times. And second, the aim is to reduce cosmogenic activation as much as possible, because it additionally leads to further activated nuclides in the crystals, for example ^{3}H, which contribute to the background at lowest energies [118].

Thus, in the latest data taking run of CRESST (Run36), a weak ^{55}Fe source is installed inside each detector module, decaying via electron capture, constantly providing calibration peaks at 5.9 keV and 6.49 keV. However, with this method a radioactive source is placed next to the detectors, which cannot be removed during data taking. Besides the calibration peaks, additional background at low energies may thus be induced. All the mentioned low-energy calibration sources therefore have their downsides.

An optimal calibration source, especially when focusing on sub-keV recoil energies, would provide even less energetic peaks closer to the detector thresholds, which for the latest CRESST-III detectors are in the order of 100 eV and below. Furthermore, looking for nuclear recoil signals, a nuclear recoil energy calibration would be beneficial compared to the electron recoil calibration provided by the typical gamma and X-ray sources. The reason is that the energy scale might be slightly shifted due to potential creation of lattice defects in the case of nuclear recoils [150]. Hence, the nuclear recoil peak found in the simulated neutron calibration could be an ideal candidate for $CaWO_4$ detectors which feature energy thresholds in the 10 eV range.

If during the neutron calibration, the (n,γ) peak around 112.4 eV due to capture on ^{182}W would be visible, then the neutron and energy calibration could be performed simultaneously and no intrinsic source would be necessary. If the additional peak at 2.82 keV due to ^{37}Ar decays following its production via $^{40}\mathrm{Ca}(n,\alpha)^{37}\mathrm{Ar}$ reactions would be observed during and after neutron calibration as well, it could be used as a second low-energetic calibration peak. Based on these considerations and the promising simulation study, the goal in the following was to analyze the real neutron calibration data taken with detector A and to determine the statistical significance of the potentially expected peaks.

5.4.3 Peak Search in Measured Neutron Calibration Data

To analyze the measured neutron calibration data with respect to the aforementioned peaks, an unbinned extended maximum likelihood fit is performed using the SciPy [151] libraries in Python. The unbinned fit has the advantage that it is not performed based on histogrammed data, but on the raw individual energy depositions. Therefore, binning effects can be excluded. A likelihood function $\mathcal{L}(\theta|X)$ is defined, which represents the plausibility for a set of parameters θ of the function to describe the observed data X. The parameter set θ would then be varied by the fit algorithm to eventually find the values which are most likely to correspond to the observation given the underlying model represented by the likelihood function. Per definition, $\mathcal{L}(\theta|X)$ reaches its global maximum for the most likely parameter set.

The extended likelihood method is a way to deal with likelihood functions consisting of density functions, whose integral is not normalized to unity but depends on the parameter set. These likelihood functions can be interpreted to not only consider the shape of a distribution but to also consider the total amount of events in it. A so-called penalty term is then introduced to reduce the likelihood by a factor proportional to the difference between the expected and observed events. For a Poisson distributed number of events, the extended likelihood function can be written as [152]

$$\mathcal{L}(\theta|X) = e^{-\mathcal{N}} \prod_i P(X_i|\theta) \quad , \tag{5.8}$$

where $P(X_i|\theta)$ is an unnormalized function and

$$\mathcal{N} = \int P(X|\theta)\, dX \quad . \tag{5.9}$$

Due to limited machine precision, typically the logarithm of the likelihood function,

$$\ln \mathcal{L}(\theta|X) = -\mathcal{N} + \sum_i \ln\left[P(X_i|\theta)\right] \quad , \tag{5.10}$$

is formed, replacing the multiplications by summations to reduce the errors in the numerical calculations. Usually, this log-likelihood is then multiplied by -1 to turn the task into a minimization problem, for which many computer algorithms exist.

To eventually assess the significance of an expected peak, a hypothesis test can be made. In this test, the likelihood of the null hypothesis not including the peak in the underlying model is compared to the likelihood of the test hypothesis including the peak. The test statistic T,

$$T = -2\, ln \left(\frac{\mathcal{L}_{null}}{\mathcal{L}_{test}}\right) \quad , \tag{5.11}$$

according to Wilks theorem [153] asymptotically approaches a chi-squared distribution $\chi^2(n)$ with n degrees of freedom corresponding to the difference in the number of free parameters between the tested model and the null hypothesis. This can be used to determine the statistical significance of the tested hypothesis.

Applied to the CRESST data, the likelihood test has been performed as described in the following. Due to the expectation from the simulation to potentially observe the nuclear recoil peaks in the neutron calibration data, but the ^{37}Ar EC peak also in the background data, a fit is separately performed for both data sets. The data used for this purpose is that surviving all cuts (see Section 5.1.3 for reference regarding the background data). Thus, the information about the threshold and energy-dependent signal survival probability have to be considered in the fit. The only additional cut imposed to the data is a restriction of the LY values to the range between -5 and +5.

Table 5.7.: Considered peaks, associated physics processes (where EC denotes electron capture decay) and respective bounds in the likelihood fit.

Peak position (keV)	Physics process	Fit bounds (keV)
0.0858	^{186}W(n,γ)^{187}W	[0.07 , 0.10]
0.1124	^{182}W(n,γ)^{183}W	[0.10 , 0.13]
0.1602	^{183}W(n,γ)^{184}W	[0.15 , 0.17]
2.60	^{179}Ta $\longrightarrow$ ^{179}Hf (M$_1$-shell EC)	[2.50 , 2.70]
2.82	^{37}Ar $\longrightarrow$ ^{37}Cl (K-shell EC)	[2.70 , 2.90]
8.04	Cu K$_\alpha$	[7.90 , 8.10]
10.74	^{179}Ta $\longrightarrow$ ^{179}Hf (L$_2$-shell EC)	[10.60 , 11.00]
11.27	^{179}Ta $\longrightarrow$ ^{179}Hf (L$_1$-shell EC)	[11.10 , 11.40]

The fit function used in this case consists of a linear function describing an almost flat background contribution and one exponential representing the unknown excess at low energies in the background data. Additionally, in the neutron calibration data, three exponentials are added to account for elastic recoils of neutrons off O, Ca and W nuclei in the CaWO$_4$ crystal. On top of this, a predefined amount of Gaussian ($\mathcal{G}$) peaks is added. In Table 5.7, the considered peaks, associated physics processes and parameter bounds for the fit are listed. The entire fit function is multiplied by the signal survival probability $S(E)$. For the extended likelihood, the function is further multiplied by the penalty term and reads

$$\mathcal{L}\left(\theta|\mathrm{X}\right) = e^{-\mathcal{N}}\, S(E)\left(p_0 + p_1 E + \sum_i a_i \exp[-b_i E] + \sum_j c_j \mathcal{G}[E_j, \sigma(E_j)]\right) \quad , \tag{5.12}$$

where $\mathcal{N}$ is now calculated via

$$\mathcal{N} = \int_{E_{th}}^{E_{max}} S(E)\left(p_0 + p_1 E + \sum_i a_i \exp[-b_i E] + \sum_j c_j \mathcal{G}[E_j, \sigma(E_j)]\right) dE \quad . \tag{5.13}$$

The negative logarithm of the extended likelihood function can then be written as

$$\begin{aligned} -\ln\mathcal{L}\left(\theta|\mathrm{X}\right) &= \mathcal{N} - \ln S(E) - \\ &\ln\left(p_0 + p_1 E + \sum_i a_i \exp[-b_i E] + \sum_j c_j \mathcal{G}[E_j, \sigma(E_j)]\right) \quad , \end{aligned} \tag{5.14}$$

and is used in the SciPy minimization framework. In the fit, all the free parameters of the function are only loosely constrained to physically meaningful ranges and potential peak positions (cf. Table 5.7).

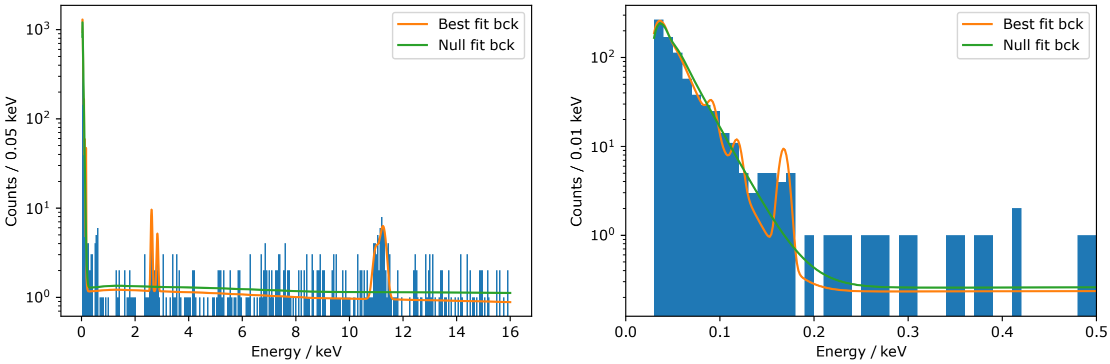

Figure 5.26.: Likelihood fit to the background data of detector A without peaks (null fit) and with peaks (best fit) in expected energy ranges. Left: whole ROI from threshold to 16 keV. Right: zoom to low-energy region below 0.5 keV.

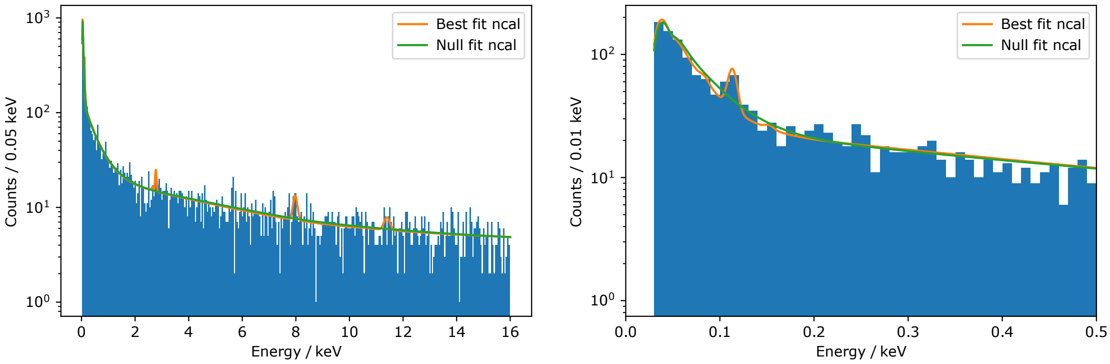

Figure 5.27.: Likelihood fit to the neutron calibration data of detector A without peaks (null fit) and with peaks (best fit) in expected energy ranges. Left: whole ROI from threshold to 16 keV. Right: zoom to low-energy region below 0.5 keV.

For optimization, a global minimum is first computed by using a differential evolution (DE) [154, 155] algorithm without the use of starting values, only constrained by the parameter bounds. Based on the results of the DE, an additional local minimization is performed using the Nelder-Mead (NM) [156] method. The fit results for background and neutron calibration data are presented in Figure 5.26 and 5.27 respectively. In these plots, only two specific fits are shown: in green a fit without considering any of the peaks, here denoted the null fit, and in orange a fit considering all of the peaks, here denoted best fit.

To calculate the significance of each individual peak, however, the best fit is compared to a fit which only disregards the peak of interest as the null hypothesis. The test statistic is attained from the formula defined in Eq. 5.11. Obtaining the value of the cumulative distribution function (CDF) of a chi-squared distribution with two degrees of freedom, due to position and amplitude of the peak, then yields the peak significance.

Table 5.8.: Fitted peak position and statistical peak significance in background and neutron calibration data of Detector A.

Background data

Peak position (keV)	0.0915	0.1184	0.1678	2.6146	2.8313	8.1000	10.9908	11.2544
Significance	0.96036	0.95101	0.99998	0.99998	0.91613	0.00000	0.98598	1.00000

Neutron calibration data

Peak position (keV)	0.0833	0.1133	0.1524	2.6408	2.7740	7.9724	10.6102	11.3999
Significance	0.13200	0.99996	0.03907	0.08061	0.92160	0.99447	0.00000	0.69889

Table 5.8 summarizes the fitted peak positions as well as the calculated significance of each of the peaks.

Discussion of the Results

Looking at the background data, the low flat background and long measuring time lead to some distinctly visible peaks. However, the unknown excess below roughly 200 eV makes an interpretation regarding the lowest energies difficult. The excess, also by eye, may not be described solely by an exponential. As some fluctuations may be seen in the spectrum, the fit tries to assign a few events to potential peaks. However, although the statistical significance according to Table 5.8 is rather high, the peak positions and the physical expectation lead to the conclusion that there should at least not be the same peaks visible as motivated from the neutron calibration simulation. At larger energies, the cosmogenic lines are nicely fitted at 2.61 keV, 10.99 keV and 11.25 keV, close to their literature values. As expected due to the low background level and apparent domination by sources intrinsic to the target crystal, no copper fluorescence line is observed. Interestingly however, with 91 % significance, events are allocated to a peak around 2.83 keV, which would correspond to the ^{37}Ar decay energy.

Even more important, however, may be the look at the neutron calibration data. Due to shorter exposure and large background from elastic neutron scattering, the cosmogenic lines are not significantly observable. However, as expected from simulation, the scattering in the surrounding copper parts leads to a visible fluorescence line fitted at 7.97 keV. Furthermore, again with a significance slightly above 90 %, a peak could be identified around 2.77 keV, which may fit the ^{37}Ar decay energy once more.

Finally, a potentially striking result seems to be obtained looking at the sub-keV peaks. As expected from theory and slightly indicated in simulations, only a single significant peak is identified at a fitted position of 113.3 eV. An error of 0.1 eV on this result is calculated using the Minuit [157] implementation in Python via the *iminuit* [158] package. While the fitted position is hence not entirely in statistical agreement with the theoretically predicted value of 112.4 eV, there could be systematic errors in the energy reconstruction of the measured events leading to an additional uncertainty on the results. Such an error could come from the extrapolation of the reconstructed energy from the calibration peaks down to the detector threshold. Furthermore, there is an uncertainty on the consistency between the electron recoil and nuclear recoil energy scale. While this is speculation at the moment, future studies will be necessary to test these hypotheses.

Additionally, the observation of the expected peak in only a single detector may prevent from making clear statements about the validity and significance of the results. The same likelihood method was hence applied to three other detector modules analyzed in CRESST-III Run34, which featured slightly higher energy thresholds and partly some stability issues. Furthermore, three additional modules operated in CRESST-III Run36 were considered, in which a lower statistic in the neutron calibration data was obtained, however. The results of the tests are presented in Appendix C and are less conclusive than the apparent findings from detector A. Thus, final statements about the validity of the peaks and the use of the neutron calibration for the purpose of energy calibration require additional dedicated studies with low-threshold $CaWO_4$ detectors and a long neutron calibration campaign.

5.5 Neutron Background

The goal of the following neutron background study is the development of a neutron background model for CRESST-III, especially considering the physics run internally referred to as *Run34* in light of the data published in Ref. [4]. The results shall indicate, if a significant neutron background is expected to be present in the measured data. For this purpose, all major neutron background sources are assessed with respect to the induced nuclear recoil rate in the detectors and the respective spectrum of energy depositions.

The detector multiplicity, i.e. the amount of detectors observing an energy deposition above threshold in the same event, is furthermore analyzed. This information can be used to define an anti-coincidence cut, as DM-induced events are expected to only occur in a single detector module. The dangerous residual neutron background rate hence only contains events, in which one single detector triggers. These events will be called "single nuclear recoil" (SNR) events in the following discussions. In the case of muon-induced events, a further cut is provided by the anti-coincidence with the active muon veto. In the course of this study, the efficiency of the muon veto is hence additionally assessed.

Besides the main result on the spectrum and rate of neutron background events, an analysis of the neutron flux at different levels inside the experimental geometry is performed. This neutron flux investigation may contribute to a better understanding of the mitigation of neutrons compared to the additional creation of free neutrons inside a specific shielding layer.

The main neutron background sources discussed in Section 3.1.2, describing the nuclear recoil background components, are assessed in the simulations presented in the following. The discussion starts with neutrons originating from radioactive decays. Two distinct components of this background are separately treated. The first one considers particles originating from any material outside the experimental setup, thus mainly from the rock and concrete surrounding the laboratory halls. This component is hence called "ambient" (Section 5.5.1). The second one considers neutrons created in the materials of the experimental setup itself and is subsequently called "internal" (Section 5.5.2). A distinction of these parts can be reasoned by the fact that the ambient particle flux is essentially present independently of the experimental setup, while the dedicated shielding setup is then planned and installed to mitigate the ambient background without introduction of significant amounts of additional internal radiogenic particle fluxes. Apart from the treatment of the specific radioactive decay neutron sources, muon-induced neutrons play an important role and will be discussed in Section 5.5.3. The combined analysis of all the components and neutron fluxes will finally be presented in Section 5.5.4.

5.5.1 Ambient Radiogenic Neutron Background

Ambient neutrons originate from (α,n) processes and spontaneous fission (s.f.) reactions in the rock and concrete surrounding the underground halls at LNGS. The energy spectrum of these neutrons can either be attained by measurements conducted in the respective halls of the laboratory or by calculation from contamination levels in the materials and cross sections for neutron creation processes, e.g. using SOURCES 4C. In the latter case, a simulation of the tracking of the neutrons through rock and concrete is further necessary to attain the spectrum entering the laboratory. Hence, details about the composition and thicknesses of the material layers would have to be known.

A simulation based study of the ambient neutron flux at LNGS can already be found in literature [159], motivated by the differences between the various neutron flux measurements conducted at LNGS. The authors performed analytical calculations and simulations of the neutron yield due to (α,n) and s.f. reactions. The Monte Carlo code MCNP4B (Monte Carlo N-Particles version 4B) [112] was then used to transport neutrons through the rock and concrete surrounding the laboratory. Results of neutrons emitted from the rock walls were then compared with experimental measurements and interpreted with respect to the different laboratory halls, even considering the dependence of the neutron flux on the humidity of the concrete. The spectrum taken from [159] and shown in Figure 5.28 has been largely adopted by other collaborations at LNGS to compute the attenuation through their experimental setup. Thus, the very same spectrum is applied for the ambient neutron simulations presented in this work. It has a bin size of 500 keV, and quotes the integrated neutron flux between 1–500 keV and the one above 500 keV as $6.5 \cdot 10^{-7}$ cm^{-2} s^{-1} and $7.9 \cdot 10^{-7}$ cm^{-2} s^{-1}, respectively.

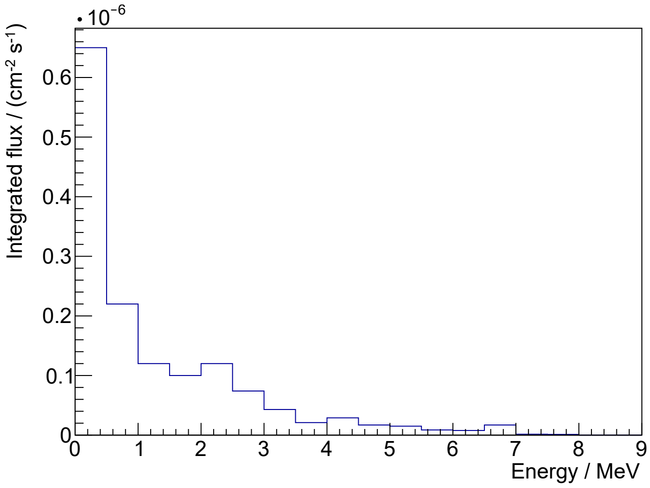

Figure 5.28.: Ambient neutron spectrum at LNGS adapted from Ref. [159].

In the geometry implemented in ImpCRESST, the ambient neutrons are started on the surface of a cuboid surrounding the outer polyethylene shielding. Their primary kinetic energy is sampled according to the spectrum presented in Figure 5.28 and their momentum vector is pointing in a random inward direction, such that the neutrons enter the experimental setup. The size of the cuboid is $245 \times 245 \times 300$ cm and leads to a total surface of 414050 cm^2, on which the neutrons are sampled. With an integral ambient neutron flux of $1.44 \cdot 10^{-6}$ cm^{-2} s^{-1}, the rate of neutrons impinging on this surface is about 0.6 s^{-1} or approximately $1.88 \cdot 10^7$ yr^{-1}. For the simulation study at hand, $4.16 \cdot 10^9$ events have been simulated, hence corresponding to an exposure of 221.3 yr.

Neutrons are effectively mitigated by low-Z materials, posing the reason for using an outer and inner polyethylene shielding in CRESST (see Section 5.1.2). As the ambient neutrons have to traverse the entire experimental setup of CRESST to reach the detectors, only a tiny fraction is able to survive the dedicated material layers surrounding the detector volume. The attainable statistic in the simulation is hence limited. In the future, additional biasing techniques in the simulation software could be implemented to enhance the statistical weight of particles getting closer to the detectors. However, in the study at hand, an unbiased event-by-event simulation (= *analog simulation*) is performed. The resulting detector energy depositions are plotted in Figure 5.29. A spectral shape of the ambient neutron background component cannot be extracted from the low number of counts. However, the event rates still allow for a statement on the significance of the contribution to the overall background.

Table 5.9 shows the attained detector multiplicities. In the two blocks presented in the table, the event count without applying any cuts as well as the one assuming the threshold and efficiency of detector A for all the detectors are shown.

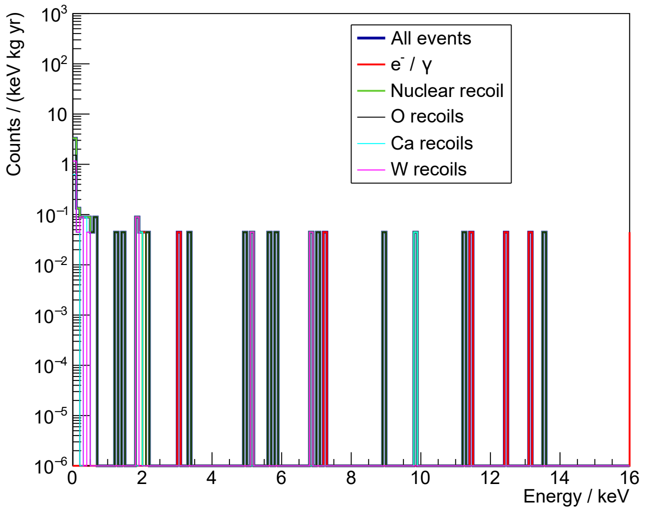

Figure 5.29.: Energy deposition due to ambient neutrons in the simulation of $4.16 \cdot 10^9$ events.

In addition, Table 5.10 lists the integral rates seen in the detectors in various energy ranges. Threshold and efficiency are not considered in this table to assess the real expected rate before cuts. Nuclear recoil events with multiplicity $m = 1$ pose the dangerous contribution to the background and are hence specifically mentioned. In the full energy range, roughly $4.5 \cdot 10^{-1}$ nuclear recoil events per kg·yr with single multiplicity are obtained. This rate decreases to approximately $1.6 \cdot 10^{-1}$ counts per kg·yr when constraining the energy range to the ROI of detector A. Statistical uncertainties of these numbers are detailed in the table. The stated 1σ error bounds are calculated from Poisson statistics. In the case of an upper limit, a 90 % confidence level is quoted.

With the assumption of a homogeneous distribution of starting positions of the ambient neutrons outside the outer polyethylene shielding, the shielding geometry is tested for potential weak spots. One obvious candidate are neutrons coming from the top and entering the experimental setup at the central circular excision in the shielding layers, where the cryostat passes through vertically. A dedicated simulation shows that indeed more than 75 % of the detected events due to ambient neutrons would originate from this circle, which only represents roughly 0.4 % of the total surface around the outer polyethylene shielding. Additional polyethylene around the top neck of the cryostat is present in the real and simulated geometry but its effect is not entirely considered due to the choice of neutron starting positions. Hence, the ambient neutron background rate may be seen as a conservative estimation. Still, if necessary, an additional reduction of the rate would potentially be achievable by further reducing the line of sight from the top part of the cryostat to the detectors, for example by placing a polyethylene hat above the cryostat.

Table 5.9.: Detector multiplicity in the simulation of $4.16 \cdot 10^9$ ambient neutrons. A combined count rate for nuclear and electron recoils is presented. 1σ Poissonian bounds and 90 % upper limits are stated to represent the uncertainties on the results.

	Without threshold & efficiency		With threshold & efficiency	
Multiplicity	Counts / (kg yr)$^{-1}$	%	Counts / (kg yr)$^{-1}$	%
1	3.2 ± 0.1	94.88 ± 3.53	2.1 ± 0.1	96.88 ± 4.49
2	$(1.6 \pm 0.3) \cdot 10^{-1}$	4.73 ± 0.79	$(6.7 \pm 1.7) \cdot 10^{-2}$	3.13 ± 0.81
3	$(1.3 \pm 0.8) \cdot 10^{-2}$	0.39 ± 0.23	$< 1.0 \cdot 10^{-2}$	< 0.48
4	$< 1.0 \cdot 10^{-2}$	< 0.3	$< 1.0 \cdot 10^{-2}$	< 0.48
5	$< 1.0 \cdot 10^{-2}$	< 0.3	$< 1.0 \cdot 10^{-2}$	< 0.48
> 5	$< 1.0 \cdot 10^{-2}$	< 0.3	$< 1.0 \cdot 10^{-2}$	< 0.48

Table 5.10.: Detected event rate in the simulation of $4.16 \cdot 10^9$ ambient neutrons in different energy ranges. 1σ Poissonian bounds and 90 % upper limits are stated to represent the uncertainties on the results.

	Nuclear recoils / (kg yr)$^{-1}$		Electron recoils / (kg yr)$^{-1}$	
Energy range	All	Multiplicity = 1	All	Multiplicity = 1
Full range	$(6.8 \pm 0.6) \cdot 10^{-1}$	$(4.5 \pm 0.4) \cdot 10^{-1}$	2.9 ± 0.1	2.4 ± 0.1
< 0.03 keV	$(2.8 \pm 0.4) \cdot 10^{-1}$	$(2.4 \pm 0.3) \cdot 10^{-1}$	$(4.5 \pm 4.5) \cdot 10^{-3}$	$< 1.0 \cdot 10^{-2}$
0.03 – 16 keV	$(1.9 \pm 0.3) \cdot 10^{-1}$	$(1.6 \pm 0.3) \cdot 10^{-1}$	$(9.4 \pm 2) \cdot 10^{-2}$	$(2.7 \pm 1.1) \cdot 10^{-2}$

5.5.2 Internal Radiogenic Neutron Background

Internal neutrons, similar to ambient neutrons, are created in (α,n) and s.f. reactions, i.e. in the course of radioactive decays. However, this specific neutron background component deals with the ones that have their origin inside the materials of the experimental setup. Dedicated shielding layers, as described in Section 5.1.2, are employed to mitigate the ambient particle fluxes and minimize the background rate in the detectors. The respective materials are selected considering their shielding power, while at the same time focusing on their radiopurity. Lowest possible levels of contamination with radioactive nuclides are necessary to guarantee optimal background conditions. Residual contaminations, however, are in principle unavoidable and can lead to a contribution to the overall background rate. In this section, the main shielding layers employed in the CRESST setup are hence assessed in this context.

Going from outside to inside, CRESST uses polyethylene (outer PE shielding), lead (Pb shielding), copper (Cu shielding) and again polyethylene (inner PE shielding) surrounding the copper cryostat and the detectors. Most of these materials have been screened for radioimpurities in the course of their installation. Only for the copper

Table 5.11.: Contamination levels of natural decay chain nuclides in the shielding materials of CRESST. The last column quotes the integral neutron yield due to (α, n) and s.f. reactions, assuming secular equilibrium in the natural decay chains, calculated using the SOURCES 4C [123] code with extended libraries [139–141].

Material	Activity / (mBq kg^{-1})				Neutron yield / (cm^{-3} s^{-1})
	^{238}U	^{235}U	^{232}Th	Ref.	
Outer PE	6.2	–*	5.3	ICP-MS (2009)	$2.2 \cdot 10^{-11}$
Pb	< 2.48	–*	< 0.81	ICP-MS (2009)	$3.1 \cdot 10^{-11}$
Cu	< 0.065	–*	< 0.002	Ref. [160]	$6.6 \cdot 10^{-13}$
Inner PE	1.1	< 0.28	0.4	HPGe (2013)	$3.2 \cdot 10^{-12}$

*No measured value given, natural abundance assumed [161].

shielding, no internal measurements are available, such that typically the upper limits provided by the CUORE collaboration in Ref. [160] are assumed because they used Cu of the same type and producer. A list of all the measured contamination levels, that are applied in the following neutron background studies, is given in Table 5.11. Only the heads of the natural decay chains are stated as secular equilibrium is assumed. The results for the material of the outer PE and the lead shielding have been obtained from ICP-MS (Inductively Coupled Plasma - Mass Spectrometry) measurements in 2009. The contamination levels of the inner PE shielding have been assessed via a HPGe (High Purity Germanium) radiation detector in 2013. While concrete values could be obtained for the polyethylene samples, the lead screening only provided upper limits. One could question the sensitivity of this measurement and ask for a repetition for more precise studies. However, such measurements have not been possible during the work for this thesis. The same is true for a screening measurement of the copper shielding. Hence, the measured and assumed upper limits for lead and copper are applied in the simulations.

For the SOURCES 4C calculation of the neutron flux and spectrum (cf. Section 5.2.1), the contamination levels listed in Table 5.11 are used as an input and secular equilibrium in the decay chains is assumed. The resulting neutron yield is quoted in the last column of this table and the neutron spectra are displayed in Figure 5.30. A detailed view on the single spectra originating in each shielding material is presented in Figure 5.31, indicating the contributions from (α,n) and s.f. reactions.

The attained spectra are now interfaced to ImpCRESST and employed for sampling the neutrons in the internal radiogenic neutron background simulations. Following the ambient neutrons as the most extrinsic background source, the internal neutron background discussion starts with the outermost shielding layer and continues towards the inner shieldings.

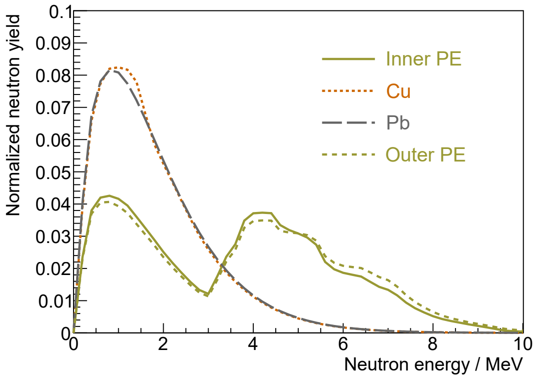

Figure 5.30.: Radiogenic neutron spectra produced in the various shielding materials in CRESST due to the contamination levels quoted in Table 5.11, each normalized to an integral of one.

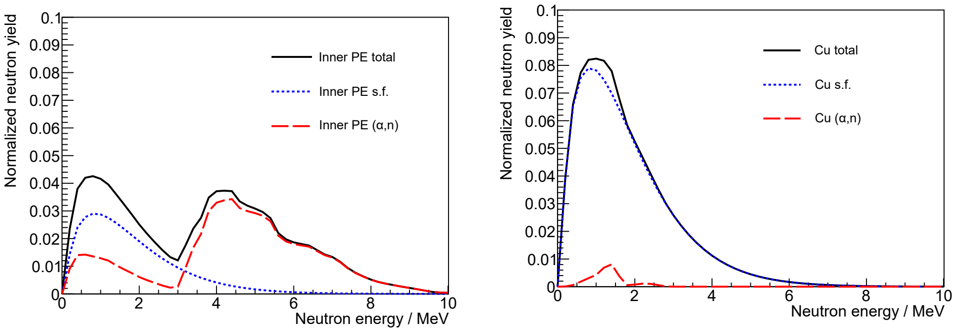

(a) Inner PE **(b)** Cu

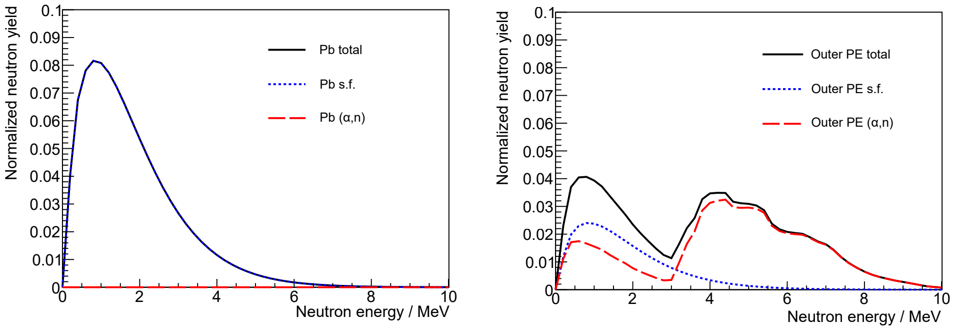

(c) Pb **(d)** Outer PE

Figure 5.31.: Contributions to the radiogenic neutron spectrum from (α,n) and s.f. reactions in the different shielding materials employed in CRESST, total spectrum normalized to an integral of one.

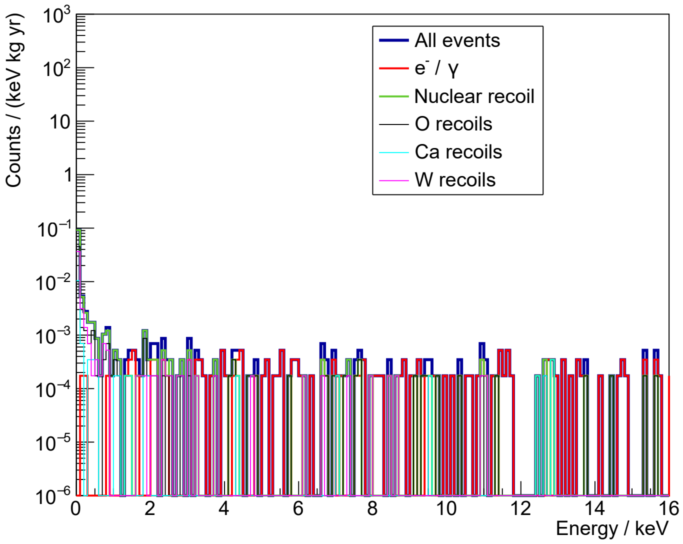

Figure 5.32.: Energy deposition due to radiogenic neutrons originating from the outer PE shield in the simulation of $1.0 \cdot 10^9$ events.

Outer Polyethylene Shielding

To simulate the radiogenic neutrons originating from the outer polyethylene shielding, the bulk contamination particle generator in ImpCRESST together with its interface to the SOURCES 4C neutron data is used (cf. Section 4.1.4). Neutrons are sampled according to a homogeneous distribution inside the polyethylene surrounding the further shielding layers (cf. Figure 5.4 and 5.13). 10^9 primary neutrons are simulated, featuring energies corresponding to the respective spectrum shown in Figure 5.31d. With a neutron yield of $2.2 \cdot 10^{-11}$ cm^{-3} s^{-1} and a polyethylene volume of $1.8 \cdot 10^7$ cm^3, this corresponds to a simulated exposure of $\sim 8.2 \cdot 10^4$ yr.

Similar as in the case of ambient neutrons, the outer polyethylene shielding itself is very effective in mitigating neutrons, in this case due to the self-shielding effect of polyethylene. Primarily neutrons produced close to the surface are able to leave the material and get closer to the central volumes. Additional reduction of the number of neutrons reaching the detectors is attained through the large distance the neutrons have to travel through the subsequent material layers. The energy deposition spectrum obtained in the ROI of detector A is displayed in Figure 5.32. Due to the large background mitigation and the distance to the detectors, the amount of simulated events observed in the detectors is again rather low, but statistical statements about obtained rates can be made. Table 5.12 shows the attained detector multiplicities, both without applying any cuts as well as with the assumption of threshold and efficiency of detector A for all the detectors.

Table 5.12.: Detector multiplicity in the simulation of $1.0 \cdot 10^9$ radiogenic neutrons originating from the outer polyethylene shielding. A combined count rate for nuclear and electron recoils is presented. 1σ Poissonian bounds and 90 % upper limits are stated to represent the uncertainties on the results.

	Without threshold & efficiency		With threshold & efficiency	
Multiplicity	Counts / (kg yr)$^{-1}$	%	Counts / (kg yr)$^{-1}$	%
1	$(1.8 \pm 0.1) \cdot 10^{-1}$	96.2 ± 0.94	$(1.2 \pm 0.1) \cdot 10^{-1}$	97.69 ± 1.19
2	$(6.8 \pm 0.3) \cdot 10^{-3}$	3.62 ± 0.18	$(2.7 \pm 0.2) \cdot 10^{-3}$	2.25 ± 0.18
3	$(3.1 \pm 0.7) \cdot 10^{-4}$	0.17 ± 0.04	$(7.0 \pm 3.5) \cdot 10^{-5}$	0.06 ± 0.03
4	$(1.7 \pm 1.7) \cdot 10^{-5}$	< 0.01	$< 4.0 \cdot 10^{-5}$	< 0.03
5	$(1.7 \pm 1.7) \cdot 10^{-5}$	< 0.01	$< 4.0 \cdot 10^{-5}$	< 0.03
> 5	$< 4.0 \cdot 10^{-5}$	< 0.02	$< 4.0 \cdot 10^{-5}$	< 0.03

Table 5.13.: Detected event rate in the simulation of $1.0 \cdot 10^9$ radiogenic neutrons originating from the outer polyethylene shielding in different energy ranges. 1σ Poissonian bounds and 90 % upper limits are stated to represent the uncertainties on the results.

	Nuclear recoils / (kg yr)$^{-1}$		Electron recoils / (kg yr)$^{-1}$	
Energy range	All	Multiplicity = 1	All	Multiplicity = 1
Full range	$(1.7 \pm 0.1) \cdot 10^{-2}$	$(1.3 \pm 0.1) \cdot 10^{-2}$	$(1.8 \pm 0.1) \cdot 10^{-1}$	$(1.6 \pm 0.1) \cdot 10^{-1}$
< 0.03 keV	$(7.9 \pm 0.4) \cdot 10^{-3}$	$(6.8 \pm 0.3) \cdot 10^{-3}$	$(7.0 \pm 3.5) \cdot 10^{-5}$	$< 4.0 \cdot 10^{-5}$
0.03 – 16 keV	$(4.5 \pm 0.3) \cdot 10^{-3}$	$(4.0 \pm 0.3) \cdot 10^{-3}$	$(5.0 \pm 0.3) \cdot 10^{-3}$	$(1.7 \pm 0.2) \cdot 10^{-3}$

In Table 5.13, the integral rates seen in the detectors in various energy ranges are listed. No specific threshold or efficiency is considered, such that the total expected values before cuts are assessed. Again, nuclear recoil events with multiplicity $m = 1$ pose the dangerous contribution to the background and are hence specifically mentioned. According to the simulation, the entire energy range features approximately $1.3 \cdot 10^{-2}$ nuclear recoil events per kg·yr with single multiplicity. In the ROI of detector A, the rate equates to roughly $4.0 \cdot 10^{-3}$ events per kg·yr. Statistical uncertainties are considered in the values listed in the table. Overall, the rate is well below the one expected from ambient neutrons. Hence, the contribution from radioactive contaminations in the outer polyethylene shielding can be rated as almost negligible.

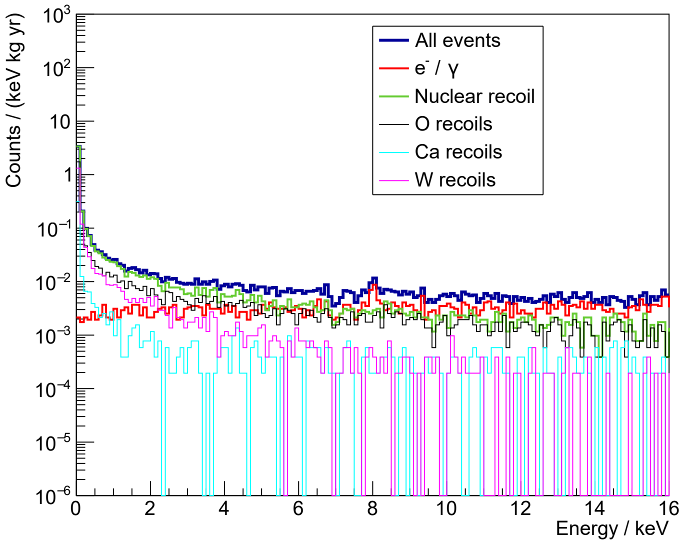

Figure 5.33.: Energy deposition due to radiogenic neutrons originating from the lead shield in the simulation of $2.0 \cdot 10^8$ events.

Lead Shielding

The next shielding material, closer to the central detector volume than the outer polyethylene, is lead. For the simulation, again ImpCRESST is used to homogeneously sample neutrons in all volumes constituted of this material. The energies of the neutrons are drawn from the, in the case of lead, pure s.f. spectrum attained from SOURCES 4C and presented in Figure 5.31c. The position of the lead shielding inside the outer polyethylene layer further leads to less low-Z material located in the line of sight to the detectors. Therefore, a lower simulated event count is sufficient to assess the corresponding background. In this study, $2 \cdot 10^8$ primary neutrons are started, corresponding to a simulated exposure of $\sim 7.3 \cdot 10^4$ yr, due to a neutron yield in lead of $3.1 \cdot 10^{-11}$ cm^{-3} s^{-1} and a starting volume of $\sim 2.8 \cdot 10^6$ cm^3.

Figure 5.33 shows the energy deposition spectrum in the detectors in the ROI below 16 keV. A list of detector multiplicities is again detailed in Table 5.14 and the count rates in the ROI of detector A as well as below this region and in the full energy range are presented in Table 5.15. Special attention shall repeatedly be drawn to the nuclear recoil events with multiplicity $m = 1$, which pose the dangerous contribution to the background. Without considering effects of threshold and efficiency, the full energy range features $4.6 \cdot 10^{-1}$ such events per kg·yr exposure. In the ROI of detector A, $1.5 \cdot 10^{-1}$ single nuclear recoil events per kg·yr are registered before cuts. Within statistical uncertainties as stated in the table, these values are very similar to the ones obtained for ambient neutrons. While the evaluation of ambient neutrons, however,

Table 5.14.: Detector multiplicity in the simulation of $2.0 \cdot 10^8$ radiogenic neutrons originating from the lead shielding. A combined count rate for nuclear and electron recoils is presented. 1σ Poissonian bounds and 90 % upper limits are stated to represent the uncertainties on the results.

	Without threshold & efficiency		With threshold & efficiency	
Multiplicity	Counts / (kg yr)$^{-1}$	%	Counts / (kg yr)$^{-1}$	%
1	4.9 ± 0.1	95.51 ± 0.19	3.2 ± 0.1	97.21 ± 0.24
2	$(2.2 \pm 0.1) \cdot 10^{-1}$	4.2 ± 0.04	$(8.7 \pm 0.1) \cdot 10^{-2}$	2.68 ± 0.04
3	$(1.4 \pm 0.1) \cdot 10^{-2}$	0.27 ± 0.01	$(3.5 \pm 0.3) \cdot 10^{-3}$	0.11 ± 0.01
4	$(9.9 \pm 1.4) \cdot 10^{-4}$	0.02 ± 0.01	$(1.2 \pm 0.5) \cdot 10^{-4}$	< 0.01
5	$(5.8 \pm 3.4) \cdot 10^{-5}$	< 0.01	$(1.9 \pm 1.9) \cdot 10^{-5}$	< 0.01
> 5	$< 4.5 \cdot 10^{-5}$	< 0.01	$< 4.5 \cdot 10^{-5}$	< 0.01

Table 5.15.: Detected event rate in the simulation of $2.0 \cdot 10^8$ radiogenic neutrons originating from the lead shielding in different energy ranges. 1σ Poissonian bounds and 90 % upper limits are stated to represent the uncertainties on the results.

	Nuclear recoils / (kg yr)$^{-1}$		Electron recoils / (kg yr)$^{-1}$	
Energy range	All	Multiplicity = 1	All	Multiplicity = 1
Full range	$(6.1 \pm 0.1) \cdot 10^{-1}$	$(4.6 \pm 0.1) \cdot 10^{-1}$	4.8 ± 0.1	4.1 ± 0.1
< 0.03 keV	$(2.9 \pm 0.1) \cdot 10^{-1}$	$(2.6 \pm 0.1) \cdot 10^{-1}$	$(3.0 \pm 0.2) \cdot 10^{-3}$	$(5.8 \pm 3.4) \cdot 10^{-5}$
0.03 – 16 keV	$(1.7 \pm 0.1) \cdot 10^{-1}$	$(1.5 \pm 0.1) \cdot 10^{-1}$	$(1.4 \pm 0.1) \cdot 10^{-1}$	$(4.3 \pm 0.1) \cdot 10^{-2}$

is based on a simulated and measured neutron flux at LNGS, the radiogenic neutrons originating from lead are estimated from upper limits on the contamination levels in the material, see Table 5.11. Compared for example to the screening results of copper, which are sensitive to contamination levels of $\mathcal{O}(1$ ppt$)$, the quoted lead results are only sensitive to $\mathcal{O}(100$ ppt$)$. A better estimation could hence be made following an updated screening measurement. Such a measurement was not possible in the course of this study and could hence be an additional task for future assessments.

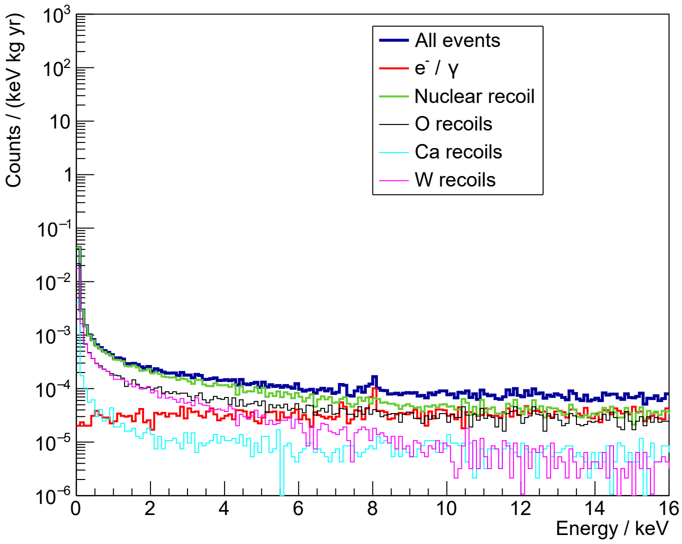

Figure 5.34.: Energy deposition due to radiogenic neutrons originating from the copper shield in the simulation of $1.0 \cdot 10^8$ events.

Copper Shielding

Copper is one of the cleanest producible materials and is hence commonly used in the experimental setup of rare event search experiments. In CRESST, copper is used as an additional gamma shielding inside the lead, to potentially cope with gammas from ^{210}Pb or other contaminants in the lead shield. In this study, however, only the neutron background contributions are assessed. Thus, the neutron yield in copper is simulated in ImpCRESST by homogeneously sampling neutrons according to the energy spectrum presented in Figure 5.31b in all copper parts, of which the copper shielding provides the largest share. 10^8 events are simulated, corresponding to an exposure of $\sim 4.9 \cdot 10^6$ yr, calculated from a neutron yield of $6.6 \cdot 10^{-13}$ cm^{-3} s^{-1} and starting volume of $9.7 \cdot 10^5$ cm^3.

In Figure 5.34, the energy deposition spectrum in the detectors is displayed in the ROI of detector A. Detector multiplicities and the count rates in various energy regions are listed in Table 5.16 and 5.17, respectively. Again, the nuclear recoil events with multiplicity $m = 1$ are considered as the most dangerous contribution to the background. Hence, the respective background rates are separately listed in the table. Covering the entire energy range, $7.6 \cdot 10^{-3}$ nuclear recoil events per kg·yr with single multiplicity are found, if threshold and efficiency are not considered. In the ROI of detector A, a reduced rate of $2.5 \cdot 10^{-3}$ such events per kg·yr before cuts is obtained. These low numbers are based on upper limits quoted in screening measurements of copper and thus provide a rather conservative limit on the respective contribution to the nuclear

Table 5.16.: Detector multiplicity in the simulation of $1.0 \cdot 10^8$ radiogenic neutrons originating from the copper shielding. A combined count rate for nuclear and electron recoils is presented. 1σ Poissonian bounds and 90 % upper limits are stated to represent the uncertainties on the results.

	Without threshold & efficiency		With threshold & efficiency	
Multiplicity	Counts / (kg yr)$^{-1}$	%	Counts / (kg yr)$^{-1}$	%
1	$(5.3 \pm 0.1) \cdot 10^{-2}$	95.02 ± 0.14	$(3.4 \pm 0.1) \cdot 10^{-2}$	96.89 ± 0.17
2	$(2.6 \pm 0.1) \cdot 10^{-3}$	4.65 ± 0.03	$(1.0 \pm 0.1) \cdot 10^{-3}$	2.98 ± 0.03
3	$(1.7 \pm 0.1) \cdot 10^{-4}$	0.31 ± 0.01	$(4.4 \pm 0.2) \cdot 10^{-5}$	0.13 ± 0.01
4	$(1.0 \pm 0.1) \cdot 10^{-5}$	0.02 ± 0.01	$(9.6 \pm 3.2) \cdot 10^{-7}$	< 0.01
5	$(6.4 \pm 2.6) \cdot 10^{-7}$	< 0.01	$(1.1 \pm 1.1) \cdot 10^{-7}$	< 0.01
> 5	$< 2.5 \cdot 10^{-7}$	< 0.01	$< 2.5 \cdot 10^{-7}$	< 0.01

Table 5.17.: Detected event rate in the simulation of $1.0 \cdot 10^8$ radiogenic neutrons originating from the copper shielding in different energy ranges. 1σ Poissonian bounds and 90 % upper limits are stated to represent the uncertainties on the results.

	Nuclear recoils / (kg yr)$^{-1}$		Electron recoils / (kg yr)$^{-1}$	
Energy range	All	Multiplicity = 1	All	Multiplicity = 1
Full range	$(9.8 \pm 0.1) \cdot 10^{-3}$	$(7.6 \pm 0.1) \cdot 10^{-3}$	$(4.9 \pm 0.1) \cdot 10^{-2}$	$(4.1 \pm 0.1) \cdot 10^{-2}$
< 0.03 keV	$(3.7 \pm 0.1) \cdot 10^{-3}$	$(3.2 \pm 0.1) \cdot 10^{-3}$	$(3.5 \pm 0.2) \cdot 10^{-5}$	$(3.2 \pm 1.8) \cdot 10^{-7}$
0.03 – 16 keV	$(2.8 \pm 0.1) \cdot 10^{-3}$	$(2.5 \pm 0.1) \cdot 10^{-3}$	$(1.6 \pm 0.1) \cdot 10^{-3}$	$(4.4 \pm 0.1) \cdot 10^{-4}$

recoil background. As the rate is much lower than the one of the previously assessed components, specifically comparing again to the ambient neutrons, it may almost be deemed negligible.

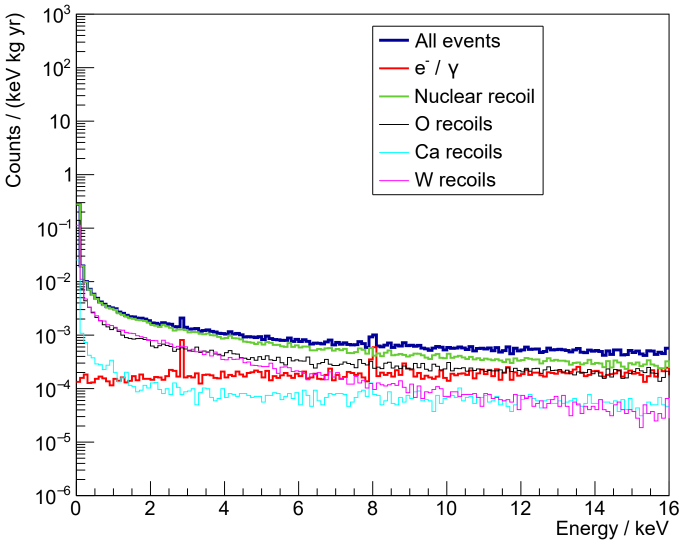

Figure 5.35.: Energy deposition due to radiogenic neutrons originating from the inner PE shield in the simulation of $5.0 \cdot 10^7$ events.

Inner Polyethylene Shielding

As discussed in Section 5.1.2, the inner polyethylene shielding (see Figure 5.5) has been installed in preparation for CRESST-II phase 2 to further mitigate the neutron background. Here, its contribution to the production of additional neutrons via radioactive contaminations in the material is assessed. Neutrons originating in the inner polyethylene shielding are simulated in ImpCRESST by homogeneously sampling them according to the energy spectrum presented in Figure 5.31a. Due to its location in the vicinity of the detectors, a reduced number of simulated events is satisfying the needs regarding feasible results. Therefore, $5 \cdot 10^7$ primary neutrons are started, corresponding to an exposure of $\sim 4.6 \cdot 10^6$ yr, calculated from a neutron yield of $3.2 \cdot 10^{-12}$ cm^{-3} s^{-1} and starting volume of $1.1 \cdot 10^5$ cm^3.

In Figure 5.35, the energy deposition spectrum in the detectors, as for the other radiogenic background contributions, is displayed for the ROI of detector A. Detector multiplicities and the count rates in various energy regions are listed in Table 5.18 and 5.19, respectively. The assessment of background events again focuses on the obtained nuclear recoil events with multiplicity $m = 1$, which pose the most dangerous background contribution. The rate of such events, which could potentially mimic a DM signal, is estimated by approximately $5.8 \cdot 10^{-2}$ events per kg·yr in the entire energy range without constraints and effects of threshold or efficiency. In the ROI of detector A, this rate reduces to $1.9 \cdot 10^{-2}$ events per kg·yr before cuts. Despite the proximity to the detectors, this estimate yields a value almost an order of magnitude lower than

Table 5.18.: Detector multiplicity in the simulation of $5.0 \cdot 10^7$ radiogenic neutrons originating from the inner polyethylene shielding. A combined count rate for nuclear and electron recoils is presented. 1σ Poissonian bounds and 90 % upper limits are stated to represent the uncertainties on the results.

	Without threshold & efficiency		With threshold & efficiency	
Multiplicity	Counts / (kg yr)$^{-1}$	%	Counts / (kg yr)$^{-1}$	%
1	$(3.1 \pm 0.1) \cdot 10^{-1}$	94.52 ± 0.09	$(2.0 \pm 0.1) \cdot 10^{-1}$	96.52 ± 0.12
2	$(1.7 \pm 0.1) \cdot 10^{-2}$	5.1 ± 0.02	$(6.9 \pm 0.1) \cdot 10^{-3}$	3.32 ± 0.02
3	$(1.1 \pm 0.1) \cdot 10^{-3}$	0.35 ± 0.01	$(3.0 \pm 0.1) \cdot 10^{-4}$	0.15 ± 0.01
4	$(8.3 \pm 0.5) \cdot 10^{-5}$	0.03 ± 0.01	$(1.1 \pm 0.2) \cdot 10^{-5}$	< 0.01
5	$(4 \pm 1.1) \cdot 10^{-6}$	< 0.01	$(9.3 \pm 5.4) \cdot 10^{-7}$	< 0.01
> 5	$< 7.2 \cdot 10^{-7}$	< 0.01	$< 7.2 \cdot 10^{-7}$	< 0.01

Table 5.19.: Detected event rate in the simulation of $5.0 \cdot 10^7$ radiogenic neutrons originating from the inner polyethylene shielding in different energy ranges. 1σ Poissonian bounds and 90 % upper limits are stated to represent the uncertainties on the results.

	Nuclear recoils / (kg yr)$^{-1}$		Electron recoils / (kg yr)$^{-1}$	
Energy range	All	Multiplicity = 1	All	Multiplicity = 1
Full range	$(7.3 \pm 0.1) \cdot 10^{-2}$	$(5.8 \pm 0.1) \cdot 10^{-2}$	$(2.8 \pm 0.1) \cdot 10^{-1}$	$(2.3 \pm 0.1) \cdot 10^{-1}$
< 0.03 keV	$(2.4 \pm 0.1) \cdot 10^{-2}$	$(2.1 \pm 0.1) \cdot 10^{-2}$	$(2.4 \pm 0.1) \cdot 10^{-4}$	$(2.5 \pm 0.9) \cdot 10^{-6}$
0.03 – 16 keV	$(2.1 \pm 0.1) \cdot 10^{-2}$	$(1.9 \pm 0.1) \cdot 10^{-2}$	$(9.7 \pm 0.1) \cdot 10^{-3}$	$(2.4 \pm 0.1) \cdot 10^{-3}$

that obtained for ambient neutrons.

All in all, after assessing the radiogenic neutron background components, the ambient neutrons hence dominate the nuclear recoil background rate, potentially together with neutrons originating from the lead shielding. The total expected rate, however, is well below 1 count per kg·yr. A study of the cosmogenic neutrons in the subsequent section will conclude the survey on the nuclear recoil background in CRESST.

5.5.3 Cosmogenic Neutron Background

This section describes the second main neutron background origin apart from radioactive decays, which are cosmic rays. So-called cosmogenic neutrons are secondarily produced by high-energy particles, which themselves are created in interactions of cosmic rays in the Earth's atmosphere. This background component is the main reason for many DM and rare event search experiments to situate their setups at deep underground laboratories. Most of the atmospheric particle flux, especially its hadronic component, is strongly mitigated by a few meters of rock overburden (see discussion in section 3.3 and graphic in Figure 3.3). High-energy muons, however, are able to survive traversing large distances of rock, and may partly reach the LNGS underground laboratory (cf. Section 3.3.1). The remaining muon flux after 3600 m.w.e. is ~1 $\mathrm{m}^{-2}\,\mathrm{h}^{-1}$, which may still be sufficient to produce a dangerous nuclear recoil background contribution via secondary neutrons.

In this thesis, the muon-induced neutron background in CRESST-III is for the first time thoroughly studied via a top-down approach starting the simulations from the muons reaching the underground laboratory. In a previous neutron background study [137] for CRESST-II, the simulations were based on a measured spectrum of muon-induced neutrons employed as primary particles in Geant4. Tracking the muons and their interactions in the simulation, however, has various advantages. While the measured neutron spectrum does not allow for the consideration of muon-induced neutrons created inside the shielding layers of the experimental setup, this neutron component is naturally part of the simulation of muons traversing the geometry. Moreover, muon-induced showers are considered in the simulation, which are an important source of secondary particles and crucial for evaluating any type of anti-coincidence cut. Furthermore, only by tracking the muons through the experimental setup, the active muon veto can be considered and assessed in the study.

In the simulation, the experimental setup displayed in Figure 5.13 is placed in an empty hall surrounded by rock, mimicking the situation at LNGS. Muons have to be started a few meters inside the surrounding rock to be able to create particle showers that may enter the hall. To attain enough statistic in the simulation, however, the size of the experimental hall is decreased in comparison to reality. The largest part of simulated muons and secondary shower particles would otherwise, at the cost of CPU time and memory space, not reach the experimental setup. Hence, a hall size of $7 \times 7 \times 13$ m is chosen and a cuboid surface of $12 \times 12 \times 13$ m is defined for sampling the muons.

The starting surface for the muons is shifted vertically, such that all of the primary particles starting in the top and lateral parts of the surrounding rock volume traverse at least 2.5 m of rock. This distance corresponds to ~700 g/cm^2, which is close to the value of 800 g/cm^2 quoted in Ref. [162] to be necessary for the shower production to reach equilibrium. As most muons do not traverse the rock exactly vertically, the required distance is typically reached. Furthermore, a cross-check with altered minimum

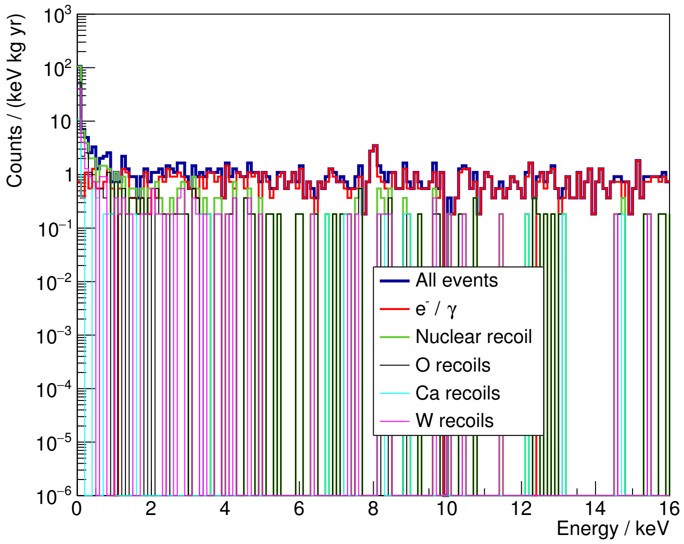

Figure 5.36.: Energy deposition due to cosmogenic neutrons in the simulation of $1.78 \cdot 10^8$ events.

rock path length of 5 m to ensure equilibrium was done. As this cross-check did not change the results, the previously chosen setup was found to be sufficient to correctly treat particle showers created in the surrounding of the experimental facility.

The integral muon flux on the specified surface is attained from MUSUN and amounts to 0.073 s^{-1} or approximately $2.3 \cdot 10^6$ yr^{-1}. In the muon-induced neutron simulation study, $1.78 \cdot 10^8$ events, corresponding to an exposure of 77.5 yr, have been simulated according to starting conditions defined in the MUSUN output files.

To assess the muon-induced background with ImpCRESST, the newly developed interface from MUSUN to ImpCRESST is employed (cf. Section 4.1.4). The MUSUN output files can hence directly be read in, such that the corresponding primary muon data are defining the starting conditions of each event in the Geant4-based simulation. The data attained from the respective simulation of the $1.78 \cdot 10^8$ events is analyzed with respect to the energy depositions in the $CaWO_4$ crystals, especially in the ROI of detector A. Muon-induced neutrons can feature much larger energies than those created in radioactive decays. While the spectrum of the latter is mostly concentrated below ~10 MeV (cf. Figure 5.30), muon-induced neutron energies may extend up to the GeV range. High-energy neutrons are more penetrative and hence more difficult to shield. As a significant reduction to negligible background levels is often impossible, a muon veto is typically a necessity for rare event searches that are sensitive to nuclear recoil backgrounds. However, the results without considering the effect of the muon veto will be discussed first, before focusing on a detailed description of the simulated muon veto data and comparison to the measurement.

Table 5.20.: Detector multiplicity in the simulation of $1.78 \cdot 10^8$ cosmogenic neutrons. A combined count rate for nuclear and electron recoils is presented. 1σ Poissonian bounds and 90 % upper limits are stated to represent the uncertainties on the results.

	Without threshold & efficiency		With threshold & efficiency	
Multiplicity	Counts / (kg yr)$^{-1}$	%	Counts / (kg yr)$^{-1}$	%
1	556 ± 3.2	74.76 ± 0.43	421.8 ± 2.8	78.36 ± 0.52
2	104.3 ± 1.4	14.02 ± 0.19	68.4 ± 1.1	12.7 ± 0.21
3	34.2 ± 0.8	4.6 ± 0.11	21.6 ± 0.6	4.01 ± 0.12
4	17.6 ± 0.6	2.37 ± 0.08	11.6 ± 0.5	2.15 ± 0.09
5	9.7 ± 0.4	1.31 ± 0.06	6.2 ± 0.3	1.15 ± 0.06
6	6.6 ± 0.3	0.89 ± 0.05	3.7 ± 0.3	0.68 ± 0.05
7	4.2 ± 0.3	0.57 ± 0.04	2.2 ± 0.2	0.41 ± 0.04
8	3.2 ± 0.2	0.43 ± 0.03	1.4 ± 0.2	0.26 ± 0.03
9	2.3 ± 0.2	0.31 ± 0.03	$(9.4 \pm 1.3) \cdot 10^{-1}$	0.17 ± 0.02
> 9	5.6 ± 0.3	0.75 ± 0.04	$(5.9 \pm 1.0) \cdot 10^{-1}$	0.11 ± 0.02

Table 5.21.: Detected event rate in the simulation of $1.78 \cdot 10^8$ cosmogenic neutrons in different energy ranges. 1σ Poissonian bounds and 90 % upper limits are stated to represent the uncertainties on the results.

	Nuclear recoils / (kg yr)$^{-1}$		Electron recoils / (kg yr)$^{-1}$	
Energy range	All	Multiplicity = 1	All	Multiplicity = 1
Full range	35.1 ± 0.8	9.9 ± 0.4	1129.5 ± 4.6	519.3 ± 3.1
< 0.03 keV	9 ± 0.4	5 ± 0.3	$(1.8 \pm 0.6) \cdot 10^{-1}$	$< 4.2 \cdot 10^{-2}$
0.03 – 16 keV	6.2 ± 0.3	3.2 ± 0.2	15.6 ± 0.5	6.1 ± 0.3

Figure 5.36 shows the histogrammed energy depositions in the cryogenic detectors in the ROI of detector A below 16 keV. However, no threshold or efficiency is again applied to assess the true spectrum. In Table 5.20, the detector multiplicities, again defined by how many detectors see an energy deposition per event, are listed. Two separate blocks are presented in the table. The first one states the event count without applying any cuts, while the second one assumes the threshold and efficiency of detector A for all the detectors. Due to the higher energies involved in the muon-induced background and the creation of particle showers, an energy deposition in one detector is more likely accompanied by additional energy depositions in other detectors. Hence, events up to very high multiplicities can be obtained with the percentages listed in the table. When assuming the threshold of detector A as a trigger condition, it becomes obvious

that many events feature only tiny energy depositions below threshold in some of the detectors. Thus, in general, the multiplicities are shifted to lower values in this case. However, compared to the multiplicity $m = 1$ percentage in the radiogenic neutron studies, the share is well reduced and lies below 80 %. More events can hence be vetoed using an anti-coincidence cut.

Table 5.21 presents the integral count rates seen in the detectors in various energy ranges. Their majority belongs to events with a detector multiplicity larger than one. The dangerous events for the DM search are again those, in which only a single detector triggers. In the development of the neutron background model, specifically the neutron-induced nuclear recoils with detector multiplicity $m = 1$ are thus considered. In the full energy range, a single nuclear recoil rate of 9.9 events per kg·yr is obtained. Looking at the ROI of detector A, the corresponding rate amounts to 3.2 events per kg·yr. According to these numbers, the cosmogenic neutron background is much larger than the ambient and internal radiogenic one. Due to this reason, almost all rare event search experiments, for which nuclear recoils in their region of interest are a dangerous background, make use of an active muon veto. In the following, the muon veto of CRESST is discussed in detail.

Considering the Active Muon Veto

The active muon veto of CRESST has been added in the upgrade to CRESST-II in addition to the outer polyethylene shielding to deal with the cosmogenic neutron background. It consists of 20 plastic scintillator panels made of Bicron BC-408 [163], featuring a specified light output of 64 % Anthracene [163], corresponding to roughly 11100 photons/MeV. Each panel is read out via a PMT of type 9900B from Electron Tubes [164]. The panels are placed around the Radon box, encompassing the lead and copper shielding, but itself surrounded by the outer polythelene. The position is indicated in the setup sketched in Figure 5.4 and the exact panel layout is presented in Figure 5.37. Different panel sizes are used as detailed in Table 5.22.

The PMTs of the top and bottom panels are located at the center of the long edge, while the ones of the side panels are located at the center of the short edge. As the attenuation length for scintillation light (wavelength of maximum emission: 425 nm) in BC-408 [163] is approximately 210 cm, photons can typically freely travel within the entire extensions of the panels. The plastic scintillators are additionally covered by a reflective material to enhance the chance of light reaching the PMTs.

As seen in Figure 5.37, the panels cover the entire solid angle except for a hole of 295 mm at the top, which is necessary to make room for the hanging cryostat. This hole corresponds to an uncovered solid angle of about 4 %. However, high energy muons have a very low chance of being captured inside the materials and typically traverse at least one additional panel at the side or the bottom even if they pass through the hole in the top. Essentially though, this fact impacts the considerations regarding the

Table 5.22.: Dimensions of CRESST muon veto panels.

Panel position	PMT position in panel	Dimension (mm)
Top	Center of long edge	1620×800 (excision radius 295)
Bottom	Center of long edge	1430×720
Side	Center of short edge	1350×770

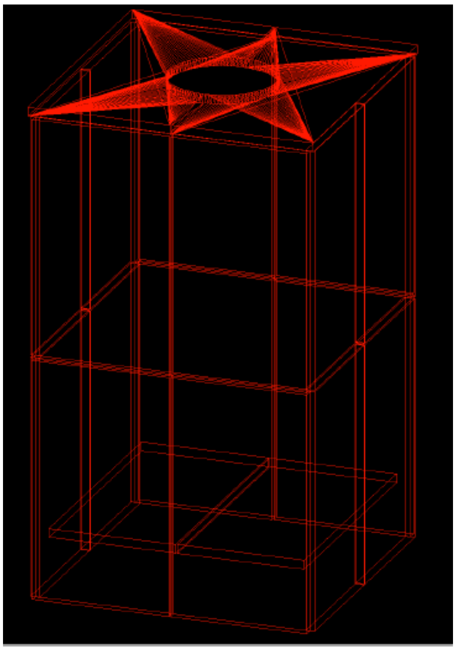

Figure 5.37.: Arrangement of the 20 muon veto panels visualized from the simulated experimental geometry. The entire solid angle except for a circular hole on the top with a radius of 295 mm is covered (the star-like structure around the hole is an artifact of the visualization). Exact dimensions of the panels are detailed in Table 5.22.

muon veto trigger condition. A clear muon event, due to the penetrating nature of the muons, mostly leads to (at least) two veto panels observing a signal.

However, posing a trigger condition on this minimum panel multiplicity would lead to missing some of the events, in which the muons pass through the top hole. Furthermore, other muon-correlated events, in which only secondary particles reach the muon veto, may also only lead to energy deposition in a single panel. While a loose trigger condition increases the dead time of the experiment, as most of the single muon panel triggers originate from radioactivity rather than muons and lead to random coincidences, it enhances the safety of removing all the muon-correlated events. For this reason, the CRESST muon veto trigger condition only requires a single panel to measure an energy deposition above a defined threshold well below the Landau distribution expected from events in which the muon itself traverses the panel. Thus, additional dead time in the experiment is accepted for the sake of a safe and effective veto. In principle, a trigger for each single panel as well as a trigger for the sum signal can be defined. While triggering on the sum was found to be sufficient in the past, a trigger condition for each single panel is currently used. In Run34 and thereafter, the signal of each panel is recorded once one of them triggers, such that coincidences can be analyzed. The threshold of the single panels is set to 50 mV, which can however not be easily converted to a corresponding energy deposition in the material. For reference regarding the information summarized in this paragraph as well as for additional details, the reader is referred to Ref. [165–167].

In CRESST-III Run34, the experimental run in the focus of this thesis, any event in the cryogenic detectors within a time window of [-5 ms, +10 ms] before or after the muon veto trigger was removed from the data set. The veto cut consequently reduced the collected data by approximately 7.6 %. No statistical correlation between events in the cryogenic detectors and muon veto triggers could be found, again leading to the conclusion that the majority of events are vetoed due to random coincidences with radioactive decays in the vicinity of the PMTs [4].

In Figure 5.38, the measured muon veto data of CRESST-III Run34 are shown for the individual scintillator panels. The measured signals in the PMTs are converted into QDC channels during readout. 4096 digitizer channels are available to approximately represent the deposited energy in the panel. The last one is used as an overflow bin containing all events exceeding the dynamic range of the QDC. All signals sit on a pedestal, set to some finite value due to the QDC response becoming non-linear at low energies. The typical pedestal is centered roughly around QDC channel 180. Muons traversing the panels, acting as minimum ionizing particles, lead to energy depositions following a Landau distribution. Originally, the panels were calibrated in a way that the peak of the distribution was located roughly around channel 2000, in the middle of the digitizer range. In subsequent experimental runs, it could however be seen that the peak drifted to slightly lower values.

To select muon events, a cut on the panel multiplicity (m) has to be applied, requiring a value of at least 2, as the events seen in a single panel are dominated by radioactive decays. Indeed, Ref. [167] states that the contamination of the borosilicate glass windows of the PMTs can essentially explain the entire amount of $m = 1$ events. While Figure 5.38 comprises all panel multiplicities, Figure 5.39 limits the energy depositions to the cases of $m \geq 2$. A Landau distribution above the pedestal can then clearly be identified. The Run34 measurement also shows the peaks of the distributions mostly located at QDC values below 2000. All distributions are slightly shifted against each other, but an average peak position located roughly around QDC value 1800 can be calculated.

For comparison to the measured data, the results of the muon simulations in Imp-

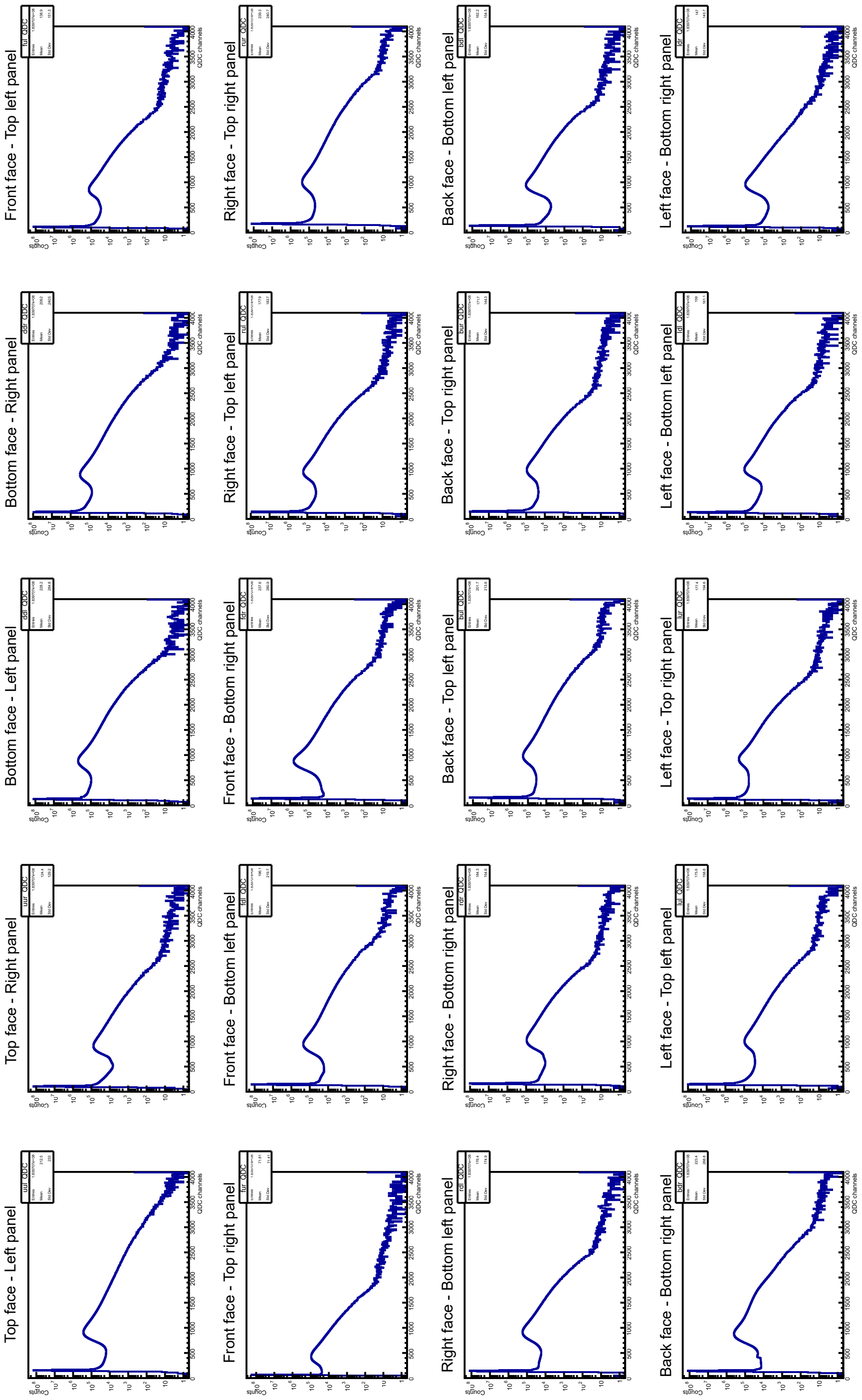

Figure 5.38.: Real muon veto data collected in the 20 plastic scintillator panels during CRESST-III Run34. All multiplicities $m \geq 1$ between panels are considered.

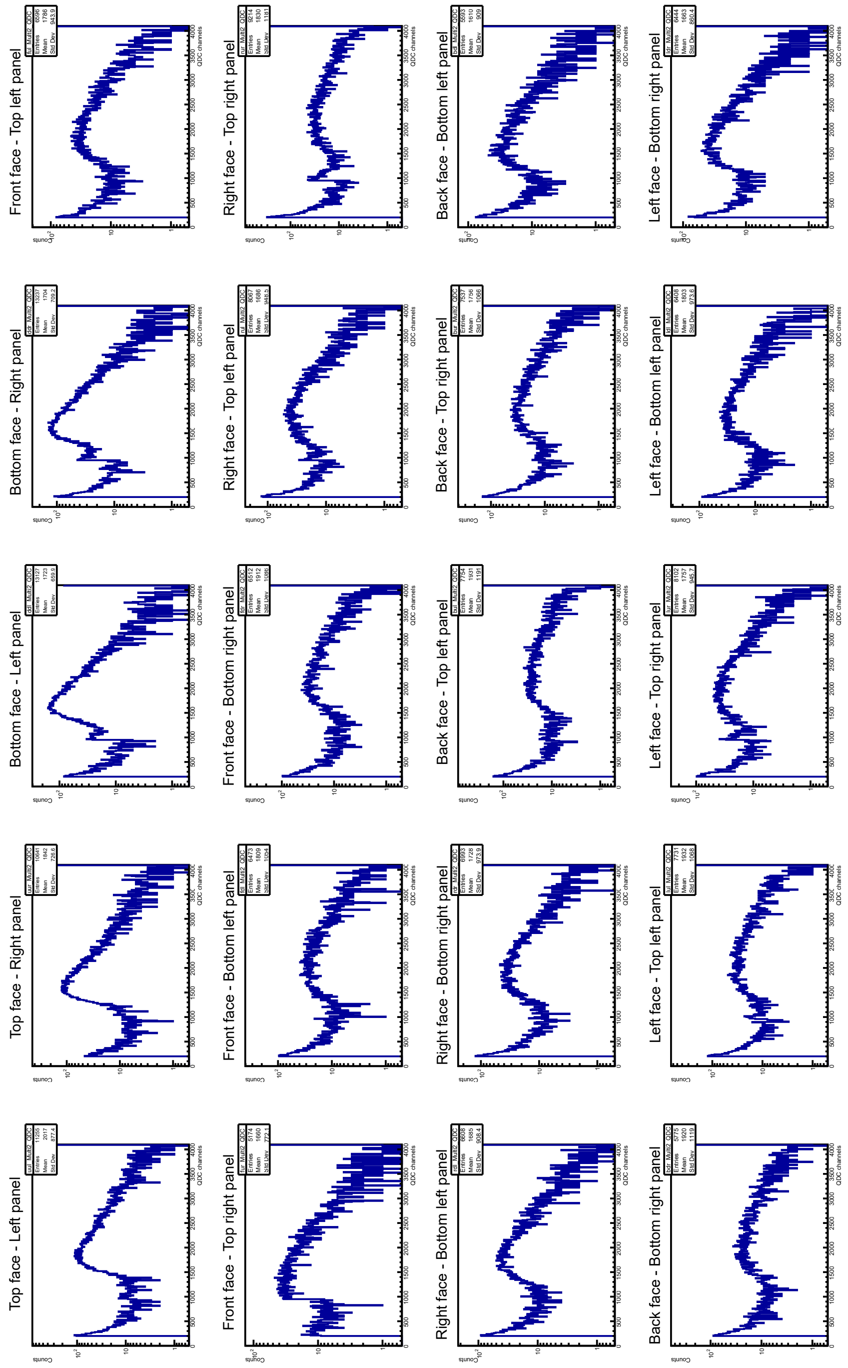

Figure 5.39.: Real muon veto data collected in the 20 plastic scintillator panels during CRESST-III Run34. Only multiplicities $m \geq 2$ between panels are considered to remove background from gamma interactions.

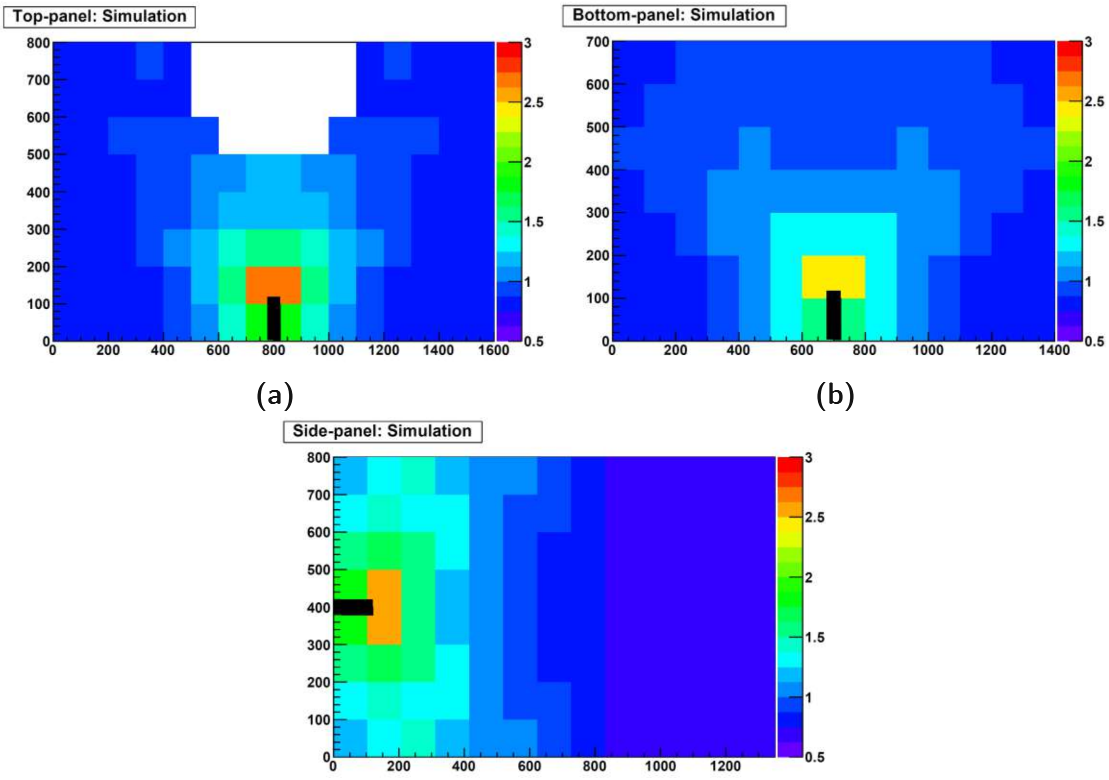

(a)

(b)

(c)

Figure 5.40.: Simulated light response map of the muon veto panels, taken from Ref. [165]. Indicated in black are the positions of the PMTs.

CRESST are analyzed in the following. First, the muon veto data independent of the cryodetector events are studied, before coincidences between cryodetector and muon veto triggers are considered and the efficiency of the veto is assessed.

The high light yield of BC-408 leads to 10^5–10^6 photons created in most of the events. As the tracking of all these scintillation photons in the plastic scintillators would be too time-consuming in the simulation and hence not feasibly applicable to the large number of simulated events, the energy depositions in the panels and their locations are instead evaluated. Using a map of the light response as a function of position in the panels, the deposited energy can then be scaled accordingly, to represent the relative light signal detected by the PMTs. A simulation study of this position dependence in the muon panels has been performed in Ref. [165] and is used for this purpose. The light response maps of the top, side and bottom panels are shown in Figure 5.40. Indicated in black in these heat maps is the position of the PMT in each panel. The scaled simulated energy deposition histograms of the individual panels are presented in Figure 5.41.

A differentiation in this plot is made between two types of events, which we call "muon events" (red) and "shower events" (green). While in the former case, the muon itself

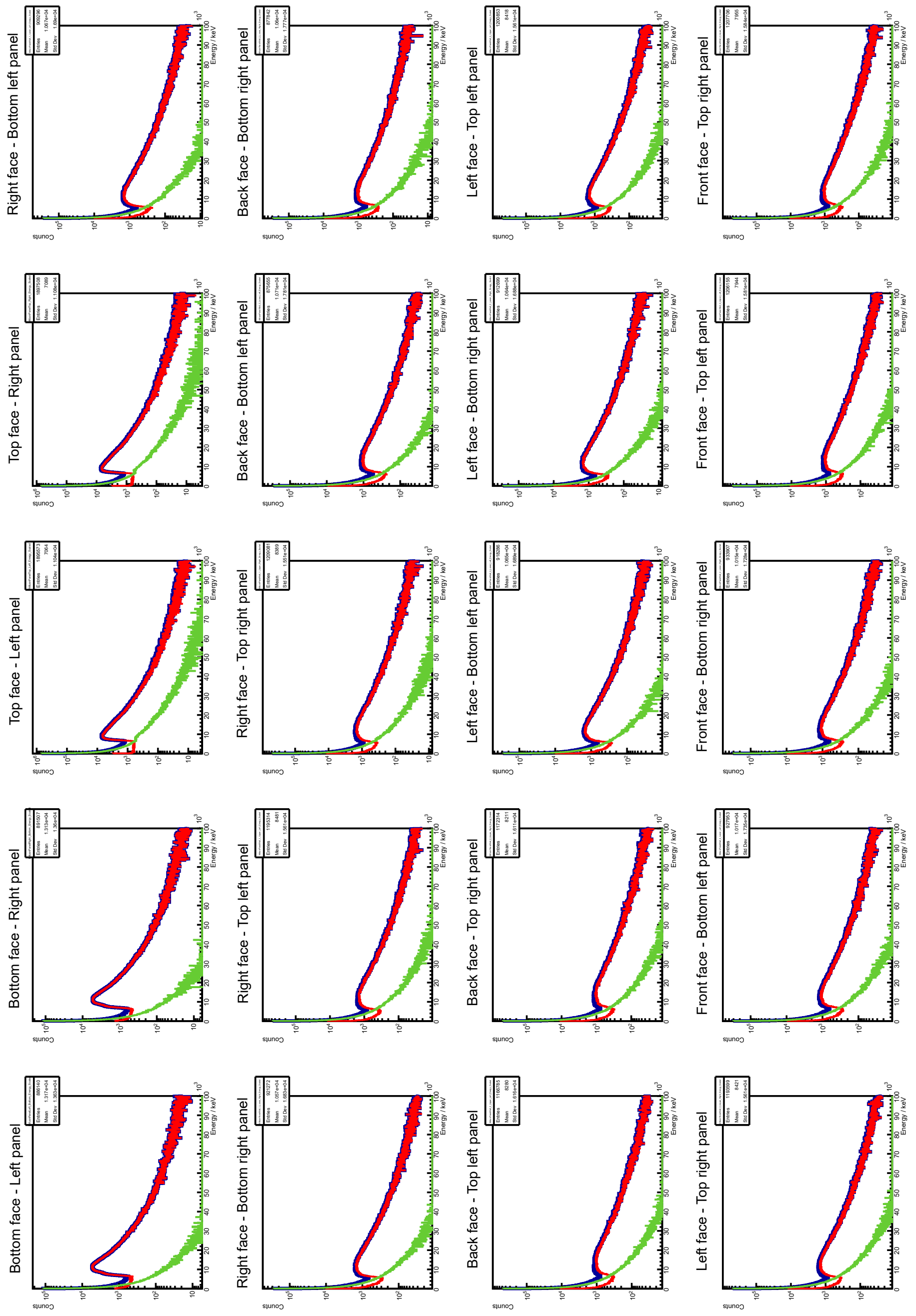

Figure 5.41.: Simulated energy deposition in the 20 muon veto panels in the cosmogenic background simulation starting with $1.78 \cdot 10^8$ incident muons. Colored in red are events with a muon traversing at least one panel, while shower particles leading to energy depositions are shown in green. The sum of both is displayed in blue.

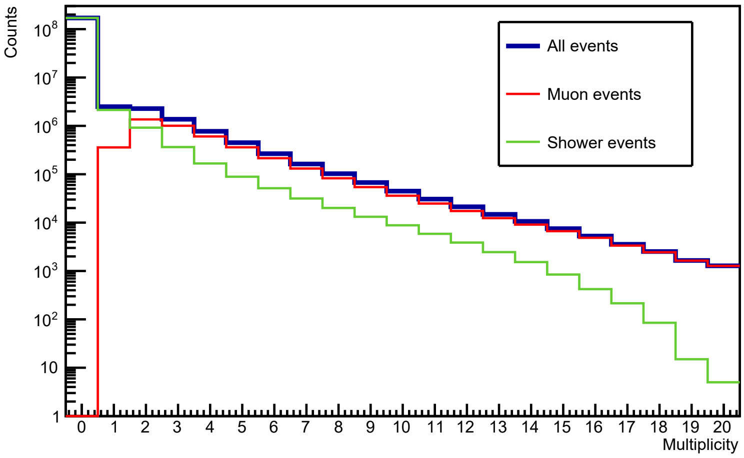

Figure 5.42.: Simulated muon veto panel multiplicity in the cosmogenic background simulation. Colored in red are events with a muon traversing at least one panel, while all other events are shown in green. The sum of all events is displayed in blue.

traverses at least one of the panels, only secondary shower particles may reach the panels in the latter. The Landau distribution of the muons traversing the panels can clearly be seen without an additional cut on the multiplicity, as the simulation in contrast to the real data only considers signals induced by muons reaching the LNGS underground laboratory. The muon panel multiplicity attained in the simulation is displayed in Figure 5.42. As expected, the multiplicity of muon events peaks at a value of 2. The fraction of $m = 1$ events corresponds mostly to some muons traversing the hole at the top of the veto system or traversing one of the side panels at a position below the bottom panel location.

For a comparison to the measured muon veto data, a cut on a multiplicity greater than or equal to 2 is made. Furthermore, light response-scaled energy deposition values are converted to QDC channel signals and a pedestal is added. For simplicity and because the real muon panel response apparently changes from run to run, the individual panel data attained in the simulation are processed by applying a global scaling function to each of them,

$$\mathrm{QDC} = \frac{E/keV}{7} + 180 \quad . \tag{5.15}$$

This leads to the resulting histograms presented in Figure 5.43. These data may now be compared to the real muon panel energy depositions shown in Figure 5.39. Such a comparison is presented in Figure 5.44 exemplary for two out of the 20 panels. Based on the overlay of simulated and measured data, the following statements can be made: The spectral shape features some similarities with respect to the pedestal, the dip above the pedestal region and the rise of the Landau distribution due to traversing muons. However, the simulated spectra seem to implicate a longer tail of the distribution, also leading to a larger amount of events allocated to the overflow channel. Possible

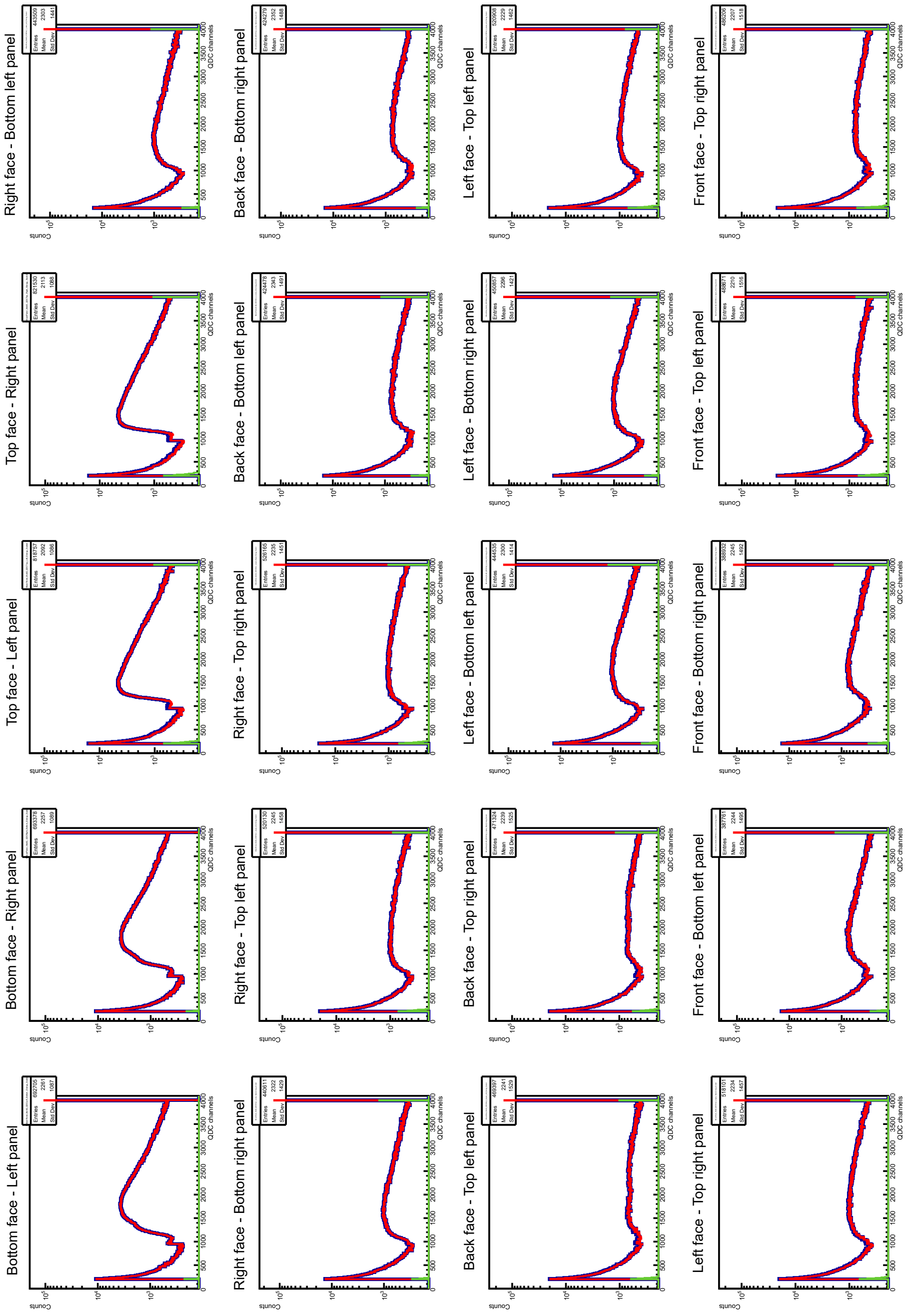

Figure 5.43.: Simulated muon veto data in the 20 plastic scintillator panels converted from an energy deposition in units of MeV to a QDC channel signal via Eq. 5.15. Only panel multiplicities $m \geq 2$ are considered. Colored in red are events with a muon traversing at least one panel, while shower particles leading to energy depositions are shown in green. The sum of both is displayed in blue.

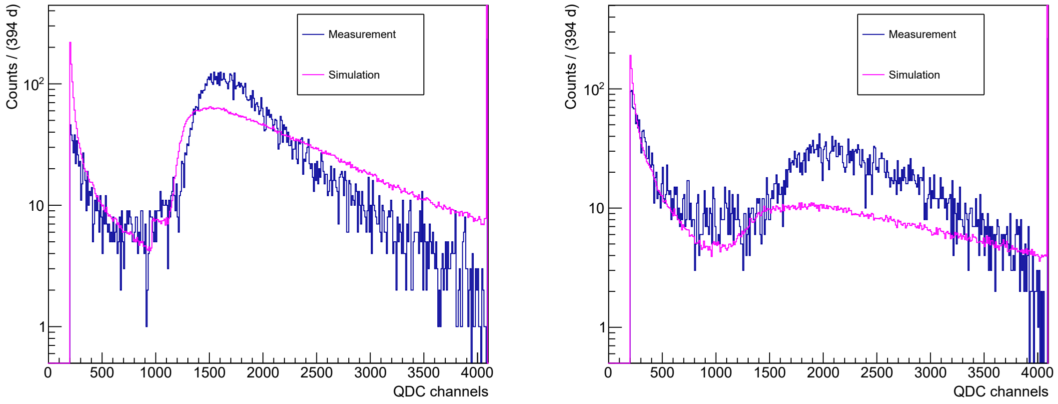

(a)

(b)

Figure 5.44.: Comparison of simulated (magenta) and measured (blue) muon veto data for two exemplary chosen panels, (a) the right panel on the top face, (b) the bottom right panel on the front face. The data are normalized to the measured exposure of 394 d.

explanations could be a quenching mechanism in the scintillation light creation for large energy depositions, or some other non-linearity in the response to high-energy signals.

A comparison of the pure rate of $m \geq 2$ events between simulation and measurement is presented in Table 5.23. The values are normalized to the respective exposures of 28306 d and 394 d of simulated and measured data. A grouping and averaging over panels is applied. Due to the different type and location, the top, bottom and side panels are viewed individually. For the side panels, a further distinction is made between those located in the upper and those in the lower positions. Averaged over all panels together, the rate is roughly 12 % higher in the measurement than in the simulation. A slight difference would potentially be explainable by radioactive decays and further background events leading to random coincidences in the real data in contrast to the simulation, which solely considers the muon-induced signals. In the individual panel types, however, very diverging discrepancies are obtained. In the top and side muon veto panels, the mean rates are essentially in statistical agreement between simulation and measurement. The large difference is hence almost solely caused by the obtained rate in the bottom panels. Here, the measurement yields a rate which is much higher than in the simulation and even exceeds the measured rate in the top panels. This might hint to some form of background mostly seen by the bottom panels, leading to additional coincidences. A thorough study of potential sources causing this observation was however out of the scope of this thesis.

In the following, the simulated muon veto data are now analyzed in the context of events, in which an energy deposition in one of the cryogenic detectors is registered.

Table 5.23.: Rate of events with multiplicity $m \geq 2$ in the muon panels, compared between simulated and measured data of CRESST-III Run34. An average is calculated for each type of panel, i.e. top, bottom and (upper and lower) side. The stated uncertainty is the standard deviation from the respective mean value.

	Event rate in panel type (d^{-1})			
Dataset	Top	Bottom	Upper Side	Lower Side
Simulation	28.97 ± 0.07	24.48 ± 0.02	17.67 ± 0.84	15.04 ± 0.88
Measurement	27.79 ± 1.10	33.46 ± 0.20	19.09 ± 3.03	16.12 ± 1.15

Figure 5.45a shows the muon panel multiplicity for these events. Obviously, the vast majority of events leading to an energy deposition in a detector are induced by a muon traversing the experimental setup including the plastic scintillator panels of the veto. Less than 0.1 % of the corresponding events are found to be shower events.

For the assessment of the efficiency of the muon veto, different trigger conditions are assumed. Similar to the real muon veto, a trigger threshold for the single panels as well as one for the sum of all panels is defined. In the experiment, the threshold for the single panels is set sufficiently low to guarantee a safe veto against muon-induced events, leading to an already quoted dead time of almost 8 % during background data taking due to random coincidences. In the simulation, this approach shall be resembled by choosing a single panel trigger threshold of 2 MeV and a sum threshold of 5 MeV. As mentioned before, a conversion of the real mV threshold value to an energy or QDC channel cannot be done unambiguously. Hence, the single trigger threshold is chosen close to but below the highest gamma energy originating from the natural decay chains. This is done in conformity with the choice of a rather safe cut, which leads to triggering for some of the radioactive background yielding the few-percent-level dead time in the measurement. Additionally, the results are compared to two other trigger conditions. In one case, no threshold is defined such that any energy deposition would cause the veto to trigger. In the other, higher thresholds of 4 MeV for the single panels and 10 MeV for the sum are assumed. Like in the experiment, a single panel triggering is sufficient to veto an event.

Figure 5.45b now shows the muon panel multiplicity for events with a registered energy deposition in the cryogenic detectors (cf. Figure 5.45a) in the context of those which could be vetoed using the first trigger condition of 2 MeV for the single panels. The graphic breaks down the results for all events seen in the detectors, as well as especially for the single nuclear recoil (SNR) signals seen in only one of the detectors which pose the most dangerous background for DM search. A conservative estimate without considering the signal survival probability of the detector is again made. In the entire energy range, $(1.6 \pm 0.5) \cdot 10^{-1}$ SNR events per kg·yr in the simulated exposure of muons entering the LNGS halls during 77.5 years do not lead to any coincident energy

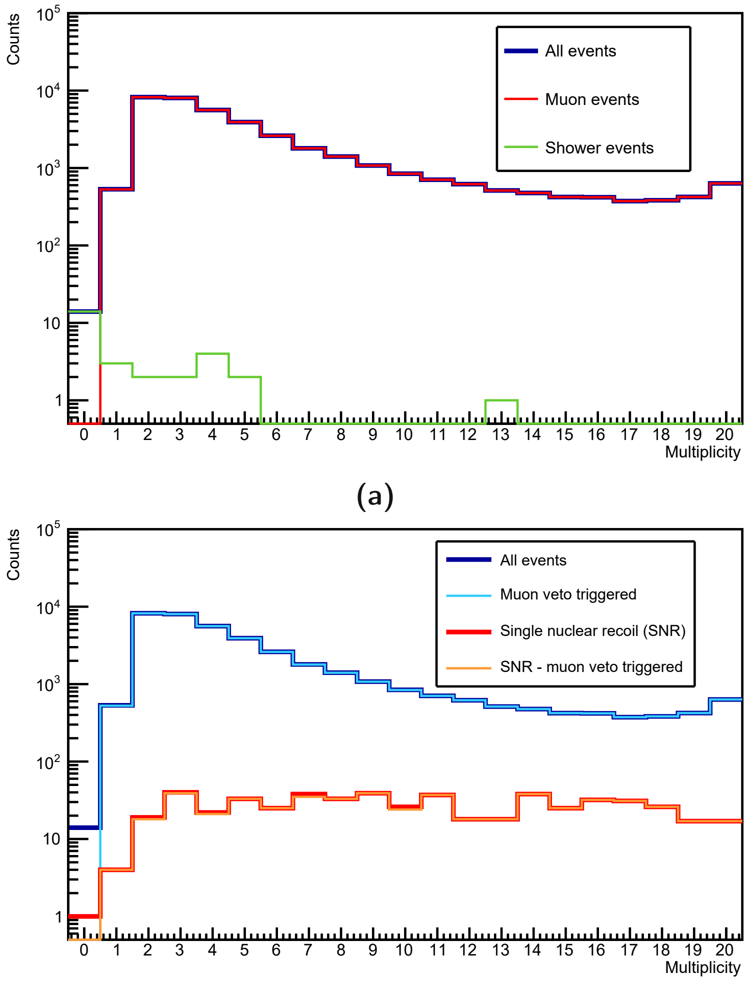

(a)

(b)

Figure 5.45.: Simulated muon veto panel multiplicity for events in the cosmogenic background simulation, in which an energy deposition is recorded in one of the cryodetectors in coincidence with the muon veto. (a) shows events are colored in red if a muon is traversing at least one panel, while all other events are colored in green. (b) highlights the events tagged and vetoed assuming the muon veto trigger conditions detailed in the text.

deposition in a muon panel or do not fulfill the trigger condition. These events thus cannot be vetoed and pose an irreducible background.

In Table 5.24, the respective numbers corresponding to the altered trigger conditions are summarized. Furthermore, the number of surviving events in the ROI of detector A is assessed. For the previously discussed medium trigger condition, only two SNR events are not vetoed in this region in the simulation of $1.78 \cdot 10^8$ incident muons. While the statistics is very low, this corresponds to a reduction of SNR events by almost 99 %,

Table 5.24.: SNR events obtained in the cryodetectors during the cosmogenic background simulation not tagged by the muon veto, based on different trigger conditions. These events would pose a dangerous, irreducible nuclear recoil background. 1σ Poissonian errors and 90% upper limits are given.

Single Panel	Surviving SNR events (kg yr)$^{-1}$	
Trigger Threshold	full energy range	ROI
0 MeV	$(1.8 \pm 1.8) \cdot 10^{-2}$	$< 4.2 \cdot 10^{-2}$
2 MeV	$(1.6 \pm 0.5) \cdot 10^{-1}$	$(3.7 \pm 2.6) \cdot 10^{-2}$
4 MeV	$(2.2 \pm 0.6) \cdot 10^{-1}$	$(5.5 \pm 3.2) \cdot 10^{-2}$

proving a very efficient mitigation of the muon-induced background rate. Normalized to the simulated exposure, this corresponds to a surviving nuclear recoil background rate of roughly $(3.7 \pm 2.6) \cdot 10^{-2}$ events per kg·yr. In the low and high trigger conditions, zero and three SNR events survive, respectively. As all the conditions yield rates in the ROI below 10^{-1} per kg·yr, the uncertainty on the actual trigger threshold energy does not significantly influence the statement on the efficiency of the veto and the summarizing conclusions drawn in the following sections.

5.5.4 Total Neutron Background

Before moving to a combined analysis of the ambient radiogenic, internal radiogenic and cosmogenic neutron background simulation, focusing on the effect of the individual shielding layers, an overview of the background contributions in the ROI of detector A are presented and a summary on the total estimated single nuclear recoil rate is provided.

The rates obtained from the simulations described in the previous sections are presented in Table 5.25. All of them are well below a single count per kg·yr and the largest contributions from the lead shielding and the ambient neutrons are mostly based on conservative assumptions. The screening results of lead used in the course of the study are upper limits on the contamination levels. And in the case of ambient neutrons, the starting positions especially of the neutrons entering the cryostat from the top have conservatively been chosen. Hence, from all these known neutron background sources, usually not a single nuclear recoil event is expected to be observed in typical exposures of a few kg·d taken with CRESST-III detectors. The probability to observe at least one SNR event within a collected exposure t can be calculated using the integral rate R via

$$p(t) = 1 - e^{-R \cdot t} \quad . \tag{5.16}$$

With an exposure of $t = 3.64$ kg·d after cuts [4] in the official detector A data set and

Table 5.25.: Comparison of single nuclear recoil (SNR) rates in the ROI of detector A, i.e. nuclear recoils between 0.03 – 16 keV without a coincident energy deposition in any other detector, due to the various neutron background sources.

Neutron origin		SNR rate in ROI (kg yr)$^{-1}$
Internal	Inner PE	$(1.8 \pm 0.1) \cdot 10^{-2}$
	Cu	$(6.8 \pm 0.1) \cdot 10^{-3}$
	Pb	$(1.5 \pm 0.1) \cdot 10^{-1}$
	Outer PE	$(4.0 \pm 0.3) \cdot 10^{-3}$
Cosmogenic		3.2 ± 0.2 | with veto: $(3.7 \pm 2.6) \cdot 10^{-2}$
Ambient		$(2.2 \pm 0.4) \cdot 10^{-1}$

an integral SNR rate in the ROI of $R = 4.36 \cdot 10^{-1}$ (kg yr)$^{-1}$, this probability would roughly be 0.4 %.

5.5.5 Impact of the Passive Shields

In the following, the properties of neutrons entering the various shielding layers used in the CRESST setup are assessed. The muon veto is not considered in this case, such that true neutron data are examined. For the purpose of this study, a so-called "parallel world" (see description in Section 4.1.4) additional to the usual world volume used for tracking in Geant4 is implemented. The specific "scorers" in this parallel geometry are set to correspond to the shielding layers plus a few additional volumes in the cryostat. At these specified stages, data about neutron fluxes and energies are stored during the simulation. Specifically, data are obtained for neutrons entering the outer polyethylene shielding, the lead shielding, the copper shielding, the cold box (essentially corresponding to the surface of the inner polyethylene shielding), the detector carousel and, finally, the target crystal of detector A.

In Figure 5.46, the neutron flux entering these different stages and originating from the various sources discussed in the previous sections is presented. It is worth mentioning again that the experimental geometry in the simulation is placed in an empty hall surrounded by rock, such that the neutrons originating from any shielding layer can still lead to a neutron flux entering the outmost one if they are backscattered from the rock. While the ambient neutron flux entering the outer PE shielding is by far the largest, other sources hence still show non-vanishing rates at this stage. The same is true for any further shielding layer, which can lead to backscattering of neutrons towards the more intrinsic volumes. Typically, the flux of each individual neutron origin peaks at the surface of the volume it encloses. For example, the neutrons originating from the

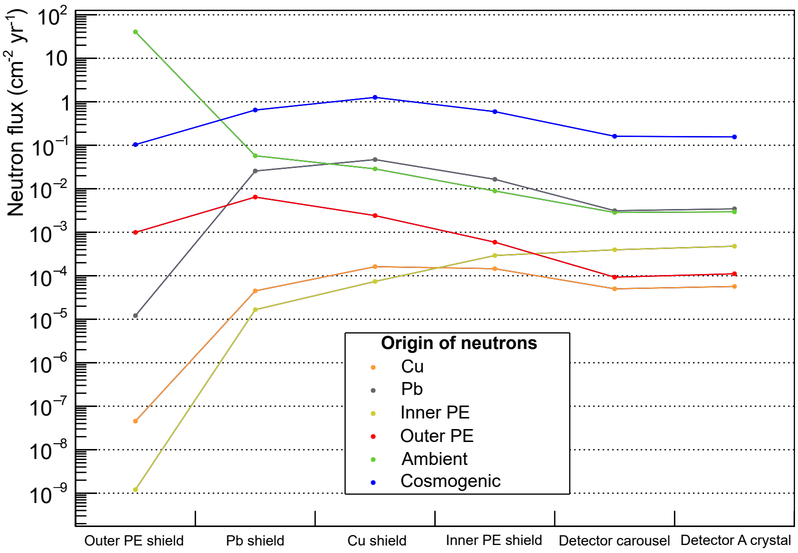

Figure 5.46.: Neutron flux entering various stages in the experimental setup of CRESST. The colored lines correspond to the assessed neutron sources as detailed in the legend of the plot. From left to right, different surfaces are considered in the study, starting from the outermost polyethylene volume to the more intrinsic shielding layers and the detector crystal.

outer PE shielding have the largest flux at the surface of the lead shielding, and the ones originating from the lead shielding have the largest flux at the stage of the copper shielding. The neutrons then typically get scattered and mitigated, such that their number is reduced at the further levels.

The most efficient reduction is happening in low-Z materials. This is proven by the large mitigation attained for ambient neutrons entering the lead shielding after traversing the outer polyethylene. Similarly, a comparatively large reduction of all the neutron sources can be obtained between the flux entering the inner PE shield and the one entering the carousel. In this latter case, besides looking at the absolute reduction displayed in the graphic, the relative thickness of the inner polyethylene layer compared to copper and lead has to be considered. While the inner PE shield is much thinner, it still leads to similar or even larger absolute attenuation compared to the high-Z shields.

The presented arguments are especially true for the ambient and internal radiogenic neutron contributions. When considering the cosmogenic neutrons, the discussion has to be extended by the fact that the neutrons in this case are not exclusively originating from a specific material or location, but that cosmogenic neutrons may be produced in all the materials of the experimental setup and the surrounding rock. As identifiable from Figure 5.46, however, the flux seems to be dominated by neutrons created in the experimental setup. Furthermore, in line with the discussion in Section 3.1.2, the muon-induced neutron production is most efficient in high-A materials, such that a peak in the flux after the lead shielding, i.e. entering the copper shield, can be obtained.

Overall, the neutron flux entering the detector has its by far largest contribution from muon-induced neutrons. The further ranking according to the share of the flux is very similar to the ranking of the estimated background rates detailed in Table 5.25, when not considering the muon veto in the case of cosmogenic neutrons. For a detailed discussion of the neutron flux and of those neutrons that are able to contribute to the dangerous nuclear recoil background via elastic scattering, however, the energy of the neutrons additionally has to be assessed.

In Figure 5.47, the neutron energy spectra at each of the stages are hence displayed. Starting from the origin of the neutrons until reaching the detectors, scattering processes lead to moderation and thus to a decrease in the mean energy. This can best be observed from the spectrum of ambient neutrons, which start outside the experimental setup and have to traverse all the shielding layers to reach the detectors. Here, in the corresponding green line, a clear reduction of the flux and shift to lower energies can be seen. Of course, the same inference is true for the other neutron sources, which are already located further inside the experimental setup. The radiogenic neutrons originating from the inner polyethylene shielding are subject to the least moderation and thus, their energies at the location of the detector crystal extend to larger values. The spectrum governs the range of potential maximum nuclear recoil energies. Hence, the flux reaching the detector and the nuclear recoil rate in the ROI do not necessarily have a one-to-one correspondence. Compared to the ambient and internal radiogenic neutrons, the muon-induced ones in general feature larger incident energies and hence a harder spectrum reaching the detectors. While the spectrum is only shown up to 10 MeV in the figures, their energies can extend to the GeV range. Higher neutron energies in principle enhance the chance of an energy deposition above threshold, but they also increase the chance of energy depositions well above the ROI used in the analysis of the detector.

In general, the neutron flux and background rate is low in comparison to the typical exposure time during data taking, potentially with the exception of muon-induced neutrons. However, these can be efficiently vetoed as discussed in the previous section. Thus, the neutron flux and background rate in CRESST-III is found to be on a negligible level. If large exposures collected in future stages of the experiment may induce a re-thinking about improvements of the setup with respect to the nuclear recoil background, however, some advice can be given. In a first step, a new screening measurement of lead would be necessary to evaluate its contribution more precisely. In case the contamination level stays the same, the simulation predicts that the lead shielding poses the largest contribution to the internal radiogenic background and furthermore leads to the biggest share in muon-induced neutrons. To reduce the neutron-induced nuclear recoil rate in this hypothetical scenario, a potential replacement of the lead shielding

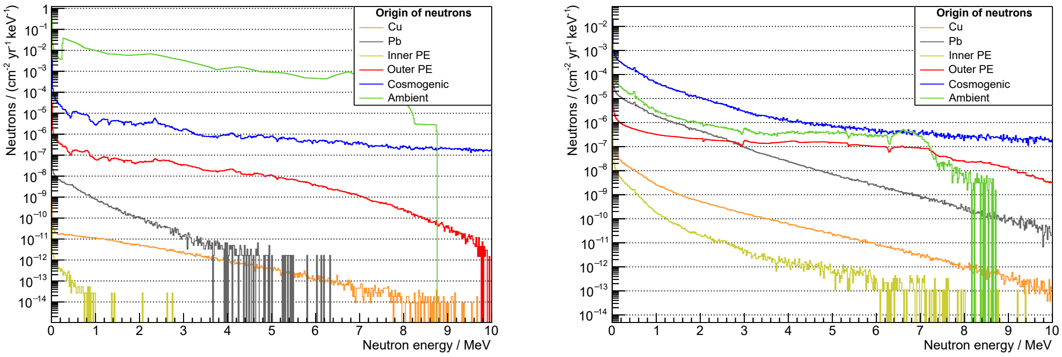

(a) Outer PE shield

(b) Pb shield

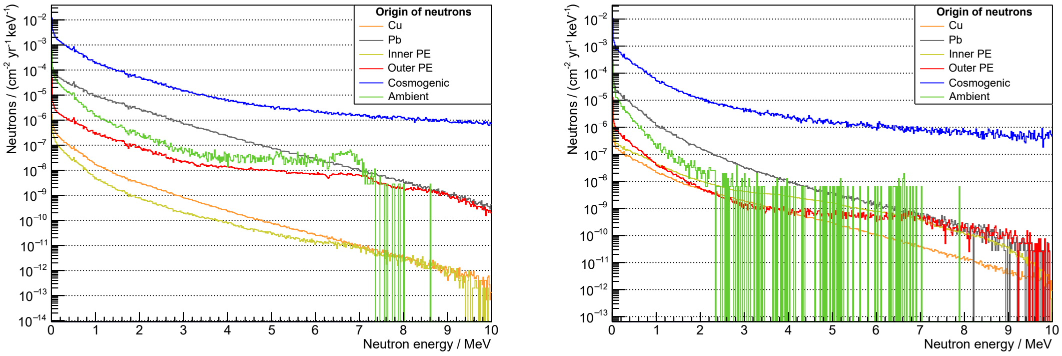

(c) Cu shield

(d) Inner PE shield

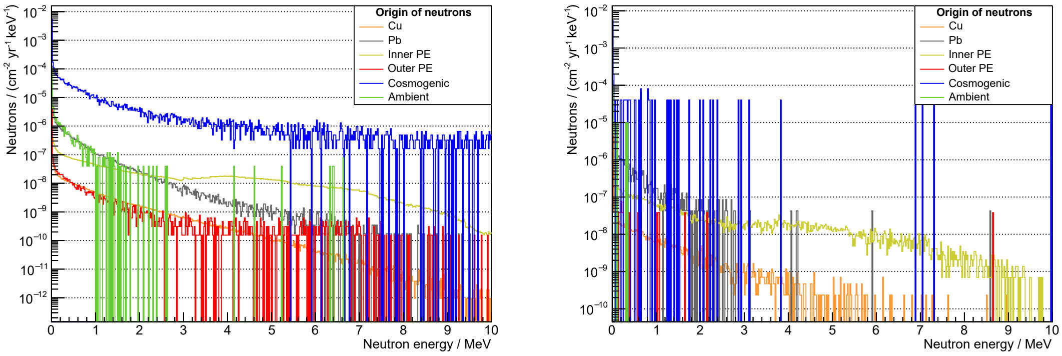

(e) Detector carousel

(f) Detector A crystal

Figure 5.47.: Neutron energy spectrum at the different stages in the experimental setup. The same stages as in the previous neutron flux analysis are considered. Therefore, the integral over the energy for each neutron source corresponds to the flux displayed in Figure 5.46.

would then have to be considered. If, on the other hand, lead is found to contribute less to the radiogenic background than estimated, ambient radiogenic neutrons would dominate the total rate. As especially those entering the cryostat from the top are leading to a large share of the respective rate, an additional polyethylene hat above the cryostat could be considered. Of course, any potential change in the setup would have to be additionally evaluated with respect to the electromagnetic background, which at very low energies leaks into the nuclear recoil bands and hence dominates the overall background in this energy range. The most dangerous nuclear recoil background would thus be the one above the energy range where the bands start overlapping. A detailed study of this combined background model could be the topic of a future work, if an overall reassessment of the employed shielding geometry is found to be necessary. In the current state, it can be repeatedly claimed that the neutron-induced nuclear recoil background is on a negligible level for typical CRESST-III exposures and that hence solely the electromagnetic background is expected to contribute to the obtained signals.

5.6 Conclusion

The neutron simulation studies for CRESST, specifically tuned for the analysis in the context of the low-threshold $CaWO_4$ detector A operated in CRESST-III Run34, offered interesting results that are briefly summarized in the following.

In the neutron calibration study, it was found that a large share of neutrons is thermalized upon reaching the detectors. Thermal neutron capture reactions are thus enhanced and are expected to lead to signatures that could potentially provide new references for the energy calibration of experimental data.

On ^{40}Ca, (n,α) reactions are expected to lead to the production of ^{37}Ar, which decays via EC to ^{37}Cl. The K-shell and L-shell energies correspondingly observable as peaks in the detectors are quoted as roughly 2.8 keV and 0.27 keV.

Even more important may however be the potential nuclear recoil peaks obtained in the W bands in the simulation. These peaks around 100 eV originate from (n,γ) reactions, in which one or many gamma particles with energies summing up to the Q-value of few MeV are emitted. If a single gamma particle is emitted, the nucleus undergoes a recoil of defined energy, that may potentially be observed. While Geant4 does not treat these processes correctly, analytical calculations can be employed to show that the capture peak on ^{182}W around 112.4 eV is expected to be the most prominent one by far. A likelihood-based peak search in the real neutron calibration data of detector A lead to the striking result that a peak at an energy close to the expected value is found with a significance of more than 99.9 %. Further cross-checks with additional neutron calibration measurements in the future are necessary to test the results. However, in case the capture peak is indeed observable in the data, the neutron calibration can give an essential contribution to the energy calibration at lowest recoil energies. Especially the nature of the peaks, originating from nuclear recoils, is highly relevant for determining the exact energy scale of similar signals expected from DM-nucleus scattering.

As a second step, a neutron background model for CRESST-III was developed. Ambient and internal radiogenic as well as cosmogenic neutrons were simulated in the whole experimental setup. Without an active muon veto, the cosmogenic background rate is found to be at least an order of magnitude larger than the rate due to any other neutron background component. Hence, the muon veto was implemented and studied in detail in the simulations and compared to the measurement. Removing events in the cryodetectors that are in coincidence with a muon veto trigger, the simulated efficiency of the veto is found to be close to 99 %. As a result, the muon-induced neutron background rate is reduced below the background rate expected from ambient and internal radiogenic neutrons. Ambient neutrons together with neutrons originating from lead, according to the upper limits on its contamination levels, are then constituting the largest share of single nuclear recoils in the detectors. However, the overall rate is assessed with less than 1 count / (kg·yr) and thus negligible during typical CRESST-III exposures of a few kg·d, not affecting the search for DM. It can furthermore be deduced from this estimated count rate, that neutrons, originating from known sources, are excluded as the origin of the low energy excess obtained in CRESST-III data.

While the shielding is hence found to sufficiently reduce the neutron-induced nuclear recoil rate, the neutron flux at various stages in the shielding arrangement is additionally evaluated to assess the strengths and weaknesses of various shielding layers. Based on the results of this study, possibilities to even further increase the neutron attenuation power of CRESST's passive shielding were formulated.

6 Shielding Design for COSINUS

In this chapter, the COSINUS (Cryogenic Observatory for SIgnatures seen in Next-generation Underground Searches) [6] experiment and corresponding simulation studies are presented. First, the physics motivation, detector concept, prototyping status and basic setup idea are described in Section 6.1. Then, in Section 6.2, the simulations performed to define the optimal passive shielding configuration are presented. Subsequently, the remaining nuclear recoil background is evaluated in a more detailed geometry implementation in Section 6.3, before presenting the optimization of an active muon veto system in Section 6.4. Finally, the results and implications of the simulation studies are concluded in Section 6.5 and a brief outlook on the future tasks following up on this principal simulation campaign is given.

6.1 The COSINUS Experiment

The COSINUS experiment aims to probe dark matter using cryogenic NaI detectors based on the detector technology developed within CRESST over the past decades, with the goal of cross-checking the long-standing DAMA/LIBRA [7] results. In the following subsections, the motivation behind this objective and the strategy of realization are explained.

6.1.1 Potential DM Signals in NaI

Uniquely among the various direct detection experiments, DAMA/LIBRA [7] is measuring an annual modulation signal (cf. Section 2.6) compatible with the phase and period expected from DM particles in our galactic halo [168]. Located at the LNGS, the experiment is taking data since 1995, counting in its predecessor DAMA/NaI (1995-2002) [169]. DAMA/LIBRA itself, in its various phases, has collected data since 2003 and is still operating. Over all the analyzed annual cycles, the results presented by the collaboration feature the modulation signature, as shown in Figure 6.1. The latest results published by the collaboration yield a total statistical significance of the modulation of $13.7\,\sigma$ [170] in the region between 2 and 6 keV_{ee} (i.e. electron equivalent). Intriguingly, no other experiment has seen a similar signal yet. In fact, many experiments

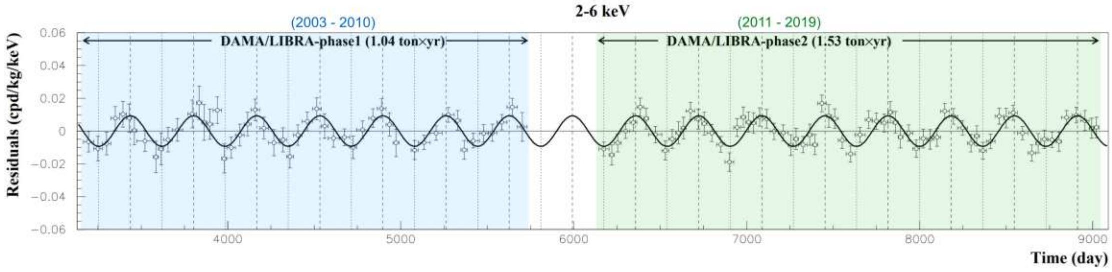

Figure 6.1.: Annual modulation signal of the DAMA/LIBRA experiment in the 2-6 $\mathrm{keV_{ee}}$ energy range, taken and adapted from [170].

exclude the DAMA findings in the so-called standard scenario, in which the standard halo model (cf. Section 2.5.3) as well as spin-indepedent elastic DM-nucleus scattering are assumed [3]. However, these excluding results are obtained with detectors made of different target materials[1]. Hence, there are two major issues in these comparisons. First, the interaction with the target nucleus may be material-dependent, such that a model-independent cross-check is only possible using the same target material, i.e. NaI. Second, an exclusion in the standard scenario may not necessarily yield an exclusion in any other potential scenario, i.e. in the case of a non-standard interaction mechanism, a non-standard DM halo, or a combination of both.

A further complication in the standard scenario comparison comes into play when looking at the detection concept of DAMA/LIBRA. The measured signal is the scintillation light emitted by NaI following a particle interaction and collected by a PMT connected to the target crystal. This single-channel signal does not allow for particle identification on an event-by-event basis. Thus, one cannot determine, if a signal was induced by an electron recoil or a nuclear recoil. However, the light output for the same amount of total deposited energy is different in both cases. The scintillation light emitted following a nuclear recoil is quenched with respect to the light emitted following an electron recoil (see e.g. [98] and references therein), as described in Section 3.2. For the energy calibration of the obtained signal amplitudes, known gamma peaks are used, such that the resulting energy scale is obtained in electron-equivalent units. Hence, if the measured signals shall be interpreted in the standard scenario assuming nuclear recoils, the scale has to be converted according to the quenching factors (QFs). DAMA/LIBRA uses constant QFs of 0.3 for Na and 0.09 for I [169], meaning that a 1 $\mathrm{keV_{ee}}$ signal may correspond to a 3.3 $\mathrm{keV_{nr}}$ recoil on Na or a 11.1 $\mathrm{keV_{nr}}$ recoil on I.

However, quenching factors are in general energy-dependent [172] and in fact, large spreads in QF measurements of NaI crystals are reported from various groups. Shown in Figure 6.2 are QFs obtained by collaborators of the COSINE-100 [98] experiment, together with additional independent measurements. Also ANAIS-112 has recently

---

[1] Except for COSINE-100, which puts strong constraints on the DAMA/LIBRA results in the standard scenario using NaI(Tl) crystals [171].

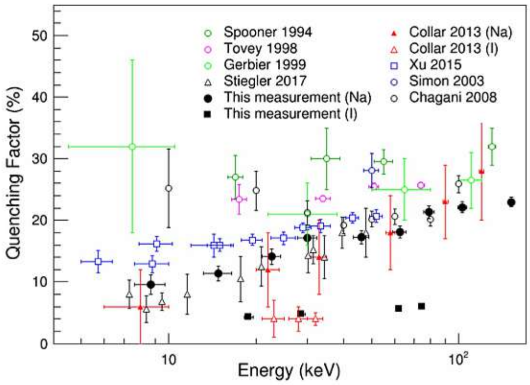

Figure 6.2.: Quenching factors measured for NaI by various groups, taken from [98].

published new QF results [99]. As can be seen from Figure 6.2, the quenching factors and their energy-dependence remain uncertain or are very much dependent on the crystal or the measurement procedure. A possible factor of influence might be the Tl content in doped NaI(Tl) crystals. Indeed, pure NaI does not scintillate at room temperature and hence has to be doped with Tl for usage in DAMA/LIBRA, COSINE-100 and ANAIS-112. To test the potential hypothesis of Tl dependence, COSINUS is at the time of writing this thesis analyzing QF measurements performed with different crystals of known Tl dopant concentrations. It is worth mentioning at this point, that COSINUS itself will not require Tl doped crystals, as the detectors are operated at mK temperatures. At these low temperatures, pure NaI itself is a scintillator.

COSINE-100 and ANAIS-112, mentioned above, are two of the experiments currently trying to cross-check the DAMA/LIBRA signal with NaI(Tl) detectors, and the only ones already providing results. COSINE-100 is taking data since 2016 and found that in the standard scenario, they can exclude the DAMA/LIBRA result [171, 173]. However, their modulation analysis is inconclusive and the data are currently compatible both with no and with an annual modulation [174, 175]. ANAIS-112, on the other hand, recently published its latest analysis [176] showing an incompatibility with the DAMA/LIBRA modulation with a sensitivity of 2.5 σ, expecting to reach 3 σ within two more years of data taking. While this is a model-independent comparison, it slightly suffers from the discussed QF uncertainties. With SABRE [177] and PICO-LON [178], there are two further NaI-based experiments currently being planned.

COSINUS joins the effort of testing DAMA/LIBRA with a competetive time-scale and unique features, posing a complementary approach to the experiments currently taking data. All previously listed experiments measure light-only like DAMA/LIBRA and perform annual modulation searches. COSINUS, on the other hand, is developing cryogenic NaI detectors with a dual-channel readout of heat and light, providing event-by-event particle discrimination and in-situ QF determination. With this technique, an analysis of the total rate will be performed in the first stage of the experiment to test the DAMA/LIBRA modulation.

6.1.2 Cryogenic NaI Detectors

In 2016, COSINUS was started as an R&D project, applying cryogenic detector technologies developed within CRESST [5] to NaI as a target material. The operation of NaI as a scintillating cryogenic calorimeter, operated at milli-Kelvin temperatures, has some unique advantages compared to scintillation-only detectors. With simultaneous readout of phonon and light signal using W-TESs and SQUID circuits (cf. description in Section 5.1.1), particle identification on an event-by-event basis is possible. The reason for this is that the phonon signal provides a robust measurement of the total energy deposited, almost independent of the type of interaction [6], while the light signal, as discussed in the previous section, is strongly particle dependent.

This has various implications, which shall be discussed based on Figure 6.3 [179], where a simulation of dark matter events, assuming 10 GeV/c^2-WIMPs with a scattering cross section of $2 \cdot 10^{-4}$ pb that are compatible with a DM interpretation of the DAMA/LIBRA modulation [73], is presented (red events). Additionally, background levels quoted by DAMA/LIBRA are assumed (black events). The plot shows the simulated events in the light yield (LY)-energy plane, where the LY is again the signal in the light channel divided by the one in the phonon channel and normalized to LY = 1 for β/γ events. The advantages of the applied detector technology are hence the following.

Nuclear recoils and electron recoils can be displayed on the same energy scale using the phonon signal, hence no conversions are necessary. The respective bands in Figure 6.3 are painted in black for electron recoils, blue for Na recoils and green for I recoils. The separation of the different interaction bands at the same phonon energy can be used to intrinsically determine the QFs for nuclear recoils, e.g. based on neutron calibration data. Furthermore, assuming DM-nucleus scattering, the attained data can be cleaned from the dominant background caused by electrons and gammas. The larger the separation of the bands, the better the discrimination of background events. Additionally in Figure 6.3, the regions that DAMA/LIBRA would be sensitive to, considering results attained in the 2-6 keV$_{\text{ee}}$ energy range, are roughly indicated. This yields a further advantage of measuring the phonon signal with a low threshold. If COSINUS reaches its design goal of a nuclear recoil threshold in the order of 1 keV, it will be sensitive to a much larger portion of a hypothetical dark matter signal.

However, the usage and operation of NaI as a cryogenic detector is very difficile, as NaI is hygroscopic and fragile. Handling of these crystals and implementing a cryogenic readout to them while preserving their quality has brought the need for an extended R&D phase. The W-TES, that is used to measure the phonon signal, cannot be evaporated directly onto the crystal surface due to the material properties. The potential layouts of a COSINUS detector and results of prototype measurements are hence discussed in the following paragraphs, describing the baseline as well as the recently developed remoTES [180] design.

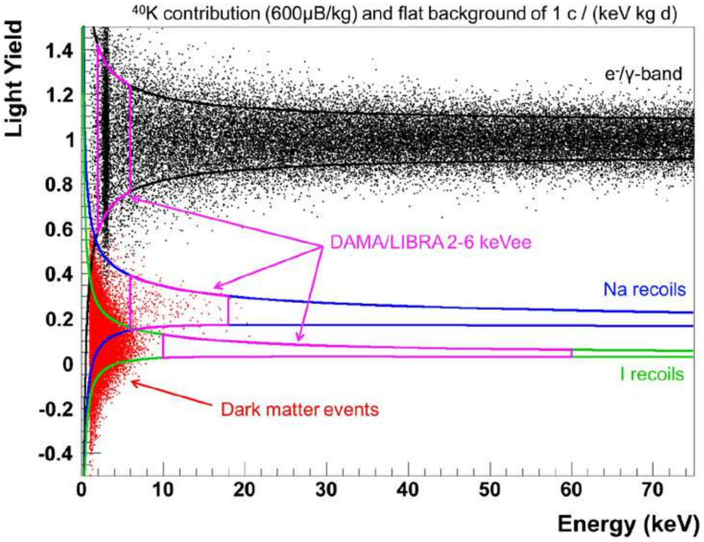

Figure 6.3.: Mock data of a simulated COSINUS measurement, assuming quenching factors according to Ref. [172] and 10 GeV/c^2-WIMPs with a scattering cross section of $2 \cdot 10^{-4}$ pb compatible with a DM interpretation of the DAMA/LIBRA modulation [73]. Black events are β/γ-background in accordance with contamination levels quoted by DAMA/LIBRA, red events are DM-nucleus scattering. Blue and green regions are 80% bands for Na and I recoils. The magenta regions correspond to the energy range of 2-6 keV$_{\mathrm{ee}}$ tested by DAMA/LIBRA. Plot taken from [179].

Baseline Design

In Figure 6.4a, the baseline design of a COSINUS detector is schematically depicted. As the temperature sensor cannot be directly evaporated onto the crystal surface, a carrier crystal is introduced. This wafer-like crystal of roughly 40 mm diameter and 1-2 mm thickness is made of a different material (e.g. $CdWO_4$) and interfaced to the NaI absorber via silicon oil or epoxy resin. The phonons induced in the NaI crystal are then measured via a TES evaporated onto the carrier crystal. Size and shape of the NaI crystal in this detector design have not been fixed. Prototypes of cubic, cylindrical and hexagonal shape with masses of about 50-100 g have been tested. For light collection, a Si beaker of about 500 µm wall thickness and 40 mm diameter and height surrounds the absorber. The signal readout is provided via a second TES. This detector design is described in detail in various publications on prototype measurements [179, 181, 182].

Exemplary, the results of the second prototype detector, as presented in Ref. [179], are briefly discussed. Using a cubic 20x20x30 mm^3 NaI target crystal the spectrum shown in Figure 6.5 was obtained. Compared to Figure 6.3, besides the 3.2 keV line due to intrinsic ^{40}K, additional event clusters at ~60 keV and ~30 keV can be seen due to a ^{241}Am source placed next to the cryostat. The band around LY = 0 is formed by events

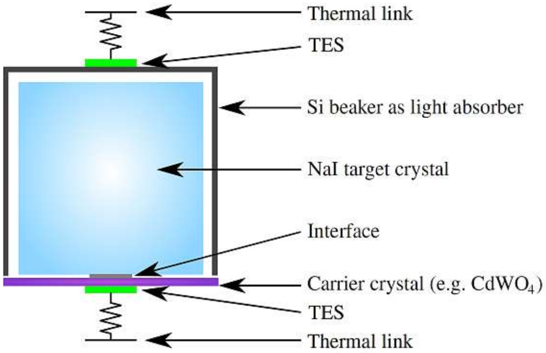

(a)

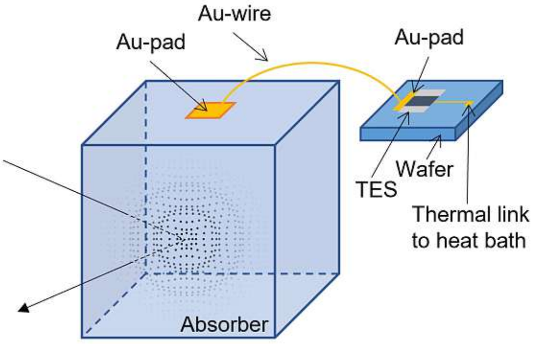

(b)

Figure 6.4.: Schematic of the two COSINUS detector designs. In (a), the baseline design is shown. It uses a NaI crystal glued to a carrier crystal equipped with a TES for phonon signal readout. The plot is taken from [179]. In (b), the remoTES detector design is presented. Here, the NaI crystal is equipped with a gold pad directly bonded to the TES on a separate wafer via a gold bond. The plot is taken from [180].

depositing energy directly in the $CdWO_4$ carrier crystal.

RemoTES Design

The recently developed remoTES design is based on a description in Ref. [183], suggesting a concept avoiding some of the downsides of the baseline design, in which phonons first have to propagate through the interfaces between absorber, glue and carrier before being detected by the TES. These interfaces may lead to large signal losses, specifically for COSINUS due to the acoustic mismatch between the NaI absorber and the $CdWO_4$ carrier crystal. The respective signal losses can possibly be prevented using the remoTES design [180]. As depicted in Figure 6.4b, the absorber in this case is directly coupled to the TES, sitting on a separate wafer crystal, via a gold pad and bond wire. A first proof-of-principle measurement of this design using Si and TeO_2

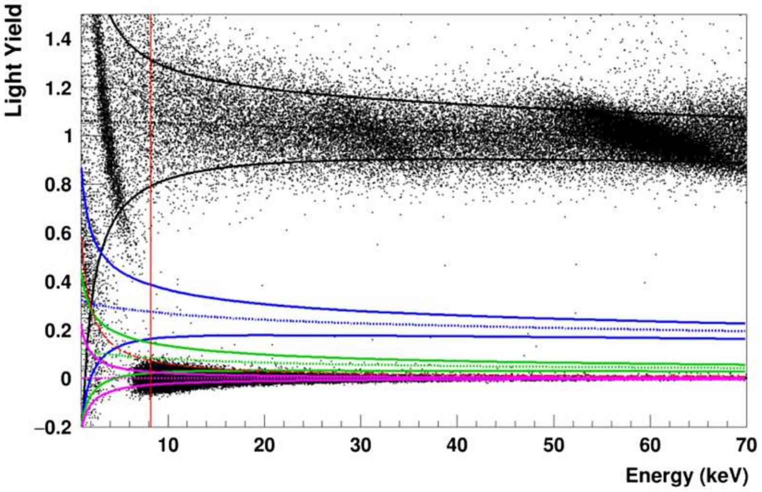

Figure 6.5.: ^{241}Am calibration data obtained with the second prototype detector of COSINUS. Plot taken from [179].

absorbers, achieving convenient resolutions and thresholds, has lately been presented by COSINUS in Ref. [180]. Follow-up measurements using NaI are being analyzed at the time of writing this thesis.

6.1.3 Physics Potential

The main goal of the first phase of the COSINUS experiment, called COSINUS-1π, is to test if the origin of the DAMA/LIBRA modulation could be nuclear recoils. In contrast to other experiments trying to cross-check the DAMA/LIBRA signal with a modulation search, COSINUS-1π will provide a measurement of the total rate and energy spectrum of nuclear recoils, exploiting its particle-identification capability. In simple terms, if this rate is lower than the modulation amplitude reported by DAMA/LIBRA, a nuclear recoil origin of the modulation can be excluded. This argument can solely be based on the evident statement that, in each energy bin, the modulation amplitude can never exceed the mean rate.

In Ref. [184], the required background rate and exposure to attain conclusive results is discussed. The looser we set the bounds on the tested model, the lower the required background rate and the higher the necessary exposure. COSINUS is aiming for a model-independent cross-check, meaning that the result holds for any type of dark matter halo and any interaction mechanism, except demanding that dark matter particles interact with the nuclei of the target crystal. With the calculations performed in Ref. [184] for the DAMA/LIBRA data featuring a threshold of 2 keV_{ee}, the requirements for COSINUS are a nuclear recoil threshold of about 1.8 keV and a bound of $10^{-2}\,(\text{kg}\cdot\text{d})^{-1}$ on the rate of nuclear recoils. These results may have to be updated slightly for the lowered threshold in DAMA/LIBRA. However, without a large change in the modulation amplitude, the requirement on the observed rate should be less affected. Given the required nuclear recoil threshold and assuming a radiopurity of our crystals similar to that of the crystals used in DAMA/LIBRA, the estimated exposure, calculated in the same paper, to achieve a model-independent cross-check is approximately 1000 kg·d. Depending on the final target mass, this may be achieved within 1.5-3 years of data taking.

Depending on the results obtained with COSINUS-1π and by competitors in the field, in a second phase of the experiment, COSINUS-2π, the target mass could potentially be scaled up to perform a modulation search in the nuclear recoil or the electron recoil channels.

6.1.4 Basic Design of the COSINUS Setup

To achieve the required low background rate, one has to take into account various aspects. According to the background models of other NaI-based experiments, a major background component usually comes from the crystals themselves [185–188]. The dominating contributions are often the following: ^{3}H originating from cosmogenic activation, ^{210}Pb in the bulk and on the surface originating from the natural ^{238}U decay chain and ^{222}Rn emanation and deposition on the crystal surfaces, and ^{40}K originating from contamination in the powder used for crystal growth. These contributions have to be considered when selecting the crystal powder and deciding on how and where to store the final crystals. However, the studies conducted for this thesis focus on additional external background components, discussed in detail in Chapter 3, which ask for a dedicated decision on the location of the experimental site and the layout of passive and active shielding around the detectors.

In planning the experimental setup, it should be recalled that our sought-for signal are nuclear recoils and that COSINUS can identify the type of recoil on an event-by-event basis. Thus, the focus of the shielding design has to be on minimizing neutron-induced nuclear recoil events that could mimic a signal. However, at the same time, especially at low energies, the β/γ background has to be carefully examined, as it can partly leak into the nuclear recoil band. The total leakage depends on several factors, among which are the contamination level of employed materials, the band width (resolution of the light channel and Poissonian distribution of the scintillation photon production), and the quenching factor values. This can readily be understood looking again at the LY plot presented in Figure 6.3. The narrower the indicated recoil bands and the larger their separation, the smaller the potential overlap at low energies. Assuming quenching factors according to Ref. [172] and setting the acceptance region to below the 90% (50%) upper confidence interval of the Na band, a leakage from ^{40}K events of 2.3% (0.4%) is estimated [179]. According to personal communication, the leakage from the flat electron recoil background in the 1-40 keV range is furthermore estimated as 0.4% (0.1%). The main leakage will occur at low energies, while at energies higher than a few

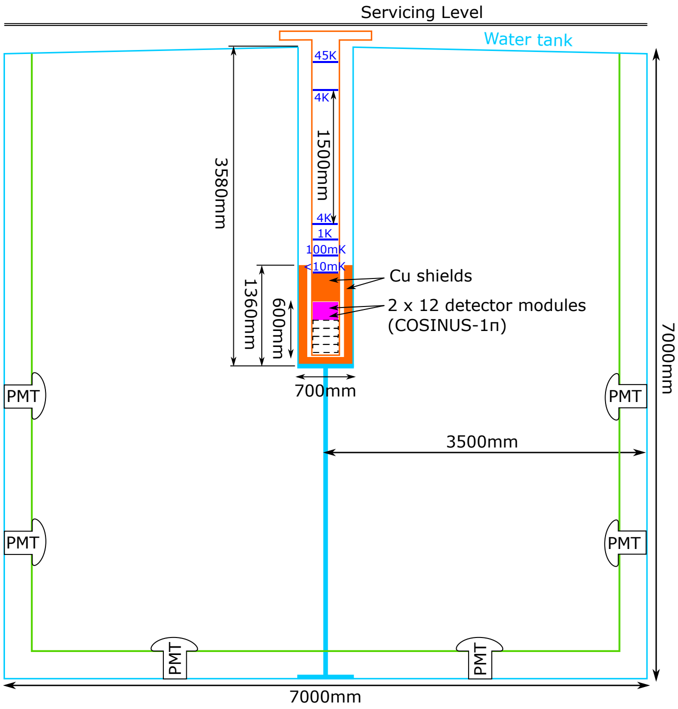

Figure 6.6.: Sketch of the COSINUS water tank with the cryostat in the dry-well. Stainless steel parts are colored in light blue, copper parts in orange, the experimental volume needed for COSINUS-1π and -2π in solid magenta and dashed black, respectively, and the temperature stages of the cryostat in dark blue. A light-tight curtain is indicated at the water tank walls creating a passive layer outside the active Cherenkov veto region. This schematic is based on the favored shielding design according to the results presented in Section 6.5.

keV, COSINUS is essentially background-free in the absence of a neutron background. According to Figure 6.3, a large part of the nuclear recoil range corresponding to 2-6 keV_{ee} lies already in this background-free regime.

The strategy in shielding against external background is the following. To reduce the amount of muons and hence of muon-induced events, the COSINUS setup will be located underground in hall B of LNGS, providing an average vertical rock overburden of roughly 1400 m (3600 m.w.e.) [107]. For the shielding around the detectors, a typical approach in many experiments is using subsequent layers of low-Z, high-Z and again low-Z materials. An example is CRESST (cf. Figure 5.4 in Section 5.1.2), using an outer polyethylene layer to moderate ambient neutrons, lead to shield ambient gammas, copper to deal with gammas originating from the ^{210}Pb isotope contained in lead, and an inner polyethylene layer mitigating neutrons originating from interactions in the shielding materials. To deal with events induced by the residual muon flux at LNGS, a muon veto is furthermore crucial. In COSINUS, the usage of a large steel tank filled with ultra-pure water shall fulfill multiple of these purposes. It provides a passive shielding against ambient radiation as well as, instrumented with PMTs, an active veto against muons. By tuning the size of the water volume, the requirements on additional shielding layers around the detectors can be assessed. Figure 6.6 shows an early sketch of the conceptual shielding design, based on results presented in the subsequent sections.

At the time of writing this thesis, the construction of the water tank and the auxiliary buildings at LNGS has started. The dimensions of the water tank and of the additional shielding layer around the cryostat, as well as the planned arrangement of the muon veto system are based on the simulation studies conducted in the course of this thesis and presented in the following.

6.2 Optimization of the Passive Shielding

In this section, the simulation study performed for laying ground for the conceptual design of the passive shielding of COSINUS are described. Background simulations in a simplified geometry are conducted to estimate the optimal configuration of water tank and inner shielding dimensions. The respective section is based on and extends the publication on the passive shielding design study [189].

All the Monte Carlo (MC) simulations performed in this as well as in the subsequent sections are based on Geant4 (version 10.2.3) [115–117], SOURCES [122, 123] and MUSUN [127], and most of the analysis is done in Root [121]. As the original SOURCES 4A [122] code only treats (α,n) reactions up to α-energies of 6.5 MeV, a modified version with extended cross section data up to 10 MeV [139–141] was employed. In this work, the obtained extended libraries were integrated in the SOURCES 4C [123] code and used to attain the internal radiogenic neutron spectra and rates. These approaches are similar to those described for CRESST in Sections 5.2.1 and 5.2.2.

For the Geant4-based simulations, an autonomous version has been branched off from ImpCRESST5.7.0. The ImpCRESST software [118] has originally solely been developed within CRESST, but is in the meanwhile used by CRESST and COSINUS in various applications. In the specific version used for the COSINUS simulation studies presented in this thesis, many drastic changes were applied to the type of data collected during simulation as well as to the entire resulting data structure. These modifications were necessary to reduce the amount of consumed disk space and to attain necessary additional information, especially in the optical photon simulation performed for the Cherenkov muon veto. The type of information stored and used as well as the analysis procedures will be described up to feasible level of detail in the corresponding sections.

Table 6.1.: The options of the COSINUS shielding design tested in Geant4 simulations, using different thicknesses of water, Pb, Cu and PE. In Figure 6.7, the five options are visualized.

	Thickness / cm									
Option	Tank	Water	Dry-well	Inner shielding			Cryostat	Top shielding		
	(steel)		(steel)	(Pb)	(Cu)	(PE)	(Cu)	(Pb)	(Cu)	(PE)
1	1.5	150	0.4	10	15	10	0.8	10	15	10
2	1.5	200	0.4	0	15	10	0.8	0	40	10
3	1.5	200	0.4	0	15	0	0.8	0	40	0
4	1.5	300	0.4	0	8	0	0.8	0	30	0
5	1.5	300	0.4	0	0	0	0.8	0	40	0

6.2.1 Basic Shielding Design

For our primary study on the conceptual shielding design, a simplified geometry of the foreseen water tank and additional shielding layers is used. As an evaluation of all potential sizes and thicknesses of individual shields is impossible, the tests are restricted to five distinct configurations chosen according to educated considerations.

The onion structure consisting of concentric cylinders features the water tank made of steel and entirely filled with water as the outermost layer. In the center of the tank, a thin cylindrical steel structure extends from the top of the tank down below the middle. This excision, the so-called "dry-well", provides a dry central volume inside the water-filled tank. It can host the inner shielding layers and the cryostat, ensuring that the detectors are positioned in the middle of the tank. The inner shielding layers could be made of Pb, Cu and PE, following the typical low-Z/high-Z/low-Z approach, or only use single selected materials. Surrounded by these inner shielding layers, the thermal shields of the cryostat are approximated by a single shield made of Cu with the aggregated thickness. In the bottom part of the cryostat, i.e. in the middle of the tank, the detector volume is located. Above this volume, there will be the mixing chamber of the cryostat, which is not included in our simulation geometry. Between detector volume and mixing chamber, however, additional material layers are used to shield against any particles originating from the top parts of the cryostat or heading towards the detector volume in vertical direction, not traversing the water tank and inner shields. These shields above the detector volume are referred to as "top shielding" in the following. The height of the inner shielding around the cryostat is chosen such that it extends up to the top shielding, to minimize the line of sight between detector volume and surroundings.

The exact measures of the five tested geometries within the simulation are detailed

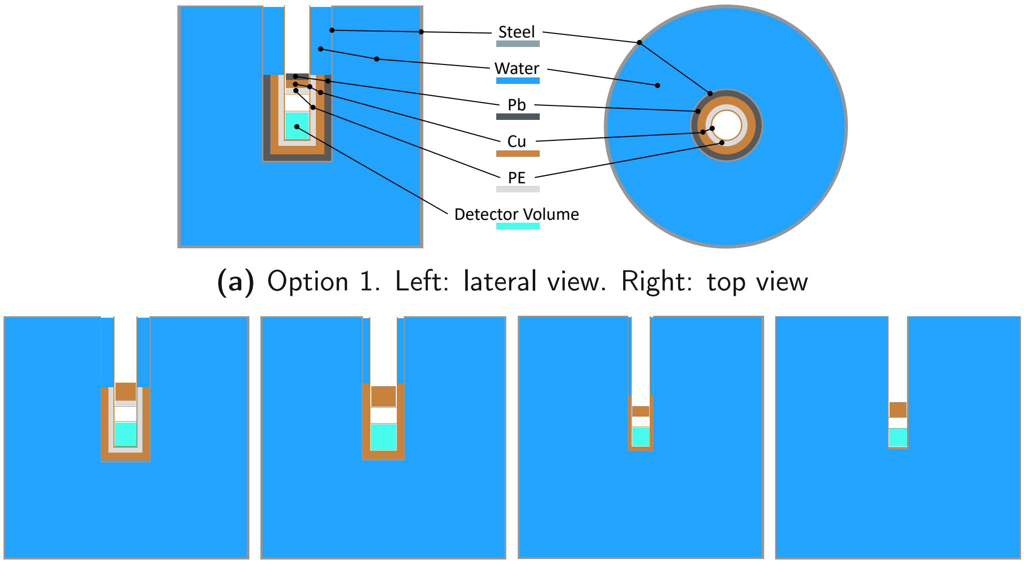

(a) Option 1. Left: lateral view. Right: top view

(b) Option 2. (c) Option 3. (d) Option 4. (e) Option 5.

Figure 6.7.: The five simplified experimental setups tested in the Geant4 simulations. Different materials are indicated via the color scheme defined in (a). Thicknesses of the various layers are detailed in Table 6.1.

in Table 6.1. Furthermore, sketches of them are presented in Figure 6.7. In the following, referring to the various configurations, the term "option N", where N is a number between 1 and 5, according to the naming in Table 6.1 and Figure 6.7, will be used. Option 1 is the basic option discussed above. All the other options omit using Pb, because high-Z materials have an enhanced cross section for muon-induced neutron production and preliminary tests showed that the shielding power of the setup is sufficient without this additional layer, if the water volume is slightly increased. Options 3 and 4 even omit using an innermost PE shield and only employ different thicknesses of the Cu shield and water. Finally, option 5 is the extreme case, in which only the bare cryostat is placed inside the dry-well without any additional inner shields.

Of course, for all the geometries being tested, the maximum available space for the experimental facility of COSINUS at LNGS has to be taken into consideration. In the final design, it has to be possible to lift the entire cryostat out of the dry-well, so that a total height of more than 1.5 times the height of the water tank is required for the entire setup. Based on the dimensions of the LNGS halls, the maximum allowed height of the water tank will thus be approximately 7 m, if accounting for all auxiliary buildings, especially the cleanroom on top of the tank. Some details on the infrastructure at LNGS and preliminary setup drawings in hall B can be found in the conceptual design report of COSINUS [190].

Table 6.2.: Literature values for the activities of main contaminants in the materials considered for the COSINUS shielding geometry. The references quoted in the table always belong to the three columns to their left. In the last column, the neutron yield due to (α, n) and spontaneous fission reactions is quoted, calculated using the SOURCES 4C [123] code with extended libraries [139–141] by assuming secular equilibrium in the natural decay chains.

Material	Activity / (mBq kg^{-1})								Neutron yield / (cm^{-3} s^{-1})
	^{238}U	^{235}U	^{232}Th	Ref.	^{40}K	^{60}Co	^{137}Cs	Ref.	
Stainless steel	< 0.2	–*	< 0.1	[191]	< 5.2	1.9	< 0.6	[192]	$3.0 \cdot 10^{-12}$
Pb	< 0.01	–*	< 0.07	[191]	–	–	–	–	$1.2 \cdot 10^{-13}$
Cu	< 0.065	–*	< 0.002	[160]	< 0.34	0.21	< 0.03	[192]	$6.6 \cdot 10^{-13}$
PE	< 3.8	< 0.37	< 0.14	[193]	0.7	< 0.1	0.06	[193]	$9.4 \cdot 10^{-12}$

*No measured value given, natural abundance assumed [161].

6.2.2 Evaluation of an Optimal Setup via Background Simulations

In the following sections, background simulations performed within the simplified shielding geometry are discussed and assessed with respect to the most prominent background components external to the detectors. To estimate an optimal design of the shielding structure, relative and overall background particle fluxes entering the detector volume are compared.

The main distinction of background particle sources is made between those induced by muons and those induced by radioactive decays. For the latter, a further differentiation is again introduced. Particles created due to radioactive decays in the materials of the experimental setup are referred to via the term "internal", while those originating in the rock and concrete surrounding the laboratory halls are called "ambient".

First, a benchmark is set for the internal radiogenic background fluxes due to neutrons and gammas originating from radioactive contamination in the various materials used for the cryostat, inner shields and dry-well. As at the time of conducting these studies, the exact materials used in our setup were not purchased and screened, the simulations are based on intrinsic contamination levels quoted by other rare event search experiments, as listed in Table 6.2. Comparing the resulting fluxes due to intrinsic contamination in the shielding materials to the surviving ambient particle fluxes, the goal is then to reduce the latter to a subordinate level.

As a further constraint for our shielding design, the background flux of muon-induced neutrons is assessed. If this component dominates the neutron background, an efficient veto system is a necessity. The water tank can be turned into an active veto if instrumented with PMTs and used as a Cherenkov detector. In Section 6.4, the study of the efficiency of such an active veto system, depending on the number, distribution and trigger condition of PMTs used to measure the Cherenkov light created in the water tank, is presented.

The data obtained from the simulation of the described background components is evaluated to assess the shielding option that minimizes the background particle flux.

After choosing the best option according to the results discussed in the following, Section 6.3 describes the implementation of a detailed experimental geometry in the simulation software. Instead of assessing the particle flux, the total neutron background rate in the detectors is then studied to prove that the respective setup can fulfil the background requirements set by COSINUS.

6.2.3 Ambient Radiogenic Neutron Simulation

Ambient neutrons, as discussed previously, are those originating from (α,n) processes and spontaneous fission (s.f.) reactions in the rock and concrete surrounding the underground halls. Similar as in the simulation study for CRESST (cf. Section 5.5.1), the assessment of the ambient neutron flux at LNGS presented in Ref. [159], see Figure 5.28 is used as a starting point.

Water is very efficiently moderating and shielding the ambient neutrons due to its large hydrogen content. For convenience, to increase the statistics in the simulation and attain results up to 1.4 m thickness of the water layer, the simulated geometry is further simplified. Instead of the geometry described in Section 6.2.1 and shown in Figure 6.7, cuboids of 2 m lateral dimension and variable thickness resembling the respective shielding layers are implemented. The particle flux transmitted through all these cuboids is studied. Indeed, for ambient neutrons, it is sufficient to look at the transmission through water by itself.

Neutrons in the respective simulations are started according to the spectrum shown in Figure 5.28 impinging perpendicularly on the center of the water cuboid surface. Each simulation consists of 10^8 events. The thickness of the water layer is increased in increments of 20 cm from one simulation to the next and the amount of simulated events is seen to be sufficient to attain surviving neutrons up to a thickness of 140 cm. Relative numbers of transmitted ambient neutrons are presented in Figure 6.8, where a comparison to additional external background components discussed in the following subsections is shown.

A reduction by a factor of 10^5 (10^7) is obtained with a water cuboid of less than 1 m (1.5 m) thickness. Thus, solely considering the shielding effect of water together with the conservative assumptions on the incident neutron direction, the flux reaching the detector volume is estimated to be lower than $10^{-13}\,\mathrm{cm}^{-2}\,\mathrm{s}^{-1}$ in all our considered shielding options. Integrating over the surface of the detector volume in the simplified shielding geometry, this corresponds to a flux of less than $3.5 \cdot 10^{-2}\,\mathrm{yr}^{-1}$ entering that volume. Hence, it is concluded that the ambient neutron flux is reduced to a negligible

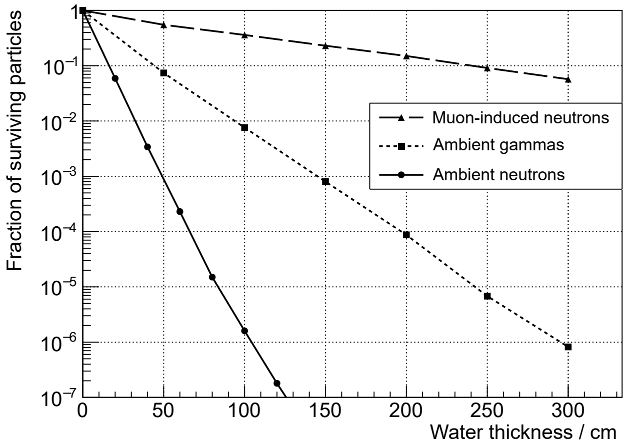

Figure 6.8.: Simulated fraction of particles transmitted through a water layer of given thickness using the respective spectra for ambient neutrons (Figure 5.28), ambient gammas (Figure 6.9) and muon-induced neutrons (Figure 6.11) for the initial energies.

value compared to the planned data taking campaigns lasting $\mathcal{O}(1\text{–}10\,\mathrm{yr})$. In addition, transmitted neutrons usually scatter while traversing the water and thereby get moderated and thermalized, such that due to their low energies, a majority may not contribute to the nuclear recoil background above detector thresholds of 1 keV. Indeed, it can be calculated from kinematics that the minimum kinetic energy for neutrons to be able to transfer 1 keV to a ^{23}Na (^{127}I) nucleus in an elastic scattering process is roughly 6.3 keV (32.3 keV).

After attaining these results, there is still a specific ambient neutron component that has to be considered separately. This component is the one entering the dry-well from the top, potentially having a direct line of sight to the detectors without having to traverse water or other low-Z materials. This component can be studied by simulating neutrons according to the ambient energy spectrum starting from the top of the dry-well towards a random direction on the hemisphere in negative vertical direction. Initial simulations in the simplified geometry tell that this background contribution may not be negligible. However, it does not play a significant role in choosing the shielding design, as all of them have a similar issue due to the opening to the top. Hence, we return to the study of this background component in Section 6.3.2, where an estimate of the background rate in the more detailed geometry of the chosen design is assessed. There, furthermore the various possibilities in shielding this background via using low-Z materials in or above the dry-well are discussed.

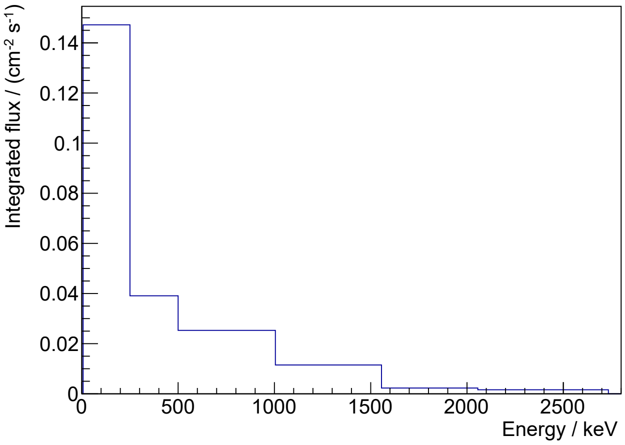

Figure 6.9.: Ambient gamma spectrum at LNGS according to Ref. [194]. The large bin size, not resolving individual peaks, and possible implications for simulations are discussed in the text.

6.2.4 Ambient Radiogenic Gamma Simulation

Ambient gammas, just like ambient neutrons, originate from rock and concrete surrounding the experimental halls of LNGS. They are induced in radioactive decays of nuclides in the natural decay chains as well as of additional radioactive contaminants like ^{40}K, ^{60}Co or ^{137}Cs. To simulate this background component, we proceed similarly as for ambient neutrons.

Measurements of the ambient gamma flux in the underground halls at LNGS have been performed in the past, for example in Ref. [194]. For this study, the energy spectrum quoted by the authors is adopted and presented in Figure 6.9. The integrated flux over the whole energy range in hall B, where the COSINUS experiment is being built, is stated as $0.23\,\mathrm{cm^{-2}\,s^{-1}}$. Both spectrum and flux are used as an input for simulation and analysis. While the real gamma spectrum consists of a lot of distinct features due to several emission lines and escape peaks on top of some Compton background, the quoted spectrum uses large energy bins and their relative contributions. However, for a general study of the gamma attenuation, taking the bin integrals is a good approximation, as long as the peaks are not systematically located at the high-energy border of the given bins. A more detailed spectrum based on simulations using radioactive contamination levels in the LNGS rock and concrete is out of the scope of this thesis and would not significantly affect the determination of the overall thickness of a given shielding layer. On the contrary, it may have implications on the exact background shape and should thus be considered for the complete background model of COSINUS in a future work.

For the simulation, again the conservative approach using a further simplified geometry made of cuboid volumes is applied. A primary study of the attenuation factors as a function of water alone is again performed, increasing the thickness by increments of 20 cm. The results are depicted in Figure 6.8. It can be seen that water is a much better neutron than gamma attenuator. This is expected as the main energy loss process for gammas above ~30 keV in water is Compton scattering [84] and the mean free path is in the order of 10 cm. Typically, in each of the scattering processes, the gammas hence only loose some part of their energy. Therefore, they can on average penetrate larger thicknesses.

To reduce the ambient neutron flux by a factor of 10^5, less than one meter of water is necessary, while ~ 250 cm are needed for the same attenuation of ambient gammas. As the reduction by water alone may not be sufficient, an inner shielding made of a high-Z material can be employed. The various cases are compared on the basis of the five shielding design options presented in Figure 6.7. For example, using the layout according to option 4 with a water thickness of 300 cm followed by 8 cm of copper yields a surviving ambient gamma flux of $\sim 4.9 \times 10^{-8}$ cm^{-2} s^{-1}, translating to $1.7 \cdot 10^4$ yr^{-1} per year entering the detector volume. The resulting values for all the considered shielding options are listed in the summary table, Table 6.5, containing all the considered background components. A comparative discussion of the values will be given at the end of this section, reporting about their implications and illustrating the choice of the optimal shielding design.

Gammas coming from the top, in contrast to the discussion about ambient neutrons, are less of an issue. The most efficient gamma attenuators are high-Z materials, of which due to the cryostat itself and the dedicated top shielding above the detector volume sufficient amount is foreseen.

6.2.5 Internal Radiogenic Neutron Simulation

In contrast to the simulation of ambient particles, where one can rely on previous studies found in literature for the incident energy spectrum and flux, the situation is different for the evaluation of the internal radiogenic background originating from shielding materials. As the dependence on the thickness and shape of the materials as well as on the assumed or measured contamination levels is large, there is no simple way of performing or finding a-priori measurements. Instead, a simulation based on material contamination levels is needed. As this thesis comprises the principal study for defining the shielding design of COSINUS, no materials are purchased at the time of performing the simulations. Thus, literature values of the contamination levels have to be assumed. Aiming for the use of the most radiopure materials on the market, a small literature search was done to quote the lowest contamination levels found by other rare event search experiments evaluating steel, lead, copper and polyethylene. The final values employed are those reported by CUORE in Ref. [160, 191] and XENON in Ref. [192, 193] and are listed in Table 6.2.

Converting the quoted contamination with ^{238}U, ^{235}U and ^{232}Th nuclides to units of

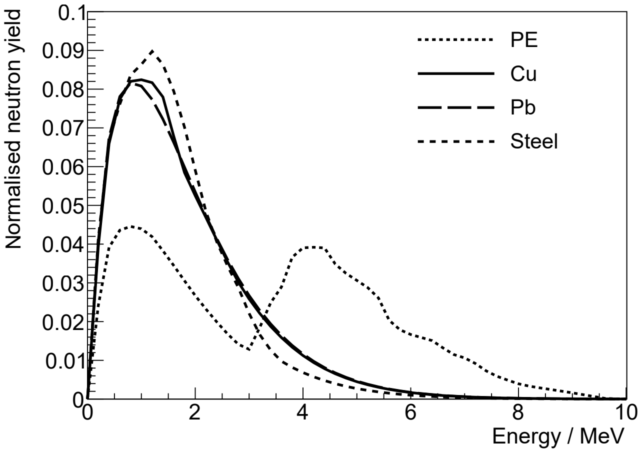

Figure 6.10.: Radiogenic neutron spectra obtained through SOURCES4C [123] with extended libraries [139–141]. Results are shown for polyethylene (PE), Cu, Pb and steel, according to contamination levels listed in Table 6.2. The second peak for PE originates from (α, n) reactions on ^{13}C. For each spectrum, the integral is normalized to unity.

atoms/cm^3 for each material and assuming secular equilibrium in the decay chains, the SOURCES 4C code with extended libraries is used to calculate the neutron yield and energy spectrum due to (α,n) and s.f. reactions. The normalized radiogenic neutron spectra are depicted in Figure 6.10, the integrated yields are reported in the last column of Table 6.2. For a detailed discussion on decays and target nuclides contributing to the creation of free neutrons via (α,n) and s.f. reactions, the reader is referred to the corresponding section in the CRESST-related simulation chapter, i.e. Section 5.2.1.

Using the newly developed interface from SOURCES 4C to ImpCRESST as well as employing the new feature for simulation of bulk contamination developed in the course of this thesis, the attained results can be used as an input for the Geant4-based simulation in the simplified shielding geometry. Taking the five geometries sketched in Figure 6.7, a homogeneous distribution of neutrons with energies according to the SOURCES 4C spectrum in all volumes made of the same material is thus simulated. Results are evaluated for the number of neutrons reaching the detector volume and scaled to the initial neutron yield.

In Table 6.3, the respective results for each shielding option are listed. These are further divided into the materials sourcing the neutrons, such that a conclusive picture on the origin of internal radiogenic neutrons is presented. In general, less material in the dry-well around the cryostat yields lower numbers of neutrons. Polyethylene, while being a good neutron moderator, leads to the largest contributions as the reported contamination levels are higher than in other materials and as the spectrum extends to higher energies due to (α,n) reactions on ^{13}C.

Only materials inside the dry-well are considered in this study, because the ultra-

Table 6.3.: Detailed list of internal radiogenic neutron background origin and contribution in the five tested shielding design options. The uncertainties are 1σ Poissonian bounds.

Option	Neutron source	Events with neutrons entering detector volume (yr^{-1})	Total (yr^{-1})
1	PE	8.86 ± 0.01	9.17 ± 0.01
	Cu	$(2.96 \pm 0.03) \cdot 10^{-1}$	
	Pb	$(7.41 \pm 0.46) \cdot 10^{-3}$	
	Steel	$(3.62 \pm 0.34) \cdot 10^{-3}$	
2	PE	8.91 ± 0.01	9.18 ± 0.01
	Cu	$(2.67 \pm 0.03) \cdot 10^{-1}$	
	Steel	$(2.06 \pm 0.24) \cdot 10^{-3}$	
3	Cu	2.16 ± 0.01	2.17 ± 0.01
	Steel	$(1.19 \pm 0.06) \cdot 10^{-2}$	
4	Cu	$(8.44 \pm 0.05) \cdot 10^{-1}$	$(9.31 \pm 0.07) \cdot 10^{-1}$
	Steel	$(8.72 \pm 0.16) \cdot 10^{-2}$	
5	Cu (cryostat)	$(2.09 \pm 0.02) \cdot 10^{-1}$	$(4.22 \pm 0.05) \cdot 10^{-1}$
	Steel	$(2.13 \pm 0.03) \cdot 10^{-1}$	

pure water surrounding this volume is a very good neutron moderator and at the same time supposed to feature contamination levels orders of magnitude below [195] the ones reported for the other materials in Table 6.2. Additionally, intrinsic sources in the materials of the detector modules are not considered in this study, mainly because these do not influence the choice of the optimal shielding against external sources. Furthermore, radiogenic neutrons originating from the target crystals themselves are not contributing to the background in the ROI, as the reactions leading to their production (α-decay and s.f.) induce a high energy signal above a few MeV.

6.2.6 Internal Radiogenic Gamma Simulation

The study of internal radiogenic gammas follows the same principle as applied to internal radiogenic neutrons. However, instead of using an auxiliary program like SOURCES 4C for the neutron yield, the full simulation is directly performed in our Geant4-based software. This means that the decaying nuclides are placed inside the shielding materi-

Table 6.4.: Detailed list of internal radiogenic gamma background origin and contribution in the five tested shielding design options. The uncertainties are 1σ Poissonian bounds.

Option	Gamma source	Events with gammas entering detector volume (yr^{-1})	Total (yr^{-1})
1	PE	$(5.41 \pm 0.13) \cdot 10^6$	$(5.68 \pm 0.14) \cdot 10^6$
	Cu	$(2.74 \pm 0.11) \cdot 10^5$	
	Pb	$(8.90 \pm 0.89) \cdot 10^2$	
	Steel	$(2.70 \pm 0.69) \cdot 10^1$	
2	PE	$(5.41 \pm 0.13) \cdot 10^6$	$(5.68 \pm 0.14) \cdot 10^6$
	Cu	$(2.74 \pm 0.11) \cdot 10^5$	
	Steel	$(1.16 \pm 0.10) \cdot 10^3$	
3	Cu	$(4.06 \pm 0.12) \cdot 10^5$	$(4.08 \pm 0.13) \cdot 10^5$
	Steel	$(2.36 \pm 0.15) \cdot 10^3$	
4	Cu	$(3.97 \pm 0.11) \cdot 10^5$	$(4.46 \pm 0.14) \cdot 10^5$
	Steel	$(4.89 \pm 0.25) \cdot 10^4$	
5	Cu (cryostat)	$(1.51 \pm 0.02) \cdot 10^5$	$(2.09 \pm 0.04) \cdot 10^6$
	Steel	$(1.94 \pm 0.04) \cdot 10^6$	

als and gammas emitted in the decay processes are analyzed. Again, the contamination levels quoted in Table 6.2 are taken into account. However, in addition to the natural decay chains, further nuclides are giving an important contribution to the internal radiogenic gamma background. Thus, also ^{40}K, ^{60}Co and ^{137}Cs are considered in our simulations due to being the most important of these.

In Table 6.4, the results of the simulation in terms of gammas entering the detector volume are presented. The results show that polyethylene and steel, if not shielded by other materials, lead to comparatively high contributions. The prime nuclide leading to the obtained rates differs between the materials according to the simulation and the normalization to the assumed contamination levels. For polyethylene and copper, the main contribution comes from nuclides of the ^{238}U decay chain, while for steel the largest contributor is ^{60}Co.

Contributions from the detectors and target crystals themselves are not considered in this study, as the goal is to find the shielding design that minimizes all external background components. After achieving this goal, however, background intrinsic to the crystals will have to be considered in detail, as it gives a major contribution to the overall background. A comprehensive background model for COSINUS will thus have to be developed in a future work, after procuring and screening all the materials of the detectors and their surroundings.

6.2.7 Cosmogenic Neutron Simulation

As discussed and found already in the CRESST chapter, atmospheric muons reaching the LNGS underground laboratory can lead to a significant nuclear recoil background contribution via secondary neutrons. Hence, the study of so-called cosmogenic neutrons is equally important for COSINUS.

Similar to the cosmogenic neutron study in CRESST (see Section 5.5.3), MUSUN is used to attain the energy spectrum and angular distribution of muons at LNGS. The respective distributions are displayed in Figure 5.12. For sampling of the muons, again a cuboid surface of $12 \times 12 \times 13$ m is defined, on which the integral muon flux returned by MUSUN equates to $2.3 \cdot 10^6$ yr^{-1}.

Employing the newly developed interface from MUSUN to ImpCRESST, these results were used to start the Geant4-based simulations. The simplified shielding geometry is, for the purpose of these simulations, surrounded by a rock volume. The cuboid surface, on which the muons start, is placed in a way such that at least 2.5 m of rock have to be traversed by each muon. For a discussion of the minimal thickness to properly account for shower development, the reader is referred to Section 5.5.3. Inside the surrounding rock volume, the water tank is shifted along the x-axis to be placed 0.5 m away from one of the rock walls and centered between the rock walls along the y-axis.

With this setup, between $1.5 \cdot 10^7$ and $3 \cdot 10^7$ muons are being simulated for the five shielding options. This corresponds to an exposure of 6.5 to 13 years, i.e. approximately 4 to 8 times the planned run time of COSINUS-1π. The spectrum of secondary neutrons is shown in Figure 6.11 and extends to much higher energies than the ambient or internal radiogenic neutron spectrum. While the radiogenic neutrons only feature energies up to ~10 MeV (see Figure 5.28 and 6.10), muon-induced neutrons may have energies up to the GeV-range. Thus, the shielding power of water is greatly reduced, which can be seen in Figure 6.8, comparing the attenuation of ambient neutrons to that of muon-induced ones.

The number of events, in which muon-induced neutrons finally reach the detector volume, is given in Table 6.5. By quoting the number of events instead of particles, the fact that many secondary particles may enter in the same event is accounted for. Similar as in CRESST, the calorimeters have a time resolution of a few ms and could hence not resolve individual energy depositions within ns or μs. If instead of in the same detector, additional energy depositions would be obtained in different detectors, they would as well be tagged as coincident and the event could in principle be vetoed without considering an active Cherenkov muon veto. The number of events with at

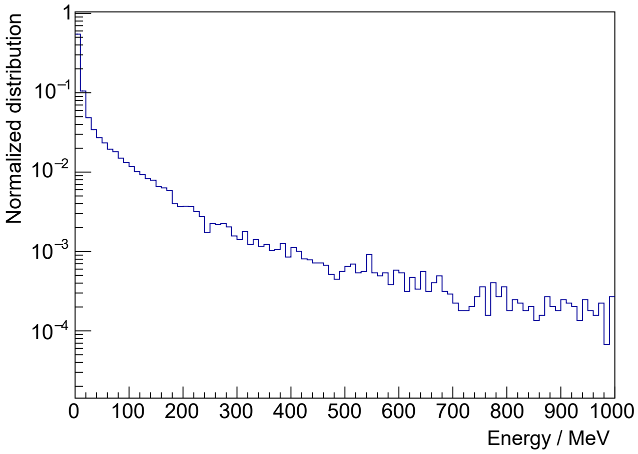

Figure 6.11.: Initial energy of muon-induced neutrons, as obtained from the Geant4 simulation of muons traversing the LNGS rock and the simplified COSINUS setup. The integral over the spectrum is normalized to unity.

least one neutron reaching the detector volume thus even represents an upper bound on the potential background contribution.

Between the five shielding options, a factor of three difference in rate of such events can be found. This rather small difference can be thought of as a result of the following effects. On the one hand, the number of secondary neutrons produced by muons scales with the mass number of the material as roughly $A^{0.8}$ [143], leading to higher numbers when using more lead and copper. On the other hand, polyethylene may provide an additional shielding. Overall, however, the numbers in all configurations are at least one or two orders of magnitude larger than for radiogenic neutrons.

To reduce the corresponding background, a Cherenkov muon veto system in the water tank is planned. Simulations for the study of its design are presented in Section 6.4, where different arrangements of PMTs and various possible trigger conditions are tested. An estimation of the actual background rate due to nuclear recoils in a more elaborate simulated geometry considering a realistic target inventory is however previously discussed in Section 6.3.

6.2.8 Optimal Passive Shielding Design

Table 6.5 comprises all the particle rates entering the detector volume in the various shielding options. Since the goal is to minimize the level of residual background reaching the detector volume, especially neutrons potentially leading to nuclear recoil signals, the following arguments can be based on the individual obtained numbers. No specifically weighted combination of neutron and gamma background is calculated, as the neutron background is the most dangerous contribution, hence discussed individually in the

Table 6.5.: Particle flux due to all major external background components entering the detector volume in the various shielding design options. The uncertainties are 1σ Poissonian bounds.

Background source		Estimated number of particles entering the detector volume (yr^{-1})				
		Option 1	Option 2	Option 3	Option 4	Option 5
Neutrons	Ambient	$< 3.50 \cdot 10^{-2}$	$< 3.50 \cdot 10^{-2}$	$< 3.50 \cdot 10^{-2}$	$< 3.50 \cdot 10^{-2}$	$< 3.50 \cdot 10^{-2}$
	Internal	$(9.17 \pm 0.01) \cdot 10^{0}$	$(9.18 \pm 0.01) \cdot 10^{0}$	$(2.17 \pm 0.01) \cdot 10^{0}$	$(9.31 \pm 0.07) \cdot 10^{-1}$	$(4.22 \pm 0.05) \cdot 10^{-1}$
	Cosmogenic	$(2.10 \pm 0.03) \cdot 10^{2}$	$(1.15 \pm 0.02) \cdot 10^{2}$	$(3.36 \pm 0.04) \cdot 10^{2}$	$(2.22 \pm 0.03) \cdot 10^{2}$	$(1.11 \pm 0.02) \cdot 10^{2}$
Gammas	Ambient	$(3.15 \pm 1.41) \cdot 10^{3}$	$(6.81 \pm 1.15) \cdot 10^{4}$	$(7.88 \pm 1.05) \cdot 10^{4}$	$(1.71 \pm 0.57) \cdot 10^{4}$	$(4.94 \pm 0.47) \cdot 10^{5}$
	Internal	$(5.68 \pm 0.14) \cdot 10^{6}$	$(5.68 \pm 0.14) \cdot 10^{6}$	$(4.08 \pm 0.13) \cdot 10^{5}$	$(4.46 \pm 0.14) \cdot 10^{5}$	$(2.09 \pm 0.04) \cdot 10^{6}$

assessment.

The thicker the shielding layer, the lower in principle the residual ambient background. Nonetheless, depending on the contamination levels, more material employed can lead to higher internal radiogenic and cosmogenic background contribution to the overall budget. Within this study, the goal was to find the best compromise between these two apparently conflicting requirements allowing to limit as much as possible the overall number of particles reaching the target, while also considering the space limitations for the water tank. Options 4 or 5 are therefore those best fulfilling this requirement with particular focus on neutrons. With these setups, the size of the water tank is maximized, leading to a larger active volume for the foreseen Cherenkov veto system. At the same time, the necessary amount of additional shielding material in the dry-well is reduced, minimizing the radiogenic background.

While the main focus is on the neutron background due to particle discrimination capability, gamma background can still play a role. At low energies, a fraction may potentially leak into the ROI (cf. Figure 6.3), and an increased total rate may affect the dead-time of the measurements. Finally, due to all considerations, the decision was made for option 4, as it is less sensitive to the contamination level of the stainless steel of the dry-well. It should be remembered that lowest values found in literature are assumed for the contamination levels of all materials and values obtained for different stainless steel batches seemed to vary a lot.

The use of the literature values was based on discussions with several colleagues at LNGS and the possibility to contact the same vendors already used by other collaborations. In parallel to and following up the decision on the final design (option 4), the procurement and screening of materials for the water tank and additional shielding of COSINUS has started. Results of the screening of copper have been received and bulk contamination levels are in good agreement with or lower than those assumed in Table 6.2. Recently, different batches of stainless steel (AISI316L) have also been screened. The lowest values found for ^{238}U and ^{232}Th are about one order of magnitude larger than those quoted in Table 6.2, backing up our earlier decision on shielding option 4 over option 5.

The entire study presented in Section 6.2 has been published in Ref. [189] and forms the basis for the experimental setup of COSINUS. Following the choice of shielding option 4 from Table 6.1, the final apparatus maximizes the size of the water tank with dimensions of 7 m in diameter and height. The dry-well is set to host the cryostat as well as an 8 cm copper shielding around it. This inner shield will extend up to the 30 cm top copper shielding above the detector volume inside the cryostat. At the time of writing this thesis, the construction of the apparatus at LNGS just started.

To deal with the dominant neutron background component induced by cosmic muons, the water tank will be instrumented as an active Cherenkov veto, described in detail in Section 6.4.

6.3 Neutron Background Evaluation in a Detailed Experimental Geometry

After fixing the conceptual design of the shielding according to the results presented in Section 6.2, a more refined structure of the setup was implemented in the simulation software. This geometry was used to evaluate the remaining nuclear recoil background rate.

6.3.1 Considered Target Inventory

The detailed geometry implemented in the simulation software is based on technical drawings of the cryostat and CAD drawings of the water tank, as depicted in Figure 6.12. The main modifications and additions compared to the simplified geometry are the following: a tripod-support structure for the dry-well, made of steel; a realistic cryostat design with its various thermal shields and its narrow prolongation; 4×11 detectors using the baseline detector design. The implemented geometry, viewed from various angles, is visualized in Figure 6.13. As the preferred solution to moderate neutrons coming from the top, at the time of this study, were water-filled polyethylene containers around the prolongation of the cryostat, these can be seen in the illustration as well.

A zoom to the detectors is shown in Figure 6.13d. As the remoTES design (cf. Section 6.1.2) had not been considered yet at the time of the simulation study, the detectors use the baseline design (cf. 6.1.2) featuring a $CdWO_4$ carrier crystal, a Si beaker and a cylindrical NaI target crystal with a mass of 90 g. Those parts are fully enclosed in a copper housing. Four layers of 11 detector modules are present in the simulated geometry.

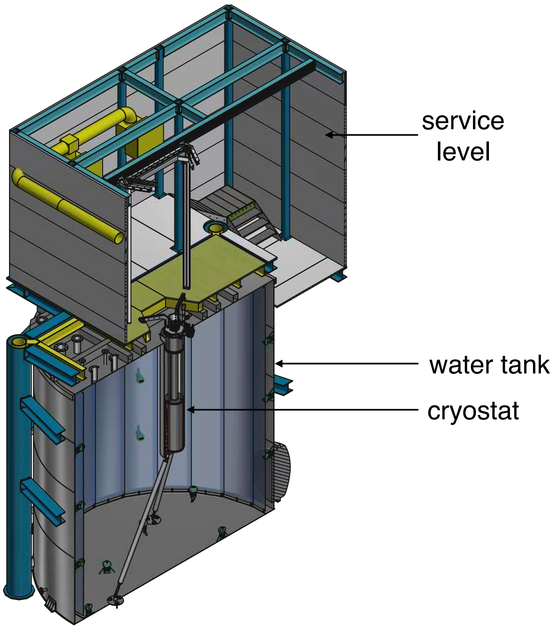

Figure 6.12.: CAD model of the COSINUS water tank created by the Max Planck Institute for Physics in Munich.

6.3.2 Neutron Induced Nuclear Recoil Rates

Using the detailed implemented geometry, simulations of the neutron background are performed to estimate the expected nuclear recoil rate. The approaches are similar to those presented for the simulation in the simplified setup. However, the analysis is different, as the recoils in the detectors are the parameter of interest instead of the particles flux entering the detector volume. The analysis is done separately for two sets of detectors, once for 10 detectors in the top layer and once for all 44 implemented detectors. Purpose of these choices is to study the effect of different numbers of detectors on the obtained results. Furthermore, 10 might be the amount used in the first run of COSINUS.

Operating various small detectors next to each other brings the possibility to veto events based on an anti-coincidence cut. Whenever an energy deposition is registered in more than one target crystal, it can be excluded from the data, as for dark matter it is highly unlikely to scatter in more than one detector due to its low interaction cross section. The anti-coincidence cut can similarly be applied to events depositing energy in the carrier or beaker of the detector.

In Figure 6.14, the nuclear recoil energy depositions obtained in both sets of detectors during a simulation of 30 million muons are presented. Electron recoils are not considered. To apply the anti-coincidence cut, the number of detectors registering an energy deposition in coincidence, the so-called "detector multiplicity" is assessed and shown in

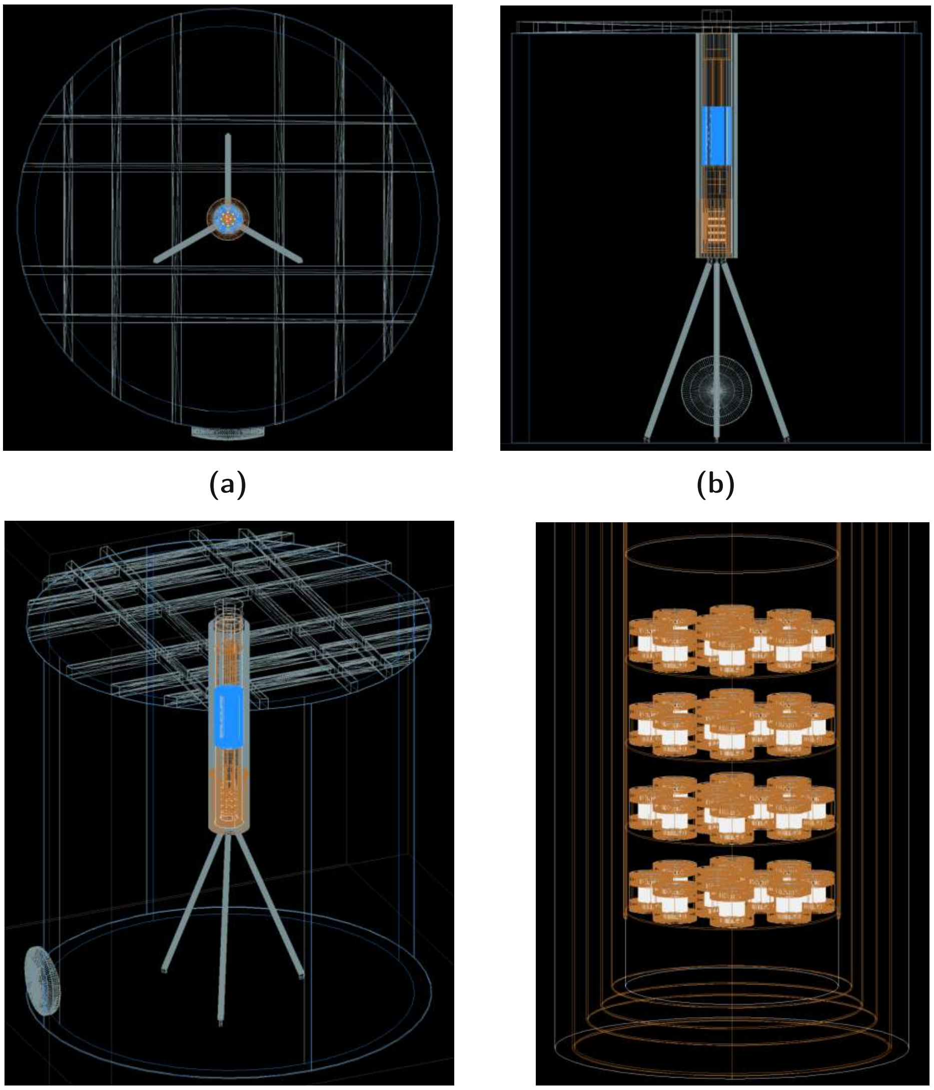

(a) (b)

(c) (d)

Figure 6.13.: Geant4 visualization of the implemented detailed geometry: (a), (b) and (c) show the setup from various angles, (d) presents a zoom to the 4×11 detector modules.

Figure 6.15. In both sets of detectors, the events with multiplicity equal to one dominate. However, with 10 detectors these are still roughly 50% of all nuclear recoils, while with 44 detectors these are less than 25% of the total number. As could be expected, this shows that more detectors lead to a more efficient anti-coincidence cut. In Table 6.6, the numbers obtained in the two analyses are summarized. By scaling the attained nuclear recoil events with the simulated exposure of ~13 years and the integrated mass of the 10 (44) target crystals of 0.9 kg (3.96 kg), the background rate is estimated. In

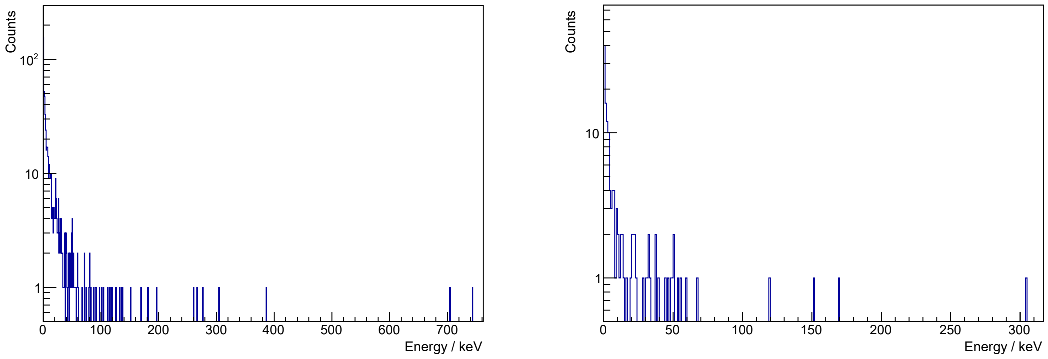

(a) Result for 44 detectors.

(b) Result for 10 detectors.

Figure 6.14.: Simulated nuclear recoil energy deposition spectrum due to muon-induced neutrons in (a) all 44 detectors and (b) only the first 10 detectors for $3 \cdot 10^7$ primary muons corresponding to roughly 13 yr life time.

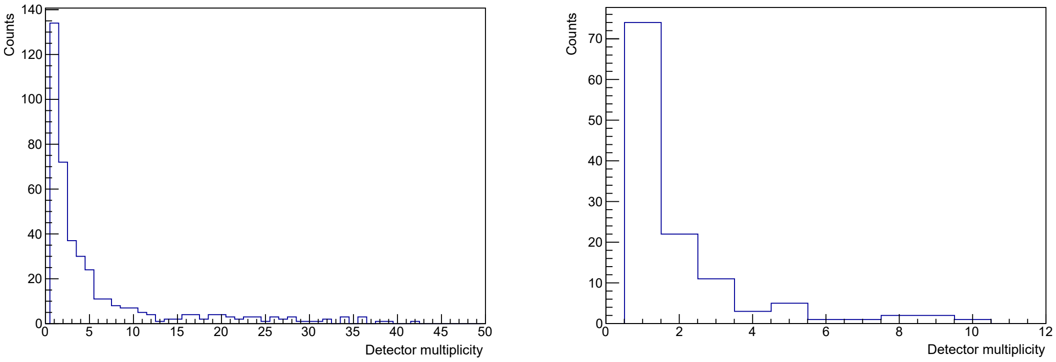

(a) Result for 44 detectors.

(b) Result for 10 detectors.

Figure 6.15.: Simulated detector multiplicity for nuclear recoil events due to muon-induced neutrons, considering (a) all 44 detectors and (b) only the first 10 detectors for $3 \cdot 10^7$ primary muons corresponding to roughly 13 yr life time.

addition to the anti-coincidence cut, in the last row of the table, a threshold of 1 keV in all the detectors is assumed, further reducing the number of single nuclear recoil events. After applying the cuts and detector thresholds, the single nuclear recoil background amounts to ~4.1 $(\mathrm{kg\,yr})^{-1}$ (~2.0 $(\mathrm{kg\,yr})^{-1}$) in the array of 10 (44) detectors. These numbers are obtained without taking into account an active muon veto and give a further strong motivation for its implementation to achieve a background-free experiment in terms of nuclear recoils. The simulation study of an active muon veto is presented in Section 6.4, and yields a feasible reduction of the attained muon-induced background by roughly 99%.

Table 6.6.: Simulated nuclear recoil background rate due to muon-induced neutrons in 44 and in 10 COSINUS detectors without muon veto. The quoted uncertainties are 1σ Poissonian bounds.

Cut conditions	Background rate (kg yr)$^{-1}$	
	44 detectors	10 detectors
No cuts	11.2 ± 0.5	11.7 ± 1.0
Anti-coincidence cut	2.3 ± 0.2	5.8 ± 0.7
Anti-coincidence cut & 1 keV threshold	2.0 ± 0.2	4.1 ± 0.6

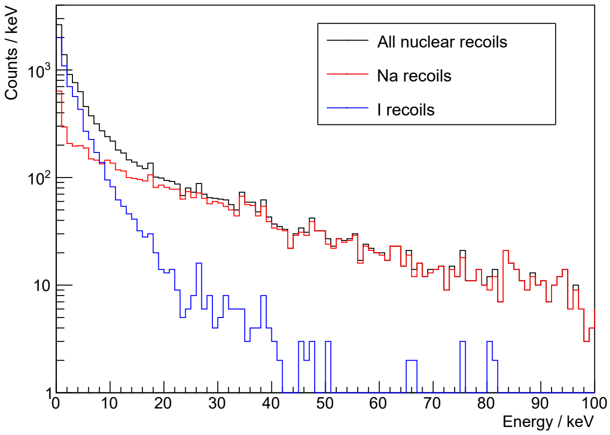

Figure 6.16.: Simulated nuclear recoil energy deposition spectrum due to muon-induced neutrons shown separately for Na and I recoils.

In addition to the study of the background rate, a high statistics simulation based on the muon-induced neutron spectrum has been performed to study the spectral shape of the energy depositions in more detail. As shown in Figure 6.16, the recoils can be separated for the different nuclei in NaI. At low energies, the recoils on the heavier I nuclei dominate, while starting from roughly 10 keV towards larger energies the Na recoils form the majority. The spectral shape and distribution can be an important input to the likelihood fit of the different nuclear recoil bands during data analysis.

Similar to the muon-induced neutrons, internal radiogenic neutrons are reassessed in the detailed experimental geometry. The nuclear recoil energy depositions obtained from a simulation of 500,000 neutrons originating in copper as well as 500,000 neutrons originating in steel, only considering the 10 detector setup, are presented in Figure 6.17. Detector multiplicities are depicted in Figure 6.18, showing a large majority at multiplicity one. This is due to the radiogenic neutrons being accompanied by

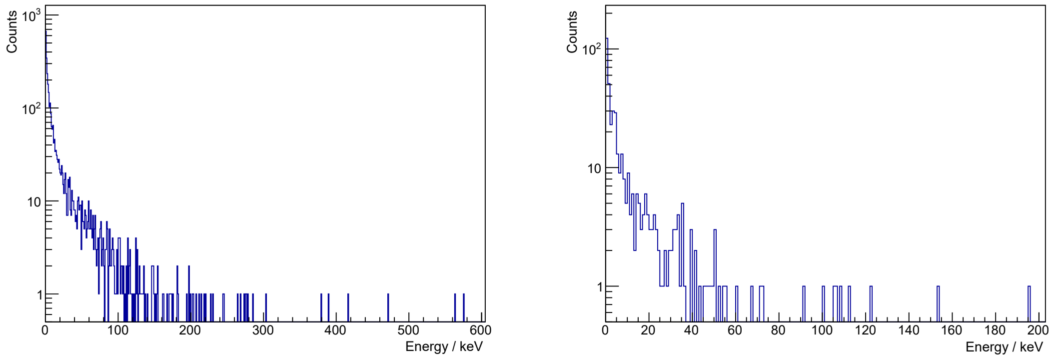

(a) Radiogenic neutrons from Cu. **(b)** Radiogenic neutrons from steel.

Figure 6.17.: Simulated nuclear recoil energy deposition spectrum in 10 detectors due to radiogenic neutrons originating from (a) Cu and (b) steel.

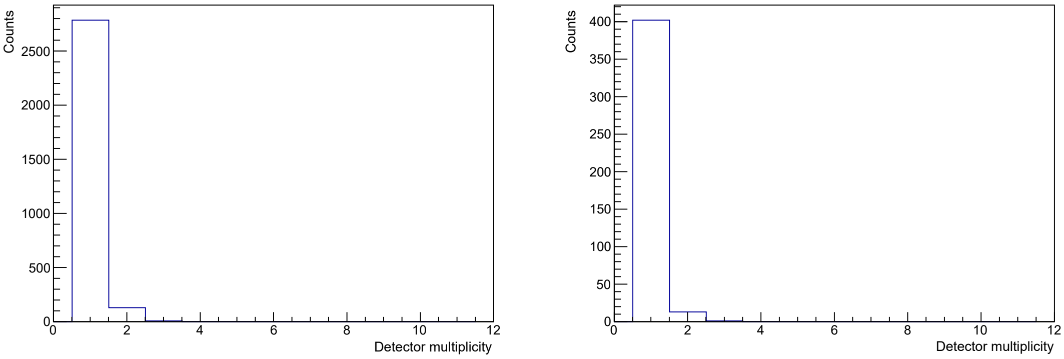

(a) Radiogenic neutrons from Cu. **(b)** Radiogenic neutrons from steel.

Figure 6.18.: Simulated detector multiplicity using 10 detectors due to radiogenic neutrons originating from (a) Cu and (b) steel.

much less secondary particles than the muon-induced ones. The anti-coincidence cut is thus less efficient, only removing a few percent of the events. However, the event rate is very low, which can be seen when normalizing it to exposure and mass as well as applying a detector threshold of 1 keV. In Table 6.7, the individual numbers are again summarized. As the simulated events in both cases correspond to roughly 100,000 years exposure, the resulting single nuclear recoil rates after cuts and threshold assumption are $\sim$0.02 $(\mathrm{kg\,yr})^{-1}$ and $\sim$0.003 $(\mathrm{kg\,yr})^{-1}$ for neutrons originating in copper and steel respectively. With the use of the active muon veto, the muon-induced neutron background may be reduced to the same order of magnitude.

For ambient neutrons, the only potentially dangerous component, i.e. the one coming from the top as discussed in Section 6.2.3, is considered. Options to shield this

Table 6.7.: Simulated nuclear recoil background rate due to radiogenic neutrons in 10 detectors. The quoted uncertainties are 1σ Poissonian bounds.

Cut conditions	Background rate (kg yr)$^{-1}$	
	Cu origin	Steel origin
No cuts	$(3.4 \pm 0.1) \cdot 10^{-2}$	$(4.7 \pm 0.2) \cdot 10^{-3}$
Anti-coincidence cut	$(3.4 \pm 0.1) \cdot 10^{-2}$	$(4.0 \pm 0.2) \cdot 10^{-3}$
Anti-coincidence cut & 1 keV threshold	$(2.2 \pm 0.1) \cdot 10^{-2}$	$(2.8 \pm 0.2) \cdot 10^{-3}$

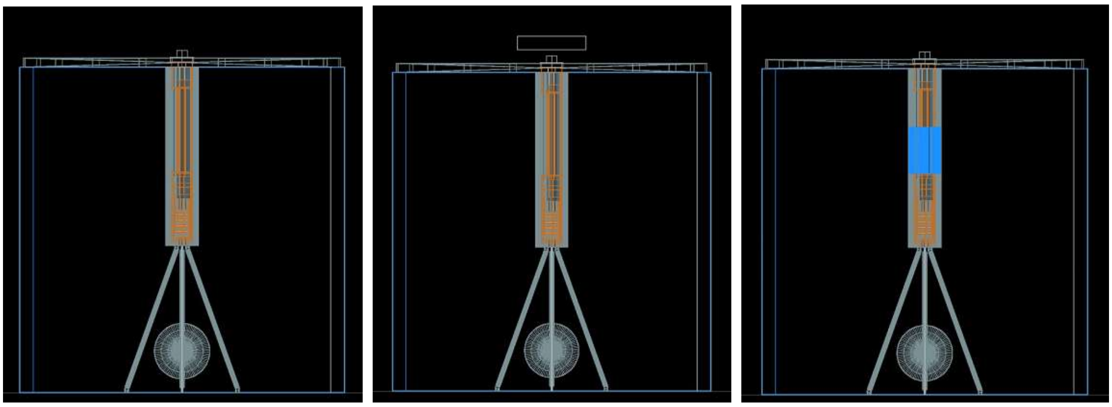
(a) (b) (c)

Figure 6.19.: Viszualisation of the different shielding options against ambient neutrons entering the dry-well from the top. The compared designs use (a) no additional shielding, (b) a polyethylene shield above the dry-well, and (c) a water (or polyethylene) shield around the prolongation of the cryostat.

background component are indicated in Figure 6.19. The shown geometries from left to right use: (a) no additional shielding at the top of the detectors, (b) 30 cm of polyethylene above the dry-well, and (c) 50 cm of either polyethylene or water around the prolongation of the cryostat. A simulation of 10^7 ambient neutrons starting from a circle above the dry-well in random downward directions within an opening angle of 30° is performed for each case. Any of the options using an additional low-Z shield leads to an estimate of less than 0.01 (kg yr)$^{-1}$, with the polyethylene shield above the dry-well performing best, likely due to covering the full line of sight. On the other hand, the simulation without additional shield yields an estimate of ~1 (kg yr)$^{-1}$, showing the necessity of considering this background component. The final design of the additional neutron moderator on the top is still under discussion as of writing this thesis.

6.4 Optimization of an Active Muon Veto

From the results in the previous sections and experience in other rare event search experiments at LNGS, it has been clear that a muon veto is necessary for COSINUS. Thus, from the beginning onwards, the water tank has been foreseen to be operated with PMTs collecting the Cherenkov light created by muons and secondary charged particles passing through the water. The optical simulations performed for the study of the Cherenkov muon veto follow a similar approach as the one published in the past by the XENON collaboration [196].

6.4.1 A Cherenkov based Muon Veto

If a charged particle traverses a dielectric material with refractive index n at a velocity higher than the speed of light in that very material, given by $\frac{c}{n}$, Cherenkov radiation is created. Threshold kinetic energies for charged particles being able to create Cherenkov light can thus easily be calculated via $E_{kin} = (\gamma\text{-}1)mc^2$, where $\gamma = (1\text{-}\beta^2)^{-1/2}$. The minimum energy necessary is attained using $\beta = \frac{1}{n}$. With the refractive index $n{\sim}1.33$ of water, a threshold kinetic energy of ~264 keV for electrons and ~55 MeV for muons is obtained. As basically all of the cosmic muons reaching the underground laboratory have energies above the threshold, they efficiently produce Cherenkov photons when traversing water.

The veto system will then use a certain number of PMTs distributed over the whole inner surface of the water tank to collect some of the photons. To improve the detection efficiency, the inner walls of the tank will be covered with a reflective foil, potentially increasing the photons' path length and their chance of reaching a PMT. If a pre-defined trigger condition for the muon veto system is fulfilled, any coincident signal in one of the cryodetectors is then vetoed.

6.4.2 Photon Hit Patterns

An optical simulation of millions of photons potentially created by muons in each event is extremely CPU- and time-intensive. Performing separate simulations for the assessment of different PMT aragements is therefore essentially impossible. A solution thus has to be found to assess various arrangements of PMTs based on results of a single simulation. For this purpose, the PMT arrangements are only virtually considered in the analysis of a single simulation storing the necessary photon tracking data.

A geometry without the actual implementation of PMTs is used in the simulation, in our case again the geometry of the chosen shielding design option 4, as defined and shown in Table 6.1 and Figure 6.7. In addition, the reflective foil on the inner tank surface is considered by defining the optical surface properties, especially setting a certain reflectivity. For the simulation, the optical physics package of Geant4 is

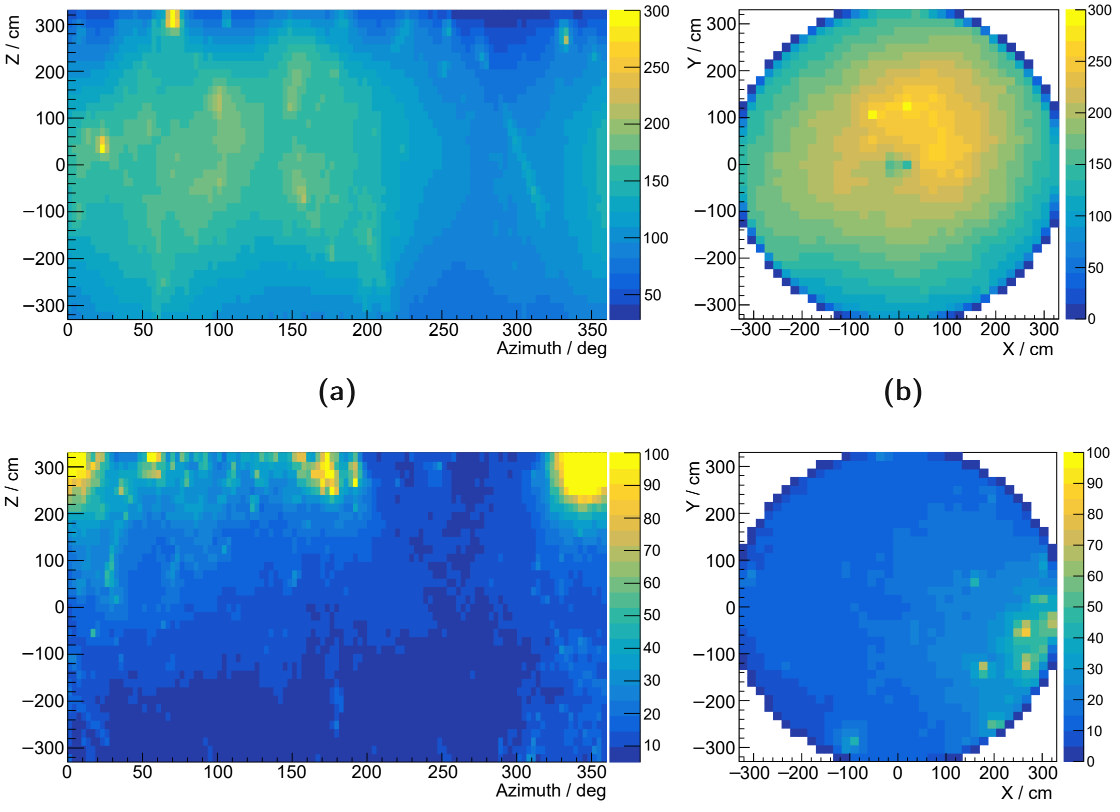

(a) (b)

(c) (d)

Figure 6.20.: Simulated average number of Cherenkov photons hitting the reflective foil at the inner surface of the steel tank per event using bins of the size of the PMT window. In (a) and (b), the photon distribution on the mantle wall as well as the bottom of the tank due to muon events is shown, in (c) and (d) the one due to shower events.

activated. Furthermore, the data structure in the simulation software has been adapted for the purpose of these simulations to store all the positions of optical photons, at which they reach the inner tank surface. This includes positions at which the photons get reflected as well as those where they may be absorbed. With this information, a photon hit map can then be created, showing the spacial distribution of photons reaching the reflective surface. Furthermore, the logical connection between stored positions of the same photon is kept, such that in the assessment of PMT arrangements the subsequent hits after reaching one of the virtually placed PMTs can be disregarded.

For the same reason of the simulation being CPU- and time-intensive, only a subset of events of the muon-induced background study presented in the previous sections, can be considered. Only events, in which a neutron reaches the dry-well, thus referred

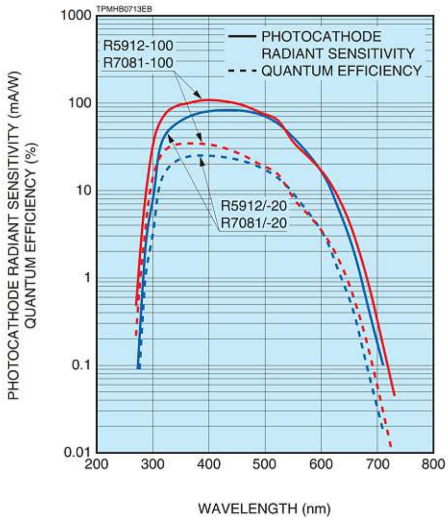

Figure 6.21.: Quantum efficiency of Hamamatsu5912 PMTs, taken from [198].

to as "dangerous events", are selected and stored for the resimulation with activated Geant4 optical physics. Out of 30 million simulated muons, 11682 dangerous events could be identified. These are further split in two categories, based on the muon path. If the muon itself traverses the water tank, the events will be called "muon events", otherwise "shower events". In the latter, where only secondary particles may traverse the tank, Cherenkov light creation is much lower and detection by the veto system is less likely. With 11171 of the dangerous events being muon events, however, the majority is expected to be tagged by the veto with high efficiency.

A simulation of the dangerous muon and shower events with activated optical physics is performed, using a specular reflective surface on the inner water tank surface with reflectivity of 95% as a conservative estimate. The foil foreseen to be used at the time of the study is DF2000MA by 3M [197], featuring a specified reflectivity of more than 99% for photons between wavelengths of 400 nm and 775 nm.

The obtained photon hit maps on the mantle and bottom of the tank for muon and shower events are presented in Figure 6.20. Bin sizes are roughly corresponding to the size of the foreseen 8-inch PMTs. The number of photons is averaged over all collected events. While the statistic of shower events is rather low, some general statements about the photon distributions can be made. Many shower particles may be stopped within short distance inside the water tank and thus create photon traces closer to the borders. This is not the case for muons themselves. The peak numbers of photons reaching the reflective surface are hence differently distributed for muon and shower events. In planning the arrangement of PMTs, this can be taken into account.

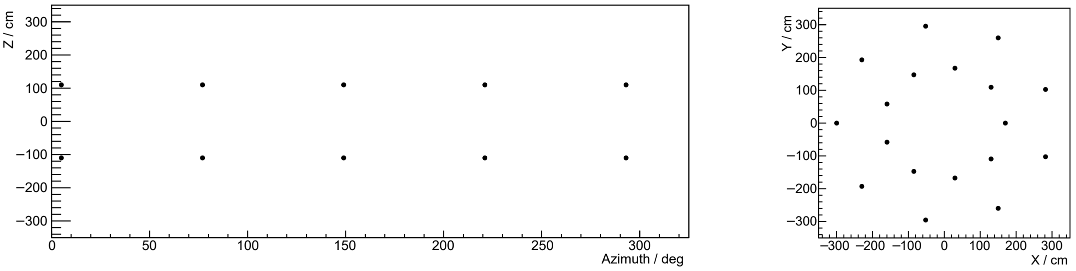

(a)

(b)

Figure 6.22.: PMT positions at the tank (a) mantle wall and (b) bottom, using the preferred option with a total of 28 PMTs.

6.4.3 Assessment of PMT Arrangements and Trigger Conditions

Based on the data obtained in the simulation, different arrangements of PMTs can be assessed. The analysis uses the raw photon wall hit position data, which includes all positions where a photon may be reflected or absorbed. As mentioned previously, the logic between the hits allows to take into account that a photon reaching a PMT is not reflected at this position, excluding possible subsequent hits from the analysis. This is not accounted for in the visualization of the hit maps shown in Figure 6.20, which only shows an integrated picture of all events and all photon wall hit positions combined.

Furthermore, the individual photon energies are necessary to determine the probability of the photon to be converted into a photoelectron and thus a signal. For this conversion, the usage of 8-inch Hamamatsu R5912-100 PMTs, with a wavelength-dependent quantum efficiency as depicted in Figure 6.21, is assumed. All its specifications are taken from the respective data sheet [198]. A 90% collection efficiency is assumed for every photon reaching a PMT, due to the specified minimum effective area given in the data sheet.

The PMTs in the analysis of the simulated data are solely defined by setting a geometrical acceptance region of 8 inch diameter at corresponding positions. With this approach, the PMTs only virtually exist at defined locations on the tank walls. This has the advantage that a single simulation can be used to assess an arbitrary amount of different PMT arrangements. With the dedicated ROOT analysis script written for this study, all the considered arrangements can even be assessed in parallel at the same time.

Due to budget constraints, it was clear from the beginning that a maximum of ~30 PMTs would be purchased. This number was expected to already yield a sufficiently effective veto. Thus, only suitable arrangements have been tested. An extended picture of various options and their estimated trigger efficiencies is presented in Appendix D.

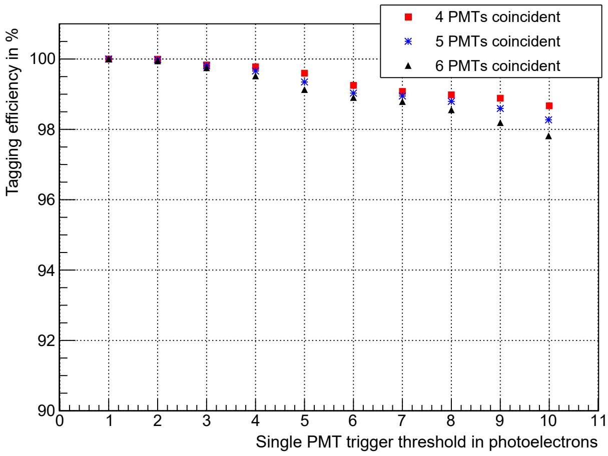

(a)

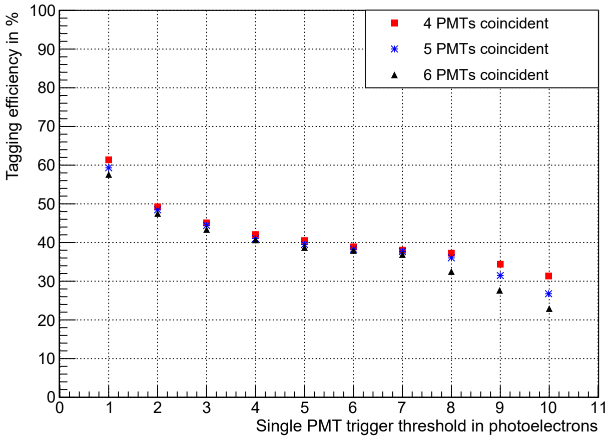

(b)

Figure 6.23.: Muon veto tagging efficiency for (a) muon events and (b) shower events, assuming the PMT arrangement presented in Figure 6.22 and different trigger conditions. On the x-axis, the amount of photoelectrons necessary to trigger a single PMT is varied. With red squares, blue stars and black triangles, the efficiency based on a requirement of 4, 5 or 6 PMTs triggering in coincidence is shown.

Here, the focus is set on the preferred arrangement found as a result of the studies, sketched in Figure 6.22. For the PMTs on the bottom of the tank, positions on a ring closer to the center or closer to the outer walls have been considered. However, due to the different distributions of Cherenkov light from muon and shower events, the best compromise is found with PMTs on both the inner and outer ring, as shown in Figure 6.22b for the example of 18 bottom PMTs. The two rings are positioned at radii of 170 cm and 300 cm. On the mantle of the tank, additional PMTs are placed. The height is chosen such that vertical distances among PMTs and between the PMTs and tank borders are equal. Going around the circle at the same height, they are placed at equally-distanced angles. The example in Figure 6.22a shows 10 PMT positions, distributed in 2 rings of 5 PMTs each. Variations are tested with different amount of PMTs and moving the lower and upper ring further to the bottom and top of the wall. Additionally, offsetting the rings against each other by rotating every second ring by half the angular distance between PMTs, is assayed. However, no significant improvements in veto efficiencies could be found. Again, the reader is referred to Appendix D for pictures and assessments of the various modifications. As also the mounting in the water tank will be easier with the PMTs vertically aligned, the baseline design as shown in Figure 6.22 is kept.

The efficiency to veto muon-correlated events shall now be discussed and presented in more detail. Two conditions have to be defined for triggering the veto system: First, the number of photoelectrons necessary to trigger a single PMT; second, the amount of PMTs triggering in coincidence. One cannot trigger the whole veto system every time a single PMT measures one photoelectron, because of the high rate and related dead time that will be discussed in more detail further below.

The tagging efficiency is defined as the number of events in which the veto system is triggered divided by the total number of events. Its value is assessed for the dangerous simulated events assuming an arrangement of 18 (2×9) PMTs on the bottom and 10 (2×5) PMTs on the wall. Results are shown in Figure 6.23, assessed for a common assumption of requiring 4-6 PMTs in coincidence, like similarly used in XENON [196, 199]. Furthermore, a decreased efficiency when triggering on a larger number of photoelectrons can be obtained. As expected, the tagging efficiency is close to 100% for muon events (Figure 6.23a), while it is greatly reduced for shower events (Figure 6.23b). Also, the dependency on the required number of photoelectrons is much larger for shower events, as less Cherenkov light is created in these events. The presented design is the preferred one among the tested options. Redistribution of the 28 PMTs, e.g. using 10 (2×5) on the bottom and 18 (3×6) on the wall, yield lower efficiencies (see Appendix D for details). The studies lead to the conclusion that the best arrangement is found with the majority of PMTs placed on the bottom of the tank, likely due to most of the muons and muon-induced particles entering the water tank from the top and due to using a specular reflector on the walls.

6.4.4 Impact of Reflective Foil Properties

The results shown in Figure 6.23 are attained with assuming a specular reflectivity of 95%. While this is a rather conservative assumption, the effect of varying the assumed reflectivity can be discussed. As a basis for a comparison, triggering for single photoelectrons and 5 PMTs in coincidence is assumed.

The following variations are tested. The DF2000MA foil is specified to act as a wave-

Table 6.8.: Simulated trigger efficiency of the muon veto system for different foil reflectivity values, using the PMT arrangement shown in Figure 6.22, assuming a trigger threshold of one photoelectron per PMT and requiring a 5-fold coincidence.

Reflective foil properties	Tagging efficiency	
	Muon events	Shower events
95% reflectivity + WLS	99.96%	60.57%
95% reflectivity	99.92%	57.92%
85% reflectivity	99.81%	49.57%
0% reflectivity	99.22%	43.82%

length shifter (WLS), benefitting the efficiency by absorbing UV photons and reemitting them at higher wavelengths, for which the PMTs are more sensitive. According to Ref. [200], this basically doubles the average efficiency of tagging Cherenkov photons. With this information, the simulation using the 95% reflectivity is reassessed for including the WLS properties in the analysis post-simulation. Additionally, two simulations are performed with reduced foil reflectivity of 85% and 0%, the first to check the tagging efficiency if the foil is slightly damaged, the second to do the test for the assumption of not using a reflective foil at all.

Results for the four assessed foil properties are listed in Table 6.8. The tagging efficiency for muon events is only influenced marginally and lies always above 99%. For shower events, the effect is larger due to the lower amount of Cherenkov light. Tagging efficiencies range from over 60% using a good reflector with WLS to below 45% without employing a reflective foil. Again, however, one has to recall that only a few percent of all dangerous events are shower events.

6.4.5 Trigger Rate and Dead Time Considerations

The trigger condition chosen for the muon veto system usually requires only a single photoelectron to trigger an individual PMT in order to maximize the tagging efficiency. Especially for shower events, the efficiency otherwise drops drastically. Setting this condition, the amount of PMTs that have to trigger in coincidence is then chosen such that a sufficiently low trigger rate is attained. A sufficiently low trigger rate is equivalent to an acceptable dead time in the measurement.

As the cryodetectors feature a rather slow response with pulse rise times of a few milliseconds and decay times in the order of hundred milliseconds [180], the muon veto trigger rate should not exceed $\sim$1–10 s^{-1}. This can be estimated by using Eq. 6.1 to calculate the probability of randomly vetoing events, which resembles the dead time in the measurement. The rate R, in this case, is the total muon veto trigger rate and

Table 6.9.: Correlated trigger rates (simulated) in the PMTs of the veto system due to ambient gammas entering the water tank.

Coincidence requirement	1 PMT	2 PMTs	3 PMTs	4 PMTs	5 PMTs
Trigger rate / s^{-1}	13576	171	2.0	0.02	<0.01

Δt is the time interval around a muon veto trigger used to reject cryodetector events. With $\Delta t = 10\,\mathrm{ms}$, similar to conditions in CRESST [4], $R = 1\,\mathrm{s}^{-1}$ ($10\,\mathrm{s}^{-1}$) would lead to roughly 1 % (10 %) dead time.

The rate due to muons traversing the tank is rather low and can be estimated, based on the muon flux of ~$1\,\mathrm{m}^{-2}\,\mathrm{h}^{-1}$ and the size of the water tank, to ~$0.02\,\mathrm{s}^{-1}$. A much larger rate, depending on the PMT coincidence requirement, may however come from random coincidences due to the dark counts of the PMTs as well as due to ambient gammas creating Cherenkov light via secondary electrons.

Gamma events may lead to correlated coincident triggering of one or more PMTs. The gamma flux at LNGS can conservatively be approximated to ~$1\,\mathrm{cm}^{-2}\,\mathrm{s}^{-1}$, such that $\sim 2 \cdot 10^6\,\mathrm{s}^{-1}$ would be entering the water tank. A simulation is performed with $2 \cdot 10^7$ gammas, only corresponding to $\sim$10 s exposure, but providing decent statistics. The trigger rates due to correlated photons from the same gamma event, for different numbers of PMTs in coincidence, are given in Tab. 6.9. Single PMT triggers among the 28 PMTs occur roughly 13576 times per second. Correlated events between two PMTs occur with a rate of $171\,\mathrm{s}^{-1}$, between three with $2.0\,\mathrm{s}^{-1}$, and so on, as listed in the table. Sensitivity to less than $0.1\,\mathrm{s}^{-1}$ with a simulated exposure of only 10 s is achieved via feeding the same data multiple times to the analysis chain, where the quantum and collection efficiencies of the PMTs are considered.

Dark counts are mostly induced by thermionic emission currents and are thus uncorrelated between PMTs. The mean dark count rate found by XENON in their Hamamatsu R5912 PMTs is ~$1200\,\mathrm{s}^{-1}$ [199]. However, the rate specified by Hamamatsu in the data sheet [198] is $6000\,\mathrm{s}^{-1}$ on average with a maximum of $10000\,\mathrm{s}^{-1}$. Different numbers can be assumed and compared in the following calculations.

To assess the total rate for various trigger conditions, random statistical coincidences between dark counts in different PMTs as well as triggers due to ambient gammas have to be considered within a certain trigger time window. The time window for the coincidence condition is chosen according to the simulation performed for the trigger efficiencies. In Figure 6.24, the time between first PMT trigger and the last one to reach the required coincidence (in this case 5-fold) is shown. Based on these plots, a time window of $\Delta t = 500\,\mathrm{ns}$ is assumed. To calculate the random coincidence rates in this time frame, the exponential waiting time distribution,

$$w(t) = R \cdot e^{-R \cdot t} \quad , \tag{6.1}$$

with the rate R is used. The probability for a trigger happening within the time window

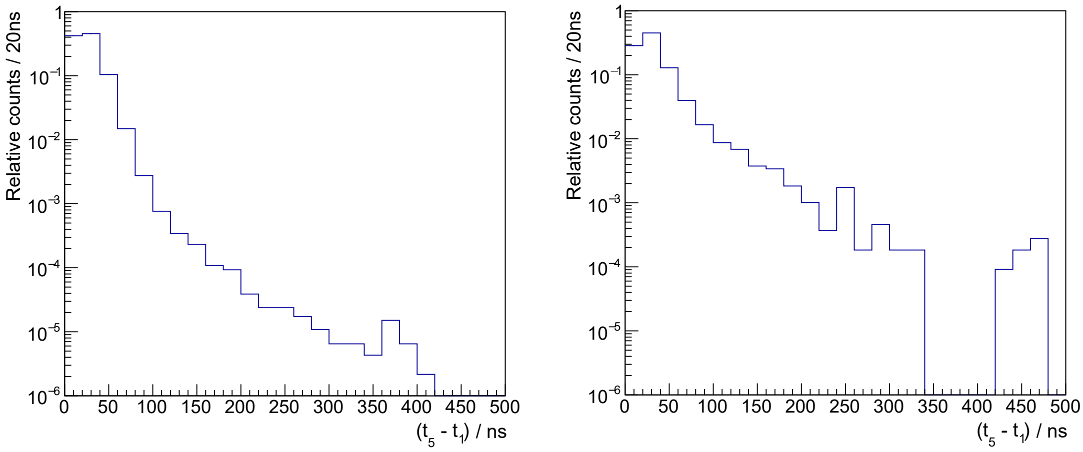

(a) (b)

Figure 6.24.: Simulated time difference between first and fifth single PMT triggering for (a) muon events and (b) shower events, i.e. the simulated true muon veto response time assuming a 5-fold PMT coincidence requirement.

Δt is then given by the integral from zero to Δt,

$$p(\Delta t) = \int_0^{\Delta t} R \cdot e^{-R \cdot t} \, dt = 1 - e^{-R \cdot \Delta t} \quad . \tag{6.2}$$

If the rate R is much lower than $(\Delta t)^{-1}$, the probability in Eq. 6.2 can be approximated by $R \cdot \Delta t$. For higher number of coincidences, the probabilities can be combined by multiplication. Furthermore, all the combinatorial options according to the number of PMTs have to be considered. The coincidence rate is then attained by multiplying the combined probability with the rate, such that

$$R_n = \binom{N-1}{n-1} \cdot R^n \cdot \Delta t^{n-1} \quad , \tag{6.3}$$

where N is the total number of PMTs and n the number of PMTs required to be in coincidence. However, Eq. 6.3 is only true for a single uncorrelated rate in all the PMTs, e.g. the dark counts. In Tab. 6.10, the rate only considering random coincidences between dark counts is hence listed. To take into account the random coincidences between dark counts and ambient gammas as well as between various ambient gamma events, further combinatorial options have to be added to the equation. The extended equation then reads

$$R_n \approx \binom{N-1}{n-1} \cdot R_d^n \cdot \Delta t^{n-1} + \sum_{j=1}^{n} \binom{N-j}{n-j} \cdot R_{\gamma,j} \cdot R_d^{n-j} \cdot \Delta t^{n-j} + \sum_{k=1}^{n/2} R_{\gamma,k} \cdot R_{\gamma,(n-k)} \cdot \Delta t \quad , \tag{6.4}$$

Table 6.10.: Random coincidence rate between n PMTs due to dark counts, as calculated using Eq. 6.3 with $\Delta t = 500\,\mathrm{ns}$.

Dark count rate / s^{-1}	Coincidence rate / s^{-1}			
	n = 2	n = 3	n = 4	n = 5
1200	19.4	0.2	$7.6 \cdot 10^{-4}$	$2.7 \cdot 10^{-6}$
6000	486.0	19.0	0.5	$8.5 \cdot 10^{-3}$
10000	1350.0	87.8	3.7	0.1

Table 6.11.: Random coincidence rate between n PMTs due to ambient gammas and PMT dark counts combined, as calculated using the approximated formula in Eq. 6.4 with $\Delta t = 500\,\mathrm{ns}$.

Dark count rate / s^{-1}	Coincidence rate / s^{-1}			
	n = 2	n = 3	n = 4	n = 5
1200	502.5	7.7	0.1	0.01
6000	1848.8	78.3	2.2	0.06
10000	3445.9	232.3	10.3	0.3

where R_d is the dark count rate and $R_{\gamma,x}$ the rate due to ambient gammas inducing an x-fold coincidence. Further additions would have to be made to consider the contribution due to coincidences between two or more ambient gamma events in the second term as well as three or more ambient gamma events in the third term. However, for the sake of simplicity, Eq. 6.4 is used as an approximation to get an estimate on the order of magnitude. Based on this equation and ambient gamma rates in Tab. 6.9, the total random coincidence rates are calculated and presented in Tab. 6.11. As mentioned, this is an order of magnitude approximation. Actual numbers could be higher and, depending on the maximum allowed rate, too high for low PMT multiplicities. Setting the requirement to a 4- or 5-fold coincidence to veto an event may however be realistic when looking for a number in the order of $1\,s^{-1}$ or below, comparing to the calculated values.

The largest contribution to the rate comes from the second term in Eq. 6.4 due to coincidences between ambient gamma events and PMT dark counts. Discussions with experts from other rare events search experiments using water Cherenkov muon veto systems yield that it might be beneficial to split the water volume into a passive border and an active central region. This could be achieved by mounting the reflective foil at a certain distance from the tank walls and would lead to a much reduced random coincidence rate due to ambient gammas. A detailed study of using a passive border region is out of the scope of this work. Only a preliminary test with a 30 cm passive border has been performed. The size is chosen according to the length of the PMTs and their support with the idea in mind that the PMTs themselves can be mounted directly to the tank wall with only their windows looking through holes in the reflective foil curtains. With a passive border only on the mantle wall, the trigger rates due to ambient gammas could be reduced by slightly more than 50%. Adding this layer also on the bottom and top, the trigger rate is even reduced by more than 90%. This may reduce the total trigger rate and allow for vetoing events based on a reduced coincidence condition. However, a more in-depth study of various thicknesses of such a passive border region and the effect both on the random coincidence rate as well as on the muon tagging efficiency has to be studied in a future work.

6.4.6 Optimal Muon Veto Design

To sum up, arrangements of PMTs in the water tank were assessed based on simulating events, in which a secondary neutron reaches the dry-well. The employed and tested options took into account the potential number of PMTs available for the veto system. In the evaluation, both the veto efficiency and the total trigger rate and hence dead time were considered.

According to the attained results, a preferred solution is found employing 18 (2×9) PMTs on the bottom at radii of 170 cm and 300 cm as well as 10 (2×5) PMTs on the wall at heights of 230 cm and 460 cm. A reflective foil increases the tagging efficiencies, especially for events, in which only shower particles traverse the water tank. As a feasible trigger condition for the veto, triggering each PMT for single photoelectrons and requiring coincidence between 4 or 5 PMTs is found. With this configuration, depending on the actual dark count rate, a veto trigger rate of the order of $1\,\mathrm{s}^{-1}$ may be achieved, yielding an acceptable dead time.

Future studies will additionally assess if a dead layer at the border of the tank can help in further improving the compromise between setting a certain trigger condition and coping with a distinct amount of dead time in the experiment.

6.5 Conclusion and Outlook

The studies presented in this chapter were laying the ground for the design of the COSINUS apparatus, which will be used to conduct a model-indepedent cross-check of the DAMA/LIBRA results. Background simulations in variations of a simplified shielding geometry were performed, determining the one that minimizes the particle flux reaching the detectors, focusing on neutrons as the most dangerous background. Based on the results, COSINUS decided on building a water tank of 7 m in diameter and height, with a dry-well (~70 cm diameter) housing the inner copper shielding (8 cm thickness) and the cryostat. According to technical drawings of the cryostat and early CAD drawings of the water tank, a more detailed geometry of the final setup was implemented in the Geant4 based software. This was used to estimate the neutron background rate in an arrangement of 10 or 44 detector modules, assuming a threshold of 1 keV and applying an anti-coincidence cut. The muon-induced neutron background rate without a muon veto was estimated to be in the order of a few counts per kilogram and year. As already hinted by the results of the simulation in the simplified geometry, this manifested the need for instrumenting the water tank with PMTs for an active veto. Simulations were hence performed to estimate the efficiency of such a veto when using ~30 PMTs. A preferred arrangement with 18 PMTs on the bottom and 10 PMTs on the wall was found, providing a total tagging efficiency for dangerous events of ~99% when triggering each PMT for single photoelectrons and requiring 4 or 5 PMTs to trigger in coincidence. This will allow to achieve the background goals of the experiment with respect to neutrons. To reduce the total trigger rate due to random coincidences, the idea to implement a passive water region at the tank border was further brought up. A detailed study of its influence on trigger efficiencies and random coincidences due to ambient gammas, however, was out of the scope of this work and will have to be assessed in the future.

At the time of writing this thesis and after finalizing the presented simulations, the construction of the COSINUS setup at LNGS and the procurement of required materials has already started. The water tank has been put in its place in hall B of the LNGS underground laboratory and the cryostat has been ordered. As the commissioning run is only a few steps away, a lot of simulation studies will be necessary, building upon the work performed in this thesis.

Besides the in-depth study regarding the passive layer in the water tank, the focus should be on the development of a comprehensive background model. Recently received screening results of procured materials used for dry-well, copper shielding, cryostat and detector holder can be used to update the internal radiogenic background simulations. Additionally, simulations will rely on measurements of the intrinsic contamination in the NaI crystals that will be employed in the setup. As intrinsic sources are expected to provide an important contribution to the total rate, a detailed model of this background and its leakage into the nuclear recoil bands is of primary importance. For this study, however, at first a final design of the detector modules has to be specified and integrated in the simulated geometry.

7 Summary and Conclusion

This work comprises detailed neutron simulation studies for the CRESST and COSINUS dark matter search experiments. The respective results yield important implications in both cases.

In CRESST, the goal of the studies was to model the neutron calibration and neutron background, and to compare the simulations to data taken during CRESST-III Run34 with detector A.

Initially, the neutron simulation models were tested on the AmBe neutron calibration of this experimental run. The thereby obtained nuclear recoil spectra can in the future be used as an input to refine the modeling of measured data. In the analysis of the simulation, besides the elastic nuclear recoil spectra, distinct features due to thermal neutron capture reactions could be identified. While Geant4 was found to calculate the recoil energies in these processes incorrectly, some of the peaks may be expected to be found in real data, especially the one due to ^{182}W(n,γ)^{183}W located around 112.4 eV. This peak could provide a fundamental input to the direct energy calibration of nuclear recoils in $CaWO_4$ and the comparison between the nuclear recoil and electron recoil energy scales. Indeed, in the subsequent analysis of the measured data, a statistically significant peak around 113.3 eV was found. Due to systematic uncertainties on the energy reconstruction, this peak could be compatible with the expected one. While this is already a highly promising result, a higher statistics neutron calibration campaign will be necessary to conclude the findings and verify the peak in additional detector modules.

Subsequently, the major radiogenic and cosmogenic neutron background sources were evaluated. In the context of the muon-induced background simulation, the active muon veto, essential for the reduction of the neutron background, was thoroughly assessed. A tagging efficiency close to 99 % was found, reducing the cosmogenic below the ambient and internal radiogenic neutron background level. After muon veto and anti-coincidence cuts, an integral nuclear recoil background rate of $\sim 4.36 \cdot 10^{-1}$ (kg yr)$^{-1}$ in the ROI is estimated. By assessing the flux of neutrons entering different volumes in the simulation, additional insight could be gained about the production and mitigation of neutrons in the various employed shielding layers. The estimated rate of nuclear recoils obtained, however, already only leads to a negligible background contribution, as the probability of one nuclear recoil event being observed in the ROI during the background exposure of detector A can be calculated to roughly 0.4 %. Hence, neutrons originating from known sources can furthermore be excluded as a significant contribution to the low energy excess in CRESST-III.

In COSINUS, the principal simulation study, laying ground for the passive and active shielding design of the experiment, was performed in this work.

With a simplified geometry, the attenuation power of the basic shielding design against neutron and gamma background was optimized. Given the spacial constraints at LNGS, the assessment lead to the choice of using a water tank of 7 m in diameter and height and an additional 8 cm copper shielding around the central cryostat. With this setup, currently under construction at LNGS, the external background particle flux can be minimized.

A detailed optical simulation was furthermore performed to optimize the arrangement of PMTs in the water tank for the active Cherenkov muon veto. A layout with 18 PMTs in two rings on the bottom and 10 PMTs in two rings on the wall was evaluated as the preferred solution. It provides a tagging efficiency of roughly 99 % for events, in which neutrons reach the dry-well housing the cryostat. This value is based on the assumption of triggering each PMT for single photoelectrons and requiring a coincidence between 4 or 5 PMTs in a time window of 500 ns. Based on these conditions, the corresponding total trigger rate due to random coincidences was estimated at a feasible rate in the order of 1 s^{-1}, considering ambient gammas and PMT dark counts. Further detailed studies evaluating a passive border region in the water tank to better estimate and further reduce this rate are subject of an ongoing and future study. All in all, the neutron background study yields an estimated nuclear recoil background rate in the order of 10^{-2} $(\mathrm{kg\,yr})^{-1}$above a 1 keV threshold, hence reaching the goal of an almost negligible nuclear recoil rate in 1000 kg·d projected exposure to be taken during COSINUS-1π.

With the identification of a possible new energy calibration technique in CRESST, the potential input to a likelihood-based background model via providing simulated nuclear recoil spectra, the shielding design study for COSINUS and the detailed assessment of an active Cherenkov muon veto, the simlation studies presented in this work strongly contribute to the future research conducted in the respective experiments.

A | Neutron Interaction Cross Sections in $CaWO_4$ and NaI

Supplementary to the discussion of neutron interactions in matter in Section 3.1.2, cross sections for elastic and inelastic processes of incident neutrons within the typical materials used in CRESST, i.e. $CaWO_4$, and in COSINUS, i.e. NaI, are presented in the following. As the main interest in accordance with the topics discussed throughout this thesis are the overall elastic and inelastic interaction cross sections as well as specifically the cross sections for radiative neutron capture processes, the plots are restricted to showing these respective curves. Furthermore, the graphics are limited to depicting only the isotopes of each element with a natural abundance of more than 1 %. All plots are created with and taken from the ENDF online database [90, 91].

In Figure A.1, the cross section data for the natural W isotopes are displayed. In the MeV range, elastic (green) and inelastic (gray) processes are of similar importance. Below, elastic scattering dominates, before the inelastic processes via radiative neutron capture (red) become the main interaction channel.

Figure A.2 shows the cross section data for the natural Ca isotopes. Here, the elastic processes (green) start dominating already at slightly higher energies, and radiative neutron capture (gray) is a rather subdominant process, except at lowest energies.

In the cross section data for an O target, presented in Figure A.3, a similar picture is found. An even stronger statement can be made about radiative neutron capture processes (red), which are almost negligible in this case.

The situation for neutrons interacting with Na, depicted in Figure A.4, is also similar and roughly comparable to that obtained for Ca and O targets.

Finally, the cross sections for I, presented in Figure A.5, again show a larger radiative neutron capture cross section (red), dominating for low incident neutron energies.

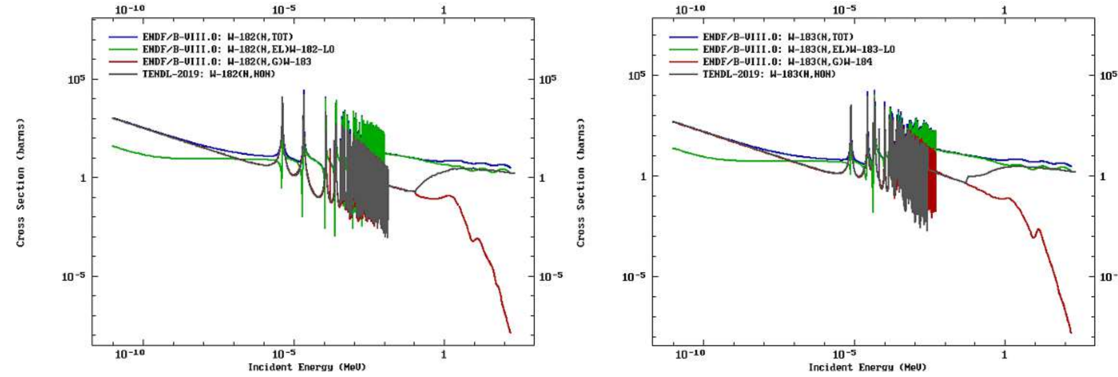

(a) ^{182}W (b) ^{183}W

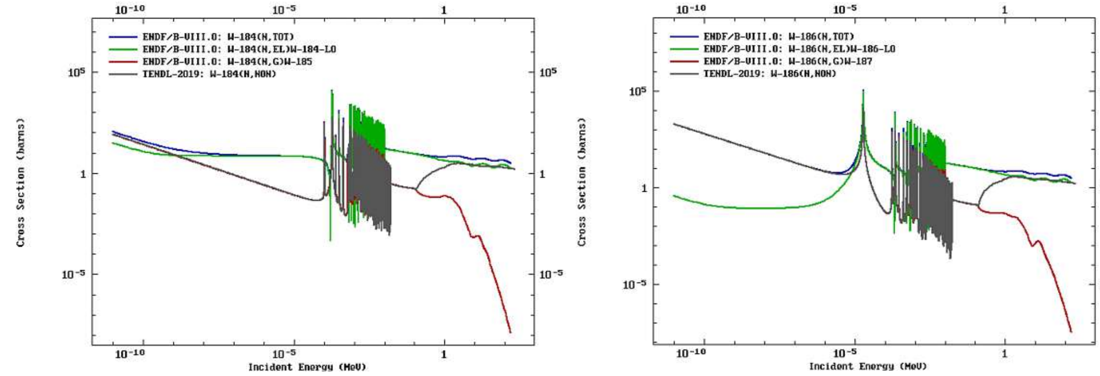

(c) ^{184}W (d) ^{186}W

Figure A.1.: Cross section data for neutrons impinging on W isotopes, according to the ENDF online database [90, 91]. The depicted curves represent the total cross section (blue) as well as the individual cross sections for elastic (green), inelastic (gray) and (n,γ) processes (red).

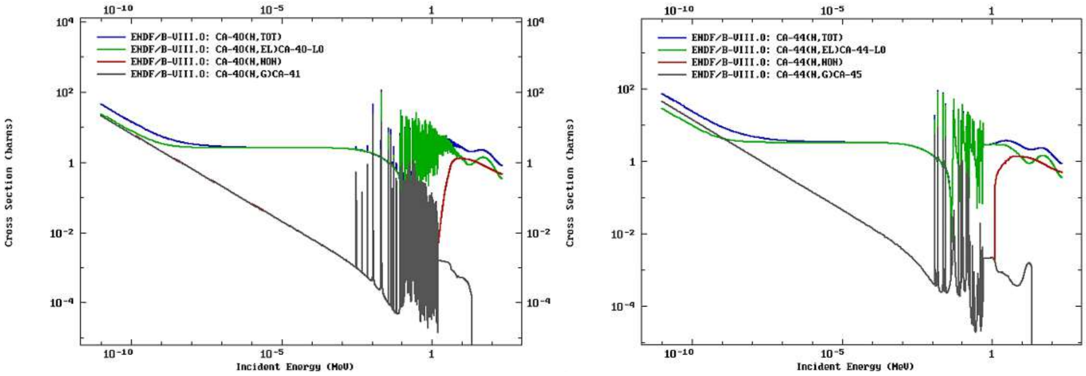

(a) ^{40}Ca (b) ^{44}Ca

Figure A.2.: Cross section data for neutrons impinging on Ca isotopes, according to the ENDF online database [90, 91]. The depicted curves represent the total cross section (blue) as well as the individual cross sections for elastic (green), inelastic (red) and (n,γ) processes (gray).

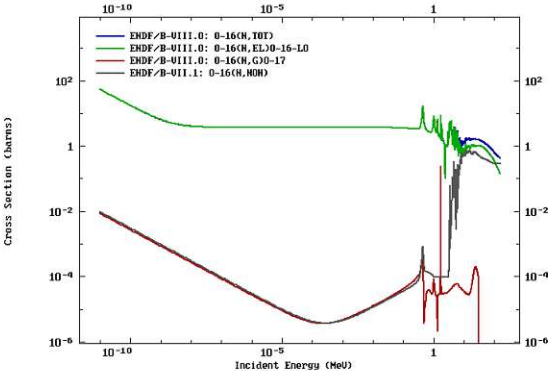

Figure A.3.: Cross section data for neutrons impinging on ^{16}O, according to the ENDF online database [90, 91]. The depicted curves represent the total cross section (blue) as well as the individual cross sections for elastic (green), inelastic (gray) and (n,γ) processes (red).

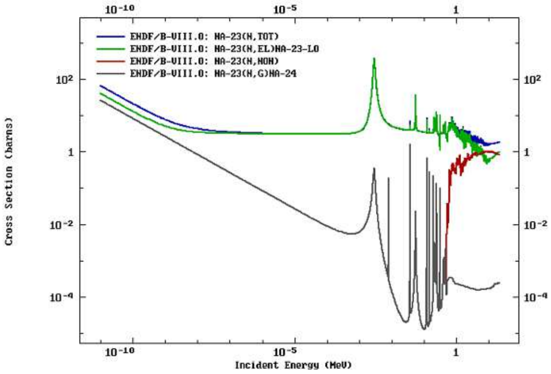

Figure A.4.: Cross section data for neutrons impinging on ^{23}Na, according to the ENDF online database [90, 91]. The depicted curves represent the total cross section (blue) as well as the individual cross sections for elastic (green), inelastic (red) and (n,γ) processes (gray).

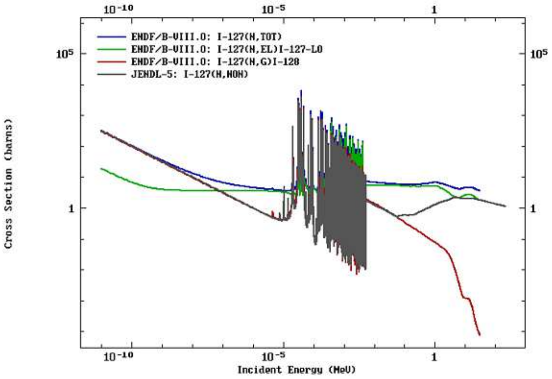

Figure A.5.: Cross section data for neutrons impinging on ^{127}I, according to the ENDF online database [90, 91]. The depicted curves represent the total cross section (blue) as well as the individual cross sections for elastic (green), inelastic (gray) and (n,γ) processes (red).

B Usage of new ImpCRESST Features

As an addendum to the description of newly implemented features to the ImpCRESST simulation software presented in Section 4.1.4, the usage of respective commands shall be discussed in a bit more detail in the following.

B.1 Bulk Contamination Particle Generator

As described in Section 4.1.4, the bulk contamination particle generator has been programmed to allow for a versatile selection of volumes as starting position for the primary particles in the simulation. The positions would then be homogeneously sampled inside all the respective volumes.

In a macro file, to use this so-called *contaminantSource*, the type of particle source can be selected via the UI command

```
/source/type contaminantSource
```

and a level of verbosity

```
/contaminantSource/verbose <integer value>
```

can be set to select the details printed to the log. The <integer value> that denotes the verbosity ranges from 0 to 3, with higher values providing a more detailed print out.

After selecting the *contaminantSource* and building the geometry for the simulation, the commands for choosing the contaminated volumes can be used.

With the command

```
/contaminantSource/confineToVolume <volume name>
```

a specific volume can be chosen by specifying its name according to the definition in the respective geometry code.

With the command

```
/contaminantSource/confineToMaterial <material name>
```

all volumes present in the geometry, which are made of the same material, can be selected.

With the command

```
/contaminantSource/confineToMaterialInVolume <material name> <volume
    name>
```

the selection of volumes made of the same material can be constrained to those geometrically enclosed by the specified volume. As we typically make use of the hierarchical geometry structure of Geant4, this could be the volumes made of the respective material down the hierarchy.

With the command

```
/contaminantSource/excludeVolumesInside <volume name>
```

all volumes geometrically fully enclosed by the specified volume can be excluded from the previously selected ones.

With the command

```
/contaminantSource/excludeDetectorVolumes
```

specifically the detector modules can be excluded from the previous selections. This is done, for example, if the simulation is split into two parts, where one deals with background external to the detector modules and the other with the internal background.

With the command

```
/contaminantSource/confineToMaterialInDetectors <material name>
```

volumes only inside the detector modules and made of the same specified material can be selected.

Any number of such commands can be used together in a single macro file to choose a dedicated combination of volumes as starting positions. Once the selection via these commands is finished, an additional line

```
/contaminantSource/init
```

is necessary to initialize the particle generator with the selected volumes before starting the simulation.

The type of primary particle as well as its energy can still be set using the commands of the Geant4 general particle source (gps)

```
/gps/particle ion
/gps/ion 82 210
/gps/ang/type iso
/gps/energy 0 MeV
```

where in this example a contamination with ^{210}Pb at rest inside the volumes would be chosen and subsequently simulated by using the typical

```
/run/beamOn <number of events>
```

command.

B.2 SOURCES Interface

The SOURCES software, as explained in Section 4.1.4, calculates the neutron yield due to (α,n) and s.f. reactions in materials, based on the specified contamination with radioactive nuclei. In one of the output files of SOURCES, named *tape7*, the number of neutrons in units of $1/(\mathrm{cm}^3\,\mathrm{s})$ due to each individual reaction as well as the total of all reactions is given in tabulated form. This data can be used with the newly written SOURCES interface in ImpCRESST to sample primary neutrons accordingly.

The interface is an extension to the *contaminantSource* primary particle generator, such that it is used in combination with the commands detailed in Section B.1. The difference is solely the definition of the primary particle, previously done via the Geant4 general particle source and now via the SOURCES interface. For this, first the command

```
/contaminantSource/useSOURCESInterface
```

is used to specify the selection of the interface, before the line

```
/contaminantSource/SOURCESfile </path/to/tape7-file>
```

specifies the respective SOURCES file used for sampling the energy of the primary neutrons with isotropically distributed momentum direction.

B.3 MUSUN Interface

MUSUN, as mentioned in Section 4.1.4, provides a discrete list of energy, position and direction of each single muon at the respective underground location and on a user-defined surface. This list can then be read in with the newly developed MUSUN interface in ImpCRESST for further simulation, using the muons as primary particles.

In a macro file controlling the simulation, the command

```
/source/type musun
```

specifies the usage of the MUSUN interface for primary particle generation. With the additional command

```
/source/musun/filename </path/to/musun.dat-file>
```

the data file with the list of the muon parameters produced by MUSUN is selected.

When starting the simulation with

```
/run/beamOn <number of events>
```

the software would read the data file line by line to simulate a different muon starting condition in each event. The number of events should maximally correspond to the amount of lines in the data file.

Two additional commands to adapt the initial conditions can be applied before starting the simulation.

With the command

```
/source/musun/filename/startAtLine <line number>
```

the data file will not be read from the beginning but starting from the chosen line. This is very useful if the number of lines in the file exceeds the feasible number of events to be simulated in a single run and hence the simulation has to be divided in several parts. For example, to simulate muons with attributes specified in lines 1001 to 2000 in the MUSUN file, one has to issue:

```
/source/musun/filename/startAtLine 1001
/run/beamOn 1000
```

With the command

```
/source/musun/zShift <real number> <unit of length>
```

the positions of the muons given in the MUSUN data file can be shifted along the z-axis which is used if the volumes, especially the defined hall surrounded by rock, is not vertically centered in the simulated *world volume*.

B.4 Parallel World Tracking

As discussed in Section 4.1.4, a *parallel world* in Geant4 can be used to attain additional information about particles and their tracks while not affecting the tracking of particles through the physical geometry. To allow for a versatile definition of the parallel world via macro commands at run time with ImpCRESST, a special class called *ParallelWorldConstruction* was developed in the course of this thesis. So-called *scorers* defined in a separate class called *SurfaceScorer* can be associated to a volume to store information about energies or currents of particles entering or leaving the volume at its outer surface.

In the macro file of the simulation, the layout of the parallel world is set after building the *physical world* used for tracking. The scorers in the parallel world are defined by applying commands of the pattern

```
/geometry/addScorer <volume name> <particle name> <type> <surface flag
    > <direction>
```

which allow for maximum flexibility. The volume name is the name of a volume in the physical world that should be copied to the parallel world and assigned a scorer. For the particle name, the user can choose between attaining the information for a specific particle (e.g. *neutron*, *gamma* or *e-*) or for all possible particles combined by typing *all* for this parameter. The type can either be *current* to get an amount of particles per cm^2 or *energy* to store the energy of each of the particles. The surface flag can be used to attain the information only for particles traversing a specific surface according to the definition in the SurfaceScorer class, or for all surfaces by entering a value of *0*. Finally, the direction has to be specified as *in* or *out*, meaning either storing information about particles entering or particles exiting the respective volume at its surface.

Any number of commands defining scorers accordingly, then have to be followed by a line reading

```
/geometry/buildParallelWorld
```

to eventually build the volumes in the parallel world and to associate the scorers to them subsequently.

C | Additional CRESST Neutron Calibration Data

The following discussions are complementary to those in Section 5.4.3. Additional neutron calibration data collected with $CaWO_4$ detectors in CRESST-III are presented and analyzed in the context of the potentially observable (n,γ) peaks around 100 eV and the possible EC line located at ~ 2.8 keV due to ^{37}Ar.

The additional modules that were analyzed in CRESST-III Run34, besides detector A, are detector B, E and J. Their neutron calibration data together with an unbinned extended maximum likelihood fit are presented in Figure C.1. The procedure is the same as in Section 5.4.3, such that the "null fit" is the fit without considering any peaks, while the "best fit" includes all the discussed potential peaks. However, the higher energy thresholds have to be considered in the process, such that peaks below the threshold are naturally excluded from the fit. In general, the thresholds of 119.6 eV, 64.8 eV and 83.4 eV of detectors B, E and J, which are closer to the location of the potential (n,γ) peaks than the 30.1 eV threshold of detector A make the discussion more difficile. Due to the high threshold of detector B and issues in the operation of detector J, the results of the fits are very inconclusive and would not allow to identify the expected peak around 112 eV. Detector E, on the other hand, may allow for a better analysis and the fit returns a potential peak around 114 eV with 99.6 % significance.

For another comparison, a brief look at the $CaWO_4$ detectors Comm1, Comm2 and TUM93A operated in CRESST-III Run36 was made. Due to the neutron source being placed further away from the detectors in this run, the situation is not entirely the same. Also, the detectors all have an intrinsic ^{55}Fe source for energy calibration. Still, neutrons reaching the detectors will be expected to feature a similar or even softer spectrum because of traversing more material. Hence, the same or a larger amount of thermal capture reactions may occur. However, the statistics collected in the detectors during calibration is rather low. In Figure C.2, the histogrammed data together with the fits are presented. The energy range is now restricted to below 5 keV, which is well below the iron lines located at 5.9 keV and 6.5 keV. The fit finds two peaks around 110 eV and 2.8 keV in Comm1 and TUM93A, but their significance is only between 70–95 % due to the low statistics. All other peak significances in the depicted energy range are well below 50 %. In Comm2, peaks with significances of about 75 % are found around

101 eV and 2.55 keV. Both locations are approximately 10 % below the expected peak positions, which could either be a coincidence or hint towards an issue in the energy calibration.

All in all, the results obtained from the neutron calibration data of these additional detectors, although partly hinting towards the expected peaks, are less conclusive than the apparent findings in detector A. Hence, as mentioned in Section 5.4.3, further dedicated studies, in which larger statistics are collected during neutron calibration, are necessary to clearly assess the validity and the potential of observing said peaks.

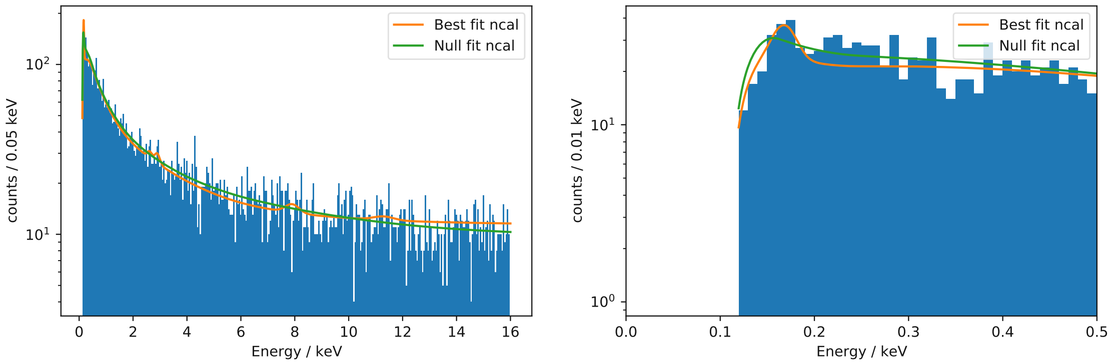

(a) Detector B.

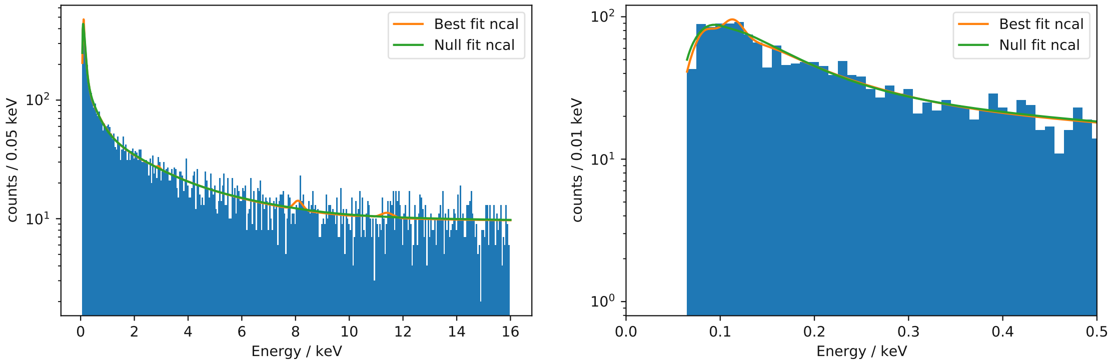

(b) Detector E.

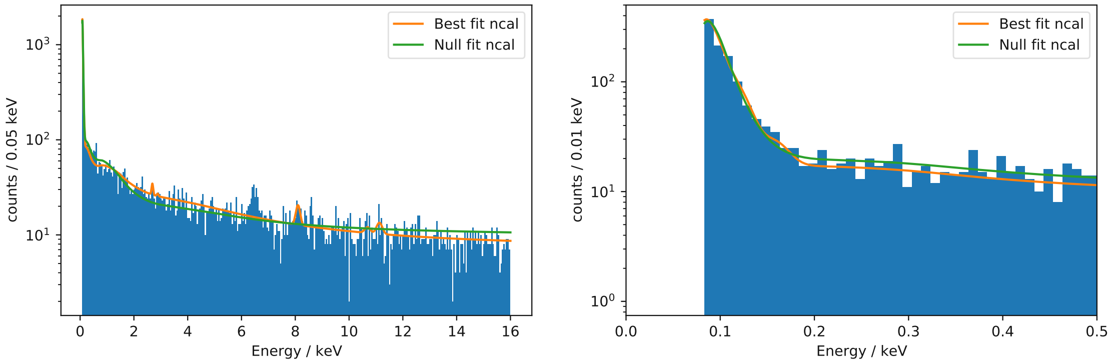

(c) Detector J.

Figure C.1.: Likelihood fit of neutron calibration data for (a) detector B, (b) detector E and (c) detector J operated in CRESST-III Run34. The left side shows the entire ROI up to 16 keV, the right side the zoom to the first 0.5 keV. The "best fit" (orange) does consider the potential peaks, while the "null fit" (green) does not.

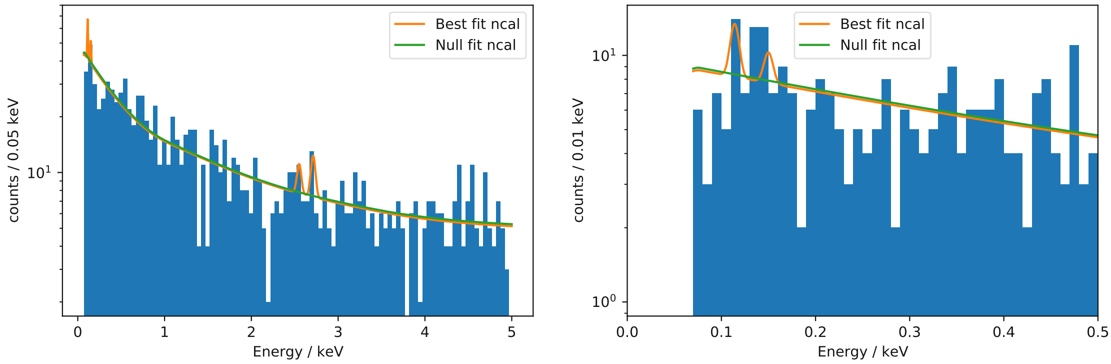

(a) Detector Comm1.

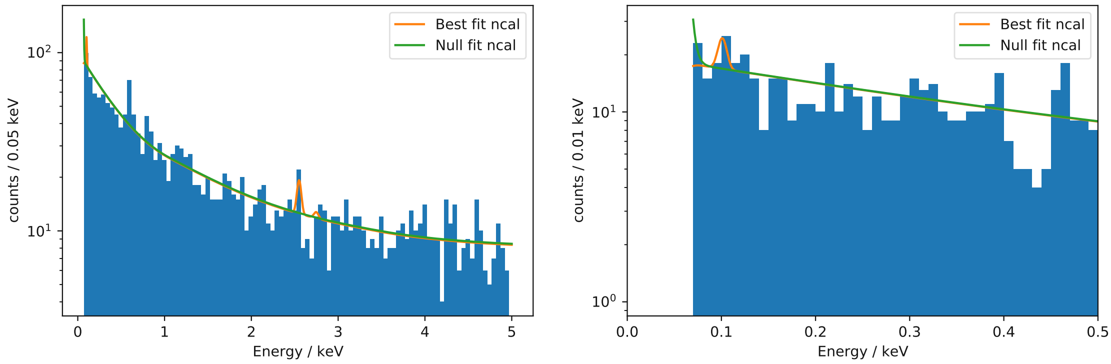

(b) Detector Comm2.

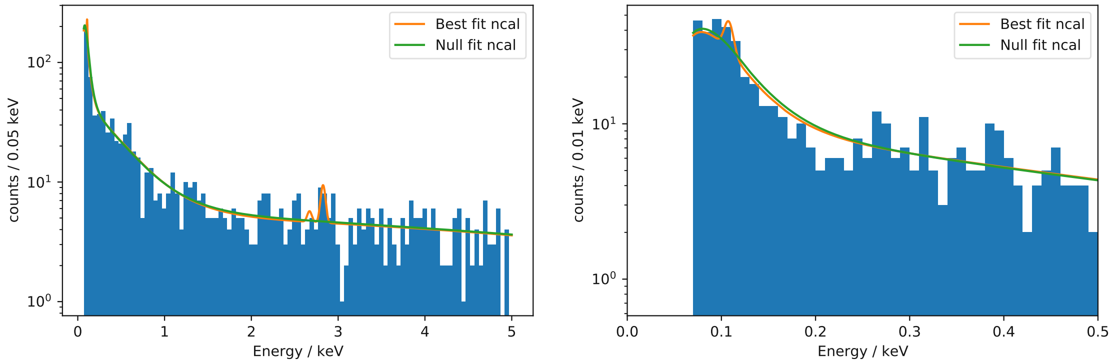

(c) Detector TUM93A.

Figure C.2.: Likelihood fit of neutron calibration data for detectors (a) Comm1, (b) Comm2 and (c) TUM93A operated in CRESST-III Run36. The left side shows the energy region up to 5 keV below the ^{55}Fe calibration lines, the right side the zoom to the first 0.5 keV. The “best fit” (orange) does consider the potential peaks, while the “null fit” (green) does not.

D | COSINUS Muon Veto Layout Assessment

In Section 6.4.3, the arrangement of PMTs in the preferred setup has been presented together with the attainable veto efficiency based on different trigger conditions. To find this optimal layout, given the constraint on the number of available PMTs (~ 30), a lot of variations have been tested. In the analysis of the respective simulation, detailed in Section 6.4, different amounts of PMTs were assumed to be placed on the bottom and on the wall of the water tank to tag the Cherenkov light created by muons and secondary charged particles. In the following, some of the variations are shown and discussed with respect to the attainable veto efficiency.

In the course of assessing the placement of PMTs in the water tank, first different positions on the bottom of the tank were assessed. Looking at the photon hit maps on the inner surfaces of the water tank, presented in Figure 6.20, it could be seen that the distribution on the bottom surface is rather clustered around the center of the tank for muon events, while the photons due to shower events are mostly found close to the border of the tank. Hence, a ring of PMTs at half the water tank radius was compared to one located close to the wall. As an example, this is shown in Figure D.1 and D.2 for arrangements of 8 PMTs in these bottom rings, combined with 3×8 PMTs on the wall. Indeed, evaluating the veto efficiencies it is found that the former arrangement with the PMTs on the bottom closer to the center favors the tagging of muon events while the latter slightly increases the efficiency for shower events. These effects are mostly visible when requiring larger amounts of photoelectrons to trigger a single PMT. While the difference looking at the foreseen single PMT trigger condition of only one photoelectron is marginal, the conclusion was to put two rings of PMTs covering both radial positions, as the tagging of either event class is similarly important.

Additional tests were then made to assess the distribution between the number of PMTs to put on the wall compared to the number on the bottom. As a comparison to the preferred option of placing 2×5 PMTs on the wall and 18 on the bottom, the same total amount of PMTs is kept with an arrangement of 3×6 PMTs on the wall and 10 PMTs on the bottom. The evaluation of this layout is presented in Figure D.3. In general, the veto efficiency was found to be higher when placing relatively more PMTs on the bottom, arriving at the conclusion regarding the preferred arrangement.

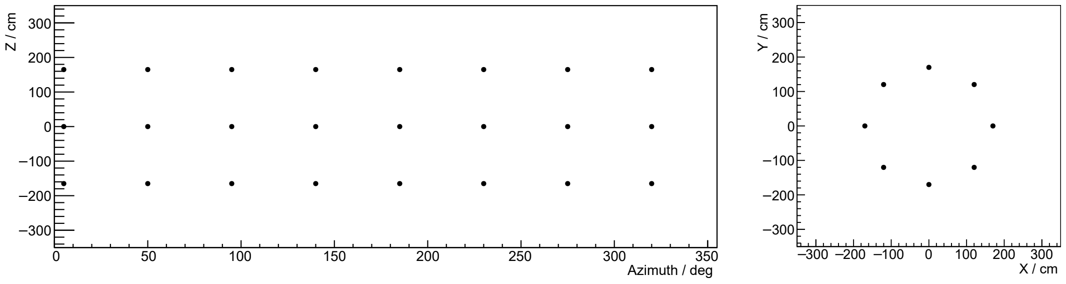

(a) PMT arrangement on wall (left) and bottom (right) of the water tank.

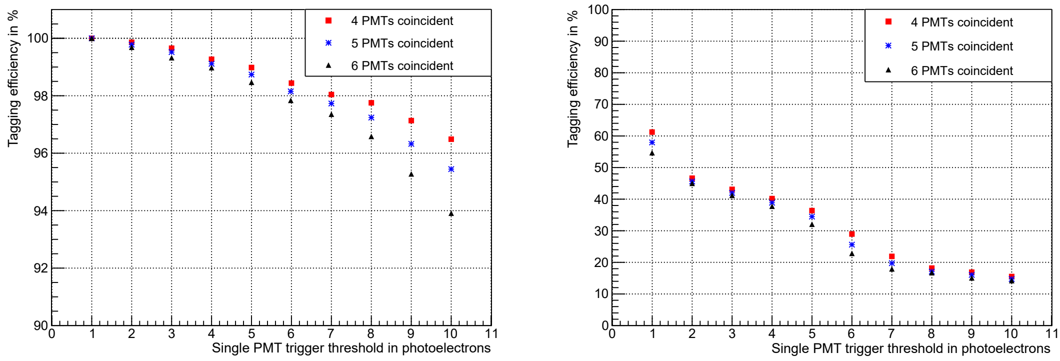

(b) Muon event tagging efficiency.

(c) Shower event tagging efficiency.

Figure D.1.: (a) Arrangement and (b,c) veto efficiency employing 24 (3×8) PMTs on the wall and 8 PMTs on the bottom of the water tank positioned at half the radius.

To further study the position dependence of the PMTs placed on the wall, various vertical and horizontal shifts were tested. As an example, Figure D.4 shows the evaluation of a horizontal shift between the rows on the wall in the arrangement of 3×6 PMTs, similar to the previously discussed option. This layout is expected to increase the tagging efficiency as it better covers the available space on the tank wall. While the results met the expectations, the improvement was not found to be significant, especially in the case of the foreseen trigger condition for the single PMTs. As furthermore the mounting and cabling of PMTs will technically be easier in case they are vertically aligned, the option without the horizontal shift was in the end favored.

More extreme scenarios with a large reduction of the amount of employed PMTs as well as with arrangements placing PMTs solely on the bottom of the tank have additionally been assessed. The latter case, in which only the 18 PMTs on the bottom of the tank from the preferred arrangement are considered, is exemplary shown in Figure D.5. As these tests, however, lead to rather significant reduction of the tagging efficiencies, the considered options were disregarded.

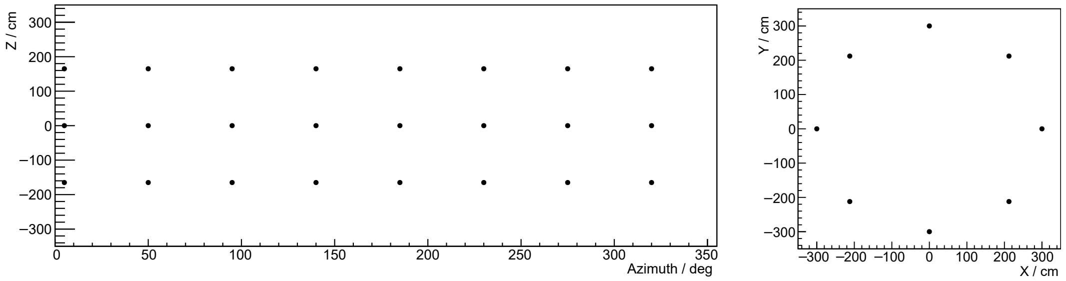

(a) PMT arrangement on wall (left) and bottom (right) of the water tank.

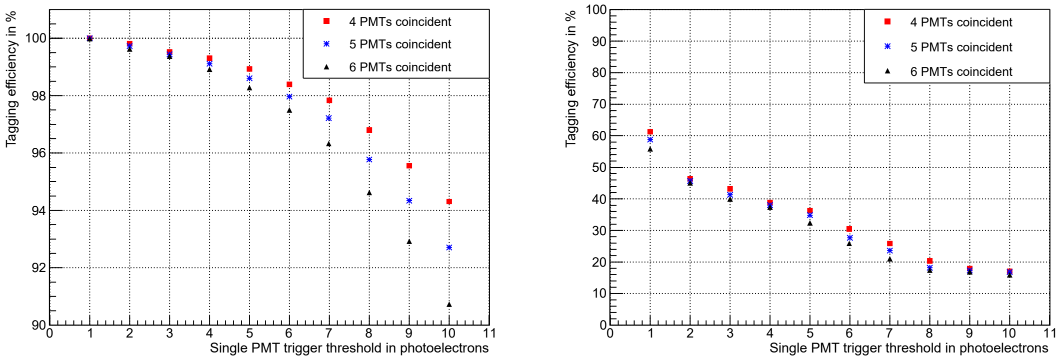

(b) Muon event tagging efficiency.

(c) Shower event tagging efficiency.

Figure D.2.: (a) Arrangement and (b,c) veto efficiency employing 24 (3×8) PMTs on the wall and 8 PMTs on the bottom of the water tank positioned close to the outer border.

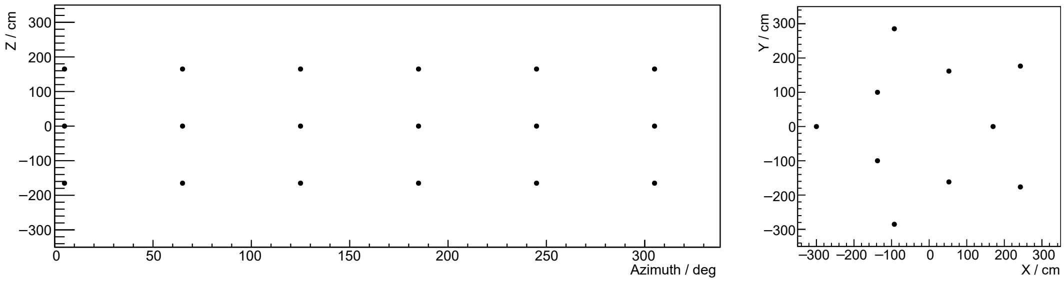

(a) PMT arrangement on wall (left) and bottom (right) of the water tank.

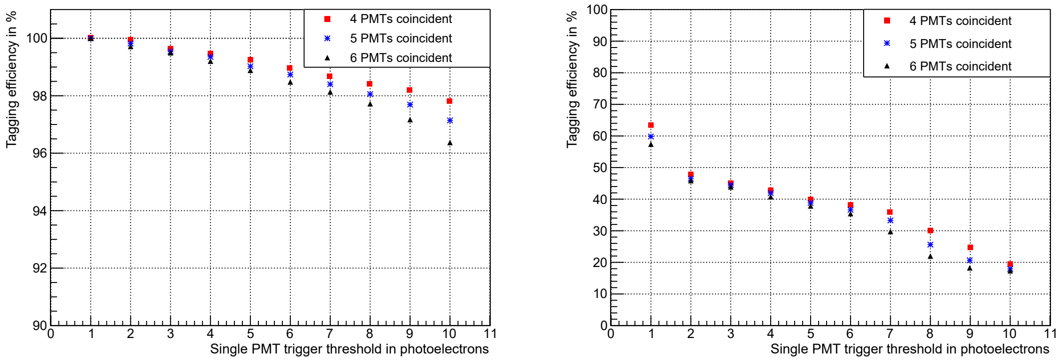

(b) Muon event tagging efficiency.

(c) Shower event tagging efficiency.

Figure D.3.: (a) Arrangement and (b,c) veto efficiency employing 18 (3×6) PMTs on the wall and 10 PMTs on the bottom of the water tank at alternating radii.

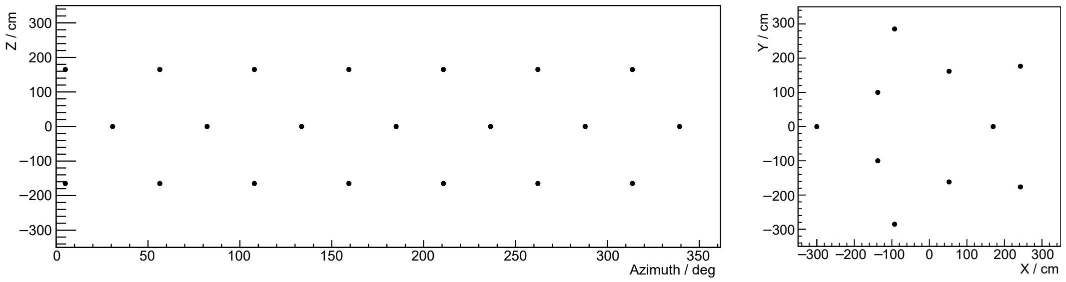

(a) PMT arrangement on wall (left) and bottom (right) of the water tank.

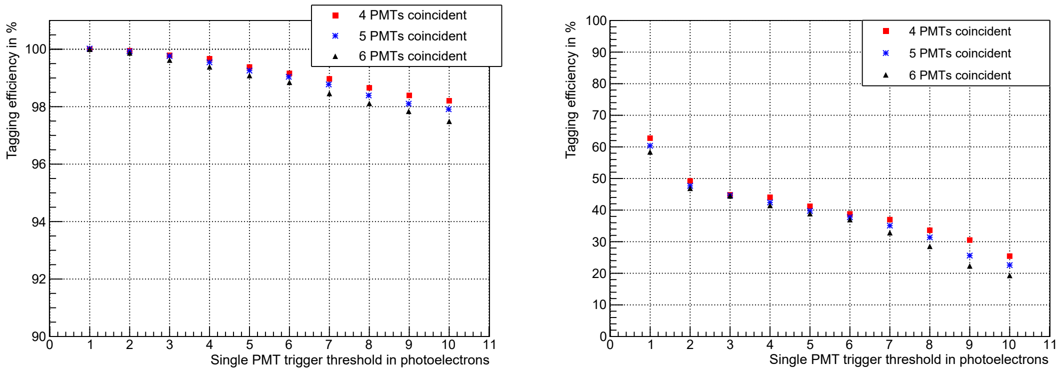

(b) Muon event tagging efficiency.

(c) Shower event tagging efficiency.

Figure D.4.: (a) Arrangement and (b,c) veto efficiency employing 18 (3×6) PMTs on the wall with horizontal shift between the 3 rows and 10 PMTs on the bottom of the water tank at alternating radii.

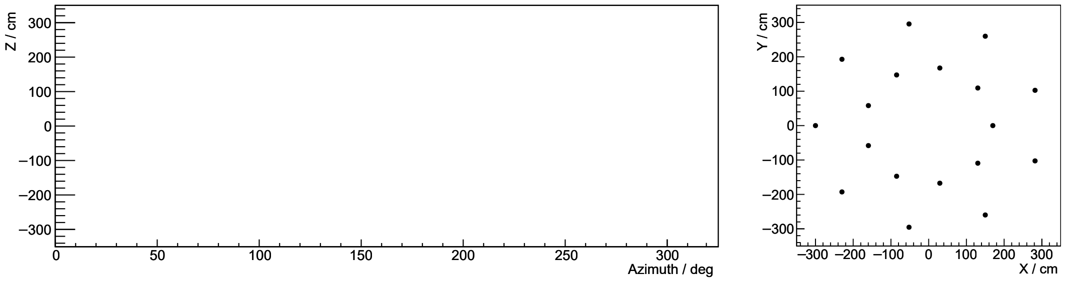

(a) PMT arrangement on wall (left) and bottom (right) of the water tank.

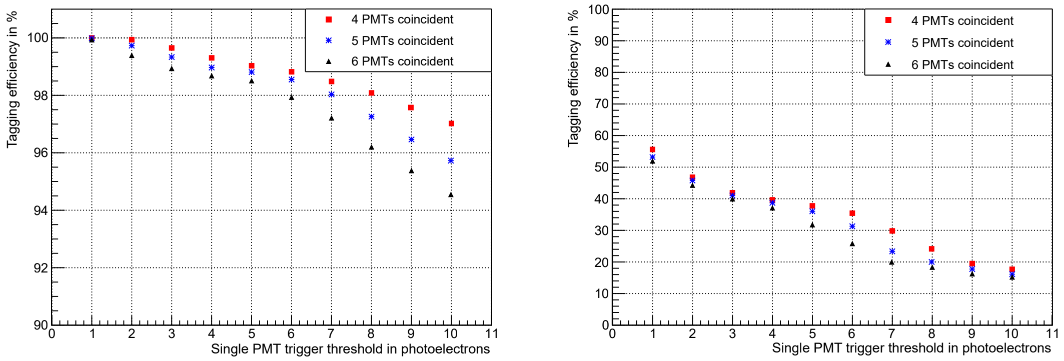

(b) Muon event tagging efficiency.

(c) Shower event tagging efficiency.

Figure D.5.: (a) Arrangement and (b,c) veto efficiency employing zero PMTs on the wall and 18 PMTs on the bottom of the water tank at alternating radii.

List of Figures

List of Tables

Bibliography

[1] Planck Collaboration. Planck 2018 results. *A&A*, 641:A6, 2020. doi:10.1051/0004-6361/201833910.

[2] P. A. Zyla et al. (Particle Data Group). Review of Particle Physics. *Prog. Theor. Exp. Phys.*, 2020(8):083C01, 2020. doi:10.1093/ptep/ptaa104.

[3] J. Billard et al. Direct detection of dark matter—APPEC committee report. *Rep. Prog. Phys.*, 85(5):056201, 2022. doi:10.1088/1361-6633/ac5754.

[4] A. H. Abdelhameed et al. First results from the CRESST-III low-mass dark matter program. *Phys. Rev. D*, 100:102002, 2019. doi:10.1103/PhysRevD.100.102002.

[5] P. Meunier et al. Discrimination between nuclear recoils and electron recoils by simultaneous detection of phonons and scintillation light. *Appl. Phys. Lett.*, 75(9):1335–1337, 1999. doi:10.1063/1.124685.

[6] G. Angloher et al. The COSINUS project: perspectives of a NaI scintillating calorimeter for dark matter search. *Eur. Phys. J. C*, 76(8):441, 2016. doi:10.1140/epjc/s10052-016-4278-3.

[7] R. Bernabei et al. The DAMA/LIBRA apparatus. *Nucl. Instrum. Methods Phys. Res. A*, 592:297–315, 2008. doi:10.1016/j.nima.2008.04.082.

[8] G. Bertone and D. Hooper. History of dark matter. *Rev. Mod. Phys.*, 90(4), 2018. doi:10.1103/revmodphys.90.045002.

[9] I. Newton. *Philosophiae naturalis principia mathematica*. Jussu Societatis Regiae ac Typis Josephi Streater. Prostat apud plures Bibliopolas., 1687. doi:10.5479/sil.52126.39088015628399.

[10] E. Brand, G. XI. Observations of Altitude and Azimuth of the Great Comet of 1843, made at St. Helena. *Mon. Not. R. Astron. Soc.*, 6(11):136–136, 1844. doi:10.1093/mnras/6.11.136.

[11] Challis. II. Account of Observations at the Cambridge Observatory for detecting the Planet exterior to Uranus. *Mon. Not. R. Astron. Soc.*, 7(9):145–149, 1846. doi:10.1093/mnras/7.9.145.

[12] A. Secchi. *L'Astronomia in Roma nel pontificato di Pio IX: memoria*. Tipografia della Pace, 1877. https://curiosity.lib.harvard.edu/expeditions-and-discoveries/catalog/38-990084213080203941.

[13] E. E. Barnard and A. C. Ranyard. Structure of the Milky Way. *Knowledge: An Illustrated Magazine of Science*, 17:253, 1894. https://ui.adsabs.harvard.edu/abs/1894KIMS...17..253B.

[14] W. Kelvin. *Baltimore Lectures on Molecular Dynamics and the Wave Theory of Light*. C.J. Clay and Sons, 1904. https://archive.org/details/baltimorelecture00kelviala/mode/2up.

[15] H. Poincare. The Milky Way and the Theory of Gases. *Popular Astronomy*, 14:475–488, 1906. https://ui.adsabs.harvard.edu/abs/1906PA.....14..475P.

[16] J. H. Jeans. The Motions of Stars in a Kapteyn-Universe. *Mon. Not. R. Astron. Soc.*, 82(3):122–132, 1922. doi:10.1093/mnras/82.3.122.

[17] B. Lindblad. *Uppsala Meddelanden 11, 30*. Uppsala universitet. Astronomiska observatoriet, 1926.

[18] J. H. Oort. The force exerted by the stellar system in the direction perpendicular to the galactic plane and some related problems. *Bull. Astron. Inst. Neth.*, 6:249, 1932. https://ui.adsabs.harvard.edu/abs/1932BAN.....6..249O.

[19] F. Zwicky. Die Rotverschiebung von extragalaktischen Nebeln. *Helvetica Physica Acta*, 6:110–127, 1933. https://ui.adsabs.harvard.edu/abs/1933AcHPh...6..110Z.

[20] M. Schwarzschild. Mass distribution and mass-luminosity ratio in galaxies. *Astronom. J.*, 59:273, 1954. doi:10.1086/107013.

[21] M. S. Roberts. A High-Resolution 21-CM Hydrogen-Line Survey of the Andromeda Nebula. *Astrophys. J.*, 144:639, 1966. doi:10.1086/148645.

[22] K. C. Freeman. On the Disks of Spiral and S0 Galaxies. *Astrophys. J.*, 160:811, 1970. doi:10.1086/150474.

[23] V. C. Rubin and J. Ford, W. Kent. Rotation of the Andromeda Nebula from a Spectroscopic Survey of Emission Regions. *Astrophys. J.*, 159:379, 1970. doi:10.1086/150317.

[24] V. C. Rubin et al. Extended rotation curves of high-luminosity spiral galaxies. IV. Systematic dynamical properties, Sa → Sc. *Astrophys. J.*, 225:L107–L111, 1978. doi:10.1086/182804.

[25] C. Alcock et al. Possible gravitational microlensing of a star in the Large Magellanic Cloud. *Nature*, 365:621–623, 1993. doi:10.1038/365621a0.

[26] E. Aubourg et al. Evidence for gravitational microlensing by dark objects in the Galactic halo. *Nature*, 365:623–625, 1993. doi:10.1038/365623a0.

[27] T. Lasserre et al. Not enough stellar mass Machos in the Galactic halo. *A&A*, 355:L39–L42, 2000. https://ui.adsabs.harvard.edu/abs/2000A&A...355L..39L.

[28] M. Fukugita et al. The Cosmic Baryon Budget. *Astrophys. J.*, 503(2):518–530, 1998. doi:10.1086/306025.

[29] C. L. Bennett et al. Four-Year COBE DMR Cosmic Microwave Background Observations: Maps and Basic Results. *Astrophys. J.*, 464(1):L1–L4, 1996. doi:10.1086/310075.

[30] G. Hinshaw et al. Three-Year Wilkinson Microwave Anisotropy Probe (WMAP) Observations: Temperature Analysis. *Astrophys. J. Suppl. Ser.*, 170(2):288–334, 2007. doi:10.1086/513698.

[31] C. L. Bennett et al. Nine-Year Wilkinson Microwave Anisotropy Probe (WMAP) Observations: Final Maps and Results. *Astrophys. J. Suppl. Ser.*, 208(2):20, 2013. doi:10.1088/0067-0049/208/2/20.

[32] M. Milgrom. A modification of the Newtonian dynamics as a possible alternative to the hidden mass hypothesis. *Astrophys. J.*, 270:365–370, 1983. doi:10.1086/161130.

[33] Paraficz, D. et al. The Bullet cluster at its best: weighing stars, gas, and dark matter. *A&A*, 594:A121, 2016. doi:10.1051/0004-6361/201527959.

[34] R. S. Ellis. Gravitational lensing: a unique probe of dark matter and dark energy. *Philos. Trans. R. Soc. A*, 368(1914):967–987, 2010. doi:10.1098/rsta.2009.0209.

[35] D. Clowe et al. A Direct Empirical Proof of the Existence of Dark Matter. *Astrophys. J.*, 648(2):L109–L113, 2006. doi:10.1086/508162.

[36] NASA - Bullet Cluster. https://www.nasa.gov/mission_pages/chandra/multimedia/photos06-096.html. Accessed: 2022-01-28.

[37] V. Springel et al. Simulations of the formation, evolution and clustering of galaxies and quasars. *Nature*, 435(7042):629–636, 2005. doi:10.1038/nature03597.

[38] M. Boylan-Kolchin et al. Resolving cosmic structure formation with the Millennium-II Simulation. *Mon. Not. R. Astron. Soc.*, 398(3):1150–1164, 2009. doi:10.1111/j.1365-2966.2009.15191.x.

[39] R. E. Angulo et al. Scaling relations for galaxy clusters in the Millennium-XXL simulation. *Mon. Not. R. Astron. Soc.*, 426(3):2046–2062, 2012. doi:10.1111/j.1365-2966.2012.21830.x.

[40] A. Einstein. Die Grundlage der allgemeinen Relativitätstheorie. *Annalen der Physik*, 354(7):769–822, 1916. doi:10.1002/andp.19163540702.

[41] B. Carr et al. Constraints on primordial black holes. *Rep. Prog. Phys.*, 84(11):116902, 2021. doi:10.1088/1361-6633/ac1e31.

[42] B. Audren et al. Strongest model-independent bound on the lifetime of Dark Matter. *J. Cosmol. Astropart. Phys.*, 2014(12):028–028, 2014. doi:10.1088/1475-7516/2014/12/028.

[43] S. Tulin and H.-B. Yu. Dark matter self-interactions and small scale structure. *Phys. Rep.*, 730:1–57, 2018. doi:10.1016/j.physrep.2017.11.004.

[44] S. D. McDermott et al. Turning off the lights: How dark is dark matter? *Phys. Rev. D*, 83:063509, 2011. doi:10.1103/PhysRevD.83.063509.

[45] R. D. Peccei and H. R. Quinn. CP Conservation in the Presence of Pseudoparticles. *Phys. Rev. Lett.*, 38:1440–1443, 1977. doi:10.1103/PhysRevLett.38.1440.

[46] J. Preskill et al. Cosmology of the invisible axion. *Phys. Lett. B*, 120(1):127–132, 1983. doi:10.1016/0370-2693(83)90637-8.

[47] P. Arias et al. WISPy cold dark matter. *J. Cosmol. Astropart. Phys.*, 2012(06):013–013, 2012. doi:10.1088/1475-7516/2012/06/013.

[48] T. Yanagida. Horizontal Symmetry and Masses of Neutrinos. *Prog. Theor. Phys.*, 64(3):1103–1105, 1980. doi:10.1143/PTP.64.1103.

[49] A. Boyarsky et al. Sterile neutrino Dark Matter. *Prog. Part. Nucl. Phys.*, 104:1–45, 2019. doi:10.1016/j.ppnp.2018.07.004.

[50] P. Matorras Cuevas. SUSY searches in ATLAS and CMS. Technical Report CMS-CR-2022-055, CERN, Geneva, 2022. https://cds.cern.ch/record/2814725.

[51] J. D. Bekenstein. Relativistic gravitation theory for the modified Newtonian dynamics paradigm. *Phys. Rev. D*, 70:083509, 2004. doi:10.1103/PhysRevD.70.083509.

[52] B. Famaey and S. S. McGaugh. Modified Newtonian Dynamics (MOND): Observational Phenomenology and Relativistic Extensions. *Living Rev. Relativ.*, 15(1), 2012. doi:10.12942/lrr-2012-10.

[53] A. Boveia and C. Doglioni. Dark Matter Searches at Colliders. *Annu. Rev. Nucl. Part. Sci.*, 68(1):429–459, 2018. doi:10.1146/annurev-nucl-101917-021008.

[54] J. M. Gaskins. A review of indirect searches for particle dark matter. *Contemp. Phys.*, 57(4):496–525, 2016. doi:10.1080/00107514.2016.1175160.

[55] T. Saab. An Introduction to Dark Matter Direct Detection Searches & Techniques. In *The Dark Secrets of the Terascale (TASI 2011) - Proceedings of TASI 2011*, pp. 711–738, 2013. doi:10.1142/9789814390163_0011.

[56] J. B. Birks. Scintillations from Organic Crystals: Specific Fluorescence and Relative Response to Different Radiations. *Proc. Phys. Soc. A*, 64(10):874–877, 1951. doi:10.1088/0370-1298/64/10/303.

[57] J. Lindhard. Influence of crystal lattice on motion of energetic charged particles. *Kongel. Dan. Vidensk. Selsk., Mat.-Fys. Medd.*, 34(14), 1965. https://www.osti.gov/biblio/4536390.

[58] N. W. Evans et al. SHM^{++}: A Refinement of the Standard Halo Model for Dark Matter Searches in Light of the Gaia Sausage, 2018. doi:10.48550/arXiv.1810.11468.

[59] J. Lewin and P. Smith. Review of mathematics, numerical factors, and corrections for dark matter experiments based on elastic nuclear recoil. *Astropart. Phys.*, 6(1):87–112, 1996. doi:10.1016/S0927-6505(96)00047-3.

[60] E. Del Nobile et al. Target dependence of the annual modulation in direct dark matter searches. *Phys. Rev. D*, 91:121302, 2015. doi:10.1103/PhysRevD.91.121302.

[61] CMS Collaboration. Dark matter summary plots, 2018. https://twiki.cern.ch/twiki/bin/view/CMSPublic/SummaryPlotsEXO13TeV#Dark_Matter_Summary_plots. Accessed: 2022-02-22.

[62] ATLAS Collaboration. The ATLAS Experiment at the CERN Large Hadron Collider. *J. Instrum.*, 3(08):S08003–S08003, 2008. doi:10.1088/1748-0221/3/08/s08003.

[63] CMS Collaboration. The CMS Experiment at the CERN LHC. *J. Instrum.*, 3:S08004, 2008. doi:10.1088/1748-0221/3/08/S08004.

[64] CMS Collaboration. Projection of the Mono-Z search for dark matter to the HL-LHC. Technical Report CMS-PAS-FTR-18-007, CERN, Geneva, 2018. https://cds.cern.ch/record/2644529.

[65] L. Roszkowski et al. WIMP dark matter candidates and searches—current status and future prospects. *Rep. Prog. Phys.*, 81(6):066201, 2018. doi:10.1088/1361-6633/aab913.

[66] T. Bringmann and C. Weniger. Gamma ray signals from dark matter: Concepts, status and prospects. *Phys. Dark Universe*, 1(1):194–217, 2012. doi:10.1016/j.dark.2012.10.005. Next Decade in Dark Matter and Dark Energy.

[67] A. Albert et al. Searching for Dark Matter Annihilation in Recently Discovered Milky Way Satellites with Fermi-LAT. *Astrophys. J.*, 834(2):110, 2017. doi:10.3847/1538-4357/834/2/110.

[68] J. Aleksić et al. Performance of the MAGIC stereo system obtained with Crab Nebula data. *Astropart. Phys.*, 35(7):435–448, 2012. doi:10.1016/j.astropartphys.2011.11.007.

[69] H. Abdallah et al. Search for Dark Matter Annihilations towards the Inner Galactic Halo from 10 Years of Observations with H.E.S.S. *Phys. Rev. Lett.*, 117:111301, 2016. doi:10.1103/PhysRevLett.117.111301.

[70] J. Carr et al. Prospects for Indirect Dark Matter Searches with the Cherenkov Telescope Array (CTA), 2015. doi:10.48550/arXiv.1508.06128.

[71] J. F. Navarro et al. The Structure of Cold Dark Matter Halos. *Astrophys. J.*, 462:563, 1996. doi:10.1086/177173.

[72] J. Einasto. On the Construction of a Composite Model for the Galaxy and on the Determination of the System of Galactic Parameters. *Trudy Astrofiz. Inst. Alma-Ata*, 5:87–100, 1965. https://ui.adsabs.harvard.edu/abs/1965TrAlm...5...87E.

[73] C. Savage et al. Compatibility of DAMA/LIBRA dark matter detection with other searches. *J. Cosmol. Astropart. Phys.*, 2009(04):010, 2009. doi:10.1088/1475-7516/2009/04/010.

[74] P. Agnes et al. Low-Mass Dark Matter Search with the DarkSide-50 Experiment. *Phys. Rev. Lett.*, 121:081307, 2018. doi:10.1103/PhysRevLett.121.081307.

[75] E. Aprile et al. Light Dark Matter Search with Ionization Signals in XENON1T. *Phys. Rev. Lett.*, 123:251801, 2019. doi:10.1103/PhysRevLett.123.251801.

[76] E. Aprile et al. Dark Matter Search Results from a One Ton-Year Exposure of XENON1T. *Phys. Rev. Lett.*, 121:111302, 2018. doi:10.1103/PhysRevLett.121.111302.

[77] M. Ibe et al. Migdal effect in dark matter direct detection experiments. *J. High Energy Phys.*, 2018(3), 2018. doi:10.1007/jhep03(2018)194.

[78] N. F. Bell et al. Observing the Migdal effect from nuclear recoils of neutral particles with liquid xenon and argon detectors. *Phys. Rev. D*, 105:096015, 2022. doi:10.1103/PhysRevD.105.096015.

[79] E. Aprile et al. Projected WIMP sensitivity of the XENONnT dark matter experiment. *J. Cosmol. Astropart. Phys.*, 2020(11):031–031, 2020. doi:10.1088/1475-7516/2020/11/031.

[80] D. Akerib et al. The LUX-ZEPLIN (LZ) experiment. *Nucl. Instrum. Methods Phys. Res. A*, 953:163047, 2020. doi:10.1016/j.nima.2019.163047.

[81] Y. Meng et al. Dark Matter Search Results from the PandaX-4T Commissioning Run. *Phys. Rev. Lett.*, 127:261802, 2021. doi:10.1103/PhysRevLett.127.261802.

[82] P. Adari et al. EXCESS workshop: Descriptions of rising low-energy spectra. *SciPost Phys. Proc.*, 9:001, 2022. doi:10.21468/SciPostPhysProc.9.001.

[83] R. Bernabei et al. First Model Independent Results from DAMA/LIBRA–Phase2. *Nucl. Phys. At. Energy*, 19(4):307 – 325, 2018. doi:10.15407/jnpae2018.04.307.

[84] M. J. Berger et al. XCOM: Photon Cross Section Database (version 1.5), 2010. http://physics.nist.gov/xcom. Accessed: 2022-03-03. National Institute of Standards and Technology, Gaithersburg, MD.

[85] G. Nelson and D. Reilly. Gamma-Ray Interactions with Matter. In *Passive Nondestructive Analysis of Nuclear Materials, LANL*, pp. 27–42, 1991. https://sgp.fas.org/othergov/doe/lanl/lib-www/la-pubs/00326397.pdf.

[86] L. Baudis et al. Neutrino physics with multi-ton scale liquid xenon detectors. *J. Cosmol. Astropart. Phys.*, 2014(01):044–044, 2014. doi:10.1088/1475-7516/2014/01/044.

[87] A. S. Malgin. Phenomenology of muon-induced neutron yield. *Phys. Rev. C*, 96:014605, 2017. doi:10.1103/PhysRevC.96.014605.

[88] N. Y. Agafonova and A. S. Malgin. Universal formula for the muon-induced neutron yield. *Phys. Rev. D*, 87:113013, 2013. doi:10.1103/PhysRevD.87.113013.

[89] H. M. Kluck. *Measurement of the cosmic-induced neutron yield at the Modane underground laboratory*. PhD thesis, Karlsruhe Institute of Technology, 2013. doi:10.5445/IR/1000039837.

[90] ENDF Database Version of 2022-02-25. https://www-nds.iaea.org/endf. Accessed: 2022-03-03.

[91] D. Brown et al. ENDF/B-VIII.0: The 8th Major Release of the Nuclear Reaction Data Library with CIELO-project Cross Sections, New Standards and Thermal Scattering Data. *Nucl. Data Sheets*, 148:1–142, 2018. doi:10.1016/j.nds.2018.02.001. Special Issue on Nuclear Reaction Data.

[92] Brookhaven National Laboratory. QCalc Q-Value Calculator. https://www.nndc.bnl.gov/qcalc/. Accessed: 2022-05-04.

[93] N. Agafonova et al. Discovery potential for directional Dark Matter detection with nuclear emulsions. *Eur. Phys. J. C*, 78(7), 2018. doi:10.1140/epjc/s10052-018-6060-1.

[94] A. E. Robinson. Coherent photon scattering background in sub-GeV/c^2 direct dark matter searches. *Phys. Rev. D*, 95:021301, 2017. doi:10.1103/PhysRevD.95.021301.

[95] A. Fuß. Light Yield and Quenching Factor Simulations based on Birks' Law for a CRESST-like CaWO$_4$ Crystal. Master's thesis, TU Wien, 2018. doi:10.34726/hss.2017.50966.

[96] R. Strauss et al. Beta/gamma and alpha backgrounds in CRESST-II Phase 2. *J. Cosmol. Astropart. Phys.*, 2015(06):030–030, 2015. doi:10.1088/1475-7516/2015/06/030.

[97] R. Strauss et al. A detector module with highly efficient surface-alpha event rejection operated in CRESST-II Phase 2. *Eur. Phys. J. C*, 75(8), 2015. doi:10.1140/epjc/s10052-015-3572-9.

[98] H. W. Joo et al. Quenching factor measurement for NaI(Tl) scintillation crystal. *Astropart. Phys.*, 108:50–56, 2019. doi:10.1016/j.astropartphys.2019.01.001.

[99] D. Cintas et al. Quenching Factor consistency across several NaI(Tl) crystals, 2021. doi:10.48550/arXiv.2111.09590.

[100] R. Strauss et al. Energy-dependent light quenching in CaWO$_4$ crystals at mK temperatures. *Eur. Phys. J. C*, 74(7), 2014. doi:10.1140/epjc/s10052-014-2957-5.

[101] A. Bonhomme et al. Direct measurement of the ionization quenching factor of nuclear recoils in germanium in the keV energy range. *Eur. Phys. J. C*, 82(9), 2022. doi:10.1140/epjc/s10052-022-10768-1.

[102] B. J. Scholz et al. Measurement of the low-energy quenching factor in germanium using an $^{88}\mathrm{Y/Be}$ photoneutron source. *Phys. Rev. D*, 94:122003, 2016. doi:10.1103/PhysRevD.94.122003.

[103] Y. Sarkis et al. Study of the ionization efficiency for nuclear recoils in pure crystals. *Phys. Rev. D*, 101:102001, 2020. doi:10.1103/PhysRevD.101.102001.

[104] G. Heusser. Low-Radioactivity Background Techniques. *Annu. Rev. Nucl. Part. Sci.*, 45(1):543–590, 1995. doi:10.1146/annurev.ns.45.120195.002551.

[105] M. Schumann. Direct detection of WIMP dark matter: concepts and status. *J. Phys. G*, 46(10):103003, 2019. doi:10.1088/1361-6471/ab2ea5.

[106] S. P. Ahlen et al. A Search for cosmic point sources of muons and for seasonal variations in the underground muon flux with the MACRO detector. In *International Symposium on Cosmic Ray Physics in Tibet*, pp. 145–154, 1994. https://inspirehep.net/literature/384351.

[107] M. Ambrosio et al. Vertical muon intensity measured with MACRO at the Gran Sasso laboratory. *Phys. Rev. D*, 52(7):3793–3802, 1995. doi:10.1103/PhysRevD.52.3793.

[108] M. Aglietta et al. Muon "depth-intensity" relation measured by the LVD underground experiment and cosmic-ray muon spectrum at sea level. *Phys. Rev. D*, 58:092005, 1998. doi:10.1103/PhysRevD.58.092005.

[109] C. Alduino et al. First Results from CUORE: A Search for Lepton Number Violation via $0\nu\beta\beta$ Decay of $^{130}\mathrm{Te}$. *Phys. Rev. Lett.*, 120(13):132501, 2018. doi:10.1103/PhysRevLett.120.132501.

[110] M. Agostini et al. Upgrade for phase II of the Gerda experiment. *Eur. Phys. J. C Part. Fields*, 78(5), 2018. doi:10.1140/epjc/s10052-018-5812-2.

[111] P. Prati. The LUNA-MV facility at Gran Sasso. *J. Phys. Conf. Ser.*, 1342(1):012088, 2020. doi:10.1088/1742-6596/1342/1/012088.

[112] MCNPX. https://mcnpx.lanl.gov. Accessed: 2021-10-30.

[113] G. Battistoni et al. Overview of the FLUKA code. *Ann. Nucl. Energy*, 82:10–18, 2015. doi:10.1016/j.anucene.2014.11.007.

[114] C. Ahdida et al. New Capabilities of the FLUKA Multi-Purpose Code. *Front. Phys.*, 9, 2022. doi:10.3389/fphy.2021.788253.

[115] S. Agostinelli et al. Geant4—a simulation toolkit. *Nucl. Instrum. Methods Phys. Res. A*, 506(3):250 – 303, 2003. doi:10.1016/S0168-9002(03)01368-8.

[116] J. Allison et al. Geant4 developments and applications. *IEEE Trans. Nucl. Sci.*, 53:270, 2006. doi:10.1109/TNS.2006.869826.

[117] J. Allison et al. Recent developments in Geant4. *Nucl. Instrum. Methods Phys. Res. A*, 835:186 – 225, 2016. doi:10.1016/j.nima.2016.06.125.

[118] A. H. Abdelhameed et al. Geant4-based electromagnetic background model for the CRESST dark matter experiment. *Eur. Phys. J. C*, 79(10):881, 2019. doi:10.1140/epjc/s10052-019-7385-0.

[119] Geant4 User Documentation. https://geant4.web.cern.ch/support/user_documentation. Accessed: 2022-03-07.

[120] Low Energy Electromagnetic Physics - Livermore. https://geant4.web.cern.ch/node/1619. Accessed: 2022-10-06.

[121] R. Brun and F. Rademakers. ROOT - An Object Oriented Data Analysis Framework. In *AIHENP'96 Workshop, Lausane*, volume 389, pp. 81–86, 1996. doi:10.1016/S0168-9002(97)00048-X.

[122] D. G. Madland et al. SOURCES 4A: A Code for Calculating (α,n), Spontaneous Fission, and Delayed Neutron Sources and Spectra. Technical Report LA-13639-MS, LANL, 1999. doi:10.2172/15215.

[123] W. B. Wilson et al. SOURCES 4C: a code for calculating (α,n), spontaneous fission, and delayed neutron sources and spectra. Technical Report LA-UR–02-1839, LANL, 2002. http://inis.iaea.org/search/search.aspx?orig_q=RN:41092883.

[124] S. Westerdale and P. Meyers. Radiogenic neutron yield calculations for low-background experiments. *Nucl. Instrum. Methods Phys. Res. A*, 875:57–64, 2017. doi:10.1016/j.nima.2017.09.007.

[125] G. N. Vlaskin et al. Neutron Yield of the Reaction (α, n) on Thick Targets Comprised of Light Elements. *Atomic Energy*, 117(5):357–365, 2015. doi:10.1007/s10512-015-9933-5.

[126] E. Mendoza et al. Neutron production induced by α-decay with Geant4. *Nucl. Instrum. Methods Phys. Res. A*, 960:163659, 2020. doi:10.1016/j.nima.2020.163659.

[127] V. A. Kudryavtsev. Muon simulation codes MUSIC and MUSUN for underground physics. *Comput. Phys. Commun.*, 180:339–346, 2009. doi:10.1016/j.cpc.2008.10.013.

[128] G. Angloher et al. Limits on WIMP dark matter using sapphire cryogenic detectors. *Astropart. Phys.*, 18(1):43–55, 2002. doi:10.1016/S0927-6505(02)00111-1.

[129] W. Seidel et al. Phase Transition Thermometers With High Temperature Resolution for Calorimetric Particle Detectors Employing Dielectric Absorbers. *Phys. Lett. B*, 236:483–487, 1990. doi:10.1016/0370-2693(90)90388-M.

[130] G. Angloher et al. Results on low mass WIMPs using an upgraded CRESST-II detector. *Eur. Phys. J. C*, 74(12), 2014. doi:10.1140/epjc/s10052-014-3184-9.

[131] R. Strauss et al. The ν-cleus experiment: a gram-scale fiducial-volume cryogenic detector for the first detection of coherent neutrino–nucleus scattering. *Eur. Phys. J. C*, 77(8):506, 2017. doi:10.1140/epjc/s10052-017-5068-2.

[132] G. Angloher et al. Probing spin-dependent dark matter interactions with ^{6}Li. *Eur. Phys. J. C*, 82(3), 2022. doi:10.1140/epjc/s10052-022-10140-3.

[133] A. Abdelhameed et al. First results on sub-GeV spin-dependent dark matter interactions with ^{7}Li. *Eur. Phys. J. C*, 79, 2019. doi:10.1140/epjc/s10052-019-7126-4.

[134] Dilution Refrigerators. https://en.wikipedia.org/wiki/Dilution_refrigerator. Accessed: 2022-03-23.

[135] R. Strauss et al. A prototype detector for the CRESST-III low-mass dark matter search. *Nucl. Instrum. Methods Phys. Res. A*, 845:414–417, 2017. doi:10.1016/j.nima.2016.06.060. Proceedings of the Vienna Conference on Instrumentation 2016.

[136] R. F. Lang et al. Scintillator Non-Proportionality and Gamma Quenching in CaWO4, 2009. doi:10.48550/arxiv.0910.4414.

[137] S. Scholl. *Neutron Background Simulation for the CRESST - II Experiment.* PhD thesis, Universität Tübingen, 2011. https://publikationen.uni-tuebingen.de/xmlui/handle/10900/49550.

[138] NNDC, Brookhaven National Laboratory. NuDat 3.0. https://www.nndc.bnl.gov/nudat3/. Accessed: 2022-05-05.

[139] M. J. Carson et al. Neutron background in large-scale xenon detectors for dark matter searches. *Astropart. Phys.*, 21:667–687, 2004. doi:10.1016/j.astropartphys.2004.05.001.

[140] R. Lemrani et al. Low-energy neutron propagation in MCNPX and GEANT4. *Nucl. Instrum. Methods Phys. Res. A*, 560(2):454–459, 2006. doi:10.1016/j.nima.2005.12.238.

[141] V. Tomasello et al. Calculation of neutron background for underground experiments. *Nucl. Instrum. Methods Phys. Res. A*, 595(2):431–438, 2008. doi:10.1016/j.nima.2008.07.071.

[142] J. Meija et al. Isotopic compositions of the elements 2013 (IUPAC Technical Report). *Pure Appl. Chem.*, 88(3):293–306, 2016. doi:10.1515/pac-2015-0503.

[143] V. A. Kudryavtsev et al. Neutron- and muon-induced background in underground physics experiments. *Eur. Phys. J. A*, 36:171–180, 2008. doi:10.1140/epja/i2007-10539-6.

[144] A. Mowlavi and R. Koohi-Fayegh. Determination of 4.438MeV γ-ray to neutron emission ratio from a ^{241}Am–^{9}Be neutron source. *Appl. Radiat. Isot.*, 60:959–62, 07 2004. doi:10.1016/j.apradiso.2004.02.008.

[145] Z. Liu et al. The 4.438MeV gamma to neutron ratio for the Am–Be neutron source. *Appl. Radiat. Isot.*, 65:1318–1321, 01 2008. doi:10.1016/j.apradiso.2007.04.007.

[146] A. Thompson et al. *X-ray Data Booklet*. Lawrence Berkeley National Laboratory, University of California, 2009. https://xdb.lbl.gov/.

[147] R. Firestone et al. EGAF: Measurement and Analysis of Gamma-ray Cross Sections. *Nucl. Data Sheets*, 119:79–87, 2014. doi:10.1016/j.nds.2014.08.024.

[148] EGAF (Evaluated Gamma-ray Activation File). https://www-nds.iaea.org/pgaa/egaf.html. Accessed: 2022-04-12.

[149] L. Thulliez et al. Calibration of nuclear recoils at the 100 eV scale using neutron capture. *J. Instrum.*, 16(07):P07032, 2021. doi:10.1088/1748-0221/16/07/p07032.

[150] M. Heikinheimo et al. Identification of the low energy excess in dark matter searches with crystal defects, 2021. doi:10.48550/arXiv.2112.14495.

[151] P. Virtanen et al. SciPy 1.0: Fundamental Algorithms for Scientific Computing in Python. *Nat. Methods*, 17:261–272, 2020. doi:10.1038/s41592-019-0686-2.

[152] R. Barlow. Extended maximum likelihood. *Nucl. Instrum. Methods Phys. Res. A*, 297(3):496–506, 1990. doi:10.1016/0168-9002(90)91334-8.

[153] S. S. Wilks. The Large-Sample Distribution of the Likelihood Ratio for Testing Composite Hypotheses. *Ann. Math. Stat.*, 9(1):60 – 62, 1938. doi:10.1214/aoms/1177732360.

[154] R. Storn and K. Price. Differential Evolution – A Simple and Efficient Heuristic for global Optimization over Continuous Spaces. *J. Glob. Optim.*, 11(4):341–359, 1997. doi:10.1023/a:1008202821328.

[155] R. Storn. On the usage of differential evolution for function optimization. In *Proceedings of North American Fuzzy Information Processing*, pp. 519–523, 1996. doi:10.1109/NAFIPS.1996.534789.

[156] J. A. Nelder and R. Mead. A Simplex Method for Function Minimization. *Comput. J.*, 7(4):308–313, 1965. doi:10.1093/comjnl/7.4.308.

[157] F. James and M. Roos. Minuit: A System for Function Minimization and Analysis of the Parameter Errors and Correlations. *Comput. Phys. Commun.*, 10:343–367, 1975. doi:10.1016/0010-4655(75)90039-9.

[158] H. Dembinski et al. scikit-hep/iminuit. *doi:10.5281/zenodo.6902850*. doi:10.5281/zenodo.3949207.

[159] H. Wulandari et al. Neutron flux underground revisited. *Astropart. Phys.*, 22:313–322, 2004. doi:10.1016/j.astropartphys.2004.07.005.

[160] C. Alduino et al. CUORE-0 detector: design, construction and operation. *J. Instrum.*, 11(07):P07009, 2016. doi:10.1088/1748-0221/11/07/P07009.

[161] Information on Uranium by the IAEA. https://www.iaea.org/topics/spent-fuel-management/depleted-uranium. Accessed: 2022-08-30.

[162] O. M. Horn. *Simulations of the muon-induced neutron background of the EDELWEISS-II experiment for dark matter search*. PhD thesis, Universität Karlsruhe, 2008. doi:10.5445/IR/200072092.

[163] BC-408 Saint Gobain. https://www.crystals.saint-gobain.com/radiation-detection-scintillators/plastic-scintillators/bc-400-bc-404-bc-408-bc-412-bc-416. Accessed: 2022-05-03.

[164] Electron Tubes – 9900B Series. https://et-enterprises.com/products/photomultipliers/product/p9900b-series. Accessed: 2022-05-06.

[165] M. Kimmerle. *Data Analysis in the Direct Dark Matter Search Experiment CRESST and Calculation of the corresponding Limit on the Cross Section of Dark Matter*. PhD thesis, Universität Tübingen, 2010. https://publikationen.uni-tuebingen.de/xmlui/handle/10900/49525.

[166] S. Pfister. *Suche nach Dunkler Materie mit dem CRESST-II-Experiment*. PhD thesis, Technische Universität München, 2010.

[167] K. Rottler. *Muons in the CRESST Dark Matter Experiment*. PhD thesis, Universität Tübingen, 2014. https://publikationen.uni-tuebingen.de/xmlui/handle/10900/53055.

[168] S. K. Lee et al. Dark-Matter Harmonics Beyond Annual Modulation. *J. Cosmol. Astropart. Phys.*, 11:033, 2013. doi:10.1088/1475-7516/2013/11/033.

[169] R. Bernabei et al. New limits on WIMP search with large-mass low-radioactivity NaI(Tl) set-up at Gran Sasso. *Phys. Lett. B*, 389(4):757–766, 1996. doi:10.1016/S0370-2693(96)80020-7.

[170] R. Bernabei et al. The dark matter: DAMA/LIBRA and its perspectives, 2021. doi:10.48550/arXiv.2110.04734.

[171] G. Adhikari et al. Strong constraints from COSINE-100 on the DAMA dark matter results using the same sodium iodide target. *Sci. Adv.*, 7(46), 2021. doi:10.1126/sciadv.abk2699.

[172] V. Tretyak. Semi-empirical calculation of quenching factors for ions in scintillators. *Astropart. Phys.*, 33(1):40–53, 2010. doi:10.1016/j.astropartphys.2009.11.002.

[173] G. Adhikari et al. An experiment to search for dark-matter interactions using sodium iodide detectors. *Nature*, 564(7734):83–86, 2018. doi:10.1038/s41586-018-0739-1.

[174] G. Adhikari et al. Search for a Dark Matter-Induced Annual Modulation Signal in NaI(Tl) with the COSINE-100 Experiment. *Phys. Rev. Lett.*, 123(3):031302, 2019. doi:10.1103/PhysRevLett.123.031302.

[175] G. Adhikari et al. Three-year annual modulation search with COSINE-100. *Phys. Rev. D*, 106:052005, 2022. doi:10.1103/PhysRevD.106.052005.

[176] J. Amaré et al. Annual modulation results from three-year exposure of ANAIS-112. *Phys. Rev. D*, 103:102005, 2021. doi:10.1103/PhysRevD.103.102005.

[177] M. Antonello et al. The SABRE project and the SABRE Proof-of-Principle. *Eur. Phys. J. C*, 79(4), 2019. doi:10.1140/epjc/s10052-019-6860-y.

[178] K. Fushimi et al. Dark matter search project PICO-LON. *J. Phys.: Conf. Ser.*, 718(4):042022, 2016. doi:10.1088/1742-6596/718/4/042022.

[179] K. Schäffner et al. A NaI-Based Cryogenic Scintillating Calorimeter: Results from a COSINUS Prototype Detector. *J. Low Temp. Phys.*, 2018. doi:10.1007/s10909-018-1967-3.

[180] G. Angloher et al. First measurements of remoTES cryogenic calorimeters: easy-to-fabricate particle detectors for a wide choice of target materials, 2021. doi:10.48550/arXiv.2111.00349.

[181] F. Reindl et al. Results of the first NaI scintillating calorimeter prototypes by COSINUS. *J. Phys.: Conf. Ser.*, 1342(1):012099, 2020. doi:10.1088/1742-6596/1342/1/012099.

[182] G. Angloher et al. Results from the first cryogenic NaI detector for the COSINUS project. *J. Instrum.*, 12(11):P11007–P11007, 2017. doi:10.1088/1748-0221/12/11/P11007.

[183] M. Pyle et al. Optimized Designs for Very Low Temperature Massive Calorimeters, 2015. doi:10.48550/arXiv.1503.01200.

[184] F. Kahlhoefer et al. Model-independent comparison of annual modulation and total rate with direct detection experiments. *J. Cosmol. Astropart. Phys.*, 1805(05):074, 2018. doi:10.1088/1475-7516/2018/05/074.

[185] J. Amaré et al. Analysis of backgrounds for the ANAIS-112 dark matter experiment. *Eur. Phys. J. C*, 79(5):412, 2019. doi:10.1140/epjc/s10052-019-6911-4.

[186] P. Adhikari et al. Background model for the NaI(Tl) crystals in COSINE-100. *Eur. Phys. J. C*, 78(6):490, 2018. doi:10.1140/epjc/s10052-018-5970-2.

[187] G. Adhikari et al. Background modeling for dark matter search with 1.7 years of COSINE-100 data. *Eur. Phys. J. C*, 81(9), 2021. doi:10.1140/epjc/s10052-021-09564-0.

[188] M. Antonello et al. Monte Carlo simulation of the SABRE PoP background. *Astropart. Phys.*, 106:1 – 9, 2019. doi:10.1016/j.astropartphys.2018.10.005.

[189] G. Angloher et al. Simulation-based design study for the passive shielding of the COSINUS dark matter experiment. *Eur. Phys. J. C*, 82(3), 2022. doi:10.1140/epjc/s10052-022-10184-5.

[190] COSINUS Collaboration. COSINUS Conceptual Design Report. Technical Report CERN-COSINUS-2021-001, CERN, Geneva, 2019. https://cds.cern.ch/record/2798447.

[191] D. R. Artusa et al. Exploring the Neutrinoless Double Beta Decay in the Inverted Neutrino Hierarchy with Bolometric Detectors. *Eur. Phys. J. C*, 74:3096, 2014. doi:10.1140/epjc/s10052-014-3096-8.

[192] E. Aprile et al. Material radioassay and selection for the XENON1T dark matter experiment. *Eur. Phys. J. C*, 77(12):890, 2017. doi:10.1140/epjc/s10052-017-5329-0.

[193] E. Aprile et al. Material screening and selection for XENON100. *Astropart. Phys.*, 35(2):43–49, 2011. doi:10.1016/j.astropartphys.2011.06.001.

[194] D. Malczewski et al. Gamma background measurements in the Gran Sasso National Laboratory. *J. Radioanal. Nucl. Chem.*, 295(1):749–754, 2013. doi:10.1007/s10967-012-1990-9.

[195] C. Arpesella et al. Measurements of extremely low radioactivity levels in BOREXINO. *Astropart. Phys.*, 18(1):1–25, 2002. doi:10.1016/S0927-6505(01)00179-7.

[196] E. Aprile et al. Conceptual design and simulation of a water Cherenkov muon veto for the XENON1T experiment. *J. Instrum.*, 9:P11006, 2014. doi:10.1088/1748-0221/9/11/P11006.

[197] DF2000MA Reflective Foil. https://www.digikey.com/catalog/en/partgroup/df2000ma/8897. Accessed: 2022-01-23.

[198] Hamamatsu Photonics K.K. https://www.hamamatsu.com/eu/en/product/type/R5912/index.html. Accessed: 2022-01-20.

[199] C. W. Geis. *The XENON1T water Cherenkov muon veto system and commissioning of the XENON1T Dark Matter experiment.* PhD thesis, Johannes Gutenberg-Universität in Mainz, 2018. doi:10.25358/openscience-2175.

[200] M. Knapp et al. The Gerda muon veto Cherenkov detector. *Nucl. Instrum. Methods Phys. Res. A*, 610(1):280–282, 2009. doi:10.1016/j.nima.2009.05.115.

Danksagung

An dieser Stelle möchte ich mich bei einer Vielzahl an Personen bedanken, die einen Beitrag dazu geleistet haben, dass diese Arbeit entstehen konnte und dass ich dabei über die vergangenen vier Jahre hinweg immer mit Interesse, Motivation und Freude an meinen Problemstellungen arbeiten konnte.

Durch meinen Betreuer, Jochen Schieck, und seine Vorlesung über Dunkle Materie bin ich Ende 2014 erstmals mit besagtem Thema in Berührung gekommen und bekam Anfang 2015 die Möglichkeit, im Zuge einer Projektarbeit in seiner – erst kurz zuvor gegründeten – Forschungsgruppe am HEPHY mitzuwirken. Daraus hat sich ein Interesse entwickelt, das mich im weiteren Verlauf zum Absolvieren meiner Master- und nun auch meiner Doktorarbeit innerhalb seiner Rare-Event-Searches-Gruppe geführt hat. Danke, Jochen, dass du mich von Beginn an unterstützt und mich während des CRESST-Kollaborationstreffens 2017 in München davon überzeugt hast, mich auf die ausgeschriebene Dissertationsstelle zu bewerben.

Auch bei meinem Zweitbetreuer, Holger Kluck, den ich ebenfalls bereits im Zuge meiner Projektarbeit kennenlernen durfte, möchte ich mich herzlich bedanken. Als langjähriger Simulationskoordinator innerhalb der Rare-Event-Searches-Gruppe war er mein täglicher Ansprechpartner für jegliche Fragen zu unserer ImpCRESST-Software, zur Analyse simulierter Daten und zu vielen weiteren Themen. Außerdem ist er ein unermüdlicher Korrekturleser, dem kein Fehler entgeht, und hat dadurch einen großen Beitrag zur verbesserten Strukturierung dieser Arbeit geleistet. Lieber Holger, danke, dass ich so viel von dir Lernen durfte.

Ich hatte weiters das Glück eines zweiten Zweitbetreuers, Florian Reindl, bei dem ich mich ganz genauso bedanken möchte. Er hat mir, als Sprecher und Mitbegründer der COSINUS-Kollaboration, zu meinem zweiten großen Themenblock innerhalb meiner Doktorarbeit verholfen, bei dem ich unbezahlbare Erfahrungen sammeln konnte. Es ist ein besonderes Gefühl, in die Entstehungsgeschichte eines Experiments involviert zu sein und das Privileg zu genießen, aktiv an der Gestaltung und Planung mitzuwirken. Danke, Florian, für deine Unterstützung und Zeit, und für dein immer offenes Ohr für jegliche Fragen zu Detektoren, Datenanalyse und vielem mehr.

Es gibt unzählige weitere Kolleginnen und Kollegen am HEPHY, die nicht unerwähnt bleiben sollten. Valentyna Mokina hat mittlerweile die Simulationskoordination für CRESST übernommen und mich immer bei meiner Arbeit motiviert – thanks for all the sweets. Gemeinsam mit Daniel Schmiedmayer, den ich bereits seit Beginn meines Studiums zu meinen Freunden zählen darf, und Christoph Schwertner habe ich ein Büro am HEPHY geteilt und tolle Kameradschaft genossen. Um mich nun ein wenig kürzer zu fassen, sage ich außerdem danke Felix, Shubham, Leonie, Jens, Rituparna, Alex, Samir, Martin, Stephan, Vasile, Wolfgang und generell allen Gruppenmitgliedern für die positive Arbeitsatmosphäre am Institut.

Bei meinem Doktoratskolleg (DKPI), durch welches meine Dissertationsstelle finanziert wurde, möchte ich mich für viele interessante Summer Schools, Retreats und Kolloquien bedanken. Zusätzlich gab mir das DKPI die Möglichkeit, innerhalb des vierjährigen Doktorats zweimal drei Monate im Ausland zu verbringen und dort spannende Erfahrungen zu sammeln.

Im Zusammenhang mit den erwähnten Auslandsforschungsaufenthalten gilt Karoline Schäffner ein besonderer Dank. Als technische Koordinatorin und Mitbegründerin der COSINUS-Kollaboration hat sie mich Ende 2018 für drei Monate in ihre Forschungsgruppe ans LNGS eingeladen. Mit ihr und Vanessa Zema durfte ich am LNGS ein Büro teilen und unzählige interessante Gespräche führen. Zusätzlich haben mich Natalia Di Marco und Luciano Pandola während des Aufenthalts zu allen erdenklichen Fragen rund um meine Simulationsaufgaben beraten und dadurch einen wichtigen Grundstein für meine Arbeit in den darauffolgenden Jahren gelegt. Vielen Dank euch allen / grazie mille a voi! Und speziellen Dank noch einmal an dich, liebe Karo, für die spannende Zeit am LNGS.

Außerdem bedanken möchte ich mich bei Raimund Strauss, dem ich ganz zu Beginn meiner Arbeit beim Montieren der Detektormodule für CRESST-III Run35 im Reinraum des Experiments im LNGS über die Schulter schauen durfte. In seiner Gruppe an der TU München war ich später im Zuge meines zweiten Auslandsforschungsaufenthalts zu Gast. Gemeinsam mit den Kolleginnen und Kollegen vor Ort, insbesondere Alexander Langenkämper, Victoria Wagner und Margarita Kaznacheeva, konnte ich dort eine arbeitsintensive, aber hochinteressante Zeit genießen.

In meinem privaten Umfeld gilt besonderer Dank meinen Freunden und vor allem meiner Familie. Die sowohl mentale als auch finanzielle Unterstützung durch meine Eltern bei all meinen Zielen hat mir meinen bisherigen Weg deutlich erleichtert. Genauso wie meine Schwester und meine Freunde haben sie zusätzlich einen wichtigen Beitrag zu meiner – wie ich denke – gesunden Work-Life-Balance geleistet.

Abschließend bedanke ich mich bei meiner Freundin, die vor allem die Endphase meiner Doktorarbeit auf vielfältige Art und Weise bereichert hat. Mit dir an meiner Seite konnte und kann ich jederzeit Ruhe, Kraft und Motivation tanken.